Synchrotron X-ray operando studies of atomic structure evolution of multi-component Al alloys in liquid state

Shi Huang

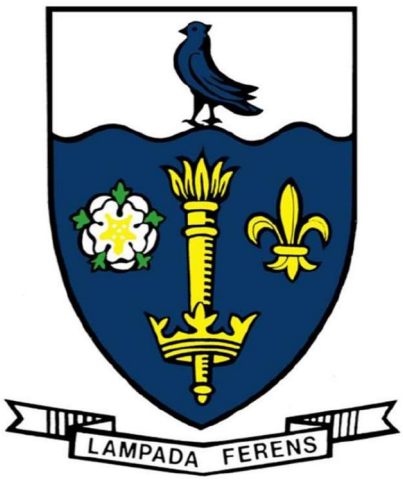

University of Hull

July 2023

Synchrotron X-ray operando studies of atomic structure evolution of multi-component Al alloys in liquid state

Shi Huang

A thesis submitted for the degree of

Doctor of Philosophy at the

University of Hull

July 2023

Abstract

This research has studied one of the challenging scientific issues in materials science, i.e., in real time, understanding quantitatively the 3D atomic structures of multiple component alloys in the liquid state and how the atomic structures evolve with temperatures until the onset of crystal nucleation. Four Al-based alloys were used in the research: (1) Al-0.4Sc, (2) Al-1.5Fe, (3) Al-5Cu-1.5Fe and (4) Al-5Cu-1.5Fe-1Si alloy (all in weight percentage). All alloys were heated up to the liquid state and then cooled down with predefined cooling rates using a dedicated solidification apparatus. During cooling, synchrotron X-ray was used to illuminate onto the samples and the total scattering data were collected at the target temperatures. Based on the total scattering data, the empirical potential structure refinement (EPSR) method was used to model and reconstruct the 3D atomic structures in the liquid state at the selected temperatures for each alloy. The research has demonstrated that the EPSR is a computationally efficient tool for searching and finding the solutions of 3D atomic structures according to the measured total scattering data. For the studied alloys, the research reveals fully the temperature-dependent structure heterogeneity and their evolutions with temperature. The key findings of the research are:

(1) For the Al-0.4Sc alloy, at the short-range scale in the liquid state, Sc-centred Al polyhedrons form icosahedral type structures with the Al coordination number in the range of 10–12. As the melt is cooled down, the Sc-centred polyhedrons become more compacted, and the connections between adjacent polyhedrons change from more vertex connection to more edge and then more face-sharing connection. At the medium-range scale, the Sc-centred clusters with face-sharing are proved to be the “precursors” for the $L1_2$ Al_3Sc primary phase in the liquid-solid coexisting region.

(2) For the three Fe-containing alloys, atomic structural heterogeneities were found to exist in the 1^{st} atomic shell and beyond. The degree of structural heterogeneities is related with the difference in atom radius, atomic bond length and the chemical preference between different atoms in each alloy. The competition resulted in that the Al-centred clusters expand, i.e., with larger bond length, while the solute atom-centred clusters contract, so with the reduced bond length.

(3) At the short-range scale, the structural heterogeneities were characterised by the co-existence and growth of the icosahedra-like (ICO-like) and crystal-like structures. During cooling, the Fe atoms show a higher degree of crystallinity than other atoms in the liquids. At the onset of crystal nucleation, relative percentage of the Fe-centred ICO-like and crystal-like Voronoi polyhedrons (VPs) reaches 8-10%, and the others in the range of 5.8-8.5%.

(4) The Fe-centred short-range orders (SROs) tend to connect together via five different modes to form larger Fe-centred medium-range orders (MROs). The percentage of the face-sharing increases almost linearly as the temperature is cooled down, approximately 18-20% at the onset of nucleation in the 3 melts. The Fe-centred MROs gradually approach to the structures of the $Al_{13}Fe_4$ primary phase (monoclinic structure) and are proved to be the nucleation precursors for the $Al_{13}Fe_4$ phases.

(5) For the quaternary Al-Cu-Fe-Si alloy melt, the research found that the liquid first transfers into a quasicrystal-like, metastable monoclinic $Al_{13}Fe_4$ phase. Such primary phase was confirmed to have a higher degree of five-fold and crystalline symmetry than the liquid. Upon cooling, the Fe-centred five-fold and crystalline symmetry both get enhanced in liquid, leading to a smaller $Al_{13}Fe_4$-liquid configuration entropy difference and interfacial free energy.

Dedication

I dedicate this thesis to my Mother (Wuying Shi), Father (Fengde Huang) and Sister (Nan Huang) for their love, support and trust in me that have shaped what I am today.

Acknowledgements

I am deeply grateful to the University of Hull and China Scholarship Council (CSC) joint PhD Studentship to support my doctoral study in the United Kingdom, a unique opportunity and experience that cannot be realised without it.

I would like to thank my supervisor, Professor Jiawei Mi, for his invaluable guidance and unwavering support throughout my PhD study. Professor Mi has patiently guided and supervised me throughout the project, provided me with many valuable opportunities of participating in many synchrotron X-ray operando experiments. Through which I have gradually learned the theories of alloy design and development and acquired hands-on skills in operating the most advanced synchrotron X-ray beamlines and instruments to study materials as well as writing and publishing scientific papers. I would also like to thank the 2nd supervisor, Dr Jiangbo Zhao (from 2021 onwards) who taught me the knowledge concerning the physics of amorphous materials, helping me write papers and correct thesis.

I would also acknowledge many of my fellow researchers in Prof Mi's group and the scientists in the Diamond Light Source, the ISIS Neutron and Muon Source, UK and the European Free Electron Laser, Hamburg Germany for the stimulating discussions and interactions, especially their strong support when conducting the challenging Synchrotron X-ray experiments at different beamlines. They are Drs Annette Kleppe (I15), Stefan Michalik (I12), Matteo Aramini (I20) of Diamond Light Source; Drs Tung Lik Lee (Engin-X), Daniel Bowron, and Tristan Youngs of ISIS. Dr Shifeng Luo, Dr Billy Koe, Mr Kang Xiang, and Miss Hongyuan Song in Prof Mi's group, Mr Yinxiu Chang of Computer Science, Mr. Chris Collins, manager of the Hull Viper Supercomputer. Supporting staff from the workshop, including Mrs Garry Robinson, Peter Lobo-Kazinczi, Simon Cowell, Stuart Butterick, Mike Jost, and Lee Wilson, just name a few.

I also sincerely thank my family and friends for their unwavering love, encouragement and patience. Their support and understanding have been invaluable for my PhD study, especially my late grandfather who sadly passed away before I started my PhD, his words of encouragement continued to resonate in my mind, motivating me all the way until I put down the last word in my thesis.

Journal papers, conference presentations and beamtimes awarded

Published journal papers

1. Wang, B.; Seffen, K. A.; Guest, S. D.; Lee, T.-L.; **Huang, S**.; Luo, S.; Mi, J., In-situ multiscale shear failure of a bistable composite tape-spring. Composites Science and Technology 2020, 200, 108348.
2. Zhang, Z.; Khong, J. C.; Koe, B.; Luo, S.; **Huang, S**.; Qin, L.; Cipiccia, S.; Batey, D.; Bodey, A. J.; Rau, C., Multiscale characterization of the 3D network structure of metal carbides in a Ni superalloy by synchrotron X-ray microtomography and ptychography. Scripta Materialia 2021, 193, 71-76.
3. **Huang, S**.; Luo, S.; Qin, L.; Shu, D.; Sun, B.; Lunt, A. J.; Korsunsky, A. M.; Mi, J., 3D local atomic structure evolution in a solidifying Al-0.4 Sc dilute alloy melt revealed in operando by synchrotron X-ray total scattering and modelling. Scripta Materialia 2022, 114484.
4. Luo, S.; Khong, J. C.; Daisenberger, D.; **Huang, S**.; McMillan, P. F.; Mi, J., Synchrotron x-ray total scattering and modelling study of high-pressure-induced inhomogeneous atom reconfiguration in an equiatomic Zr50Cu50 metallic glassy alloy. Physical Review B 2022, 105 (6), 064203.
5. **Huang, S**.; Qin, L.; Zhao, J.; Xiang, K.; Luo, S.; Michalik, S.; Mi, J. In Revealing atomic structure evolution of an Al-1.5 Fe alloy in the liquid state using X-ray total scattering and empirical potential structure refinement, IOP Conference Series: Materials Science and Engineering, IOP Publishing: 2023; p 012007.
6. Xiang, K.; **Huang, S**.; Mi, J. In Characterisations of the Al-Mn intermetallic phases formed under pulse magnetic fields solidification, IOP Conference Series: Materials Science and Engineering, IOP Publishing: 2023; p 012004.
7. Xiang, K.; **Huang, S**.; Song, H.; Bazhenov, V.; Bellucci, V.; Birnsteinova, S.; de Wijn, R.; Koliyadu, J. C.; Koua, F. H.; Round, A., Ultrasound cavitation and exfoliation dynamics of 2D materials revealed in operando by X-ray free electron laser megahertz imaging. arXiv preprint arXiv:2305.08538 2023.

Manuscript in preparation

1. **Huang, S**.; Luo, S.; Qin, L.; Xiang, K.; Michalik, S'; Shu, D.; Sun, B.; Chang, Y.; Zhao, J.; Mi, J. Synchrotron X-ray operando study of atomic structure heterogeneity and evolutions of recycled Al alloys in the liquid state, Acta Materialia, under review.
2. **Huang, S**.; Luo, S.; Qin, L.; Xiang, K.; Michalik, S'; Shu, D.; Sun, B.; Chang, Y.; Zhao, J.; Mi, J. Revealing the nucleation pathway of a metastable quasicrystal-like phase in multi-component liquid metal, under preparation.

Conference posters

1. Revealing the 3D local atomic structure in an undercooled binary Al alloy melt, Microscience Microscopy Congress 2021, 5th-9th July 2021, online.
2. Temperature dependent atomic structure evolution in an Al-0.4Sc dilute alloy melt revealed in operando by synchrotron X-ray total scattering and EPSR modelling, Neutron & Muon Science and User Meeting (NMSUM) 2022, 25th – 27th April 2022, Warwick, UK.

Conference oral presentations

3. In operando study of the transition from liquid to crystalline structure in a multicomponent Al alloy, Winter Crystallography Meeting 2021, 16th-17th May 2022, Oxfordshire, UK.
4. In operando study of the atomic transition from liquid to crystalline structure in an Al-5Cu-1.5Fe-1Si alloy", The UK Solidification Workshop 2022, 7th-8th June 2022, London, UK.
5. In operando study of the atomic transition from liquid to crystalline structure in a multicomponent Al alloy, Disordered Materials User Meeting2022, 14th-17th June 2022, Oxfordshire, UK.
6. In operando study of the atomic transition from liquid to crystalline structure in a multicomponent Al alloy, The 6th International Conference on Advances in Solidification Processes, 20th -24th June 2022, Le Bischenberg, France.

Synchrotron X-ray beamtimes awarded

1. Simultaneous in situ studies of the dynamics of multiple phase transformation of Al-base medium entropy alloys by synchrotron X-ray diffraction and tomography, 3 days (ID: MG31637) at the DIAD of Diamond Light Source.
2. Real-time study of the atomic structure and multiphase evolution of recycled Al alloys by 3D X-ray diffraction microscopy, 3 days beamtime (ID: MA 5840) at the ID11 of the European Synchrotron Radiation Facility.

Participation and contribution to other beamline experiments

I have done a number of synchrotron X-ray total scattering experiments in my PhD study. In addition, I also participated and contributed to many other synchrotron X-ray experiments conducted by other researchers in Prof Mi's group, including neutron diffraction, X-ray tomography, phytography, X-ray absorption spectroscopy, small-angle scattering, and ultrafast MHz imaging. These experiments were conducted at the Diamond Light Source, ISIS Neutron and Muon Source UK, and the Eu XFEL. The details are given in Table 1 below.

Table 1. The experiments that I have participated and contributed to

	Proposal number	Proposal title	Beamline & Facility	Experiment Date
1	EE20883-1	Studies of the Atomic Structures of Multicomponent Metal Glasses Using Pair Distribution Function and Anomalous X-ray Scattering	I15 DLS	28 Jan-01 Feb 2019
2	MG22525-1	Multimodal Imaging of the Metal Carbides in Ni Superalloys	I13-1 DLS	18 Jan-22 Feb 2019

3	RB1910213	In-situ studies of failure mechanisms of a bistable composite tape-spring under extreme conditions	Engin-X ISIS	19 Jun-23 Jun 2019
4	MG27571-2	In situ synchrotron X-ray total scattering studies of the dynamic evolution of atomic structures of metal alloys in liquid and undercooled liquid state	I12 DLS	14 Jul-23 Jul 2021
5	SM29575-1	Small-Angle X-ray Scattering Study of Ultrasound Exfoliated Multiple Nanolayer Graphite	DL-SAXS DLS	21 Sep-26 Sep 2021
6	MG27571-3	In situ synchrotron X-ray total scattering studies of the dynamic evolution of atomic structures of metal alloys in liquid and undercooled liquid state	I12 DLS	26 Sep-28 Sep 2021
7	No. 3100	Megahertz Imaging the Implosion of Ultrasonic Bubbles and Their Effects on Exfoliation of 2D Functional materials	SPB/SFX SASE1 Eu-XFEL	15 Sep-18 Sep 2022
8	SP32128-1	Revealing the evolution of electronic	I20-Scanning DLS	10 Feb-13 Feb

		state and bonding of gold atoms in coloured glasses		2023
9	MG33754-1	Kinetic pathways of nucleating gold in mechanochemistry-activated glass	E02	27 Feb-27 Feb 2023
10	MG31637-1	Simultaneous in situ studies of the dynamics of multiple phase transformation of Al based medium entropy alloys by synchrotron X-ray diffraction and tomography	DIAD	9 Mar-23 Mar 2023

Abbreviations list

SXTS	Synchrotron X-ray total scattering
DLS	Diamond Light Source
PDF	Pair distribution function
ISRO	Icosahedral short-range order
VP	Voronoi polyhedron
BOO	Bond-orientational order
EPSR	Empirical potential structure refinement
SROs	Short-range orders
MROs	Medium-range orders
XFEL	X-ray free electron laser
Eu XFEL	European X-ray free electron laser
CNA	Common neighbor analysis
CNT	Classical nucleation theory
CN	Coordination number
RDF	Radial distribution function
LCLS	Linac Coherent Light Source
NM	N-methyl morpholine
XANES	X-ray Absorption Near Edge Structure
EXAFS	Extended X-ray absorption fine structure
NMR	Nuclear magnetic resonance
IR	Infrared
RMC	Reverse Monte Carlo
LCLS	Linac Coherent Light Source
TEY	Total electron yield
MD	Molecular dynamics
AIMD	Ab initio molecular dynamics
CSRO	Chemical short-range order
AET	Atomic electron tomography
ABED	Angstrom-beam electron diffraction
HRTEM	High-resolution transmission electron microscopy
XEOL	X-ray excited optical luminescence
SFX	Serial Femtosecond Crystallography
JEEP	Joint Engineering, Environmental, and Processing
S-D	Sample-to-detector
FCC	Face-centred cubic
BCC	Body-centred cubic
HCP	Hexagonal Close-Packed

Symbols list

Q	The reciprocal space vector in scattering experiment
$F(Q)$	Reduced structural factor
$G(r)$	Reduced pair distribution function
$S(Q)$	Structural factor
$g(r)$	Total pair distribution function
$g(r)_{ij}$	Partial pair distribution function
$S(Q)_{ij}$	Partial structural factor
$S^N(Q)$	Structural factor for neutron scattering
$g^N(r)$	Pair distribution function for Neutron scattering
$S^X(Q)$	Structural factor for X-ray scattering
$g^X(r)$	Pair distribution function for X-ray scattering
c_i	c_i is the proportion (concentration) of atom i
$\bar{b}_i$	$\bar{b}_i$ is neutron coherent scattering length of atom i
$f_i(Q)$	Q-dependent X-ray scattering factors
α_{ij}	Warren–Cowley parameter for a nearest-neighbouring pair
Z_{ij}	The partial coordination number of atom pair
Z_i	The total coordination number of atom i
CN	Coordination number
RDF	Radial distribution function
U	The total potential energy of the EPSR system
$U^{(Ref)}$	The reference potential energy of the EPSR system
$U^{(Ep)}$	The empirical potential energy of the EPSR system
$U_{\alpha\beta}(\mathrm{r})$	The total potential energy between α-type and β-type atoms
$U_{\alpha\beta}^{(Ref)}(\mathrm{r})$	The total potential energy between α-type and β-type atoms
$U_{\alpha\beta}^{(Ep)}(\mathrm{r})$	The empirical potential energy between α-type and β-type atoms
r_{ij}	The separation of atoms (i,j)
$\alpha(i)$	The atom 'type' in EPSR simulation
ε_0	The permittivity of free space in EPSR
$I\ (Q)$	The total intensity of the scattered X-ray
$I_a^{coh}(Q)$	The coherent scattering intensity
$I_a^{inc}(Q)$	The incoherent scattering intensity
$I_b(Q)$	The background intensity
$I_{mc}(Q)$	The multiple-scattering intensity
$\mu(E)$	X-ray absorption coefficient
I_0	The intensities of the incident X-rays
I	The intensities of the transmitted X-rays
Q_l	A $2l+1$ dimensional complex vector
Y_{lm}	The spherical harmonics.
$\theta(r_{ij})$	The polar angle for BOO calculation

$\emptyset(r_{ij})$	The azimuthal angle
Q_4	The second-order BOO invariants ($l = 4$)
Q_6	The second-order BOO invariants ($l = 6$)
Q_{4fcc}	The Q_4 value of stand fcc structure
Q_{6fcc}	The Q_6 value of stand fcc structure

Contents

Chapter 1 Introduction

1.1 Background of the research

Material crystallization is a phase transition process from a disordered amorphous structure to an ordered crystalline structure, governed by the thermodynamics in the system. It is a dynamic process to move towards a lower and stable energy state. Understanding the dynamics of the disordered-to-ordered atomic structure transition in different material systems at different thermodynamic conditions has been one of the central topics in condensed matter physics and materials science [1-3]. The well-established classical nucleation theory (CNT) describes the formation of nuclei from the dynamic and stochastic association of monomeric units (e.g., ions, atoms, or molecules) that overcome a free-energy barrier at a critical nucleus size and grow out to a mature bulk phase in a homogeneous liquid [4-6]. However, more and more experiments [7-10] and computational studies [11-14] have indicated that liquid structure is not homogeneous, it may have more complex and heterogeneous structures with local spatial regions of different geometrical characteristics and mobility [7, 15, 16]. Very recent numerical simulations also suggested that such heterogeneous structures could further evolve into pre-ordered liquid atom clusters, serving as the precursors of crystal nuclei, i.e., there exist intermediate pre-nucleation steps in the crystallization process [2, 17-20]. For example, in metallic alloys, some recent simulation studies on pure metals (Fe [21], Ni [22-24], and Zr [25]) and binary alloy systems ($Cu_{50}Zr_{50}$ [25] and $Ni_{50}Al_{50}$ [25, 26]) have shown the presence of heterogeneous structures in the liquid state, which may facilitate nucleation or polymorph development. However, experimental validation and visualization of kinetic pathways of such precursor, the intermediate specie in between the liquid and the stable polymorph, are still missing.

Aluminium alloys are the most widely used lightweight metallic alloys in the aerospace, automotive, construction, and electrical industries. Their excellent recyclability makes them the materials of choice in many applications when sustainability and the environments are the essential requirements.

A quantitative understanding of the local atomic structure of Al-based alloys in the liquid state and their evolutions with temperature has been the central topic of many research works concerning the design and development of Al alloys. For example, in Al alloys added with transitional metal elements, Simonet and Holland-Moritz found the ISRO structures in the melts of Al-Pb-Mn [27], Al-Mn-Cr [28] and Al-Cu-Co [29] using neutron scattering and simulation. Molecular dynamics simulations also showed the existence of icosahedra in an Al-Sm [30, 31] and an Al-Cu[32] alloy. Their phase fraction decreased as the crystalline FCC clusters increased during the subsequent crystallization process. However, most simulation work lacks direct experimental evidence and validation. This poses an urgent need for robust real-time experiments in conjunction with such experimental-based 3D atomic structure simulation for revealing and elucidating the evolution of atomic structure in transition from the liquid to the solid state; this is also of significance for addressing how new phases are nucleated in the undercooled liquid or liquid-solid coexisting state that is useful for industry practice.

In addition, until now, almost all previous experimental studies on Al-based alloys used relatively high percentages (in excess of 10%) of solute elements, for example, $Al_{87.5}Fe_{12.5}$ [33], $Al_{80}Ni_{20}$ [34] and $Al_{86}Cu_{14}$ [35]. Such a high level of solute elements would result in the formation of detrimental or undesired intermetallic phases in most commercial alloy systems, except in some cases of specially designed high/medium entropy alloys [36]. For those elements added as grain refiners to Al alloys, e.g. Ti, Zr, Sc, the content is normally < 0.5wt% [37]. Therefore, an in-depth study and understanding of the dynamic interaction between Al atoms and the dilute alloy elements in the liquid and liquid-solid coexisting state are scientifically important. In this aspect, Sc and the primary Al_3Sc phases formed in the Al melt [38, 39] are also technologically important because Sc has been known as the best heterogeneous grain refiner, the most potent suppressor for recrystallization and the strongest hardener for aluminium alloys [40, 41]. Although some studies [42] on characterizing the 2D and 3D structure of Al_3Sc phases have been made, a precise understanding of how the primary Al_3Sc phase forms from a disordered liquid structure to its crystalline structure have not been seen reported.

Among many impurity elements existing in recycled Al alloys, Fe is the most detrimental one. It can form different types of plate-like and brittle Fe-rich intermetallic phases [43] which seriously damage the alloys' mechanical properties. For Al alloys containing a certain amount of Fe undergoing the solidification process, the primary monoclinic $Al_{13}Fe_4$ phase is often the first intermetallic phase to appear in the alloy melt during cooling. This may act as the nucleation site for α-Al [44], or transform to other type Fe-rich phases, e.g., hexagonal α-Al_8Fe_2Si or monoclinic orthorhombic β-Al_5FeSi [45, 46]. It is crucial to understand the nucleation mechanism of the primary $Al_{13}Fe_4$ phase and then develop a cost-effective processing strategy either to remove the excessive Fe or to alter the Fe-rich intermetallic phases into a less detrimental shape and morphology. The atomic structure of the liquid state is the parent state of the primary phase, it is thus necessary to show the atomic structure of the alloy melt to reveal the nucleation dynamics of $Al_{13}Fe_4$. Previous work on Al-Fe melts mainly focuses on binary Al-Fe alloys [33 47]. The role of Fe on the atomic structures of multicomponent alloy melts has not been seen or reported.

Given these research gaps, this research focuses on studying the atomic structure evolutions of 4 Al-based alloys from the liquid state to the onset of crystal nucleation. In particular, the structural heterogeneities in the liquid state and their evolutions with temperature, clarifying the role of structural heterogeneity that leads to the crystal nucleation.

1.2 The objectives of the research

The objectives of the research are:

(1) To precisely elucidate the temperature-dependant atomic structure evolution of Al-0.4Sc alloy in the temperature region where undercooled liquid and solid co-exist, the temperature region where active microstructure control techniques can be applied for optimising the microstructures of the alloys during solidification.
(2) To probe the local atomic structures of the Al-1.5Fe, Al-5Cu-1.5Fe, and Al-5Cu-1.5Fe-1Si alloy in the temperature range from 750 to 630 °C, i.e.,

above the liquidus, and to reveal the multiple atom interactions and the effect of alloy elements on the local atomic structures.

(3) To quantify the links between the structural heterogeneity and the primary phase at the nucleation stage.

1.3 The structure of the thesis

The thesis consists of 7 chapters as briefly described below.

Chapter 1 Introduction briefly describes the research background, objectives and structure of the thesis.

Chapter 2 Literature Review, including (1) Structures of disordered materials; (2) Synchrotron X-ray characterization techniques for amorphous materials; (3) Total scattering and data reduction (4) Modelling techniques based on a pair distribution function and the relevant experimental data (5) Geometrical structural descriptors.

Chapter 3 summarizes the design, building and commissioning of a counter gravity casting apparatus and a bespoke apparatus for in-situ synchrotron x-ray total scattering experiments, the sample manufacturing and preparation. This chapter also describes the relevant data processing methods and modelling procedures. The structure analysis methods, including the total scattering data reduction, Voronoi polyhedron (VP), bond-orientational order (BOO) and calculation of MRO connection modes etc., are also given in this chapter.

Chapter 4 is dedicated to the description of the disorder-to-order local atomic structure transition in a pure Al and a dilute Al-0.4Sc alloy melt in the temperature range from 690 °C down to 657 °C in operando conditions. The synchrotron X-ray total scattering (SXTS) and empirical potential structure refinement (EPSR) method are applied.

Chapter 5 presents a comprehensive atomic structure of Al-1.5Fe, Al-5Cu-1.5Fe and Al-5Cu-1.5Fe-1Si alloys in the cooling process and SXTS measurements in conjunction with EPSR modelling. In-operando structural heterogeneities evolution in three-dimensional are revealed. The effect of the structure heterogeneities on the nucleation of primary phases is also discussed.

Chapter 6 further discuss the nucleation mechanism of complex crystal with high five-fold symmetry in the quaternary Al-Cu-Fe-Si melt system. The degree of heterogeneities is quantified. How the development of local structure heterogeneities facilitates the nucleation of the metastable primary phase is systematically studied.

Chapter 7 concludes the major findings and contributions of this research to the disordered materials system and solidification process. Possible future work is also discussed in brief.

Chapter 2 Literature review

In this chapter, the literatures that are directly relevant to the research of atomic structures of disordered materials and liquid metals are critically analysed and reviewed. It consists of five parts: (1) the research on disordered materials; (2) the atomistic modelling and EPSR method; (3) the experimental techniques for studying disordered materials; (4) the geometrical structural descriptors for characterising geometry, and (5) the very recent research progress on disorder-to-order structural transition in metallic alloys.

2.1 The research on disordered materials

2.1.1 The concept of icosahedral type local atomic structures in liquid metals

This research is focused on the atomic structure of liquid metals, hence the historical development and the relevant literatures in this field are briefly reviewed and analysed. When a metastable liquid metal is cooled, its structure may undergo two possible transformations: crystallization or vitrification[48] (Fig. 2.1). Crystallization involves the formation of stable crystal nuclei that grow into an ordered crystal lattice structure.

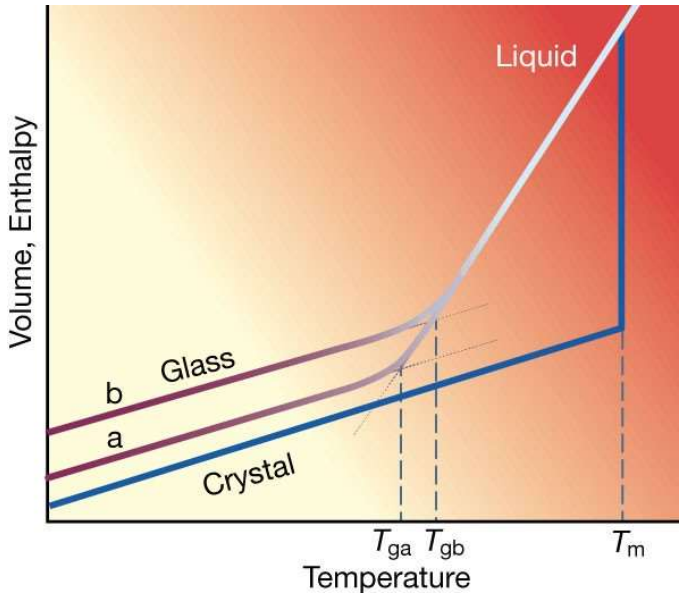

Fig. 2.1. A schematic, showing the volume/entropy as a function of temperature and the competition between glass transition and crystallization [49].

On the other hand, vitrification is that the liquid structure is "frozen" into the solid state and maintains the random atom arrangement from the liquid state. The first observation of vitrification was made in 1836 by the French scientist Joseph Louis Gay-Lussac [50], who also discovered the phenomenon of supercooling when water was found to maintain its liquid structure at the temperature below the freezing point. After that, researchers [51-53] invented and defined the term “vitrification”. The competition between crystallization and vitrification is driven by many factors, including cooling rate, alloy compositions, and inherent stability of the liquid [54].

In the crystallization pathway, to overcome the energy barrier for initiating crystal nuclei, the liquid needs to be undercooled below its equilibrium melting temperature. In 1950, Turnbull [55] demonstrated that metallic liquids could be cooled far below their equilibrium melting temperature without crystallization, suggesting a large energy barrier does exist in the formation of an ordered phase. This observation challenged the assumption that the barrier separating liquid and crystal phases in metals and alloys was small. In 1952, Frank [56] proposed that the undercooled metallic liquids have distinct local atomic structures with a significant degree of icosahedral short-range order (ISRO) (Fig. 2.2a), which is incompatible with the extended periodicity of crystals (see the unit cell example in Fig. 2.2b). A regular icosahedron exhibits 20 equilateral triangular facets, 12 vertices and 30 edges. axes linking opposite vertices correspond to fivefold symmetry axes, those going through the centres of opposite facets/edges correspond to threefold/twofold symmetry axes, respectively.

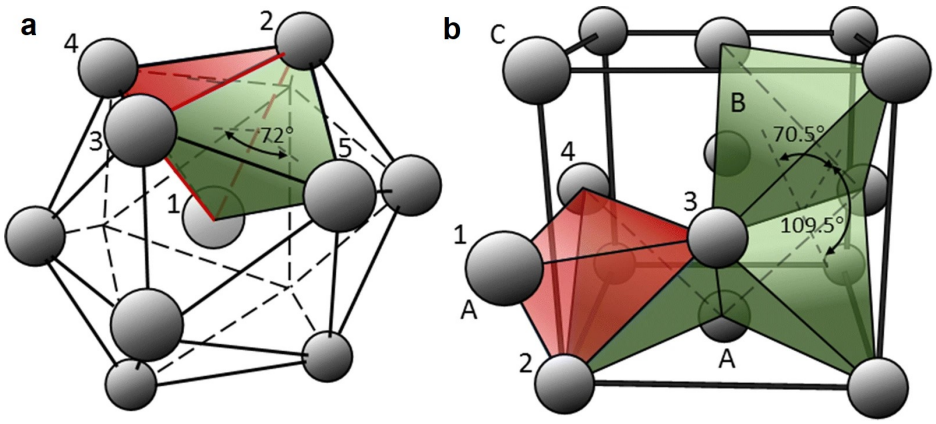

Fig. 2.2. (a) An icosahedron with two nearest-neighbours of its 20 tetrahedra shown in red and green; (b) a unit cell of the fcc structure with the representation

of 3 of the 8 tetrahedra made of (1 1 1) planes and 〈110〉 edges (in green) and one stacking fault induced by the attachment of one tetrahedron (in red) [57].

Compared to the fcc/hcp structures, the icosahedron has better rotational symmetry and more bonds. Therefore, in a cluster of 13 atoms, the icosahedron is a more energy-favourable geometrical arrangement than fcc/hcp, and it could be the dominant structure in monatomic liquids [57]. Such local structural difference between liquid and solid would result in a big configurations entropy difference and creates a barrier to crystal formation, explaining the observed undercooling behaviour.

In the next five decades, several experimental and theoretical studies agreed well with Frank's hypothesis, while do not give a direct proof [58]. In 2000, Reichert et al. [59] studied the structure of liquid Pb on a Si (0 0 1) substrate at the solid–liquid interface (i.e., the Si-Pb interface) by synchrotron X-ray diffraction at the temperature 10K above liquidus (600·6°K). The experiment revealed a five-fold local symmetry of the liquid Pb at the Si (0 0 1) interface, and this was the first direct evidence of the existence of ISRO in liquid metals. ISRO was also reported in undercooled Ni, Fe, and Zr liquid [60]. The above results confirmed Frank's hypothesis that ISRO does exist in undercooled liquids. However, the link of ISRO to the nucleation of a solid phase was not experimentally established until Kelton's work in 2003 [58]. Kelton suggested that development of the ISRO in liquid $Ti_{39.5}Zr_{39.5}Ni_{21}$ during cooling would reduce the nucleation barrier for the primary quasicrystal phase with five-fold symmetry. Such phase is metastable and will transfer to stable C14 Laves phase with further cooling. Several neutron and X-ray scattering experiments have been performed to elucidate ISRO in metallic liquids. However, only average structural information can be revealed by the 1D diffraction profiles generated by the statistical distribution of coexisting polyhedra of different geometrical distortions in real materials[32, 61]. Direct observation of local icosahedral order in liquid is still missing. Until now, a few studies on metallic glass have suggested the existence of ISRO by using angstrom-beam electron diffraction [61] or atomic electron tomography reconstruction method [62].

2.1.2 The experimental techniques for local atomic structure characterisation

To study the local atomic structures of amorphous materials, two experimental methods are routinely used. Firstly, the diffraction and scattering techniques using neutron [63], X-rays [64] and electrons [65, 66] which can measure the interatomic distances and generate the pair distribution functions (PDFs). Secondly, the resonance and spectroscopic methods, e.g., nuclear magnetic resonance (NMR) [67], Extended X-ray absorption fine structure (EXAFS) [68], (infrared) IR [69], and Raman spectroscopy[70], which can provide detailed structural information about metal coordination or molecular geometries in certain cases [71, 72]. The above techniques are able to acquire very rich structural information.

In the past 20 years, several sophisticated methods have been developed to model or reconstruct the 3D atomic models by matching or fitting to these experimentally measured data [73]. In this aspect, the reverse Monte Carlo (RMC) [74], Empirical Potential Structure Refinement (EPSR) [75] and ab initio molecular dynamics (AIMD) methods have been widely used in glasses and amorphous materials. Fig. 2.3 gives an example, comparing the structural factors and PDFs of liquid Alumina at the selected temperatures obtained from synchrotron X-ray and neutron total scattering. The diffraction patterns have been fitted with Empirical Potential Structure Refinement (EPSR) models and compared to classical Molecular Dynamics (MD) simulation results. Both EPSR and MD simulations reveal a direction of the temperature dependence of the aluminate network structure which moves further away from the glass forming ideal (nAlO = 3) during supercooling.

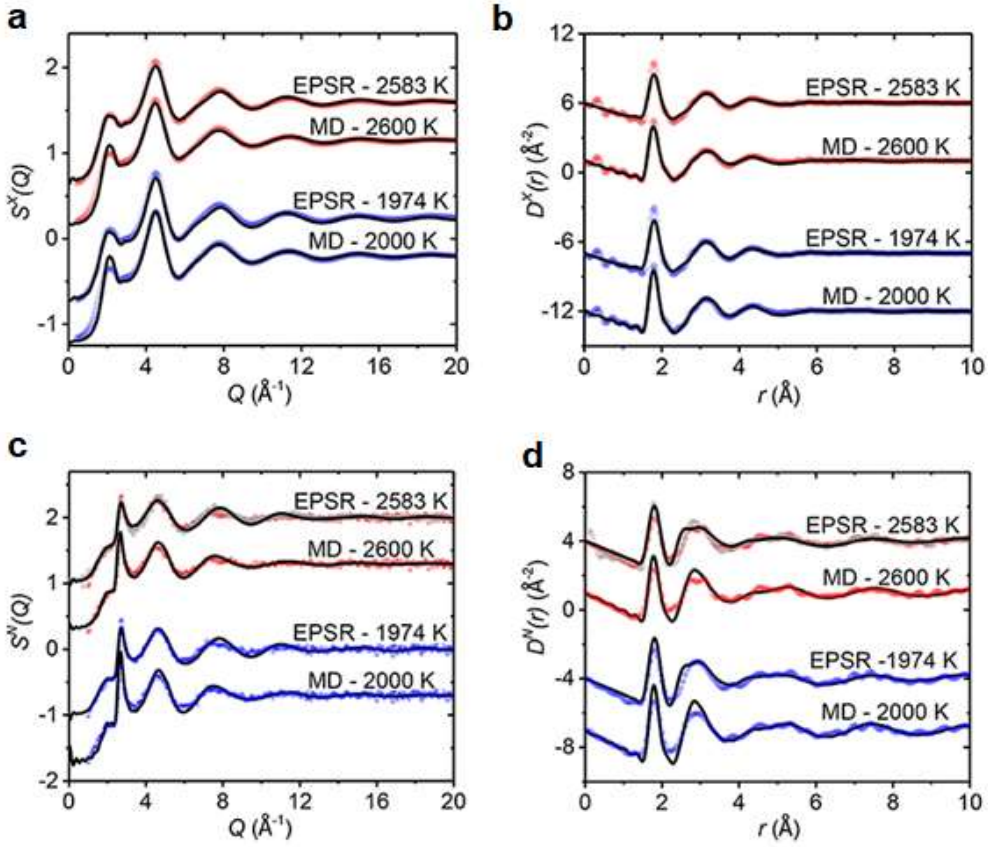

Fig. 2.3. The X-ray [76] (a, b) and neutron [77] (c, d) total structure factors $S(Q)$ (a, c) and total PDFs D(r) (b, d) of liquid alumina (D(r) is adopted to align with the original work), obtained with a Q_{max} of 20.0 Å^{-1}. Each panel compares the measured data (points) to the EPSR and MD simulation results (solid black lines).

The scattered intensity of the structure factor from neutron and synchrotron differs a lot. However, the modelled results by EPSR and molecular dynamics method agreed very well with the experimental data. In addition, other relatively new methods such as PDFFIT [78] and "Liga" [79] have been used in simulating the nanostructured solids like C60 [80] and ferrihydrite [81] according to PDF data, which are also challenging tasks in crystallography.

2.1.3 Theories of structure factor and pair distribution function

In this work, I mainly used X-ray total scattering to generate PDFs, then I used the EPSR to search and reconstruct the 3D atomic structures based on the PDFs. Hence, the basic theories about structure factor and PDFs are given in this section to provide the theoretical background.

When X-rays, neutrons, or electrons are used to illuminate onto a sample, an appropriate detector can be used to collect the scattered information (pattern) from the sample. Total scattering collects the complete scattering (diffraction) pattern, including both Bragg and diffuse information [82]. Bragg scattering arises from the constructive interference diffracted by crystal planes of the measured sample crystal lattice, which contains the averaged information about the long-range atomic structures in the scattering volume. Diffuse scattering in the diffraction patterns may arise from an irregular arrangement of atoms on the lattice sites that may contain some short-range ordering of the site occupancies or from the disordered arrangement of vacancies, interstitials or impurity atoms[83] [84]. Total scattering measurements can be used to quantify the local, instantaneous, atomic structure of a material, glass or liquid. As local non-crystalline order only gives rise to weak or very weak diffuse scattering information, total scattering measurements often require a clean and coherent radiation beam like monochromatic Synchrotron X-rays coupled with high sensitive detector [85, 86].

PDF, i.e., $g(r) \sim r$ as schematically illustrated in Fig. 2.4, is a statistical function for calculating the distribution probability of atoms relative to a reference atom at a certain distance [87]. Dependent on the research fields, sometimes, PDF is also called radial distribution function or pair correlation function [86].

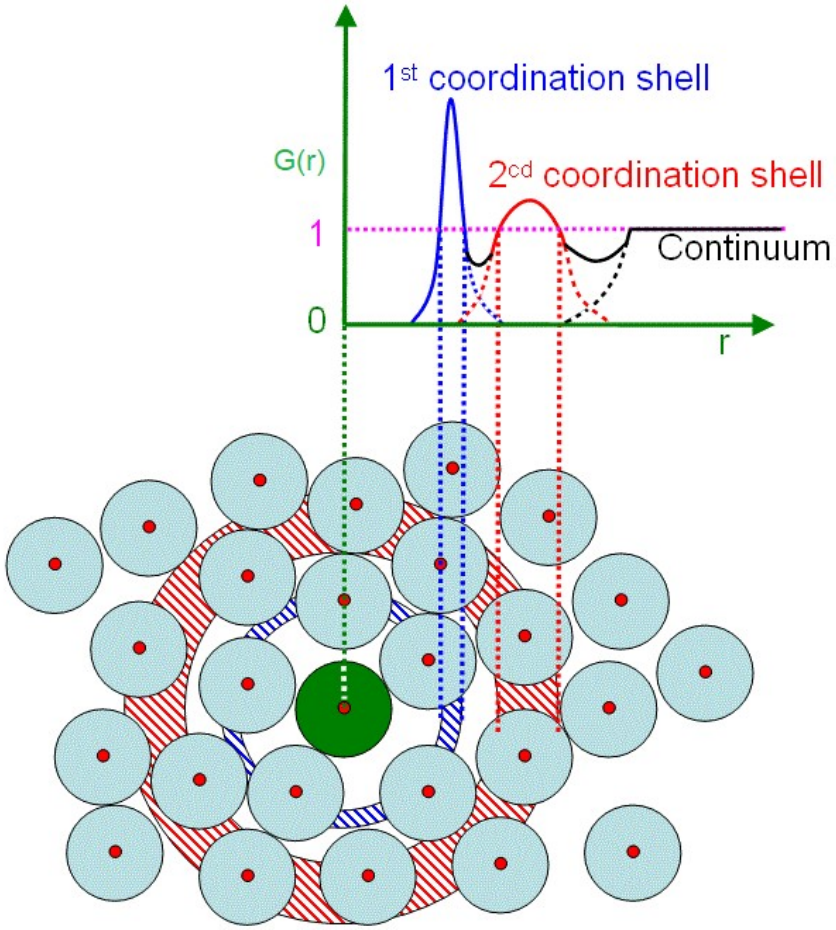

Fig. 2.4. A schematic illustration of PDF[88], i.e., $g(r)$ ~ r and r is the atomic separation distance.

It normally takes three steps to get the $g(r)$ from a total scattering experiment (see Fig. 2.5). First, to obtain the raw scattering data via experiments. Second, to reduce the raw data to obtain the structure factor $S(Q)$ (Q is the wavevector). Finally, to Fourier transform the $S(Q)$ to get the $g(r)$. PDFs have been widely used in many research fields in which different mathematic formula were often used to emphasize the particular physical features or structural characteristics [89]. This often leads to confusion to those new to the uses of PDFs.

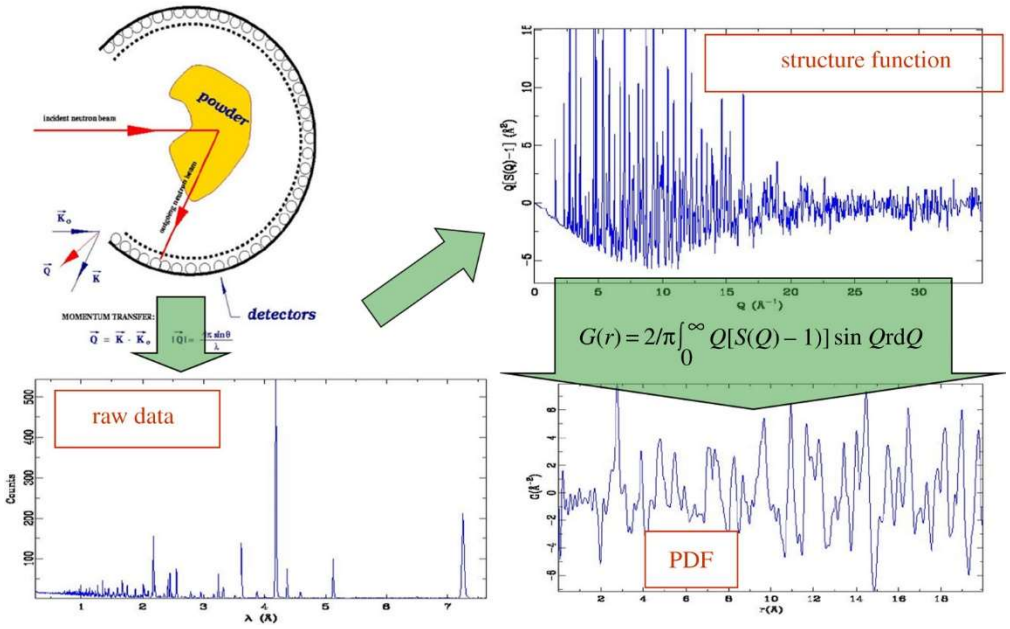

Fig. 2.5. Schematic of the process for obtaining atomic PDFs [90].

2.1.3.1 The formula for structure factors and PDFs

To solve this confusing formulism of PDFs in different fields, in 2001, Keen[91, 92] defined a self-consistent set of formulae for total scattering using neutrons and X-rays. For neutron scattering, the total scattering structure factor, $S^N(Q)$ is written as (the superscript *N* denotes neutron scattering):

$$S^N(Q) - 1 = \frac{1}{M}\frac{d_\sigma}{d_\Omega} - \sum_{i=1}^{n} C_i \overline{b_i^2} \tag{2.1}$$

Where $(\frac{1}{M})(\frac{d_\sigma}{d_\Omega})$ is the differential neutron scattering cross-section, c_i is the proportion (concentration) of atom i, and $\bar{b}_i$ is neutron coherent scattering length of atom i [93].

For *M* atoms and n atom species in a material system, $4\pi r^2 \sum_{i=1}^{n} C_i \overline{b_i^2}$ is the neutron total scattering cross-section of the material. $S^N(Q)$ can be also expressed as [94]:

$$S^N(Q) - 1 = \sum_{i,j=1}^{n} \bar{b}_i \bar{b}_j c_i c_j [S_{ij}(Q) - 1] \tag{2.2}$$

where $S_{ij}(Q)$ is the partial structure factor.

By Fourier transformation of $S_{ij}(Q)$, the partial PDF $g_{ij}(r)$ can be obtained as below:

$$g_{ij}(r) - 1 = \frac{1}{(2\pi)^3 \rho_0} \int_0^\infty 4\pi Q^2 \left[S_{ij}(Q) - 1\right] \frac{\sin(Qr)}{(Qr)} dQ \tag{2.3}$$

where ρ_0 is the number density [91] typically expressed in atoms per Å^3.

Based on $g_{ij}(r)$, the total PDF for neutron, $g^N(r)$, is calculated by [89]:

$$g^N(r) = \sum_{i,j=1}^{n} c_i c_j \bar{b}_i \bar{b}_j [g_{ij}(r) - 1] \tag{2.4}$$

The X-ray formalism is a bit more complex because the neutron scattering lengths, $\bar{b}_i$ used in the Eq. 2.1 above must be replaced by Q-dependent X-ray scattering factors, $f_i(Q)$. The total scattering structure factor, $S^X(Q)$ from synchrotron X-ray can be expressed as (the superscript *X* denotes X-ray scattering):

$$S^X(Q) - 1 = \frac{\left[\frac{1}{M}\frac{d_\sigma}{d_\Omega} - \sum_{i=1}^{n} c_i f_i\,(Q)^2\right]}{\left[\sum_{i,j=1}^{n} c_i f_i(Q)\right]^2} \tag{2.5}$$

where $\left[\sum_{i,j=1}^{n} c_i f_i(Q)\right]^2$ is the 'sharpening' term used to enhance the high-Q scattering by counteracting the natural fall-off in intensity due to the form of the X-ray scattering factors. $\sum_{i=1}^{n} c_i f_i\,(Q)^2$ is used as an alternative sharpening term [92]. Following the similar derivation as Eq. 2.2:

$$S^X(Q) - 1 = \sum_{i,j=1}^{n} c_i c_j f_{ij}\,(Q)[S_{ij}(Q) - 1] \tag{2.6}$$

where

$$f_{ij}(Q) = \frac{f_i(Q) f_j(Q)}{\left[\sum_{i,j=1}^{n} c_i f_i(Q)\right]^2} \tag{2.7}$$

By Fourier transformation of $S^X(Q)$, the total PDF is typically calculated as

$$g^X(r) = \frac{1}{(2\pi)^3 \rho_0} \int_0^\infty 4\pi Q^2 \left(S^X(Q) - 1\right) \frac{\sin(Qr)}{(Qr)} dQ \tag{2.8}$$

The coordination number of atoms surrounding a specific reference atom is the average number of the nearest neighbouring atoms. The positions of these neighbours are statistically described [95] by the radial distribution function:

$$RDF = 4\pi\rho r^2 g(r) \tag{2.9}$$

It represents the number of atoms on a spherical surface of radius r. ($\mathrm{g(r)}$ is the total PDF). The integral of the RDF between two distances r_1 and r_2 (two consecutive local minima as illustrated in Fig. 2.4) gives the average number of the neighbouring atoms and it is called the coordination number:

$$CN = \int_{r1}^{2} RDF(r)dr = \int_{r1}^{r2} 4\pi r^2 g(r)dr \tag{2.10}$$

The region between the two consecutive minima is called the coordination shell. The coordination number is often used to track the change or evolution of local atomic structures during phase transition, providing insights into the bond formation, bond breaking, and atom rearrangement. For example, there are numerous experimental reports on coordination number changes near the melting point, providing valuable data on structural transformations during phase transitions [96, 97].

The spatial resolution PDF is directly linked to the maximum value of Q, (i.e., Q_{max}) in diffraction experiments. Q_{max} is proportional to the maximum scattering angle and inversely proportional to the wavelength of the radiation used (usually >20 Å^{-1}). Therefore, to achieve the largest possible Q_{max} and attain maximum resolution in the PDF, total scattering experiments typically employ the shortest practicable radiation wavelength, usually less than or equal to 0.5 Å. Such short radiation wavelengths are readily available at neutron sources like Institut Laue–Langevin (ILL) in Grenoble, France, or ISIS in the UK, as well as at synchrotron X-ray sources (ESRF, DLS). PDFs are less commonly used in laboratory X-ray sources.

Several errors may occur when generating the PDF data, potentially leading to inaccurate or spurious results. These errors might come from the following aspects [98]:

(1) Termination errors arise when the collected data does not extend to a sufficiently high Q_{max} value. They manifest as ripples in the data at unphysically low radii and satellite ripples near the peaks. To mitigate termination errors, damping methods can be employed cautiously. However, the best approach is to collect data with a higher Q-resolution, reaching as high a value of Q_{max} as possible [99, 100].

(2) Statistical errors: Increased noise at higher Q can lead to statistical errors in the PDF data. Choosing an appropriate Q_{max} value requires balancing this noise with the termination errors produced.

(3) Insufficient Q-resolution: Inadequate Q-resolution affects r_{max}, which is the upper limit of the range over which oscillations are observed in the PDF pattern. Ideally, the Q-resolution should be as high as possible, although this often involves sacrificing intensity [101, 102].

(4) Systematic errors: Systematic errors can arise from incorrect absorption correction, background subtraction, and intensity normalization [98]. Special care must be taken when performing these procedures to minimize systematic errors. Good signal-to-noise data are necessary for both the sample and the background (e.g., the sample holder, furnace chamber) [103].

In the late 1980s, the first PDF measurements were conducted to study the local structure of quasicrystals, initially with measurements using anomalous X-ray diffraction [104, 105] and then using neutron diffraction [106], taking advantage of the new developments of Synchrotron X-ray and spallation neutron sources, respectively [92]. Since that, new diffractometers using (1) neutrons (2) synchrotron X-rays and (3) electrons are developed, providing opportunities for the development of total scattering techniques. Concurrently, the emergence of modelling methods such as Reverse Monte Carlo modelling [107], PDFFIT [108], and Empirical Potential Structure Refinement (EPSR) modelling have greatly contributed to the study of a diverse range of materials. These modelling

approaches have played a significant role in interpreting and analysing total scattering data, allowing for a deeper understanding of materials' structures.

2.1.4 Fine structures behind pair distribution function

In PDF analysis, the structure of liquid is generally described in terms of two-body correlation functions, that is, the structure factors and the PDFs. The structure factor refers to the two-point correlation function of the microscopic density; the PDF refers to the two-point correlation function of variation of density as a function of distance from a reference particle. For the two-body correlation, the PDF technique can provide insights into the average interatomic distances, coordination environments, and certain structural features. On a microscopic level, particles in liquids can exhibit short- and medium-range order. The length scale of these two structural orderings can be quantified by the peak position analysis. Medium-range order, typically on a length scale of 5-10 Å, refers to structural ordering in amorphous systems beyond the nearest neighbour distances (short-range order, typically within 5 Å) [109]. One of the most famous local structures directly revealed by PDF is the splitting of the second peak in the PDF, such phenomenon often indicates the emergency of local structure order in colloidal hard spheres and metallic glasses system [110]. Many researchers also found in the cooling process of liquid metal, the peak height of PDF always gets higher, sign of the liquid is becoming more ordered upon cooling [111].

In spherically averaged systems, e.g., liquid metals, two-body correlations may not be sufficient to probe the local structure, or there are still much more fine structures to be found. For instance, within a narrow temperature range, the PDF might not show significant changes. However, there is a strong tendency towards local ordering as having been found in systems as diverse as simple liquids (such as hard spheres) and liquids interacting with directional bonding (such as water).

Many-body correlations become increasingly important in the supercooled state of a liquid, with strong influences on the local mobility and crystallization dynamics [112]. For liquid metal, researchers focus more on structure ordering interacting with isotropic potentials. Because there are no symmetry-breaking directional interactions, the main driving force in the liquid metal comes from packing and excluded-volume effects, which are essentially many-body effects. The relevant

geometrical structural descriptors include Voronoi face analysis, common neighbour analysis, bond-orientational order analysis, Minkowski structure metrics, local packing capacity, etc. Here some cases of the hidden structure that could be revealed by many-body correlations are presented.

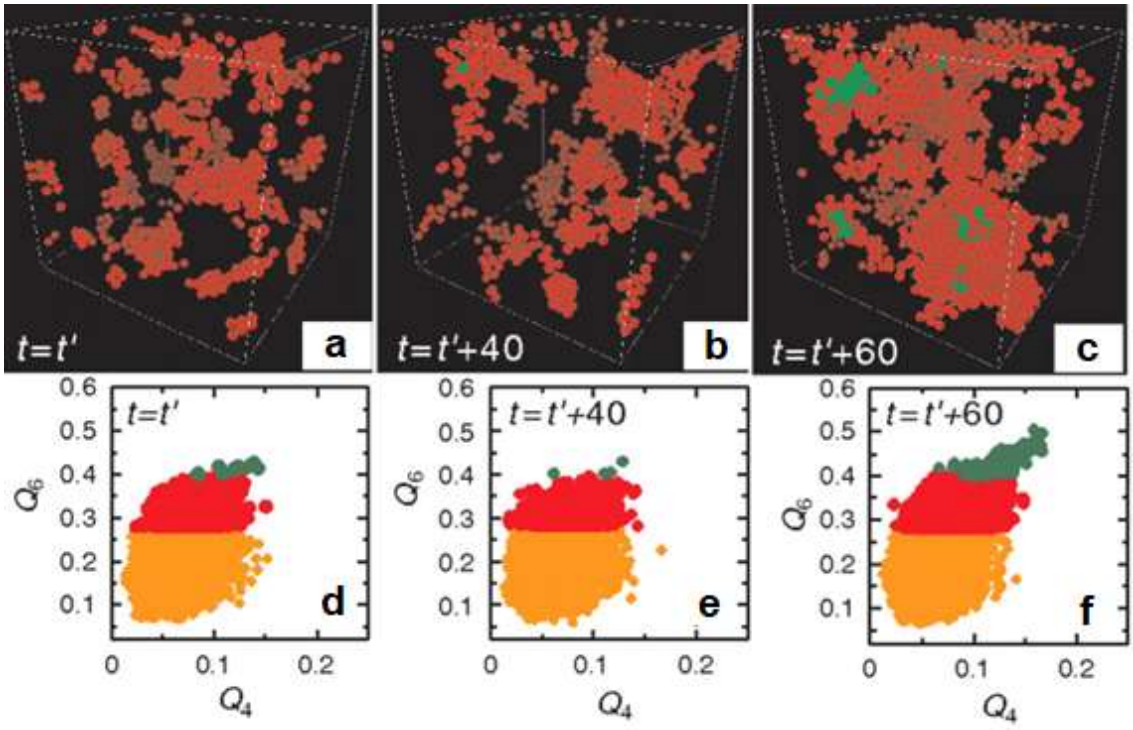

Fig. 2.6. Birth of fcc crystal nucleus from medium-range structural order characterized by temporal bond-orientational order analysis [2].

Fig. 2.6 illustrates how fcc crystal nucleated in a supercooled state of a monodisperse hard-sphere (colloidal) system. The bond orientational order before crystal nucleation ($t = t'$) is characterized by hcp-like symmetry (red atoms in Fig. 2.6a, b and c; the red dot on the $Q_4 - Q_6$ map), whereas the crystals nucleated have a mixed character of hcp and fcc-like order (the green atoms in the simulation box and green dots on the map). When $t = t' + 60ns$, the pre-ordered atoms (red) connect with each, forming medium-range orders. The crystallinity degree (Q_4) of the system gets dramatically increased as well as the lattice match degree (Q_6), forming the primary nuclei. Such fine structure cannot be probed by PDF only. To address the challenging issues in amorphous materials, it is necessary to reveal and quantify the fine structures behind PDFs.

2.2 Atomistic modelling and empirical potential structure refinement method

In this section, the main atomistic modelling techniques are briefly introduced, including the EPSR methods I used in this research.

2.2.1 “small-box” and “big-box” modelling

Small-box modelling often refers the use of a simulation box containing <1000 atoms, for example, the PDFgui [113] for calculating structures from crystals and has recently been extended to nanocrystals according to the PDF data. By incorporating a regression loop, PDFgui automatically updates structural parameters to improve the fit with the data. This method is robust against most data normalization issues encountered in reciprocal space total scattering structure factor data, allowing for more tolerance of scattering data quality [114-117].

While the big-box methods, such as RMCProfile [118-122] and EPSR work on systems of >1000 atoms and rely on the uses of normalized total scattering data. Due to their dependence on normalized data, big-box refinements emphasis more on obtaining high-quality data [123-126]. Any smoothly varying offset or inconsistencies in the reciprocal space data can adversely affect the fit to $F(Q)$, leading to poorer results. It is important to note that while such inconsistencies may cause problems in the low-r region of the PDF, they are typically ignored in small-box refinements. Additionally, big-box refinements generally require longer setup times, as they involve more complex modelling procedures. Data normalization becomes critical during the setup, ensuring that the data is appropriately scaled and consistent across different scattering techniques. Tools such as, PDFgetX3 and GudrunX, are specifically designed for X-ray data normalization, ensuring that the PDF data is placed on an appropriate scale, which is essential for accurate big-box refinements.

When choosing the "small-box" or "big-box" modelling, certain things need to be considered [92]. If extensive disorder is present within the atomic structure, big-box modelling is more suitable. Conversely, if the disorder is short-ranged or results in minor distortions, PDFgui is appropriate. RMCProfile or EPSR are better choices for refining structures with large atom displacements, atom diffusion, or

when disorder extends beyond the size limitations of small-box models. In this work, EPSR was chosen.

2.2.2 Empirical potential structure refinement modelling

The EPSR has been developed by the Disordered Materials Group (ISIS, UK), and it is utilized to calculate three-dimensional structures by leveraging the information found in diffraction data [127]. EPSR iterates a direct Monte Carlo simulation of a molecular system, correcting the pair interaction potential between molecules at each stage of the iteration by comparison with the diffraction data sets, aiming to construct structural models for glass and liquid materials [123-126]. The working flowchart can be found in Fig. 2.7.

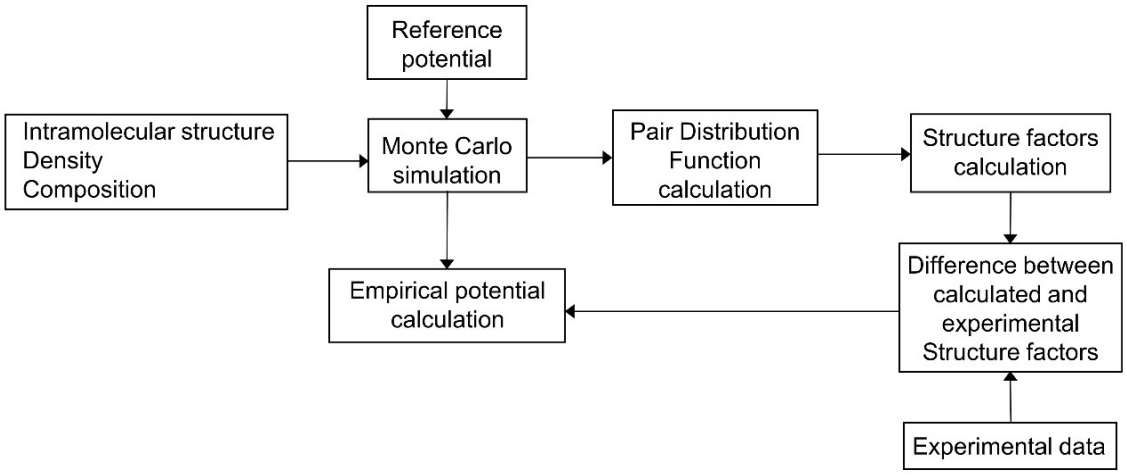

Fig. 2.7. Flowchart of the EPSR simulation algorithm [75].

EPSR simulations typically involve four types of atom movements [128]: (1) whole molecule translations, (2) whole molecule rotations, (3) rotation of specific molecular sidechains (if applicable), and (4) individual atomic moves within molecules. If a "molecule" consists of only one atom, only whole molecule translations are needed. Hence, during the EPSR simulation for liquid metal, there only are the 'whole molecule translations'. The acceptance of an atom move within EPSR follows the standard Metropolis condition [129]. If the change in potential energy of the system due to the move, when $\Delta U = U_{after} - U_{before}$ is less than zero, the move is always accepted. If ΔU is greater than zero, the move is accepted with a probability given by $exp(-\frac{\Delta U}{kT})$, where k is the Boltzmann

constant and T is the temperature. This approach ensures that the system evolves along a Markov chain and, over time, explores a significant portion of the available phase space.

The potential energy in EPSR comprises two primary components: the reference potential energy $U^{(Ref)}$ and the empirical potential energy $U^{(Ep)}$. This potential is utilized throughout the EPSR simulation [130], initially, it is employed independently to generate the molecules (if present) and to position the simulation box within a plausible region of phase space for the studied system. This ensures sensible molecular geometries and avoids atomic overlap, among other considerations. The $U^{(Ref)}$ follows a standardized form and its parameters can typically be found in the literature. On the other hand, $U^{(Ep)}$ does not conform to a standard form. Once the simulation with the reference potential alone reaches equilibrium, $U^{(Ep)}$is utilized to guide atomic and molecular movements in directions that best represent the diffraction data. The total potential energy of the system is expressed as

$$U = U^{(Ref)} + U^{(Ep)} \tag{2.11}$$

Each term in this context can be divided into components associated with the separation of individual atoms and molecules, wherein atoms of distinct types exhibit varying interaction potentials. For instance, the potential energy between α-type and β-type atoms, separated by a distance r, can be expressed as follows:

$$U_{\alpha\beta}(\mathrm{r}) = U_{\alpha\beta}^{(Ref)}(\mathrm{r}) + U_{\alpha\beta}^{(Ep)}(\mathrm{r}) \tag{2.12}$$

with the total potential energy of the system given by

$$U = \frac{1}{2}\sum_{i}\sum_{j\neq i} U_{\alpha(i)\alpha(j)}\,(r_{ij}) \tag{2.13}$$

where r_{ij} is the separation of atoms (i,j), and $\alpha(i)$ represents the atom “type”.

More specifically, the reference potential is based on a combination of Lennard-Jones12-6 potential and Coulomb potentials [128]:

$$U_{\alpha\beta} = 4\varepsilon_{\alpha\beta}\left[\left(\frac{\sigma_{\alpha\beta}}{r}\right)^{12} - \left(\frac{\sigma_{\alpha\beta}}{r}\right)^{6}\right] + \frac{1}{4\pi\varepsilon_0}\frac{q_\alpha q_\beta}{r}, \tag{2.14}$$

where $\varepsilon_{\alpha\beta} = \sqrt{\varepsilon_\alpha \varepsilon_\beta}$, $\sigma_{\alpha\beta} = 0.5(\sigma_\alpha + \sigma_\beta)$, and ε_0 is the permittivity of free space. $\varepsilon_{\alpha\beta}$ is the well depth parameter, $\sigma_{\alpha\beta}$ is the range parameter, q_α and q_β are Coulomb charges of atoms *α* and *β*.

A fundamental principle in establishing the empirical potential is to ensure that it should represent the true differences between the simulation and diffraction data, without incorporating artefacts arising from statistical noise, systematic errors, or truncation effects present in the diffraction data. By avoiding these artefacts, the estimated distribution functions of the system can be more accurately determined.

Generating the empirical potential $U^{(EP)}$ in practice is challenging, the most successful one thus far involves utilizing a series of power exponential (Poisson) functions [127]:

$$U^{(EP)} = kT \sum_i C_i p_{n_i}(r, \sigma_r) \tag{2.15}$$

where

$$p_{n_i}(r, \sigma_r) = \frac{1}{4\pi\rho\sigma^3(n+2)!}\left(\frac{r}{\sigma}\right)^n \exp\left(-\frac{r}{\sigma}\right) \tag{2.16}$$

The C_i coefficients are estimated directly from the diffraction data by fitting a series of forms to the data in Q space using Eq. 2.17. It is real but can be positive or negative, and σ_r is a width function to be set by the user. The total atomic number density of the simulated system is ρ.

$$U_{EP}(\mathrm{Q}) = \sum_i C_i p_{n_i}(r, \sigma_Q) \tag{2.17}$$

In EPSR simulations, explicit corrections for long-range effects on the potential energy are not included for two main reasons. Firstly, the empirical potential (EP) used in EPSR simulations is typically unreliable for distances beyond a certain threshold, represented as r_{max}. Secondly, incorporating the necessary long-

range corrections can be computationally demanding without providing significant benefits or significantly altering the local arrangement of atoms.

In EPSR simulations, the partial PDF, $g(r)_{ij}$, is typically calculated only up to half the box dimension (or the corresponding maximum distance in the case of a non-cubic box). Fig. 2.8 illustrates an example of a uniform atom distribution in a silica simulation using a cubic box with dimensions of 27.9988 Å and an atomic number density of 0.06834 atom/Å³. The distribution shows an obvious increase until reaching the edge of the box at 13.9994 Å. Beyond this point, there is a sharp decline as the volume sampled in the corners of the box becomes progressively smaller. Eventually, the distribution completely vanishes at a distance of r = √3 × 13.9994 = 24.2477 Å.

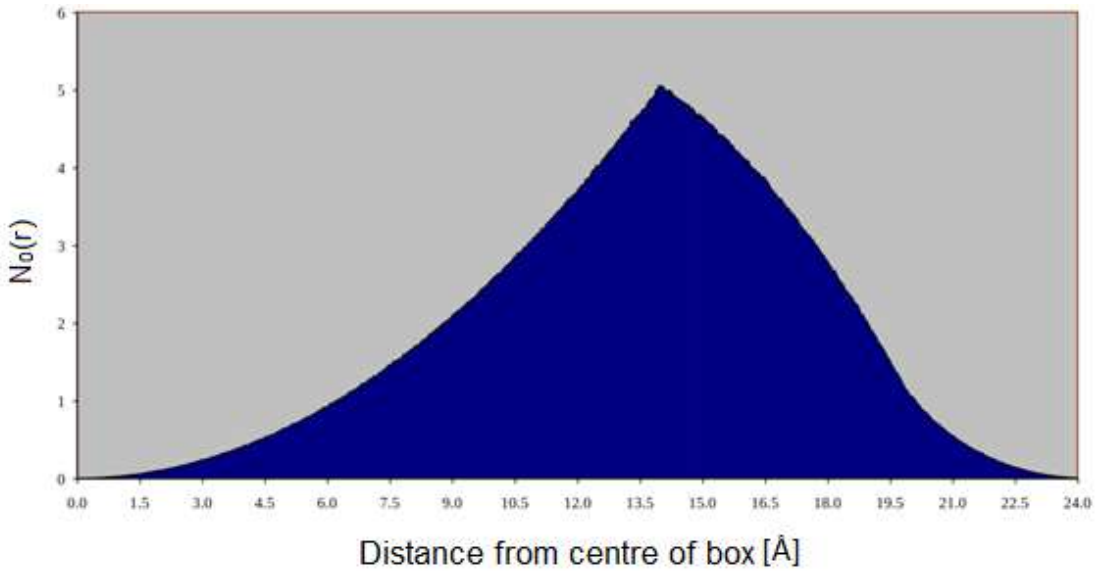

Fig. 2.8. Uniform atom distribution for simulation box of SiO_2 [128].

During the modelling process, three steps are involved in obtaining the final atomic configurations. In the first step, the refinement of atomic positions is carried out using only the reference potential until the simulation's energy reaches a constant value. Following that, the empirical potential refinement procedure begins, where the empirical potentials are refined simultaneously with the atomic positions. This refinement aims to minimize the discrepancy between the simulated $F(Q)$ and the experimental data. Once a satisfactory fit is achieved, the last step involves accumulating simulation cycles to obtain an averaged representation of the system. Three primary benefits result from using EPSR: (1) Confidence Building: EPSR enhances researchers' confidence by utilizing

scattering data obtained from the actual distribution of atoms and molecules. This reliance on real data helps validate the accuracy and reliability of the obtained results; (2) Comprehensive PDF: Unlike simple Fourier transform methods, EPSR can provide complete partial PDFs. This comprehensive analysis offers more detailed insights into the spatial arrangements and correlations of atoms within the structure. (3) Avoidance of truncation artefacts: EPSR avoids the inherent truncation artefacts associated with Fourier transformation methods. This artefact can arise due to the limited resolution or range of Fourier-based techniques, while EPSR effectively circumvents such issues.

2.3 Experimental techniques for studying the disordered materials

In this section, experimental techniques using synchrotron X-rays, neutron beam and electron beam are briefly discussed. As this work primarily used synchrotron X-rays, the historical development of the X-ray sources, X-ray total scattering data reduction and the two DLS X-ray beamlines are presented here.

2.3.1 X-ray scattering

2.3.1.1 X-ray scattering theory

X-ray interactions with matter can generate many different types of signals that have been explored in many scientific and technological fields, such as imaging, diffraction analysis, spectroscopy, and material characterization. Fig. 2.9 illustrates all possible X-ray interactions with matters [131], and they are generally classified into (1) Rayleigh scattering (2) Compton scattering (3) photoelectric absorption and (4) Pair Production [132]. Rayleigh scattering was named after Lord Rayleigh, who described this phenomenon in the context of visible light scattering [133]. This process is also known as coherent or elastic scattering, and it occurs by temporarily raising the energy of the electron without removing it from the atom [132, 134]. The electron returns to its previous energy level by emitting an X-ray photon of equal energy ($E_r = E_o$) but with a slightly different direction, as illustrated in Fig. 2.9. Most X-rays are scattered forward by this mechanism

because the atom cannot experience significant recoil without otherwise removing the electron. There is no absorption of energy, and the majority of the X-ray photons are scattered at a small angle.

Compton scattering is an inelastic scattering that occurs when X-rays interact with outer-shell electrons. This inelastic process involves the transfer of energy from the X-rays to the electrons, resulting in a change in direction and a decrease in energy (increase in wavelength) of the scattered X-rays [135]. During the Compton scattering, an X-rays photon of energy E_o that is much greater than the binding energy of an atomic electron. Partial energy transfer to the electron causes recoil and removal from the atom at a certain angle. The remainder of the energy,E_s, is transferred to a scattered X-rays photon with a trajectory of angle relative to the trajectory of the incident photons while the scattered photon may travel in any direction (i.e., scattering through any angle from 0° to 180 the recoil electron may only be directed forward relative to the angle of the incident photon (0° to 90°) [132, 136].

Photoelectric absorption involves the interaction of an incident X-ray photon with an inner-shell electron in the absorbing atom [137]. The electron's binding energy is comparable to but lower than the energy of the incident photon. During the interaction, the X-ray photon transfers its energy to the electron, resulting in the ejection of the electron from its shell (usually the K shell). The kinetic energy of the ejected electron is equal to the difference between the incident photon energy,E_o and the electron shell binding energy E_{BE}. After the ejection of the inner-shell electron in the photoelectric absorption process, the resulting vacant electron shell is filled by an electron from an outer shell with lower binding energy (such as the L or M shell) [138, 139]. This electron transition releases a characteristic X-ray photon with energy equal to the difference in electron binding energies between the initial and final electron shells. If the energy of the incident photon is lower than the binding energy of the electron, the photoelectric interaction cannot take place. However, when the energy of the X-ray photon matches the binding energy of the electron ($E_0 = E_{BE}$), the photoelectric effect becomes energetically favourable, leading to a significant increase in attenuation or absorption of the X-ray beam. As the incident photon energy increases above that of the electron shell binding energy, the likelihood of photoelectric absorption decreases at a rate

proportional to $\frac{1}{E^3}$. The K absorption edge refers to the sudden jump in the probability of photoelectric absorption when the K-shell interaction is energetically possible. Similarly, the L absorption edge refers to the sudden jump in photoelectric absorption occurring at the L-shell electron binding energy (at much lower energy) [140]. The photoelectric effect is extensively utilized in X-ray imaging techniques, such as radiography [141] and tomography (CT) [139].

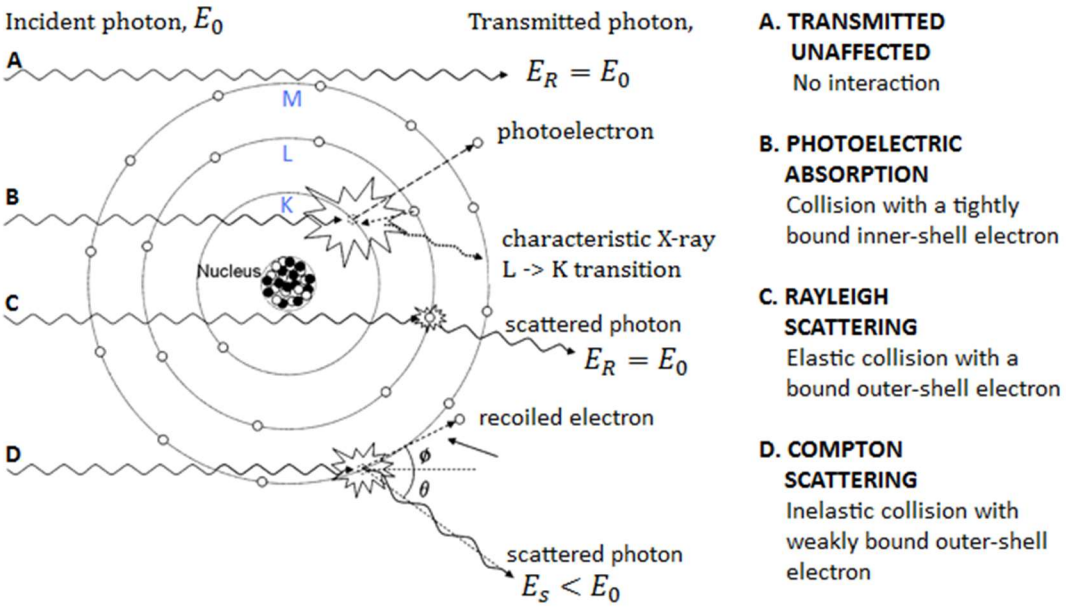

Fig. 2.9. Illustration summary of x-ray and x-ray interactions [132].

Pair production can occurs when X-rays with high energies (above 1.022 MeV), X-ray photons can interact with the electric field near the nucleus of an atom and convert their energy into the nucleus, creating of an electron-positron pair [142]. When pair production occurs, photon energy greater than 1.022 MeV, will be converted into motion of the electron-positron pair equally.

2.3.1.2 The historical development of X-ray Sources

The historical development of X-rays is depicted in Fig. 2.10 after its discovery in 1895. Early X-ray tubes, pioneered by Bragg and his son in 1915, utilized a heated filament to generate electrons directed at a metal target. However, these sources had limitations with low X-ray intensity and limited control over the energy spectrum [143, 144].

In the 1940s and 1950s, the discovery of synchrotron radiation demonstrated the great potential for being used in spectroscopy and diffraction measurements, leading to increased awareness in the 1960s and 1970s. The first dedicated synchrotron light source, Tantalus, USA [145], commenced operations in 1968 at the Synchrotron Radiation Center. The first-generation synchrotrons were built primarily for high-energy particle physics, with synchrotron light experiments performed parasitically. The second-generation synchrotrons were solely dedicated to the production of synchrotron light, and used bending magnets to generate synchrotron light; the UK built the first of these at Daresbury in 1980 [146].

The development of third-generation synchrotron radiation facilities has brought us to the present. The third-generation synchrotrons are different, because they used special arrays of magnets called insertion devices, which cause the electrons to wiggle, creating even more intense and tuneable beams of light. The European Synchrotron Radiation Facility (ESRF) in Grenoble became the first operational third-generation hard X-ray source in 1994, featuring a 6-GeV storage ring and a partial complement of commissioned beamlines [147].

Looking ahead, the fourth generation of X-ray sources commenced in 2009 with the establishment of the Linac Coherent Light Source (LCLS) at Stanford. As the first operational X-ray free-electron laser (XFEL) facility, XFELs produce remarkably intense and ultra-short X-ray pulses, enabling the study of ultrafast processes and facilitating high-resolution imaging [148].

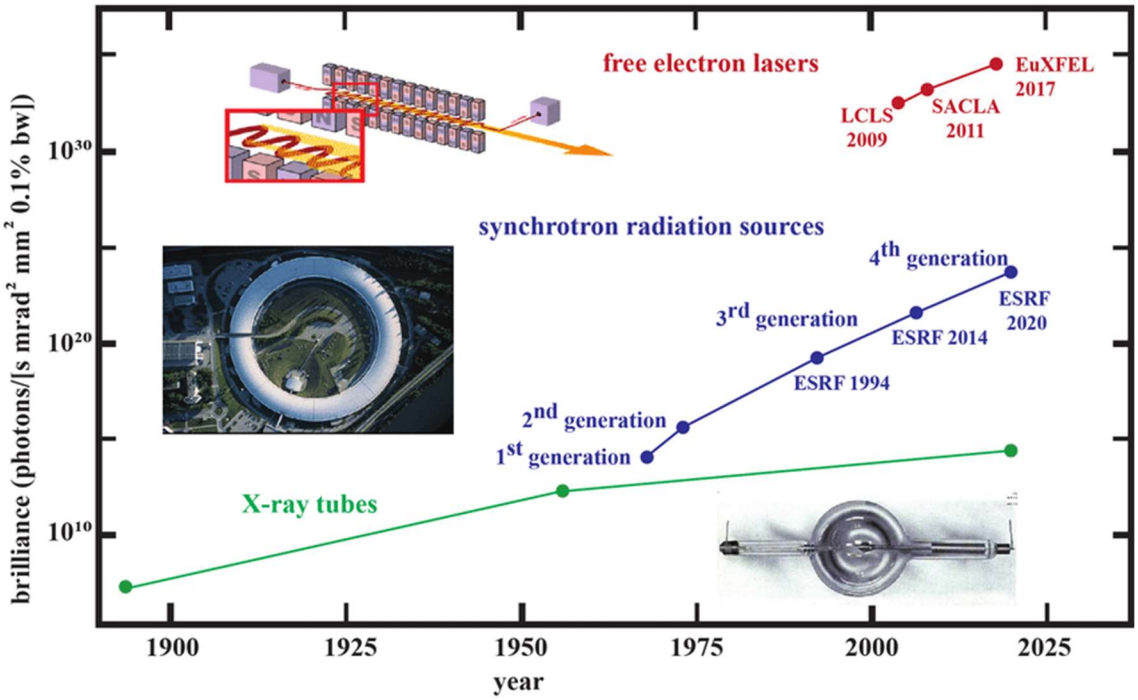

Fig. 2.10. Historical development of x-ray brilliance over time and development of new x-ray sources [149].

XFELs provide extremely short and intense X-ray pulses, allowing scientists to investigate ultrafast processes at the atomic and molecular levels. Fig. 2.11 compares the peak brightness as a function of photon energy between conventional lasers, synchrotron X-ray sources and XFELs sources. Such extremely high brightness enable time-resolved experiments in XFELs to capture the dynamics of chemical reactions, structural changes in materials, and biological processes on timescales ranging from femtoseconds to milliseconds [150]. Fig. 2.12 presents a total scattering experiment with ultrashort X-ray pulse performed in the coherent X-ray imaging instrument at the LCLS at the SLAC National Accelerator Laboratory, where Stankus et al. mapped the evolution of the molecular geometry of N-methyl morpholine with femtosecond resolution. The X-ray probe pulse was generated from LCLS, which operated at 120 Hz with ~1012 photons per pulse at 9.5 keV photon energy with a 20 eV full-width at half-maximum bandwidth and a ~30 fs pulse duration. The cross-correlation time of the pump and probe pulses was determined to be 89 ± 7 fs from the onset of the observed time-dependent scattering signals. There are also some other advancements XFEL enable researchers to obtain. For example, Serial Femtosecond Crystallography (SFX) techniques were used XFELs to collect diffraction data from nanocrystals, overcoming limitations encountered in

traditional crystallography methods [151]. XFELs can be used for single-particle imaging techniques, where individual particles, such as large protein complexes or viruses, are studied without the need for crystallization. By collecting diffraction patterns from individual particles, researchers can reconstruct their three-dimensional structures [152].

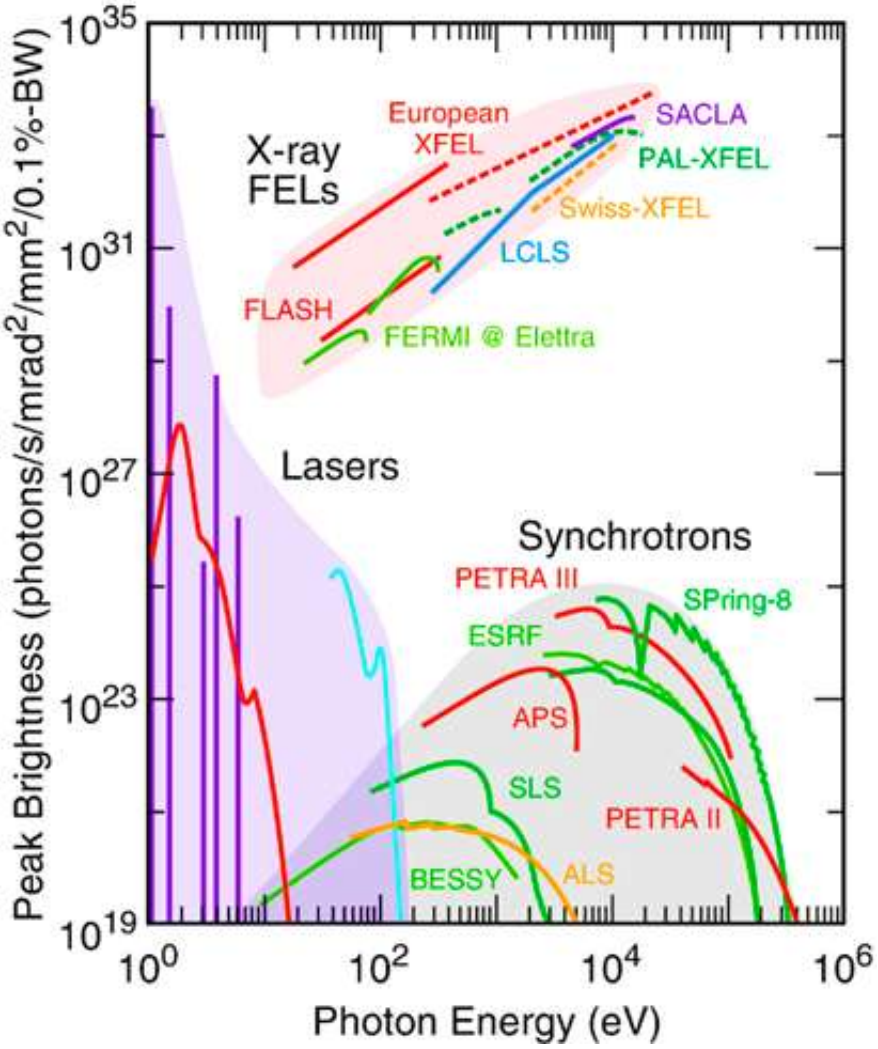

Fig. 2.11 Comparison of peak brightness as a function of photon energy between conventional lasers and higher harmonic generation sources, synchrotron sources, and X-ray free electron lasers [153].

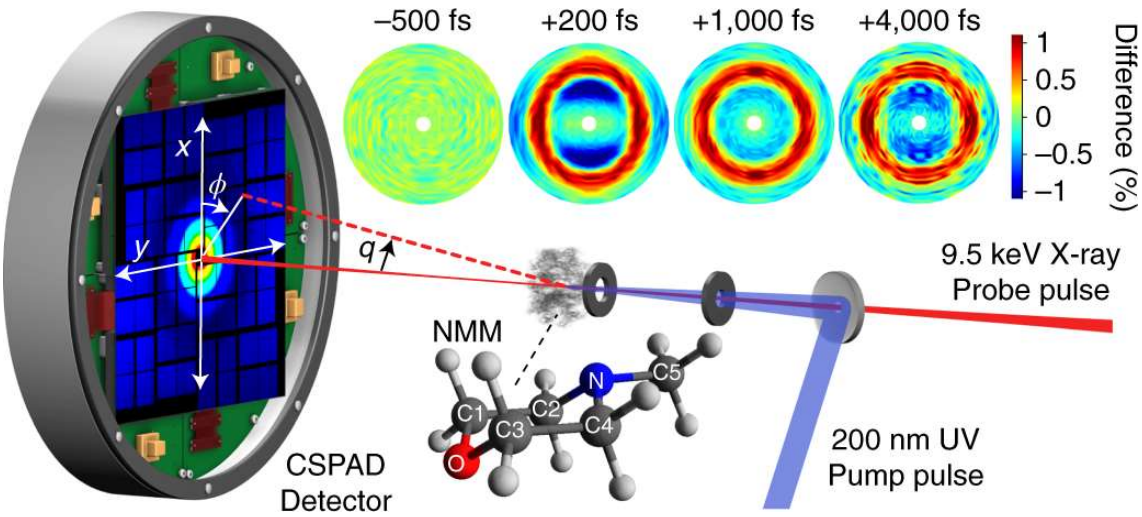

Fig. 2.12 The reaction of NMM is initiated with a 200 nm UV pump pulse, and the time-evolving molecular structure is probed [154].

2.3.1.3 X-ray total scattering data reduction

X-ray total scattering measures all X-ray photons scattered from a sample, taking into account all possible interactions with the incident X-ray [16]. The total intensity of the scattered X-ray, denoted as $I\ (Q)$, is composed of several components:

$$I\ (Q) = I_a^{coh}(Q) + I_a^{inc}(Q) + I_b(Q) + I_{mc}(Q) \tag{2.18}$$

$I_a^{coh}(Q)$ represents the coherent scattering (Rayleigh scattering) intensity that mention in section 2.3.1.1. It contains valuable atomic structure information about the sample. $I_a^{inc}(Q)$ corresponds to the incoherent scattering intensity, which arises from Compton scattering. It does not provide specific atomic structure information. $I_{mc}(Q)$ represents the multiple-scattering intensity, which arises from multiple scattering events within the sample. It can interfere with the coherent scattering signal and needs to be accounted for. $I_b(Q)$ represents the background intensity originating from the sample environment, such as the sample holder or container. It is unrelated to the atomic structure of the sample. Data reduction can help us to get an intensity that only comes from the sample during the interaction process. In other words, here are some reasons why we need to perform data reduction when performing PDF:

(1) Background Subtraction: The total scattering signal obtained in experiments includes contributions from various sources, such as instrumental background, sample holder, and other environmental factors. These background signals can interfere with the desired signal from the amorphous material. Data reduction techniques help subtract the background signals and isolate the scattering information related to the amorphous structure.

(2) Noise Reduction: Experimental data often contain noise and uncertainties due to instrumental limitations, measurement errors, or statistical fluctuations. Data reduction techniques aim to minimize noise and improve the signal-to-noise ratio, ensuring more reliable and accurate PDF calculations.

(3) Data Corrections: Data reduction may involve applying corrections for various systematic effects, such as absorption, polarization, and instrumental resolution. These corrections help to account for the experimental conditions and improve the accuracy and consistency of the obtained PDF information.

Overall, data reduction in collecting PDF information for amorphous materials is crucial for extracting correct structural information from the scattering data, minimizing background and noise, and ensuring accurate comparisons and analysis between different samples and experimental conditions. In this section, we mainly introduce two common tools to do data reduction. In our work, all the data reduction was performed by using GudrunX [155] .

2.3.1.4 Brief description of the two beamlines of Diamond Light Source

I conducted all total scattering experiments at the I12 and I15-1 beamlines of the Diamond Light Source, located at the Harwell Science and Innovation Campus in Oxfordshire, UK. They belong to the engineering and environment village. I12 is the Joint Engineering, Environmental, and Processing (JEEP) beamline [156]. It was constructed during Phase 2 and serves the purpose of imaging, diffraction, and scattering. The beamline offers the flexibility to conduct experiments using either monochromatic or polychromatic ("white beam") X-rays within an energy range of 53 KeV to 150 KeV. The utilization of high-energy X-rays is particularly

important for effectively penetrating large and dense engineering samples. In both operational modes mentioned above, the beam size can vary from 0.05 mm × 0.05 mm to 100 mm × 30 mm (H × V). With its adaptable hutch design, high photon energy, and substantial flux, I12 caters to a wide range of experimental techniques for the user community, including (1) Static and time-resolved radiography and tomography. (2) Static and time-resolved powder diffraction using monochromatic radiation. (3) Powder diffraction using energy-dispersive radiation. (4) Diffuse scattering analysis on crystalline materials (single-crystal diffuse scattering) or amorphous materials (pair-distribution function analysis "PDF"). (5) High-energy X-ray small-angle scattering.

Additionally, the beamline supports the sequencing of monochromatic imaging through the automated switching-off of the detectors. Taking advantage of I12's capabilities, we submitted a proposal (MG27571-1) to conduct an in-situ study on the structural evolution of Al and Mg-based alloys during solidification, utilizing a combination of imaging and total scattering techniques. However, due to Covid-19 control measures and the AP28 operation mode at the Diamond Light Source, it was necessary to simplify the research tasks. Consequently, we proceeded with conducting only the in-situ total scattering experiments during the awarded beamtime (MG27571-2 and MG27571-3).

Fig. 2.13 illustrates the schematic of the beamline, which comprises two in-line experimental hutches: Experimental Hutch One (EH1) and Experimental Hutch Two (EH2). EH1 is located within the Diamond Experimental Hall, approximately 51m from the source. This hutch is suitable for experiments involving small-sized samples and apparatus and is available for general use. Our in-situ total scattering experiment was conducted in EH1. Experimental Hutch Two (EH2) is situated in an external building adjacent to the Experimental Hall and is aligned with EH1. EH2 provides ample space for conducting large or complex experiments in physics, material science, geology, engineering, and processing. Setup and preparation of equipment for experiments in EH2 can be carried out without interrupting ongoing experiments in EH1, allowing for longer setup times for user-provided equipment.

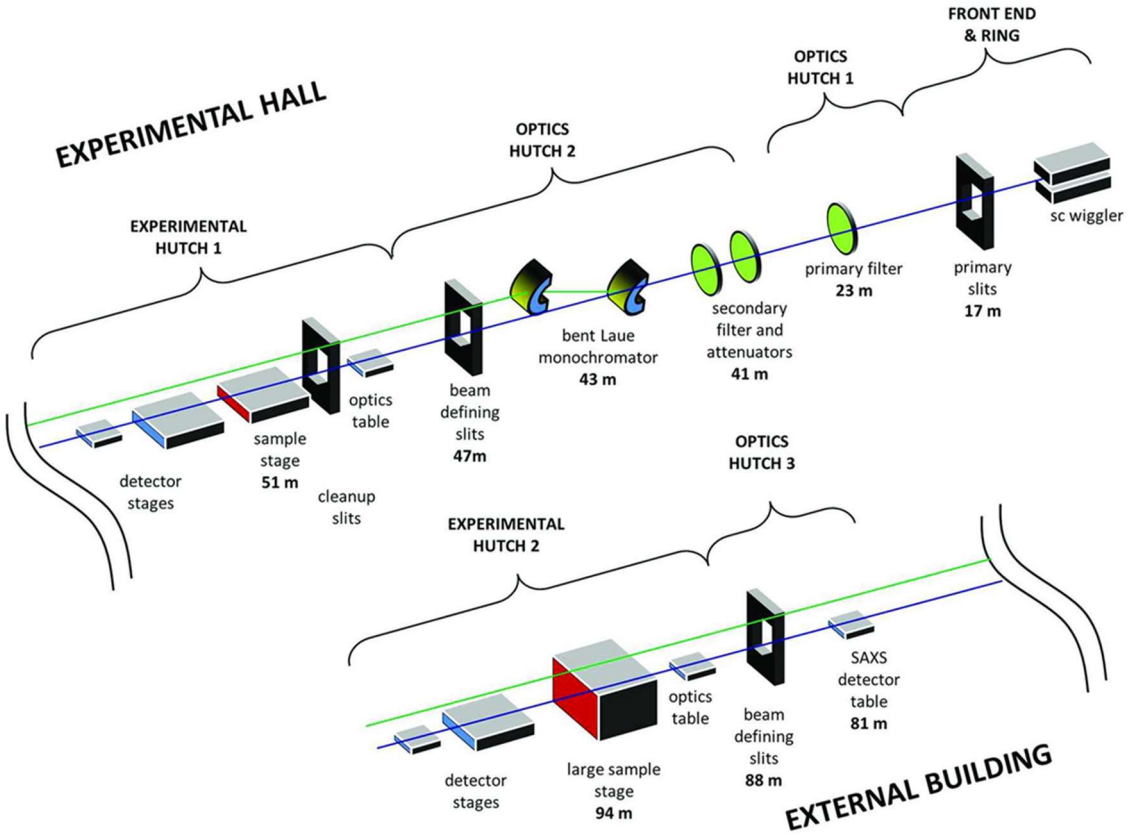

Fig. 2.13. The schematic optical and functional layout of the I12 JEEP beamline [156].

I15-1 is a dedicated X-ray PDF beamline situated adjacent to the I15 beamline [157], as illustrated in Fig. 2.14. This layout enables I15-1 to utilize a section of the infrastructure originally designated for I15, thereby facilitating research on crystalline, semi-crystalline, and amorphous solids, as well as liquids in Diamond Light Source. To obtain high-quality pair distribution function data, precise collection of both Bragg peaks and weak diffuse scattering signatures is required across a wide range of photon energies and scattering angles. I15-1 was specifically designed to meet these requirements, offering high flux, high energy, and a wide scattering range.

To achieve these objectives, a horizontally focusing cryo-cooled bent-Laue monochromator [158] and a vertically focusing multi-layer mirror [159] are utilized. The end station has been optimized to minimize background signal [160]. Within the I15-1 hutch, there are typically two detectors. One detector is that we used, which is positioned close to the sample to capture high-quality total scattering data,

enabling a high Q-range (Q_{max} up to 40 Å^{-1} at 76.7 KeV). The other detector is placed farther from the sample to simultaneously collect Bragg diffraction data. Currently, the Perkin Elmer XRD 4343 CT detector is employed, providing good indirect detection efficiency and a large detection area (41.2 cm × 41.2 cm) to enable extensive angular coverage. However, this detector exhibits a high dark current and significant image lag, which can persist for more than 15 minutes after strong scattering signals, leading to undesirable effects.

I15-1 is currently in the process of commissioning a new detector known as the "ARC" detector, which will revolutionize PDF data collection [160]. This custom-made photon-counting detector features CdTe sensors arranged in an arc shape, allowing access to a wide range of scattering angles. The photon counting technology employed by this detector effectively reduces background noise. The new detector will offer advantages such as negligible noise and a large dynamic range, enabling faster and higher-quality PDF data collection than was previously possible [161]. User operations with this new detector are scheduled to commence in January 2023. To date, it has attracted researchers from a wide range of fields, including those working on amorphous solids [162, 163], porous liquid [164], gases [165], ferroelectrics [166, 167], liquid metal [168], catalysts [169] and batteries [170].

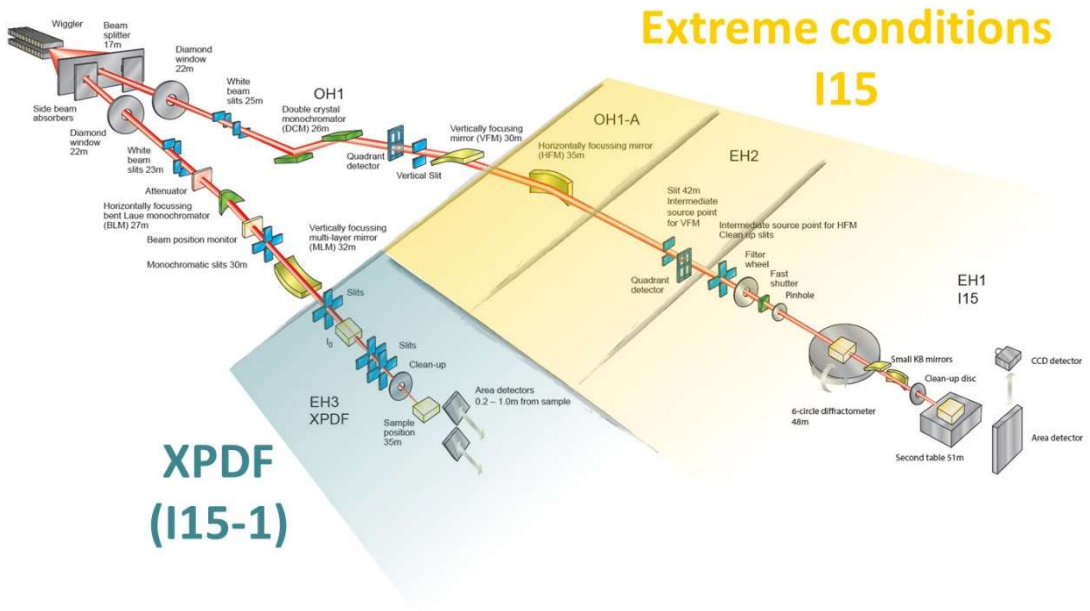

Fig. 2.14. The layout of the XPDF (I15-1) and Extreme Condition hutch [160].

2.3.2 Neutron Scattering

Neutrons primarily scatter off the atomic nucleus, while X-rays scatter off the electron cloud surrounding the nucleus. Unlike X-rays, which have scattering power proportional to the number of electrons in an atom, the scattering power (cross-section) of neutrons is not strongly correlated with the atom's atomic number. This is illustrated in the accompanying Fig. 2.15, where atoms with larger atomic numbers contribute more significantly to the scattered X-ray intensity compared to atoms with smaller atomic numbers. For instance, regular hydrogen (H) and deuterium (D) exhibit different contributions. Moreover, even in the presence of atoms with large atomic numbers, light atoms (low atomic number Z) often contribute significantly to the diffracted intensity. In contrast, neutrons directly interact with the atomic nucleus, resulting in different scattering intensities depending on the isotope. The scattering length varies across isotopes rather than linearly with the atomic number. For instance, an element like Vanadium exhibits strong scattering intensity with X-rays but demonstrates minimal neutron scattering, making it commonly used as a container material. Non-magnetic neutron diffraction directly captures information about the positions of atomic nuclei, offering sensitivity to their spatial arrangements.

Neutron scattering offers three notable advantages [171]: (1) Neutron scattering is particularly effective at detecting light atoms, such as hydrogen, even in the presence of heavier elements. This capability is valuable for studying materials where light atoms play a crucial role in the overall structure and properties. (2) Neutrons can distinguish between neighbouring elements in the periodic table based on their substantially different scattering cross sections. This ability allows for the characterization and differentiation of elements with similar chemical properties, enhancing our understanding of the composition and behaviour of materials. (3) Isotopic labelling: The nuclear dependence of neutron scattering enables the use of isotopic substitution to label different parts of molecules within a material. By substituting isotopes of the same element, significant variations in neutron scattering lengths can be achieved. This labelling technique is valuable for investigating the specific contributions and interactions of different components within complex materials.

Neutron scattering techniques can be applied to study various material systems, including crystalline solids [64, 172], liquids/amorphous materials [173, 174], and large-scale structures [175]. Wide-angle neutron scattering or total scattering is commonly employed for studying crystalline solids and liquids [126]. On the other hand, small-angle neutron scattering is frequently utilized for investigating large structures such as polymers [176], colloids [177], micelles [178], and similar systems. These techniques provide valuable insights into the structural properties and behaviours of diverse materials. Neutron total scattering became the choice for measuring from liquids and amorphous materials. This was because there is no fall-off in intensity at high-Q from the effect of Q-dependent scattering factors. There are several such instruments worldwide that are ideally suited to PDF measurements, including the GEM [179] and Polaris [180] diffractometers at the ISIS Facility in the UK, and PDF measurements make up a substantial proportion of the experimental program on these two general-purpose powder diffractometers.

A spallation neutron source generates neutron pulses with a wide range of wavelengths, detected by position-sensitive detectors that also record the neutron arrival time from the source through the sample. Time-of-flight neutron powder diffractometers employ large arrays of fixed detectors that cover a broad range of scattering angles. In PDF measurements, these instruments typically record data for wavelengths ranging from 0.1 to 4.0 Å. The combination of diverse wavelengths, including very short ones, and a substantial detector coverage enables the collection of data across a wide range of momentum transfers (typically 0.1< Q <50 Å^{-1}) Moreover, the characteristics of the source can be tuned to achieve good Q-resolution in the back-scattering detectors, such as $\frac{\Delta Q}{Q}$=0.3% for Polaris [181].

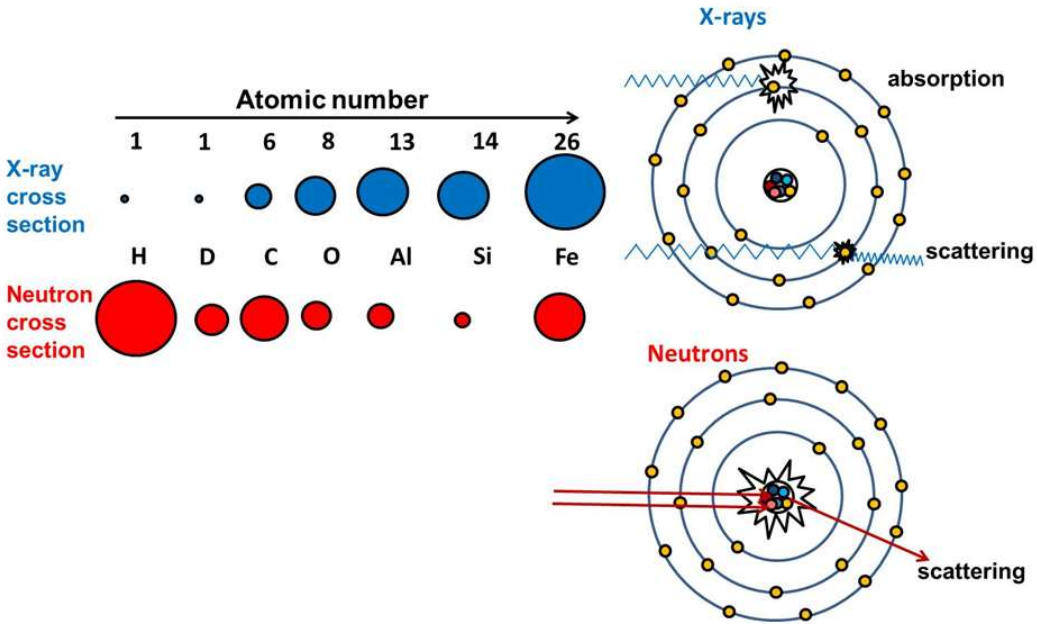

Fig. 2.15. Comparison of scattering strength between X-Rays and neutrons for a few elements (left) and interaction of X-rays and neutrons with the atoms (right) [182].

2.3.3 X-ray absorption fine structure spectroscopy

X-ray absorption fine structure spectroscopy (XAFS) encompasses a set of techniques used to investigate materials and gather chemical and structural information by examining the electronic transitions of inner shell electrons of a central atom. The XAFS station employs a tuneable, monochromatic X-ray beam with moderate energy for X-ray absorption spectroscopy measurements (see Fig. 2.16). For example, the BM23 beamline has a wide energy range from 4 keV to 74 keV in ESRF [183]. The energy of the incident beam is adjusted to match the binding energy of a specific element of interest in the sample being studied. By measuring the absorption cross-section of that element as a function of incident energy, valuable insights regarding the valence state and atomic configuration of the target element can be obtained. One technique is X-ray Absorption Near Edge Structure (XANES), which is a rapid measurement technique that directly reveals information about the electronic state of the element. The other technique is Extended X-ray Absorption Fine Structure (EXAFS), which allows for quantitative analysis of the atomic structure, providing detailed information about the local environment surrounding the target element. By scanning multiple

edges, XAFS can unveil electronic and atomic structures in complex materials. Various modes can be employed to obtain the X-ray absorption spectrum $\mu(E)$ of a sample. The transmission mode is commonly used and offers a straightforward interpretation. In this case, the X-ray absorption coefficient is determined as $\mu(E) = \frac{1}{x} ln\,(\frac{I_0(E)}{I(E)})$, where x represents the sample thickness and I_0 and I are the intensities of the incident and transmitted X-rays, respectively. However, other effects proportional to the absorption coefficient can also be utilized, such as X-ray fluorescence mode, total electron yield (TEY), or X-ray excited optical luminescence (XEOL) as shown in Fig. 2.16 [184]. XAFS can be applied under diverse external conditions, including variations in temperature, pressure, and more. It is not limited to crystalline materials but can also be used for amorphous systems, glasses, quasicrystals, disordered films, membranes, solutions, liquids, metalloproteins, and even molecular gases [185].

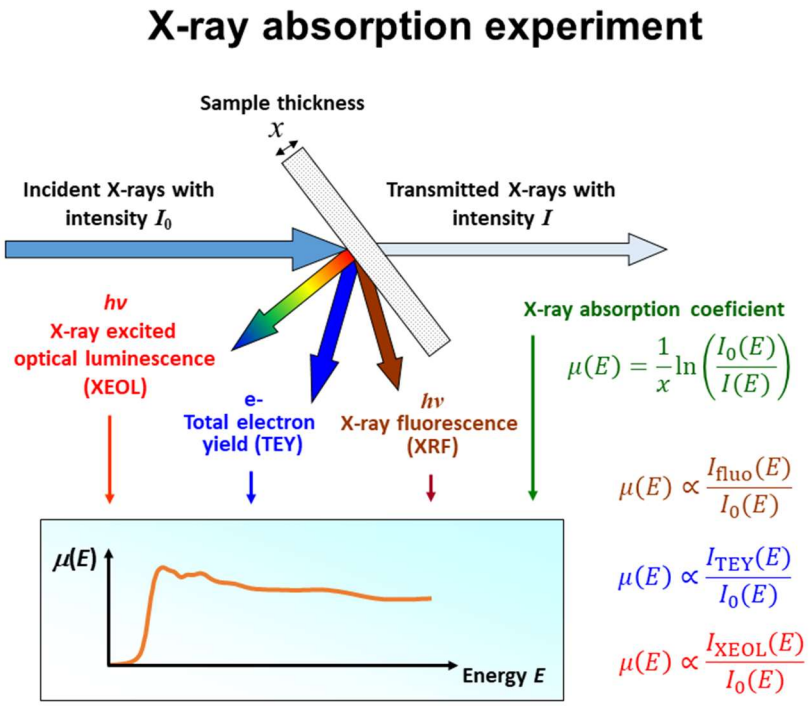

Fig. 2.16. XAFS measurements principle scheme [186].

2.3.4 Transmission electron microscopy techniques

As depicted in section 2.1.1, there is currently no established experimental technique that allows for direct observation of the local structure of liquid metals. In contrast, metallic glass is in a "frozen" state, maintaining an amorphous or non-crystalline structure due to the rapid cooling or quenching process. This stable state is “easier” for studying the local atomic structure. High-resolution transmission electron microscopy (HRTEM) is commonly used to investigate atomic structure, while such information is limited to two-dimensional representations. Over the past two decades, significant advancements have been made in the determination of the three-dimensional local structure of metallic glass. This section presents two notable cases in this regard.

One is angstrom-beam electron diffraction (ABED), which was developed by Hirata [61] group. With an electron beam with a diameter of 0.36nm (see in Fig. 2.17), Hirata et al. successfully captured diffraction patterns from sub-nanometre volumes within a metallic glass, which show some, but not all, of the expected features of an icosahedron. Simulations suggest that the patterns arise from icosahedrons distorted to include features of the face-cantered cubic structure. This observation is different from the predictions of molecular dynamics simulations and provides pivotal information in understanding the competition between the formation of the globally inexpensive long-range order and the locally inexpensive short-range order.

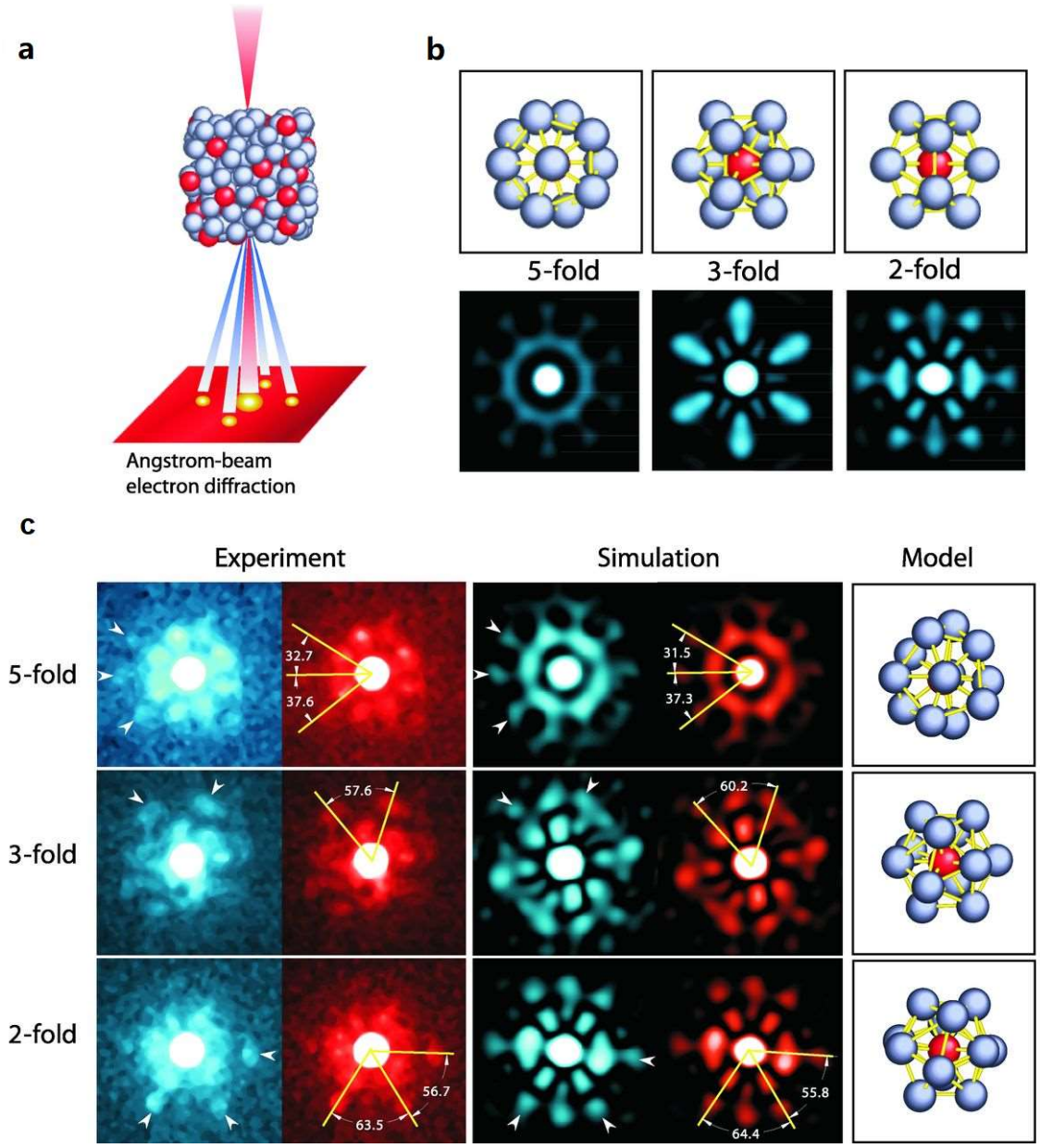

Fig. 2.17. ABED characterization of icosahedral order in metallic glasses [61]. (a) Experimental procedure of ABED of an icosahedral cluster. (b) Simulated ABED patterns of an ideal icosahedron. (c) Comparison between experimental and simulated ABED patterns of icosahedral clusters in a $Zr_{80}Pt_{20}$ metallic glass.

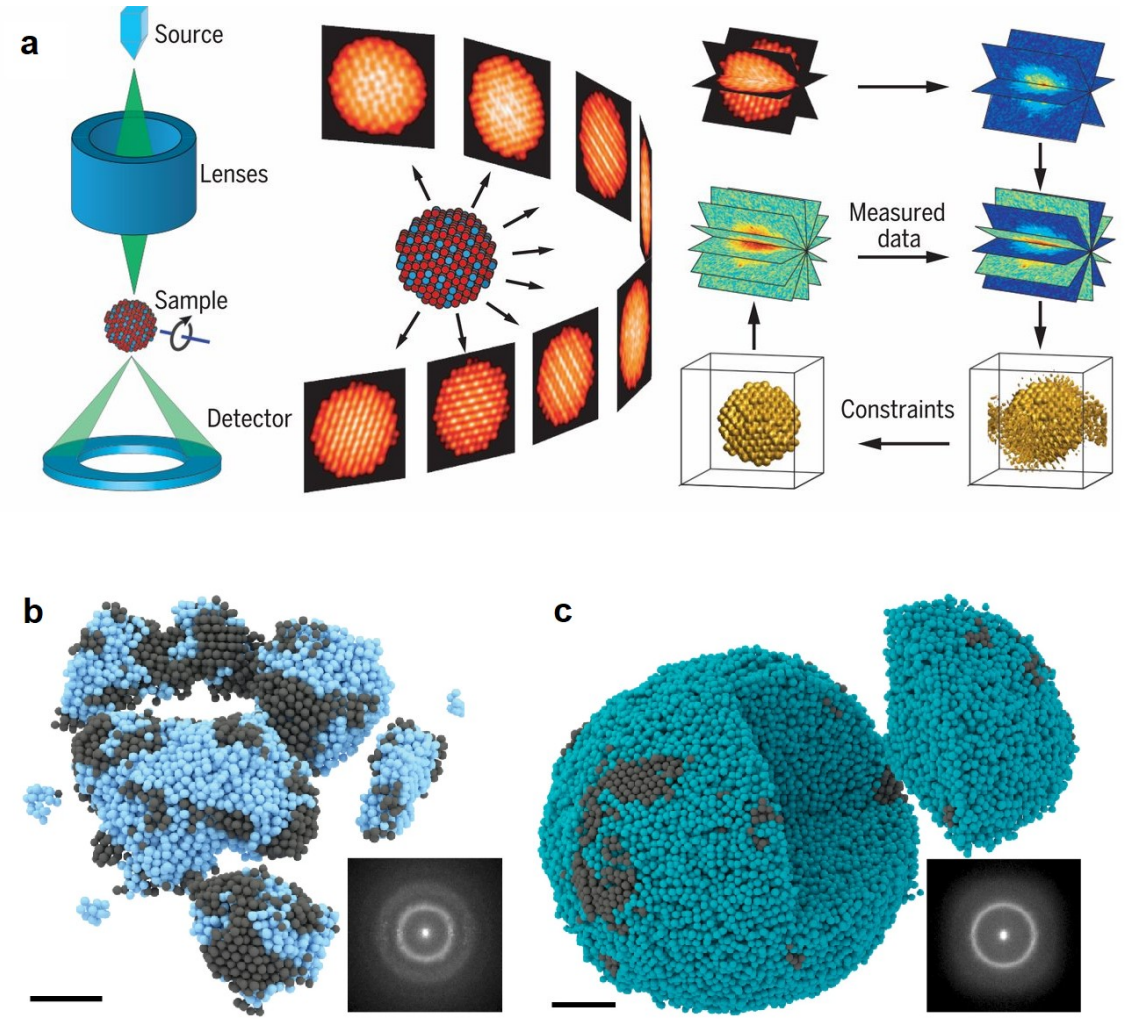

Fig. 2.18. (a) Schematic layout of AET [187]. Experimental 3D atomic model of an amorphous (b) Ta film (a) and a (c) Pd_1 nanoparticle [188] with surface crystal nuclei in grey. Scale bars: 2 nm.

More recently, significant advances have been made in the field of atomic electron tomography (AET) led by Miao's group [187, 189], enabling the precise determination of 3D structures of disordered systems at atomic resolution. The schematic layout is provided in Fig. 2.18a. AET involves the use of a focused electron beam that scans over the sample, acquiring a series of two-dimensional images. The signal at each scanning position is captured by an annular dark-field (ADF) detector. By rotating the sample around a tilt axis, a tilt series of two-dimensional images is obtained at different tilt angles. Through preprocessing, alignment, and the utilization of fractional Fourier transform (FrFT), the tilt series is transformed into Fourier slices. A Fourier-based iterative algorithm is then

employed to reconstruct the three-dimensional structure of the sample. By tracing and refining individual atom coordinates, a high-resolution three-dimensional atomic model is obtained. In 2021, Miao's group successfully determined the three-dimensional atomic structure of an amorphous metallic glass composed of eight elements [32], which is the first-ever determination of the 3D atomic structure of an amorphous solid. Fig. 2.18b and c illustrate the reconstructed amorphous Ta film and Pd_1 nanoparticle [188], with the real three-dimensional atomic structure enabling the precise identification and separation of crystalline atoms within the sample.

2.4 Geometrical structural descriptors

As illustrated in section 2.1.4, there are many fine structures behind the PDF. In this section, a detailed review of the common geometrical structural descriptors for local atomic structure is given.

2.4.1 Bond angle distribution

Bond-angle distributions are commonly used to investigate the local orientational order in liquid systems [190-193]. These distributions provide insights into the spatial arrangement of bonded atoms in the nearest-neighbour shell. To calculate bond-angle distributions, the angles formed by a central particle and particles in both the first and second coordination shells are considered. Typically, the distances between the atoms involved in the bond-angle calculation need to be specified. The atoms are specified in triplets, and the calculated angle is the included angle formed by the middle atom of the triplet. For example, in a water molecule (as shown in Fig. 2.19), the triplet would consist of the three atoms in the molecule and the bond angle would be calculated using the included angle between the two O-H bonds. To generate the bond-angle distribution, an atomic coordinate file would specify the types of the three atoms in the triplet, as well as the allowed range of distances between them (e.g., distances 1-2 and 2-3). The algorithm would then search for triplets that satisfy these specifications. For each valid triplet, the cosine of the bond angle (θ) is calculated using the cosine rule.

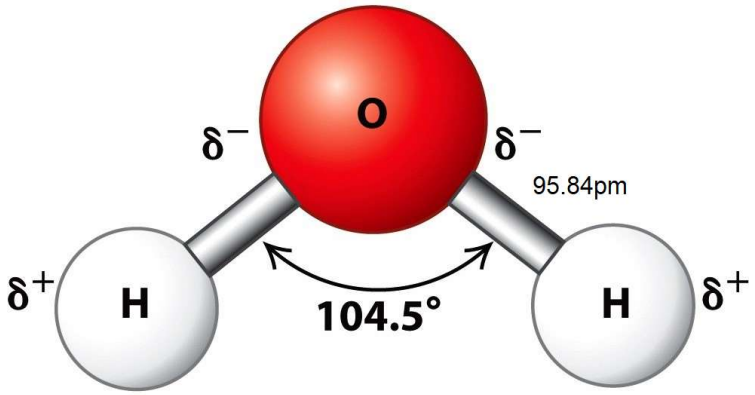

Fig. 2. 19. Structure of water molecule[194].

The resulting bond-angle distribution provides a statistical representation of the spatial arrangement of bonded atoms in the nearest-neighbour shell. In crystalline structures, such as diamond or simple cubic, the bond-angle distribution would exhibit a characteristic peak at the expected bond angle value (e.g., 109° for a diamond structure or 90° for a simple cubic structure [16]). In amorphous materials, where there is no long-range order, the bond-angle distribution would show a spectrum of angles, indicating the lack of a specific preferred angle. By analysing the bond-angle distributions during the crystallization process, researchers can gain insights into the structural changes and the development of local orientational order as the material progresses towards a crystalline state (see Fig. 2.20) [195].

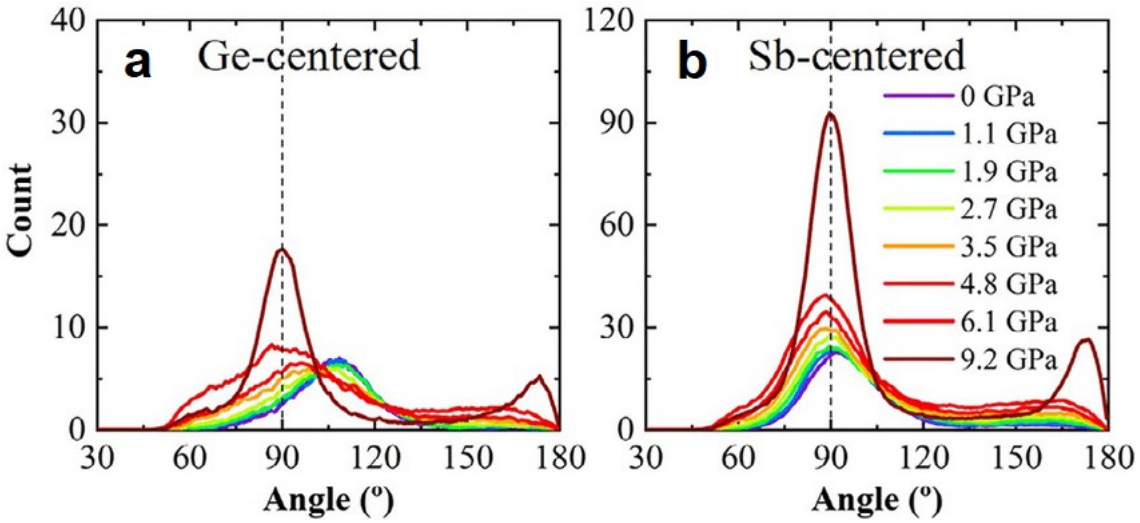

Fig. 2.20. Bond-angle distribution functions of (a) Ge- and (b) Sb-cantered configurations in amorphous $Ge_{15}Sb_{85}$ upon pressure-driven crystallization [195].

2.4.2 Chemical short-range order

Analysing the chemical composition of neighbouring atoms is valuable when dealing with structures containing multiple elements, allowing for a comparison with the alloy's composition. This assessment provides insights into the extent to which the local chemistry differs from the expected behaviour of a random solution, indicating the level of chemical short-range order (CSRO). The Warren-Cowley parameter [196] and the Cargill-Spaepen parameter [197] are commonly employed to quantify the degree of CSRO. Specifically, the Warren–Cowley parameter for a nearest-neighbouring pair is $\boldsymbol{\alpha_{ij}}$ [198] is calculated by:

$$\boldsymbol{\alpha_{ij}} = \mathbf{1} - \boldsymbol{Z_{ij}}/(\boldsymbol{c_j Z_i}) \tag{2.19}$$

where $\boldsymbol{c_j}$ is the mole fraction of atom j, $\boldsymbol{Z_{ij}}$ and $\boldsymbol{Z_i}$ are the partial and total CN [196, 198, 199]. $\boldsymbol{\alpha_{ij}} = 0$ means a completely random distribution of atoms i and j; $\boldsymbol{\alpha_{ij}} < 0$ indicates that the number of j atoms in the 1st shell of i atoms exceed the average concentration of j atoms. $\boldsymbol{\alpha_{ij}} > 0$ means there is a chemical preference not in favour of the $i - j$ nearest-neighbour pair.

2.4.3 Common neighbour analysis

Structure analysis methods employing complex, high-dimensional signatures are often more effective in distinguishing between atomic arrangements. One widely used method is common neighbour analysis (CNA), initially introduced by Honeycutt and Andersen [200]. In CNA, two atoms (α and β) are considered near-neighbours within a specified cut-off distance. Typically, the cut-off distance is determined by the first minimum (r_{min}) in the partial radial distribution function $g_{\alpha\beta}(r)$. Each pair of nearest-neighbour atoms is assigned a four-number index ($ijkl$). The value of i (1 or 2) indicates whether α and β are nearest neighbours (i=1) or not (i=2). The value of j represents the number of nearest neighbours common to both atoms in the pair, while k denotes the number of bonds between those j atoms. The fourth digit, l is used when the first three numbers are the same, but the bond geometries differ. Based on this algorithm,

an extended cluster-type-index method has been developed. For instance, a standard icosahedron can be expressed as (12, 12/1551) (see Fig. 2.21), indicating that the central atom forms twelve 1551 bonds with its twelve coordinated atoms. Similarly, fcc, hcp, and bcc basic clusters can be represented as (12, 12/1421), (12, 6/1421, 6/1422), and (14, 6/1441, 8/1661), respectively. By employing these representations, the central atoms can be identified as fcc, hcp, and bcc atoms, respectively.

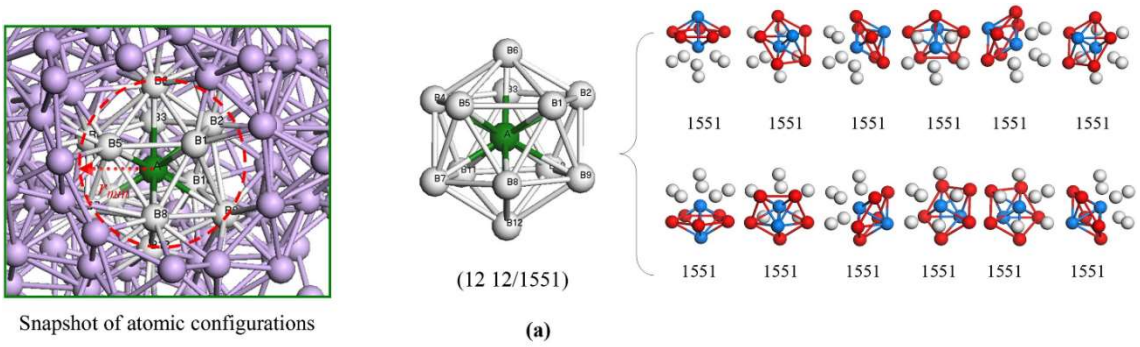

Fig. 2.21. Schematic digraph of ISRO [201]. The green and white balls denote the central atoms and shared atoms of icosahedral clusters, respectively. The blue balls and red balls represent root pair atoms and near-neighbour atoms shared by the root pair, respectively.

2.4.4 Voronoi tessellation analysis

Voronoi tessellation analysis is a more 3D approach than the Honeycutt–Anderson (H-A) pair index perspective [200] since it provides a more complete geometrical construction of a central atom with its neighbouring atoms (see Fig. 2.22) [16, 202, 203]. In this method, the perpendicular bisectors between the central atom and the neighbouring atoms will form a polyhedron about the central atom, and it is named the Voronoi polyhedron (VP). This cell is similar to the famous Wigner–Seitz cell [204] in crystallography. Each VP can be labelled as <n_3, n_4, n_5, n_6, ..., n_i, ...>, where n_i is on behalf of the number of i-edged faces around the central atom, and the sum of n_i represents the coordination number of the central atom. From the geometrical point of view, VPs can fill the entire 3D space without overlapping, but most of them are distorted because of thermal fluctuations and rounding errors in computation. To reduce this distortion, some tiny surfaces and ultra-short edges are usually eliminated [205], and consequently, the majority of

VPs can be denoted by a 4-integer index <n_3, n_4, n_5, n_6>. Usually, the standard Voronoi indexes of icosahedral (ico), face-centred cubic (fcc)/hcp and body-centred cubic (bcc) are <0,0,12,0>, <0,12,0,0> and <0,6,0,8> respectively [206]. These VPs are classified into 3 different types according to Cheng et al. [16] :(a) Icosahedra-like (ICO-like) SROs, including < 0 0 12 0>, <0 1 10 x> and < 0 2 8 x>, where x=1, 2 …4. A polyhedron with Voronoi index <0 0 12 0> represents a perfect icosahedral structure with a five-fold symmetry, while <0 1 10 x> and < 0 2 8 x> can be considered distorted icosahedral clusters. (b) crystal-like SROs, including <0 3 6 x > (x=2, 3, 4 and 5) and <0 4 4 x> (x=4, 5, 6 and 7), and (c) those not possessing the symmetries as the above two cases [16].

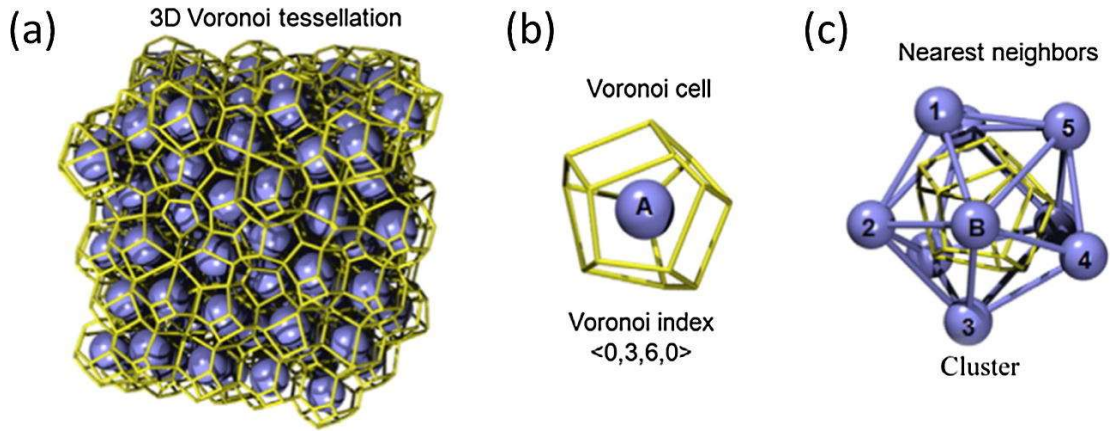

Fig. 2.22. Schematic digraph of (a) Voronoi tessellation; (b) 〈0, 3, 6, 0〉 Voronoi cell; (c) atomic cluster associated with 〈0, 3, 6, 0〉 VP [16].

2.4.5 Bond-orientational order analysis

Generally, crystal-like order in a liquid is not characterized by translational order but rotational order around an atom. The local orientational order between a central atom and its neighbour is measured by bond orientational order (BOO) parameters $Q_{lm}(i)$ developed by Steinhardt et al [207]. BOO in a metastable supercooled liquid is widely accepted as the 'shadow' of crystallization and liquid-liquid transition[208]: the water-like anomaly is a consequence of the increase in the number density of locally favoured structures having bond orientational order [209-212], whereas the liquid–liquid transition is a consequence of the cooperative formation of locally favoured structures [213, 214]. They are sensitive only to the

angles between the vectors (bonds) joining particles to their neighbours and are thus invariant to rotations (see Fig. 2.23a). When the fluctuation of the number of the nearest neighbours is small, BOO parameters are useful to characterize the local rotational symmetry [112]. To calculate the BOO parameters, a $2l+1$ dimensional complex vector (Q_l) of the l-fold symmetry for atom i was firstly computed according to:

$$Q_{lm}(i) = \frac{1}{N_i}\sum_{j=1}^{N_i}\frac{A_j}{A_{tot}}Y_{lm}(\theta(r_{ij}), \emptyset(r_{ij})) \tag{2.20}$$

where N_i is the number of the nearest neighbours of atom i, m are the integers from $-l$ to l, and Y_{lm} is the spherical harmonics. $\theta(r_{ij})$ and $\emptyset(r_{ij})$ are the polar and azimuthal angles respectively. The second-order invariants are calculated by:

$$Q_l(i) = \sqrt{\frac{4\pi}{2l+1}\sum_{m=-l}^{l}|Q_{lm}|^2} \tag{2.21}$$

Third-order invariants can also be obtained by:

$$\widehat{W}_l = \frac{W_l}{(\sum_m |Q_{lm}|^2)^{3/2}} \tag{2.22}$$

where

$$W_l = \sum_{\substack{m_1,m_2,m_3 \\ m_1+m_2+m_3=0}} \begin{pmatrix} l & l & l \\ m_1 & m_1 & m_1 \end{pmatrix} * \overline{Q_{lm1}}\,\overline{Q_{lm2}}\,\overline{Q_{lm}} \tag{2.23}$$

The spherical harmonics-based BOO analysis can provide quantitative description of local rotational symmetry around an arbitrary central reference atom. Among these parameters, the $\widehat{W}_6$ cubic invariant is the most sensitive indicator for icosahedral symmetry [57]. Q_6 is useful in measuring the degree of crystallinity (i.e., how far a precursor is away from its crystal nucleus [2]). Q_4 is useful in quantifying the difference in symmetries (i.e., lattice match) [23]. Moreover, the combination of two or more BOO parameters is often considered together to characterize the local environment of a particle, among which Q_4

plotted against Q_6 is often to distinguish between disordered (normal liquid) environments at low values of both Q_4 and Q_6 and relatively ordered (crystal-like) environments at high values for both order parameters. For example, Peng Tan [60] distinguish the nuclei, precursor particles (see in Fig. 2.23b, c and d) from liquid the distribution of all particle using Q_4-Q_6 map (see in Fig. 2.23e) which is shown in: the upper group with lager Q_6 value is composed by nuclei particles; while the lower group with smaller Q_6 value is by liquid particles, and they further varied the threshold value of precursor particle between 0.27 and 0.30. Using this method, the precursor and nuclei particle in the simulation box as presented by the light brown and brown sphere in Fig. 2.23a-c. They also combined Q_4 and W_4 to distinguish the nuclei and precursor particles with different symmetry arrangements.

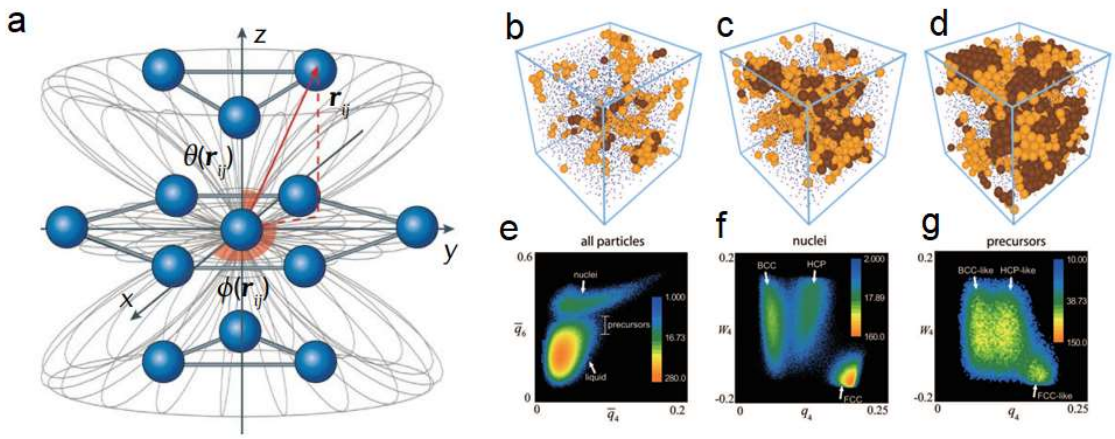

Fig. 2.23. (a) Bond-orientational order uses spherical harmonics to detect structural information. The contour lines represent the intensity of a spherical harmonic function with degree 6 and order 4, matching a local fcc environment. (b-d) Structures of nuclei and precursors in early crystallization. (e) Number distribution of all particles in the q_4-q_6 plane in the early crystallization. (f) Number distribution of nuclei of three meta-stable crystalline symmetries: BCC, HCP and FCC in the q_4-W_4 plane. (g) q_4-W_4 plot reveals BCC-like, HCP-like and FCC-like precursors in the liquid stage [17].

2.5. Very recent research progress on disorder-to-order transition in metallic alloys

Nucleation is a fundamental process in the formation of crystals, in which atoms aggregate to form stable nuclei in metastable liquid. According to classical nucleation theory [215], crystal nucleation occurs as a result of sudden or abrupt local structural change (i.e., structural fluctuation) in a homogeneous disordered liquid. The nucleation behavior is mainly governed by two factors, that is, interfacial free energy and volume Gibbs free energy (chemical potential) between liquid and crystal phases. For the case of solidification, the interfacial free energy dictates the height of the energy barrier required to nucleate stable clusters of the newly forming solid phase and is essential for producing an accurate solidification kinetics model using classical nucleation theory (CNT)-based methods. The Gibbs free energy of a system is a measure of the amount of usable energy (energy that can do work) in that system. The change in Gibbs free energy during a reaction provides useful information about the reaction's energetics and spontaneity (whether it can happen without added energy).

In terms of liquid metal, the crystal-liquid interfacial energy arises from configurations entropy difference between liquid and crystal. That is the greater difference in local structural orderings between crystal and liquid results in high interfacial free energy, which subsequently leads to a higher nucleation barrier and thus deeper supercooling. This theory has been verified in various metallic systems [58, 216, 217], and serves as an essential framework to understand crystallization. However, there remain many fundamental open questions even now above such a simplified picture. For example, Ostwald [218] argued that the crystal nucleated from a liquid is not necessarily the thermodynamic most stable one, but the one whose free energy is closest to the liquid phase. However, some studies based on Landau's theory argued that the bcc phase is favored to be nucleated at an early stage and then transformed to a stable phase in simple liquids [219]. On the other hand, recent experimental [7-10, 220] and simulation studies [11-14, 24] have revealed progressively that, in liquids, their atomic structures are not isotropic and homogeneous as introduced by CNT. It may have more complex and heterogeneous structures with local spatial regions of different geometrical characteristics and mobility [7, 15, 16]. Crystallization was suggested, to begin with

the growth of crystal-like bond orientational order and then translational order. Nucleation prefers to happen in the high crystal-like bond orientational order region, which is consistent with the crystal rather than randomly. Such transition happens through from orientational ordering then positional one [2, 17].

For most metallic alloys in the liquid-to-solid phase transformation processes, nucleation normally starts at atomic length scale and in ps to ns time scale[2, 3, 221-223]. So far, there are very limited reports on direct experimental observation of the structural heterogeneity in an undercooled liquid metal. Experimentally, it is very challenging to track and retrieve real-time dynamic evolution of the intermediate states of atomic structures and how they facilitate the onset of crystal nucleation. Only simulations of pure or binary alloy systems, e.g., Ni [22-24], Zr [25], $Cu_{50}Zr_{50}$ [25] and $Ni_{50}Al_{50}$ [25, 26] were attempted to track such transition forming simple, stable bcc or fcc phases. Fig. 2.24 shows that in the liquid $Ni_{50}Al_{50}$, the stable B2 crystal phase forms in a non-classical nucleation pathway, where bcc-like preorders formed in the supercooled liquid share the same symmetry with the stable B_2 crystal phase, whereas the other crystal-like preorders (fcc-like and hcp-like) are negligible.

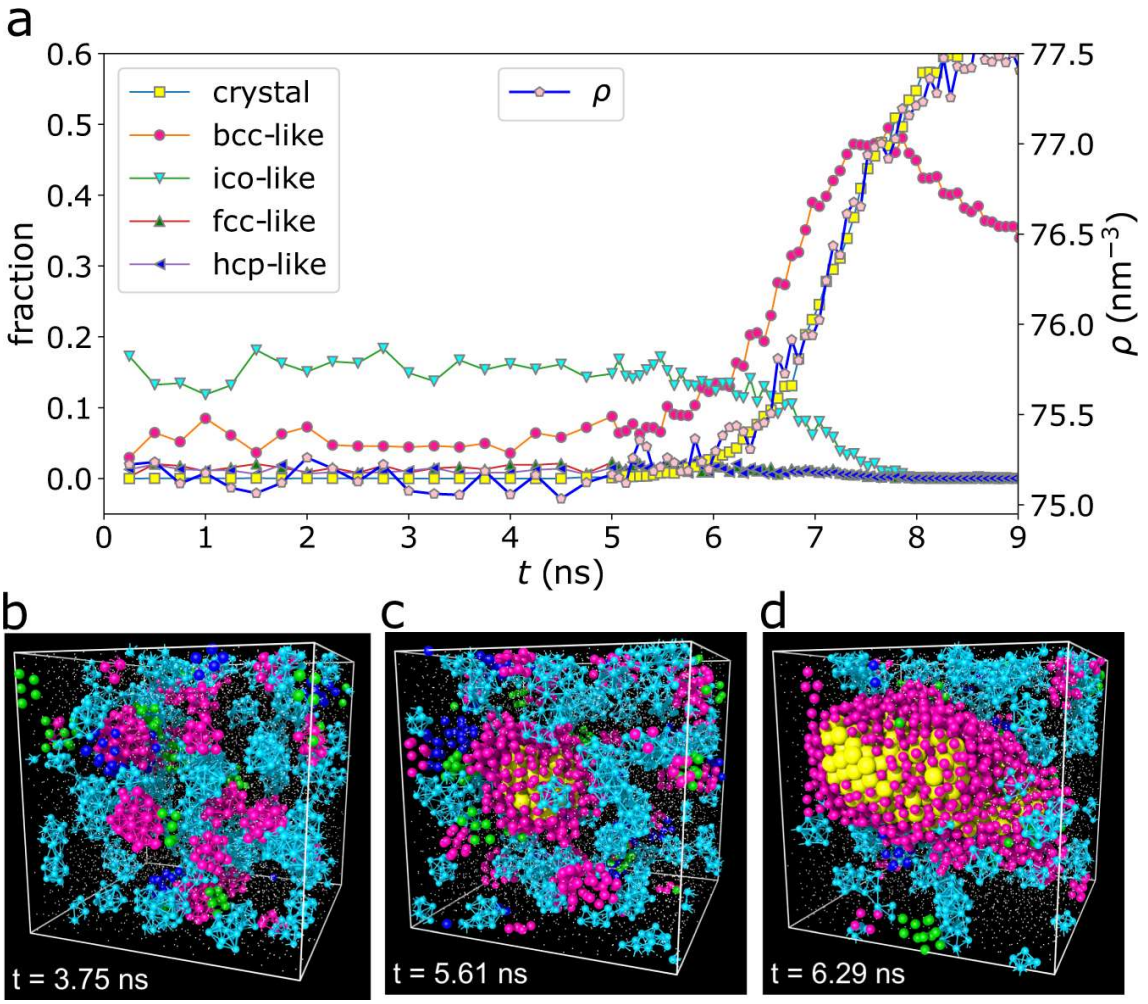

Fig. 2.24. The non-classical crystallisation process of NiAl was revealed by molecular dynamics (MD) simulations [26].

However, when working with multicomponent alloys, how complex phases nucleated in multicomponent liquid (liquid-to-solid) is still a gap, although the existence of this temperature-induced liquid-to-liquid transition has been verified in terms of both structural and dynamic characteristics. The complexity increases drastically from theoretical and experimental points of view. Affinities between different chemical species must be considered carefully since they induce multiple different chemical orders and stabilize complex solid phases. Some simulation studies revealed the liquid-to-liquid evolution of ternary melts above liquids. For example, Xu et al. [224] proposed the presence of a liquid-liquid

transition in the glass-forming $La_{50}Al_{35}Ni_{15}$ melt (see Fig. 2.25) above its liquidus temperature through ab initio molecular dynamics (MD) simulations.

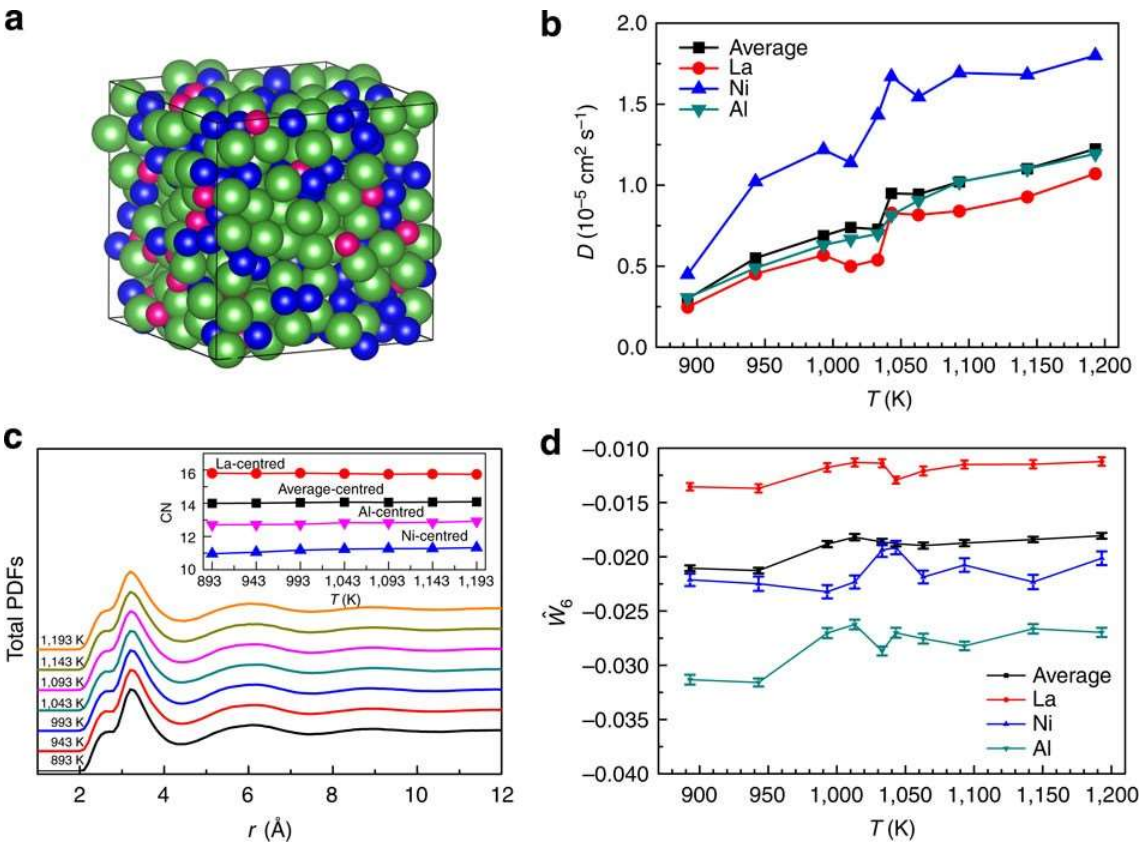

Fig. 2.25. (a) A typical atomic configuration equilibrated in the liquid state at 1,143 K modelled by *ab initio* MD simulations. Green, blue and red balls represent La, Al and Ni, respectively. (b) Temperature-dependent diffusion coefficient (c) Total pair distribution functions (PDFs), coordination number (CN) and (d) average $\hat{W}_6$ of all three elements and $\hat{W}_6$ of individual elements at different temperatures [224].

2.6 Summary

In this chapter, the background, historical development and techniques concerning the research of liquid metal structures have been reviewed and analysed, including the experimental techniques, modelling tools and data analysis methods. Based on the critical analyses, the aims, objectives and methodologies of this research are defined as described in detail in other relevant chapters of the thesis.

Chapter 3 Experiments and data analyses

This chapter consists of 4 sections. Section 3.1 describes the alloys and samples used in the experiments. Section 3.2 describes my contribution towards the upgrade and optimization of the counter-gravity casting apparatus and two special furnaces for in-situ total scattering and tomography experiments. Section 3.3 details the SXTS experiments conducted at the I15-1 and I12 beamlines of Diamond Light Source (DLS). Section 3.4 is about the theories, methods and modelling tools used for analyzing the SXTS data, including data normalization procedure, parameters optimization, the GudrunX running procedures, the EPSR simulation and atomic structure quantification.

3.1 Alloys and sample making

The alloys and samples were made in the Advanced Materials Laboratory at the School of Engineering, University of Hull. Table 3.1 lists the alloys and feedstock raw materials. Pure Fe, Cu, Si materials were purchased from Goodfellow. The high purity Al and Al-2Sc alloys were provided by partners of Shanghai Jiao Tong University, while the Al-10Ti and Al-3.5La-6.5Ce by Brunel University London.

Table 3.1. The alloys and samples used in the experiments (weight fraction).

Alloys	Feedstock raw materials	Experiment No.	Beamline
Al	Pure Al (99.999%)	EE20883-1	I15-1
Al-0.4Sc	Pure Al, Al-2Sc	EE20883-1	I15-1
Al-1.5Fe	Pure Al, Fe	MG27571-2	I12
Al-5Cu-1.5Fe	Pure Al, Cu, Fe	MG27571-2	I12
Al-5Cu-1.5Fe-1Si	Pure Al, Cu, Fe, Si	MG27571-2	I12
Al-15Cu-Sc	Pure Al, Cu, Al-2Sc	MG27571-2	I12
Al-1Ti-Sc	Pure Al, Al-10Ti, Al-2Sc	MG27571-3	I12
Al-1Zr-1Sc	Pure Al, Al-10Ti, Al-2Sc	MG27571-3	I12
Al-3.5La-6.5Ce	Al-3.5La-6.5Ce	MG27571-2	I12

The Al-0.4%Sc alloy and samples were made by melting 200g pure Al and 50g Al-2%Sc together in an alumina crucible inside an electric resistance furnace. The feedstock was first heated to 300 °C and held for 20 minutes to remove the moisture. Then the furnace was heated to ~690 °C to melt alloy in approximately 2 hours. Finally, a counter-gravity casting apparatus was used to suck the alloy melt into a 100 mm long quartz tube (10 mm inner diameter) under a negative pressure of ~5Kpa. In this way, any melt surface turbulence during melt filling was avoided and entrainment of air bubbles or oxides films was minimized. After the bar solidified, the cast bar was subsequently covered under a ceramic blanket and cooled to room temperature. The Al-0.4Sc cast bars were cut into cuboids of 4 × 4 × 30 mm. The sample surfaces were ground using SiC grinding papers as shown in Fig. 3.1, ready for being placed into a quartz sample holder with an inner diameter of 6 mm for the SXTS experiments.

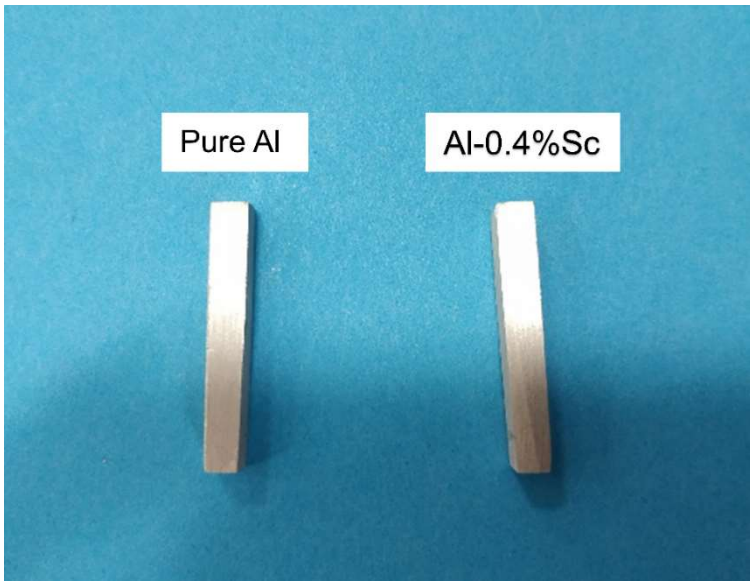

Fig. 3.1. The ground pure Al and Al-0.4%Sc samples

For the three Fe-containing Al alloys (Al-1.5Fe, Al-5Cu-1.5Fe and Al-5Cu-1.5Fe-1Si), they were made by melting pure Al (99.999%) ingot, copper (99.99%) bar, Fe (99.99%) bar and Si (99.99%) lump pieces with the designed weight ratio in an electric resistance furnace. The alloys were heated to 850 °C and held for 1h to homogenize the temperature and chemical composition. The melt was then again drawn uphill into a quartz tube (10 mm diameter, 150 mm long) by using the counter-gravity casting apparatus [225] under a pressure of ~6 KPa, and then solidified there to form a cast bar. The as-cast bars were then machined into 3

mm diameter 25 mm long rods for the subsequent SXTS experiments. Similar casting methods were used for making other samples.

3.2 Upgrade of the counter-gravity casting apparatus and furnaces for X-ray total scattering experiments

3.2.1 Upgrade of the counter-gravity casting apparatus

We routinely used the counter-gravity casting apparatus to cast round bar samples by avoiding the problems associated with gravity pouring of molten metal into a mould. I have contributed to upgrading the apparatus based on Tan's design [226], mainly by adding a differential pressure control system (see Fig. 3.2) to allow precise control of the negative pressure and air flow rate during operation. The upgrade realised safer and semi-automatic operation.

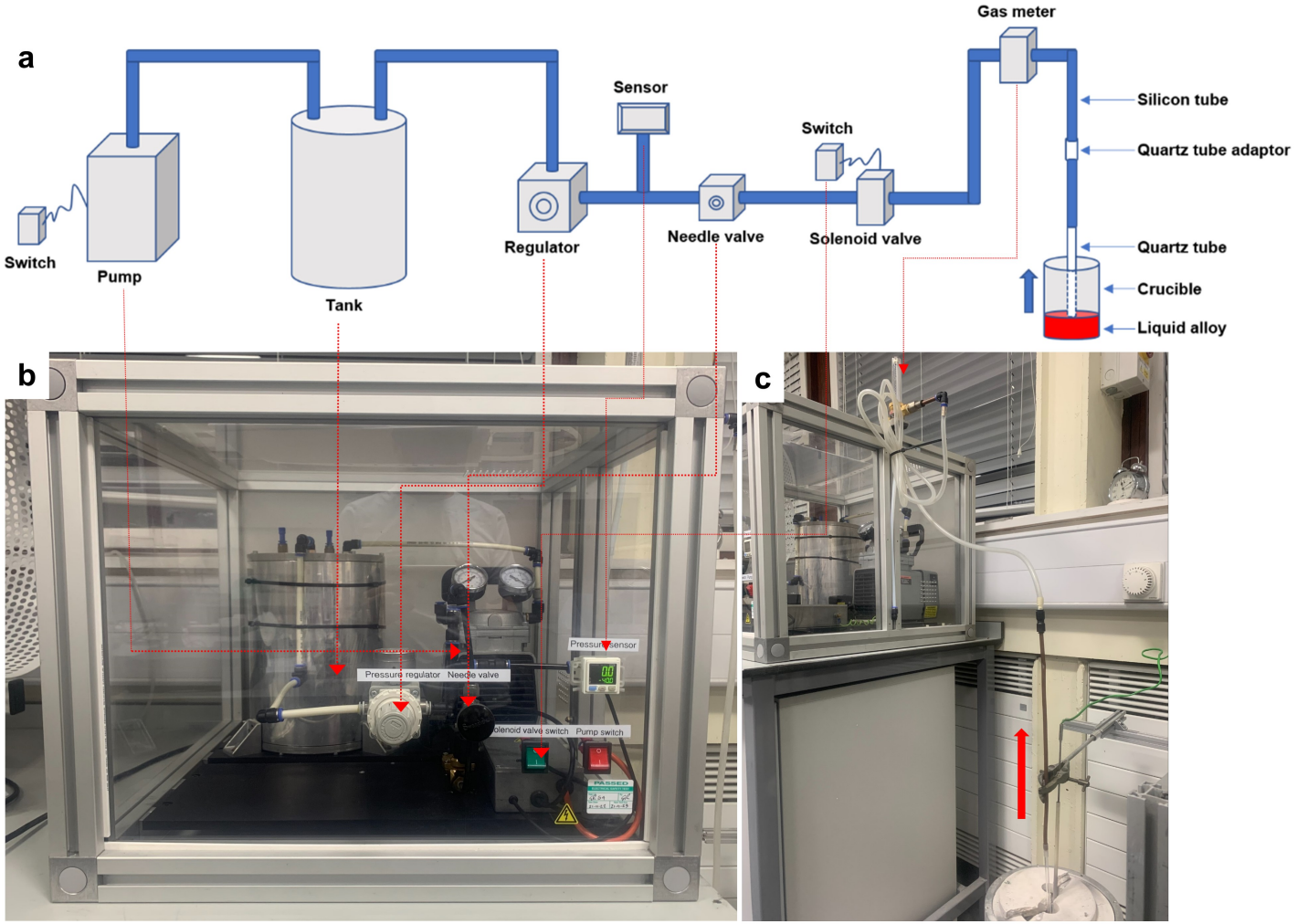

Fig. 3.2. (a) The sketch of the counter-gravity casting apparatus, (b) a front-view photo the apparatus and (c) its side-view.

Fig. 3.2a illustrates a schematic diagram of the control system, and Fig. 3.2b and c shows the actual device and components. The operation normally has the following steps: first a vacuum pump is used to pump the air out of the enclosed tank, generating negative pressure for sucking liquid metals. A gas regulator is used to control the pressure in the tank, which is displayed on the digital gas sensor screen. A stable negative pressure is a critical for controlling the "sucking" process. During the "sucking" process, fine adjustment of the pressure is also needed to “flow” the liquid alloys smoothly into the quartz tube. Such fine adjustment was achieved by adding a needle valve to regulate the speed of air flow during the "sucking" operation. Then the melt that flowed into the quartz tube solidified under the holding of the negative pressure. Through many trials, the following operation procedures were established and optimised to ensure a successful operation for making high quality samples:

(1) Check the power switches located on the box and set an alarm pressure to 40.0 KPa on the pressure sensor.
(2) Turn on the vacuum pump switch to activate the pump, ensuring it functions properly.
(3) Turn on the gas meter, needle valve, and solenoid valve switches, and then inspect the entire channel for any blockages.
(4) Turn off the solenoid valve switch and set the desired target pressure by adjusting the pressure regulator. Using what level of negative pressure is primarily dependent on the liquid metal density and the casting bar length.
(5) Securely connect the quartz tube between the gas meter and the crucible.
(6) Turn on the solenoid valve switch to draw the liquid alloys into the quartz tube.
(7) Once the desired volume of liquid alloys is sucked into the quartz tube, turn off the solenoid valve switch and vacuum pump switch.

This upgrade improved operation safety and melt flow control accuracy during the suction process, avoiding inconsistence or mishap due to manual operation.

3.2.2 Design, upgrade and optimization of two tube furnaces for synchrotron x-ray total scattering solidification experiments

Two special quartz tube furnaces with different heating capacities were used in the SXTS experiments. The early version at I15-1 and the upgraded version at I12 and DIAD. The functionalities and upgrade of the furnaces are briefly described here.

3.2.2.1 The furnace used in I15-1

The early version of the electrical resistance furnace was originally designed by Wei Zhang [227]. I made minor adjustments and improvement on the furnace, allowing it to fit the relatively small operation space for the sample environment along the X-ray beam path at the hutch of the I15-1. Fig. 3.3 depicts the CAD assemblies (opened to show the internal details) and the centre-line sectional view of the furnace and sample holder. A cone-shaped window on the sidewall of the furnace that faces the detector was machined with an opening angle of 90°, providing a clear path for the diffracted photons to reach the detector. The furnaces consist of 3 main parts:

(1) A heating unit made of a quartz tube chamber and an electrical resistance heater.
(2) A sample holder, the alloy sample inside a capillary tube was positioned on the top of a tapered quartz tube, which was then enclosed inside a larger quartz tube chamber with a diameter of 17 mm.
(3) A gas circulation system for flowing inert gases to protect the samples from oxidation during the heating and to provide additional cooling capability during solidification.

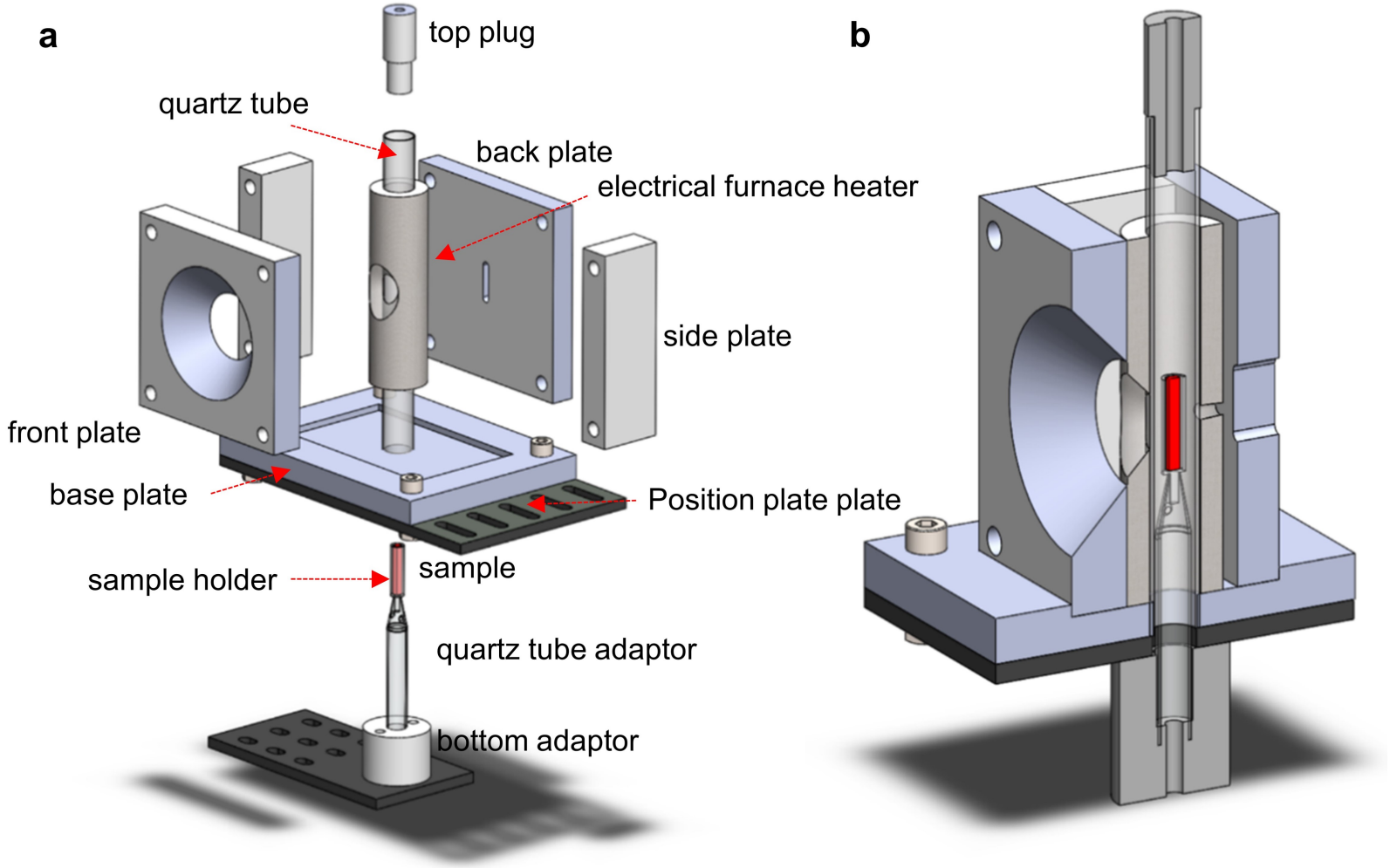

Fig. 3.3. (a) The CAD assemblies and (b) the centre-line sectional view of the experimental apparatus for the SXTS at I15-1.

3.2.2.2 The furnace used in I12

The furnace used at I12 was upgraded based on the early version with following improvements:

(1) Higher temperature insulation materials: the mastic and Duratec 750 [228] were replaced with the monalite materials (Plastic and Rubber Group Limited®) for holding the heating elements and used as the furnace cover board, increasing the stability and durability of the furnace to temperature up to 1000 °C.
(2) Higher heating capability: longer heating wire and coil were made and used, providing higher heating power and larger effective heating zone.
(3) Wider cone-shaped window: the cone-shaped window on the furnace sidewall was enlarged to 100° instead of 90°, improving the collection of more diffracted photons at higher angles.

As depicted in Fig. 3.4, the heating unit of the furnace was assembled using several components. These included a large right-angle bracket (P1, AP90RL/M Large Right-Angle Bracket ordered from Thorlabs), a monalite insulation base (P2), four monalite heat insulation side plates (P3, P4, P5 and P6), and an electrical resistance heater comprising a hollowed-out monalite part (P7), heating coil, and a quartz tube (P8). Each of the insulation plates had a thickness of 15mm.

On the back plate (P10), a slot window of 5mm wide and 40mm long was opened to allow the passage of X-rays. Additionally, a cone-shaped window with an outward angle (100°) was machined on the front side plate (P9). The same cone-shaped window was also created on the heating part. This design allowed for the acquisition of X-ray total scattering information across a high Q-range. The monalite plates were machined using CNC according to the CAD design in Appendix 1. As depicted in the diagram, there is a groove with a diameter of 6 mm designed to accommodate the heating coil. A 12-meter-long heating wire was carefully wound into a 60 mm long coil with an inner diameter of 4mm. Subsequently, the heating coil was inserted into the groove, and mastic was applied to stabilize it. The heating unit was then dried at 130 °C in an oven for 12 hours or longer.

During the SXTS experiment, a 3 mm diameter alloy sample (P13) was placed inside a capillary tube with an inner diameter of 3.5mm (P12). This capillary tube was then positioned on a monalite adaptor (P14), which was further situated on a quartz tube (P15). The monalite adaptor serves as an effective thermal insulator, which is crucial for controlling the sample's temperature during the experiment. The entire assembly, comprising the sample, capillary tube, monalite adaptor, and quartz tube, were mounted on another monalite adaptor that is specifically designed for the sample stage in beamline I12. This well-designed sample unit facilitates efficient sample changes, precise alignment, and ultimately helps save experiment time.

For gas circulation, a monalite top plug (P11) was positioned on top of a quartz tube (P8) with an outer diameter of 18mm and a thickness of 1.5mm. This quartz tube was then placed on the base plate (P2). The top surface of the bottom adapter (P16) was contacted with the underside of the right-angle bracket (P1), forming an enclosed chamber. Once the components were assembled, two gas tube fittings were connected to designated locations (P11 and P16). The protection Ar gas can be introduced into the chamber through the gas inlet hole (bottom surface of P16), filling the sample chamber, and then exiting through the gas outlet tube fitting (P11). This setup ensures proper gas circulation and protection during the experiment. The CAD drawing of each part mentioned above can be found in Appendix 1. The CAD drawing of the assembled furnace can be found in Fig. 3.5.

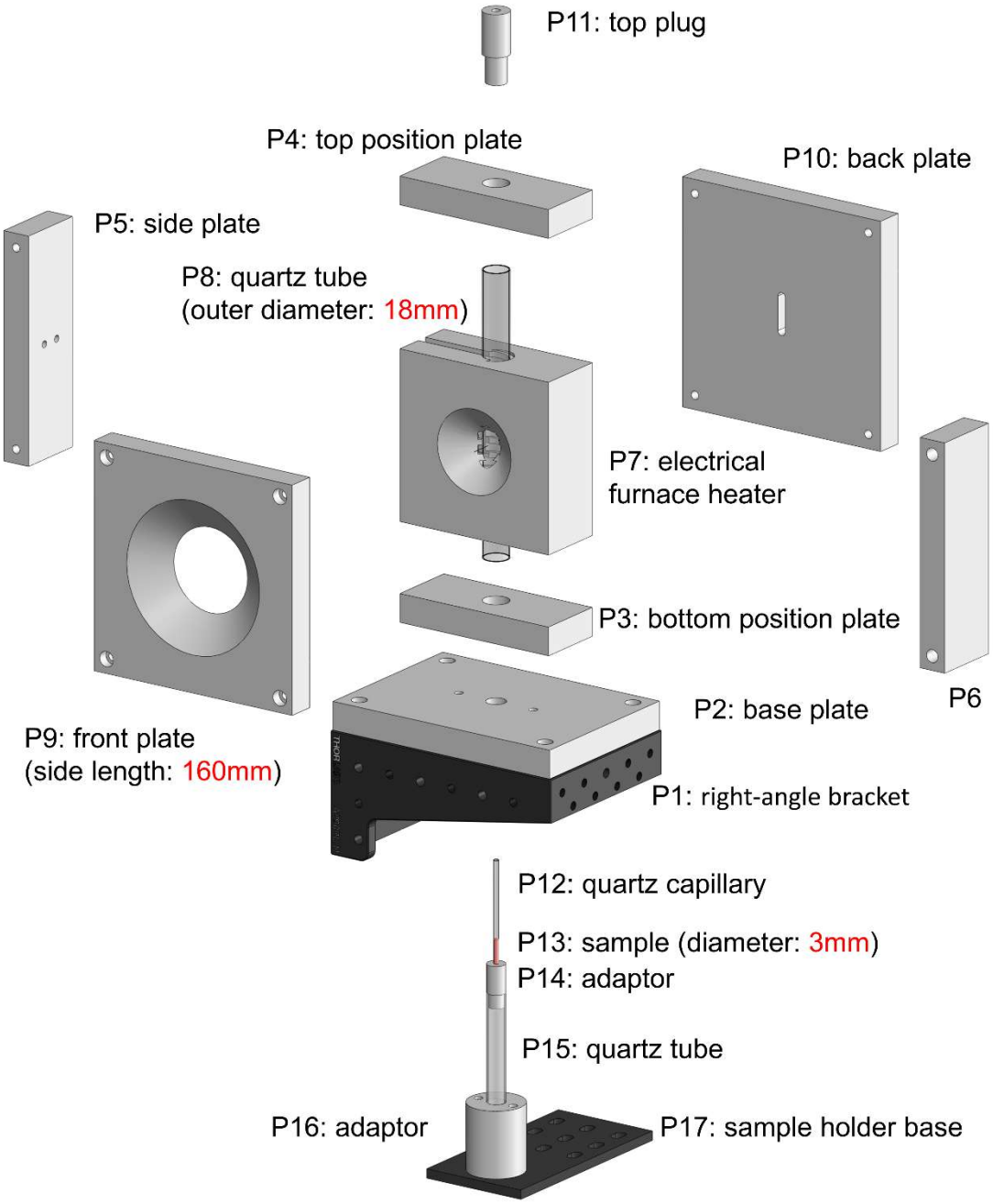

Fig. 3.4. The CAD assemblies of the upgraded furnace for higher temperature SXTS and tomography experiments.

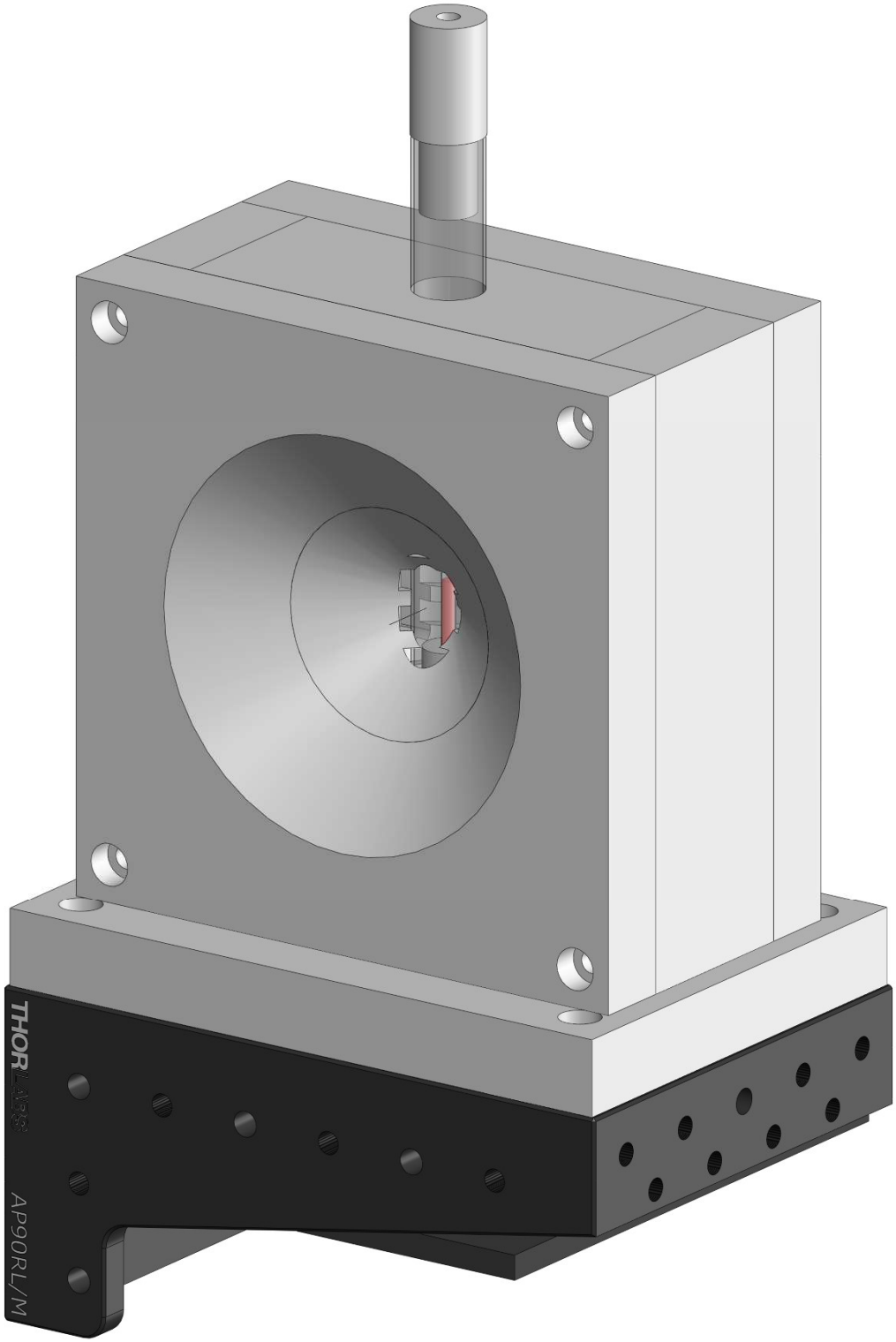

Fig. 3.5. The CAD drawing of assembled furnace used in I12 and DIAD beamlines.

3.3 Synchrotron X-ray total scattering solidification experiments

3.3.1 Experiments at beamline I15-1

Fig. 3.6 shows the X-ray, furnace and detector in the SXTS experiments at beamline I15-1 of DLS, UK. A monochromatic X-ray of 50.239 KeV was used. The Perkin Elmer 1621 EN detector size is 2048 x 2048 pixels with pixel size of 200μm^2. The beam size we used is 70*70 μm^2. The sample-to-detector (S-D) distance and beam centre of the detector were calibrated using CeO_2 as calibrant. The calibration parameters are listed in Table 3.2.

Table. 3.2. The parameters used in the experiments after calibration using the standard CeO_2 in Fit2D

X-ray Energy (KeV)	S-D distance (mm)	Detector (Perkin Elmer 1621 EN)					
		Beam centre (mm)		Pixel size (μm)		Orientation	
		x	y	x	y	Rotation	Tilt
50.239	290.46	1053.60	1018.59	200	200	176.70	1.126

At each target temperature, the melt was held there for sufficient time to homogenize the temperature before taking a scattering pattern. 240 s exposure time was used for each pattern. After the pattern was taken, the temperature change was within ±1 °C of the target temperature. Bragg spots due to the formation of crystalline phases appeared in the scattering patterns for samples cooled below the liquidus. To extract the scattering information from the remaining liquid melt only, an adaptive method was used to remove the Brag spots from the patterns, similar to that used in [229]. Calibration and conversion of the 2D patterns into 1-D intensity profile were carried out using Fit2D [230] after background subtraction and data correction by using GudrunX [155]. During the experiment, high purity Al was used as a baseline, when sample cooled down to 660°C (the liquidus of pure Al), solid phased immediately forms in liquid, indicating that the beam heating does not have an obvious effect on the sample temperature.

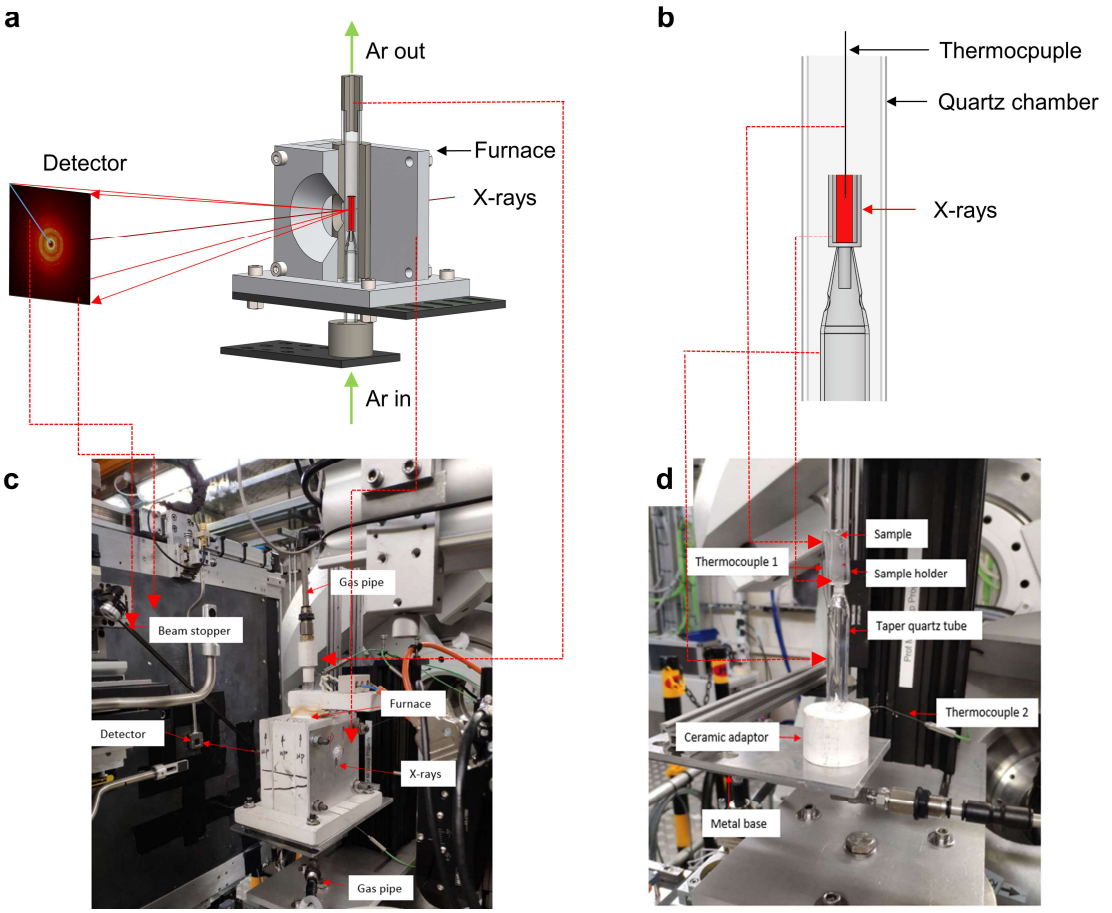

Fig. 3.6. The setup of the experimental apparatus at I15 beamline. (a) The sketch of the furnace, the quartz sample holder mounted at I15 beamline. (b) The location where the K-type thermocouple tip was inserted inside the melt, and the point where scattering patterns were taken. (c) A photo of the geometrical arrangement of the furnace, gas circulation unit, X-ray beam and detector during the SXTS experiment. (d) A photo of the sample unit.

3.3.2 Experiments at beamline I12

The operando SXTS experiments at the beamline I12 [156] were carried out from 14th to 23rd July (MG27571-2) and from 26th to 28th (MG27571-3) September 2021. The beamtimes were awarded to the proposal "*In situ synchrotron X-ray total scattering studies of the dynamic evolution of atomic structures of metal alloys in liquid and undercooled liquid state*". The first session MG27571-1 was scheduled in 2020 but was cancelled due to the COVID-19 lockdown at DLS. The experiment details of MG27571-2 were given here.

The upgraded quartz tube furnace with heating capacity to ~1000 ºC was used in the experiments. The set-up is shown in Fig.3.7a and Fig. 3.8. The rod alloy sample (the red-colour part in Fig. 3.7b) was held inside a 3.5 mm diameter capillary quartz tube during the melting and cooling process. A K-type thermocouple TC1 (0.5 mm diameter, see Fig. 3.9) was inserted inside the alloy melt to measure the temperature. Before the experiment, a groove was machined to locate the thermocouple, which can also ensure the thermocouple tip always touches the sample during heating and cooling. The thermocouple (TC1) was located at ~3mm above the point where the scattering patterns were taken, and the measured temperature data by TC1 was recorded by the data logger of I12 beamline. Among them, TC2 was used to monitor the furnace chamber temperature while TC3 was used for furnace temperature control. An Omega PID thermal controller (CN16DPT-440) was used to control the furnace temperature. A PicoTC08 data logger and the relevant software (PicoLog 6 data logging software) were used to record the temperature data measured by TC2 and TC3. Ar gas flowed into the quartz tube furnace chamber at the bottom opening to protect the samples from oxidization during melting. A monochromatic X-ray of 100.03 KeV (wavelength of 0.1236 Å) and a 2D flat-panel detector (Pilatus3 X CdTe 2M, 1475×1679 pixels with a pixel size of 172×172 μm^2) were used for acquiring the SXTS patterns. The detector was positioned off-centre to the incident X-ray beam to acquire the scattering information at higher Q up to 20 $Å^{-1}$. The sample-to-detector distance was calibrated as 408.02 mm. Fig. 3.7c shows that each alloy sample was heated to 750 ºC and held for 30 min to ensure the sample was fully melted and temperature homogenized. Then, the sample was cooled by 2.72 K/min and SXTS patterns were acquired continuously with 30s exposure time for each pattern.

The 1D scattering patterns integrated from the 2D images for the three alloys in the cooling process are shown in can be found in the experimental results part. Fig. 3.7d shows more diffraction patterns for the Al-5Cu-1.5Fe-1Si alloy, indicating that, after the primary monoclinic $Al_{13}Fe_4$ phase emerged from the liquid at 628 ºC, the α-Al appeared at 622 ºC. The total scattering data at the selected temperatures (see the EPSR modelling part) were chosen for each alloy as the experimental data to compare with the corresponding results from the EPSR modelling. Scattering pattern calibration and conversion into 1D intensity curves

were carried out using DAWN [231]. The total structure factor $S(Q)$ was obtained after standard corrections by removing the effects of background, self-absorption, polarization, fluorescence and Compton scattering using GudrunX [155]. Procedures for the data normalization, parameters optimization and alloy density determination at different temperatures were described in the data processing part. Subsequently, the PDF $g(r)$ was obtained by the Fourier transform of $S(Q)$.

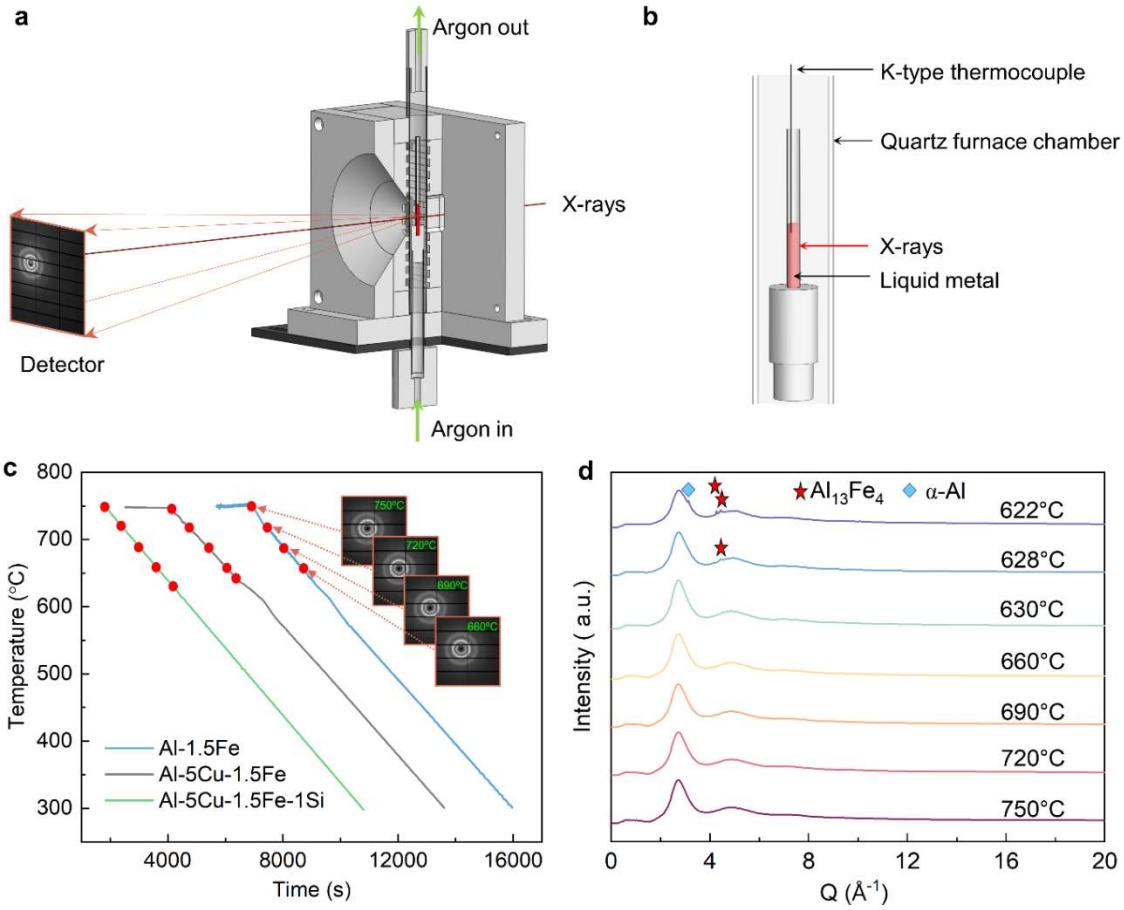

Fig. 3.7. The experimental setup for the SXTS experiments. (a) A sectional view of the quartz tube furnace, the X-ray beam, detector and sample arrangement. (b) The rod alloy melt (the red-colour part) is held inside a 3.5 mm diameter capillary quartz tube with a K-type thermocouple tip inserted inside the alloy melt. (c) The cooling profiles were applied to the three alloy samples. The red dots indicate the temperatures at which the acquired SXTS patterns were used to compare with those from the EPSR modelling. (d) SXTS patterns of the Al-5Cu-1.5Fe-1Si alloy at the selected temperatures, showing that the nucleation of $Al_{13}Fe_4$ occurred at 628 ºC.

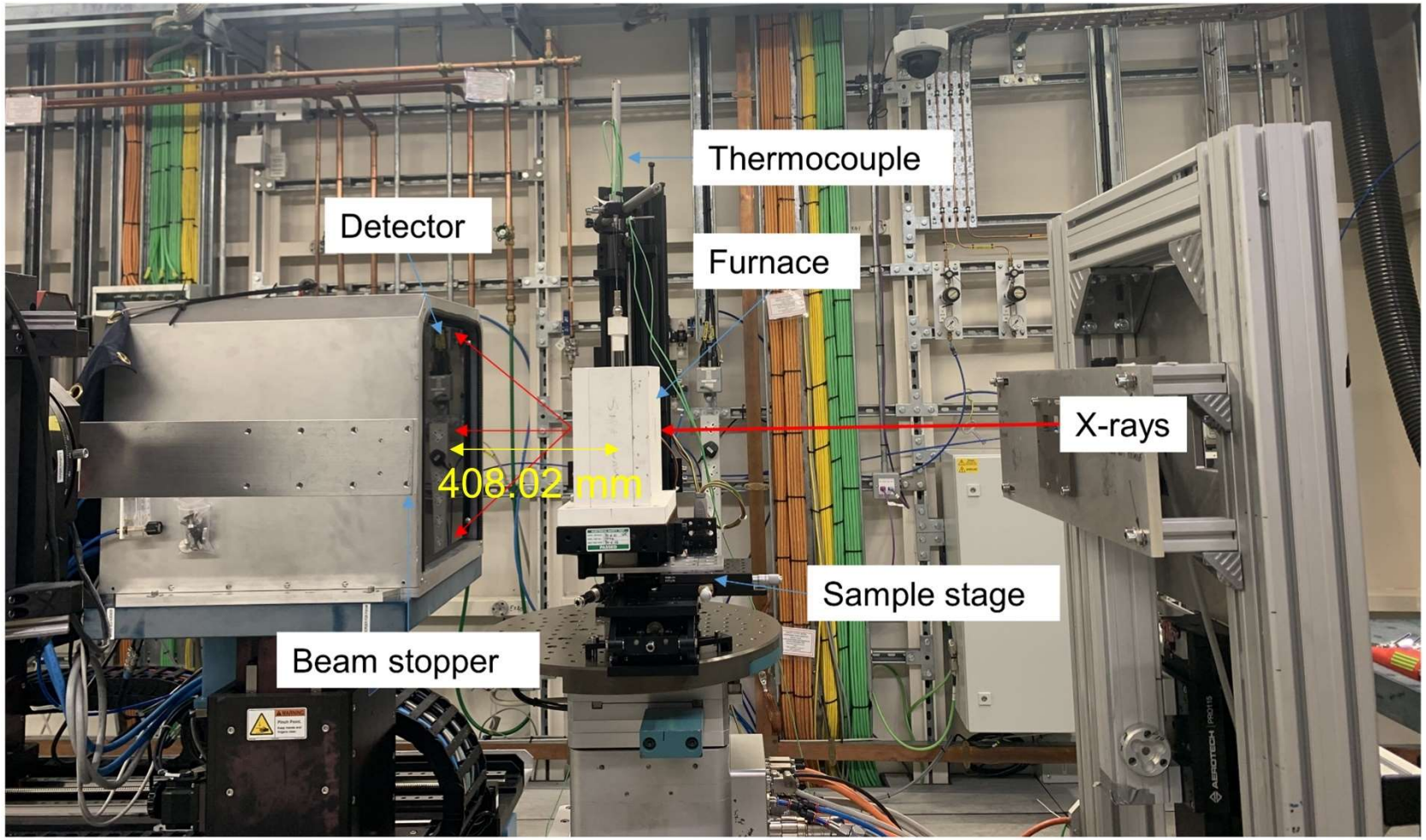

Fig. 3.8. A photo of the set-up of the total scattering experiment at I12 beamline.

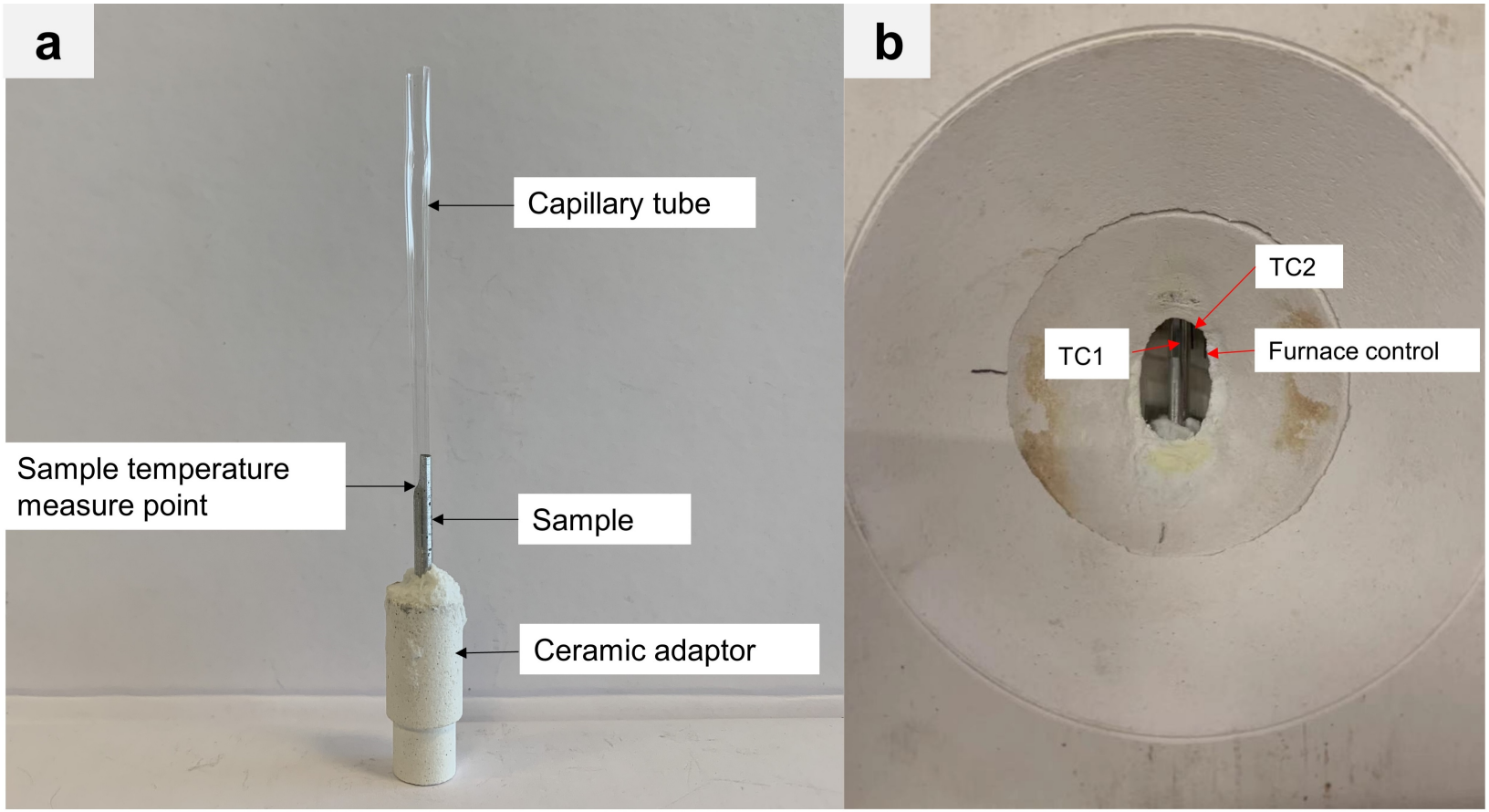

Fig. 3.9. The detailed arrangement of sample unit. (a) Sample unit: A quartz capillary with an inner diameter of 3.5mm was placed concentrically on the ceramic adapter, and then the sample was inserted into the tube. A groove was machined on the sample surface to position the thermocouple tip. (b) The arrangement of three thermocouples used in the experiment is shown. TC1's tip directly contacts the sample to record the sample temperature and is connected to the recording system of I12. TC2 is used to record the chamber temperature. The TC3 (furnace control) is connected to our own control system to regulate the sample temperature.

3.4 Data reduction and analyses

3.4.1 Normalization of the SXTS data

The SXTS data were normalized using GudrunX based on the Krogh-Moe and Normand methods [155, 232, 233]. The measured SXTS signal is a sum of the intensity from the sample and the background:

$$I^{meas}(Q) = a(Q)I^{sample}(Q) + bI^{bk}(Q) \tag{3.1}$$

where $Q = 4\pi\, sin(\theta)\,/\lambda$ is the scattering momentum, $\mathrm{a}(Q)$ is the transmission factor which can be deduced according to information about the beamline instrument and materials involved [86], b is the scale factor for background correction, $I^{sample}(Q)$ is the scattering intensity of the sample, and $I^{bk}(Q)$ describes the environment scattering intensity (without the sample).

$I^{sample}(Q)$ is regularly parsed into three parts, i.e., the coherent scattering intensity $I^{coh}(Q)$, the incoherent scattering intensity $I^{incoh}(Q)$ and the multiple scattering intensity $I^{mul}(Q)$. It is expressed as:

$$NI^{sample}(Q) = I^{coh}(Q) + I^{incoh}(Q) + I^{mul}(Q) \tag{3.2}$$

where N is the normalization factor using the Krogh-Moe-Norman method [232, 233]:

$$N = \frac{-2\pi^2\rho_0 + \int_0^{Q_{max}} Q^2 \dfrac{I^{incoh}(Q) + \sum_i c_i\, {f_i}^2(Q)}{(\sum_i c_i\, f_i(Q))^2}\, dQ}{\int_0^{Q_{max}} Q^2 \dfrac{I^{sample}(Q)}{(\sum_i c_i\, f_i(Q))^2}\, dQ} \tag{3.3}$$

where ρ_0 is the average atomic density of the sample and Q_{max} is the maximum scattering vector, c_i and f_i represent the concentration and scattering form factor of the i_{th} element, respectively.

According to the Faber-Ziman definition [234], the structure factor $S(Q)$ can be calculated as follows:

$$S(Q) = \frac{I^{coh}(Q) - (\sum_i c_i f_i{}^2(Q) - (\sum_i c_i f_i(Q))^2)}{(\sum_i c_i f_i(Q))^2} \quad (3.4)$$

The reduced pair distribution function, $G(r)$ can be obtained by a Fourier transformation of the structure factor:

$$G(r) = \frac{2}{\pi}\int_0^{Q_{max}} Q(S(Q) - 1)\sin(Qr)\, dQ \quad (3.5)$$

The pair distribution function, $g(r)$ can be calculated by:

$$g(r) = 1 + \frac{G(r)}{4\pi r \rho_0} \quad (3.6)$$

In this work, the scattering form factor of each element f_i was calculated using the analytic functions [235]. $I^{incoh}(Q)$ was computed using the analytic approximation [236]. $I^{mul}(Q)$ is ignored because of the very weak intensity. For the normalization process, Q_{max}, ρ_0 and b need to be determined, which will be described in section 3.4.2 [237-239].

3.4.2 Parameters optimization and liquid density determination

It is difficult to measure experimentally the densities of the three liquid melts at the temperatures we studied. The liquid density ρ_0 and b are thus determined using a numerical interactive procedure, consisting of five steps [237-240] below.

Firstly, $g(r)$ is calculated according to Eq. (3.5) with an estimated value at the start.

Secondly, the minimal distance r_{min} is defined in such a way that there are no atom-atom correlations (atomic cores do not overlap) before the first peak in $G(r)$. For $r < r_{min}$, no additional atoms can be present, i.e., $g(r) = 0$, so that no oscillation should be observed in the $g(r)$ [238]. According to Eq. (3.6), a particular distribution function can be expressed as $G(r < r_{min}) = -4\pi r\rho_0$.

Thirdly, the parameter $\Delta G_0(r)$ is used to represent the difference between the experimental $G_0(r)$ and the particular $G(r)$ (where subscript-0 is the value of the function before the first iteration), and it can be expressed as

$$\Delta G_0(r) = G_0(r) - (-4\pi r\rho_0) \quad (0 < r < r_{min}) \tag{3.7}$$

Fourthly, a new structural factor $S_1(Q)$ is calculated by:

$$S_1(Q) = S_0(Q)\left[1 - \frac{1}{Q}\int_0^{r_{min}} \Delta G_0(r)\, sin(Qr)\, dr\right] \tag{3.8}$$

Finally, the iterative process is executed by substituting the $S_1(Q)$ into Eq. (3.5) to obtain $G_1(r)$ and then derive $\Delta G_1(r)$.

The above five-step procedure is the first full iteration. To minimize the errors, such full iteration is repeated 5 times [238], i.e., $n = 5$. A figure of merit, χ^2 is introduced to monitor $\Delta F_n(r)$, which is:

$$\chi^2(\rho_0, b) = \int_0^{r_{min}} [\Delta G_n(r)]^2 dr \tag{3.9}$$

(ρ_0, b) couple at converge can be determined by minimizing the χ^2 value (<0.0005) [238].

To extract (ρ_0, b) at each temperature, two more parameters Q_{max} and r_{min} are also to be determined. This is achieved via a dedicated MATLAB script developed by Luo et al. [239].

The optimized liquid density ρ_0 at the selected temperatures for every alloy is listed in the EPSR modelling part. Fig. 3.10 compares the measured density of pure Al with the computationally optimized liquid density of pure Al, Al-1.5Fe, Al-5Cu-1.5Fe and Al-5Cu-1.5Fe-1Si at different temperatures [241]. Taking the pure Al as an example, the comparison shows that the discrepancy between the optimized and measured densities is < 0.5%, throughout the whole temperatures range. This confirms that the liquid density we calculated via the optimization procedure is sufficiently accurate. Hence, they are used in the following EPSR simulation.

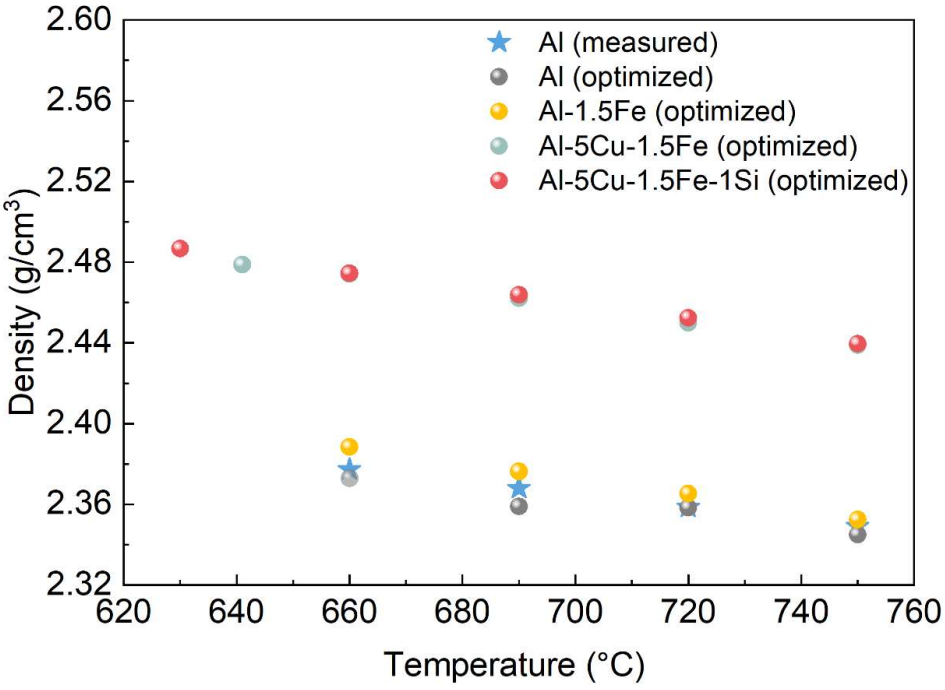

Fig. 3.10. The measured densities of the liquid pure Al from [241], and the optimized liquid density of pure Al, Al-1.5Fe, Al-5Cu-1.5Fe and Al-5Cu-1.5Fe-1Si at the selected temperatures.

3.4.3 Data processing procedure to remove diffracted information from crystalline phase

The total scattering patterns acquired at the temperatures above the melting point (Fig. 3.11a) exhibited the typical disordered characteristics of a liquid (i.e., a diffuse halo pattern). The scattering patterns acquired at temperatures below the melting point contained the Bragg spots from the solidified crystalline phases (Fig. 3.11b).

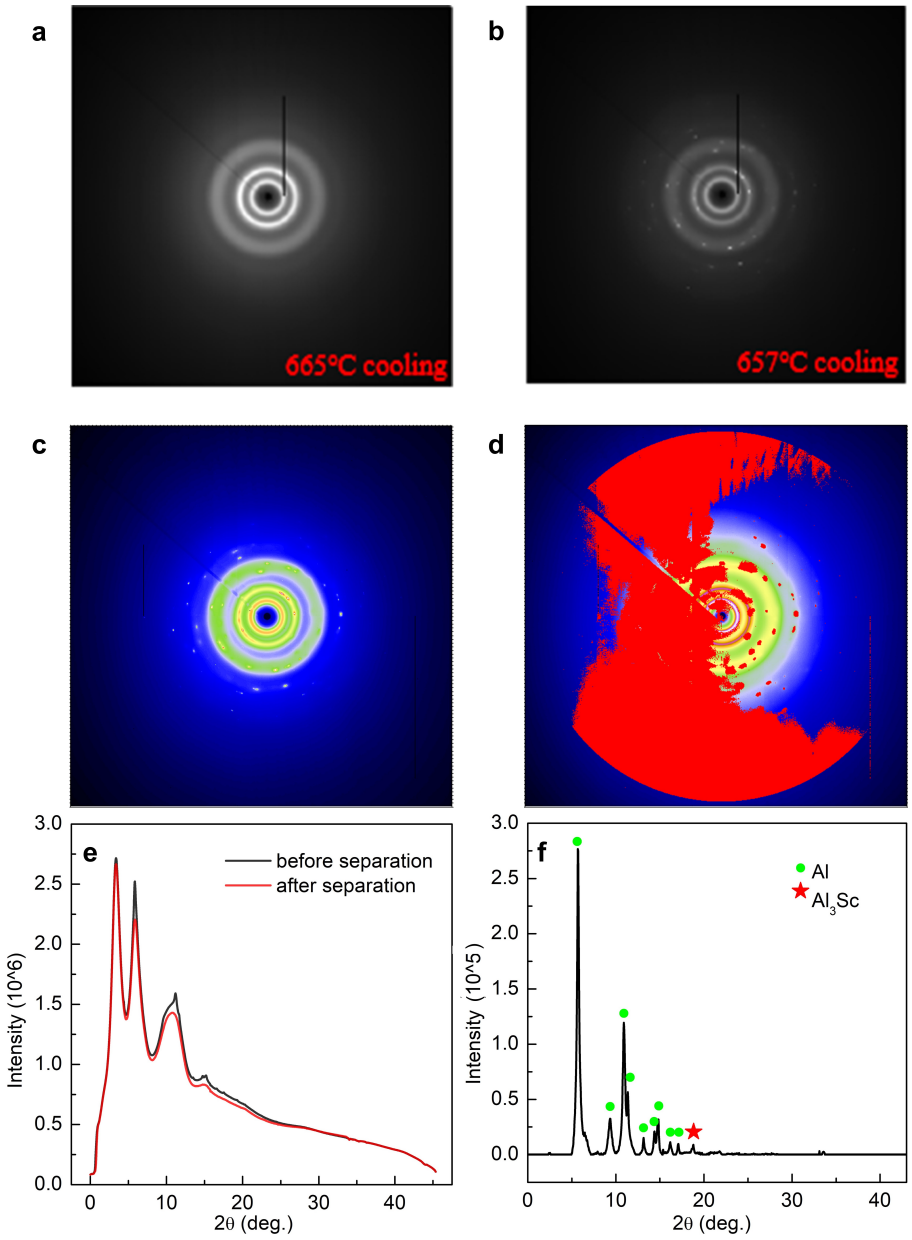

Fig. 3.11. (a) a typical raw pattern of Al-0.4Sc alloy at liquid state and (b) semi-solid state, (c) the total scattering pattern of the Al-0.4Sc at 657°C viewed in Fit2D

[230]; (d) The pattern after removing the crystalline scattering contribution (shown in red). (e) The integrated 1D scattering intensity profiles before and after removing the contribution of the crystalline phases. (f) The integrated scattering intensity from the crystalline phases (the red star indicates the Al_3Sc phase, and the green dots indicates the α-Al phase) in the Al-0.4Sc alloy at 657 °C.

To extract the scattering information from the liquid melt only (semi-solid system), an adaptive masking method was used to remove the Bragg spots from the patterns. First, the median intensity at each Q value was calculated for each pattern, and then the pixels with the intensities outside the median intensity were removed [229], as typically shown in Fig. 3.11d. The scattering information from the liquid and that from the crystalline phases were therefore both independently obtained (red line and black line in Fig. 3.11e, respectively). It is worth noting that some crystal diffraction peaks (see Fig. 3.11f) due to the Al_3Sc primary phases, indicating that this phase has formed at 657 °C in the Al-0.4Sc alloy.

3.4.4 Detailed procedures for running GudrunX

Different to most reported scattering experiments, our samples were contained in two quartz containers: a quartz chamber and a capillary tube holding the sample, making the data correction process even more challenging. To obtain a fully corrected $S(Q)$ scattering curve, the following background scattering data are needed:

(1) Empty instrument: Scattering data acquired when the instrument is empty.
(2) Empty instrument + capillary tube: Scattering data acquired with only the capillary tube in the instrument.
(3) Empty instrument + quartz chamber + capillary tube: Scattering data acquired with both the quartz chamber and the capillary tube in the instrument.
(4) Empty instrument + quartz chamber + capillary tube + sample: Scattering data acquired with the complete setup, including the sample.

During the data reduction process, it is crucial to combine the scattering information from the quartz chamber and the capillary tube and treat them as a

single one. We are grateful to the data scientist, Dr Daniel T, who developed a specially designed GudrunX template for processing the scattering data. The GudrunX interface [155], as shown in Fig 3.12, consisting of six tabs for data reduction of the scattering data acquired in I15 and I12. These tabs include:

(1) Instrument: This tab provides the directory for the total scattering section, cross-section, form factor, and Compton scattering coefficient files. These files are typically stored in the same directory as the GudrunX software. The index Q-range specifies the lowest, highest, and step values of Q for the output files $F(Q)$, while the maximum and step values of r are given for the output $G(r)$. One example showing the tuning effect of Q_{max} is given in Fig. 3.13. When r is close to 0, the $G(r)$ usually at low r this function is nearly a straight line through -1 with a slope that is proportional to the average number density of the material. Hence, $Q_{max} = 9\text{Å}^{-1}$ will be chosen for the following simulation.

(2) Beam: In this tab, the wavelength of the X-ray used in the experiment needs to be specified.

(3) Normalization: The normalization tab determines the type of normalization modes to be applied and how the scattering data should be calibrated to establish an absolute cross-section scale. For the scattering data collected in I15 and I12, the Krogh-Moe and Norman method [232, 233] was selected. Considering that atoms cannot overlap each other in a local coordination environment, the overlap factor is set to 0.

(4) Sample background: In this tab, the scattering data of the empty instrument is provided, and the sample background factor is set to 1.0. Fig. 3.12d illustrates the layout of the sample background tab, where the sample background refers to the scattering information of the empty instrument. The sample background tweak factor needs to be tuned here [242].

(5) Sample: The sample tab incorporates the scattering information from the empty instrument, quartz chamber, capillary tube, and sample. The chemical composition of the sample needs to be provided. Fig. 3.12e shows the composition of pure Aluminum and its liquid density at 690°C. Additionally, the sample shape details are specified, such as the outer diameter of the sample being equal to the inner diameter of the sample

holder (6mm), and the sample height varying from the solid state to the liquid state. Another critical parameter to be adjusted during the running process is the sample tweak factor, which was set to 1.0 for the liquid Aluminum sample.

(6) Container: The final tab, the container tab (see Fig. 3.12f), includes the scattering information from the empty instrument, quartz chamber, and capillary tube combined. The container's composition and density are also provided in this tab. The container tweak factor is a vital parameter used to subtract the scattering information of the container, and it requires careful tuning [155].

By using the GudrunX template and tuning the relevant parameters in each tab, the contributions from the different components of the experimental setup can be effectively divided.

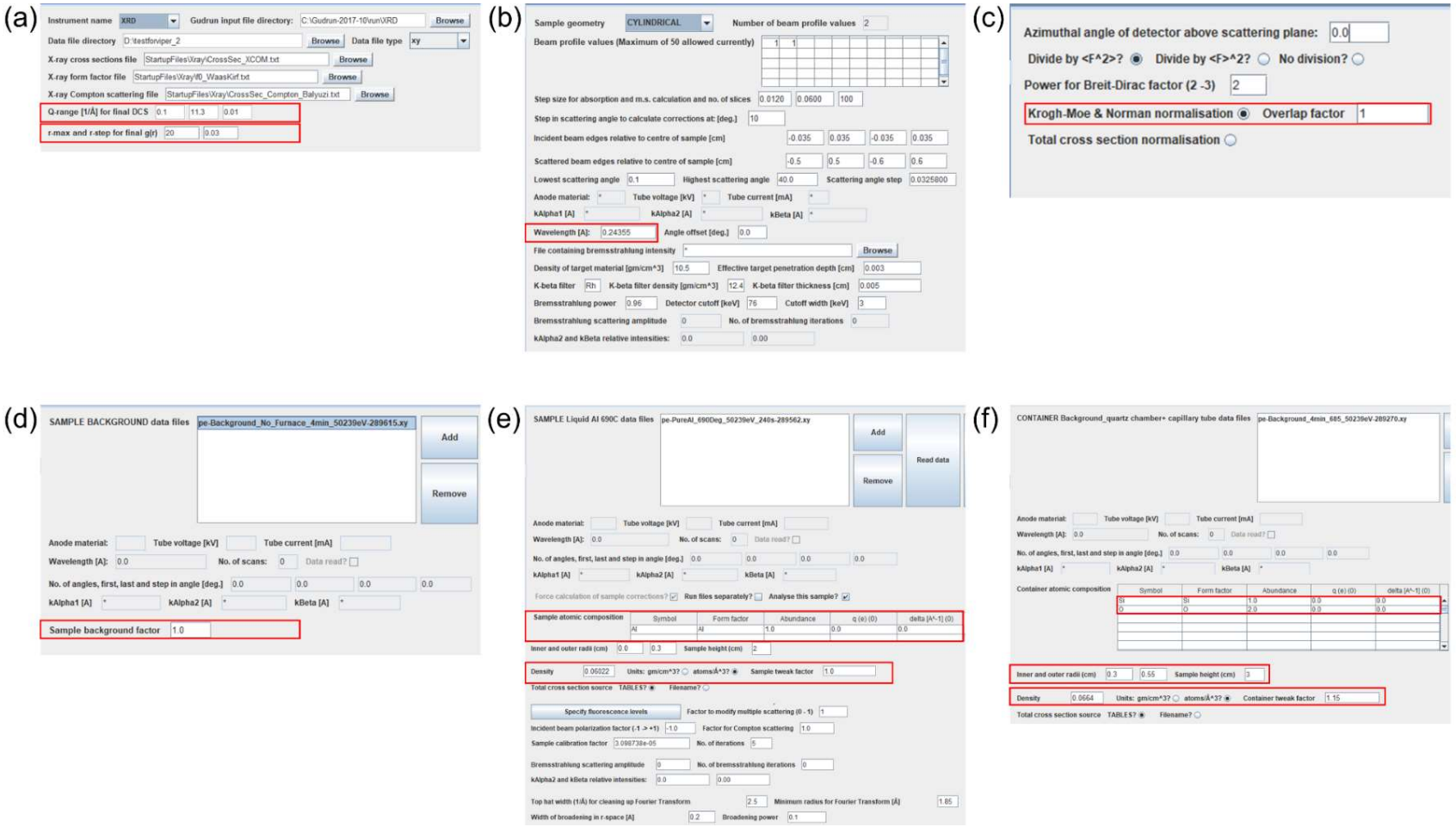

Fig. 3.12. Layout the six tabs in a specially designed GudrunX template in the data processing of pure Al sample at 690 °C: (a) Instrument (b) Beam (c) Normalisation (d) Sample background (e) Sample and (f) Container tabs, the key parameters in running GudrunX are highlighted using red rectangular.

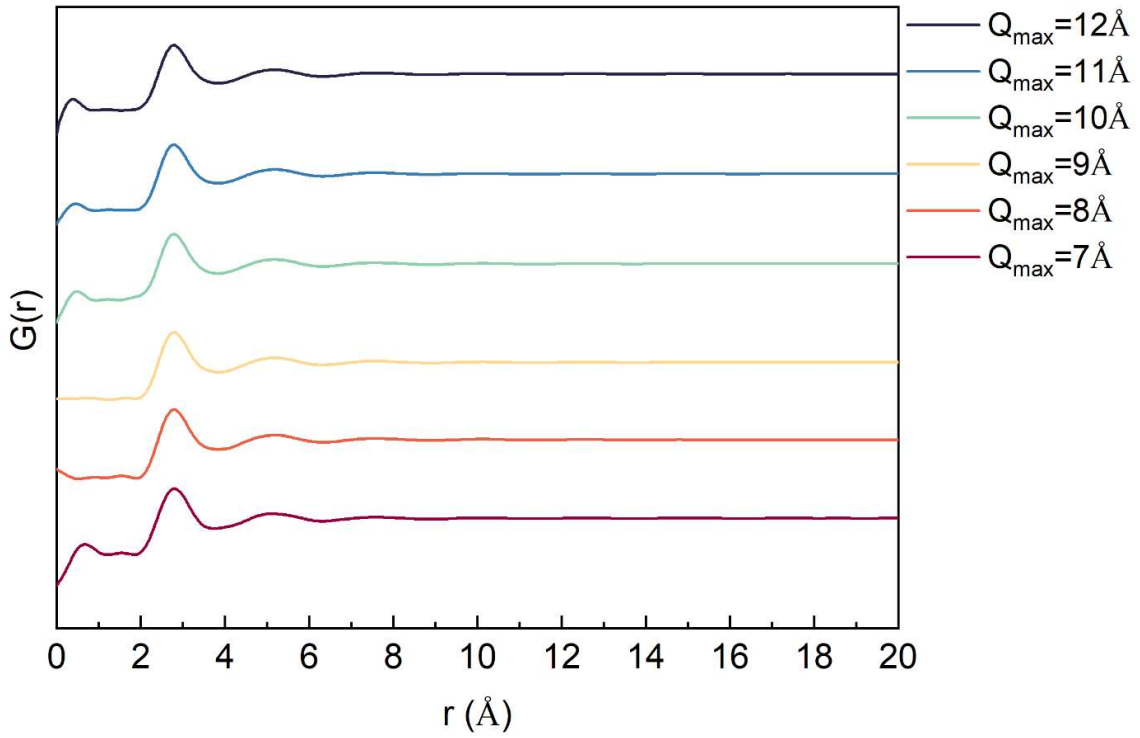

Fig. 3.13. The tuning effect of Q_{max}.

3.4.5 The EPSR modelling

3.4.5.1 EPSR simulation works based on SXTS results at I12

The EPSR package version 25 was used to model and reconstruct the 3D atomic structures for the studied alloys at the selected temperatures in the liquid state based on the acquired SXTS patterns [242]. In this section, all the important parameters for simulation works of three Fe-containing Al-based alloys are provided. Detailed simulation sunning procedures of Al-Sc case will be provided in the next section [168]. The EPSR begins with refining a starting interatomic potential and then moving the atoms' positions in 3D space to produce the best possible agreement between the simulated and the measured structure factors [243]. For each alloy, a cubic box of 72.10 Å side length was built with the optimised density shown in Table 3.3 (Section 3.4.2 describes how the optimisation was made). The box contains 20000 atoms with the atom ratios shown in Table 3.3.

Table. 3.3. The atomic number density of the 3 Al alloys used in the EPSR modelling at the selected temperatures.

Temperature (°C)	Al-Fe (atoms/Å^3)	Al-Cu-Fe (atoms/Å^3)	Al-Cu-Fe-Si (atoms/Å^3)
750	0.052030	0.052442	0.052460
720	0.052271	0.052683	0.052736
690	0.052536	0.052946	0.052982
660	0.052892	0.053201	0.053210
641		0.053452	
630			0.053472
Atom ratio	Al : Fe 19854 : 146	Al : Cu : Fe 19409 : 441 : 150	Al : Cu : Fe : Si 19209 : 441 : 150 : 200

The modelling algorithm has been provided in section 2.2.2. The Lennard-Jones, atomic mass and charge parameters used for the Al, Cu, Fe and Si atoms were listed in Table 3.4.

Table. 3.4. The Lennard-Jones, atomic mass and charge parameters used for reference potentials within the EPSR modelling [244].

Atoms	ε (kJ/mol)	σ (Å)	M (Amu)	q
Al	0.32677	2.5000	27	0
Cu	0.33807	2.5487	64	0
Fe	0.43180	2.4775	56	0
Si	0.37725	1.4000	28	0

The EPSR takes three steps to obtain the final atomic configurations [245]. It took approximately ~5000 iterations to complete a typical simulation with a satisfactory R-factor of <10^{-3}. Detailed running steps of the EPSR modelling can be found in [246]. Fig. 3.14 shows the structure factors $S(Q)$ and PDFs $g(r)$ obtained from the experiments (at the selected temperatures) and the corresponding EPSR simulations for the liquid Al-5Cu-1.5Fe-1Si alloy when it was cooled from 750 ºC

to 630 ºC. The final configurations of Al-5Cu-1.5Fe-1Si at 630 ºC can be found in Fig. 3.15. Due to the beam stopper, there is a dark region which corresponding to the small-Q region in 2D scattering pattern (in Fig. 3.11a). Hence, the scattering information for sample only in the dark region is not reliable. In our simulation for each sample, there is discrepancy between the experiment and simulation of $S(Q)$ in the small Q region.

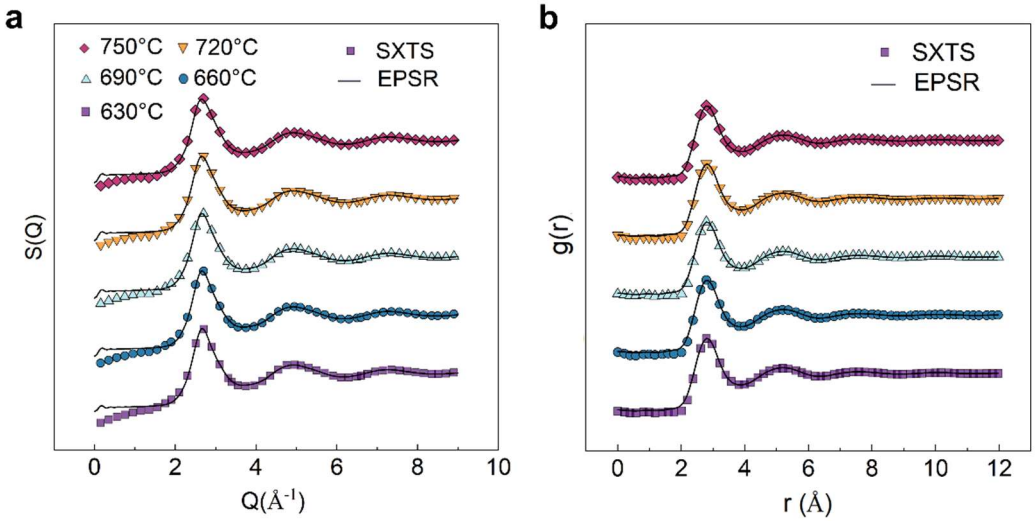

Fig. 3.14. The (a) structure factors and (b) pair distribution functions obtained from experiments and EPSR simulation for the liquid Al-5Cu-1.5Fe-1Si alloy from 750 ºC to 630 ºC.

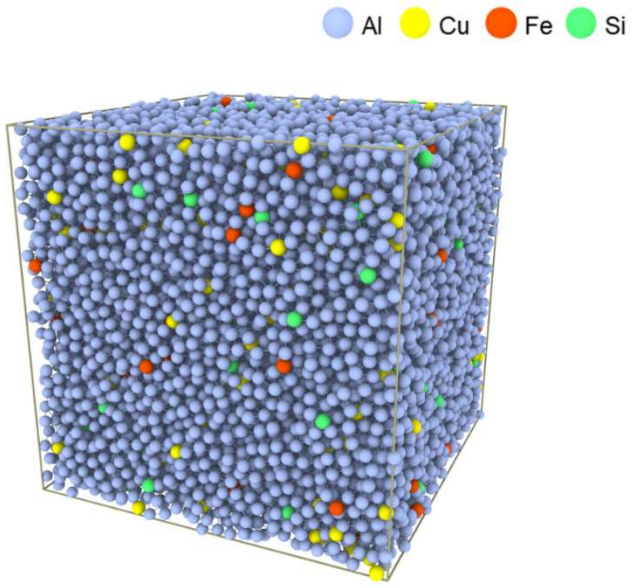

Fig. 3.15. The snapshot of the simulation box of Al-5Cu-1.5Fe-1Si liquid at 630°C, spheres of blue for Al, yellow for Cu, orange for Fe and light green for Si atoms.

3.4.5.2. The detailed EPSR package version 25 running procedures

Normally, 6 distinct procedures are normally run for each sample to ensure reproducibility and increase the statistics [247], the detailed pressures are described as follows:

(1) Create the atomic components and define their Lennard-Jones potentials.
(2) Create a simulation box containing the components, and also give the atomic number density of the sample.
(3) Create scattering weights files for each experimental dataset.
(4) Improve the Lennard-Jones potentials as required.
(5) Refine the empirical potential.
(6) Analyse the simulation results.

The key parameters for a good fitting between the scattering data and simulated results are Lennard-Jones potentials for each component and the empirical potential. To do the fitting, the Lennard-Jones parameters were first tuned. Once the fitting has been improved as well as can be obtained from the reference potential alone, then it is time to refine the empirical potential. More detailed running steps can be found in the tutorial in the EPSR manual. Taking the Al-0.4Sc for example, the input parameters for running the simulation are shown in the following sections:

(1) The components tab

In the current tab (see Fig. 3.16), the components of aluminium (Al) and scandium (Sc) in the simulation box were provided. These components can be generated using either the "create new" option or by loading existing data from previous simulations. To define the interactions between these atoms, initial Lennard-Jones parameters need to be given first, which can be referenced from previous studies. As my sample is a liquid metal, the partial charges assigned to the atoms in this simulation were set to 0. To ensure accurate simulations, refined Lennard-

Jones parameters were utilized. The specific values for these parameters [244] can be found in Table 3.5.

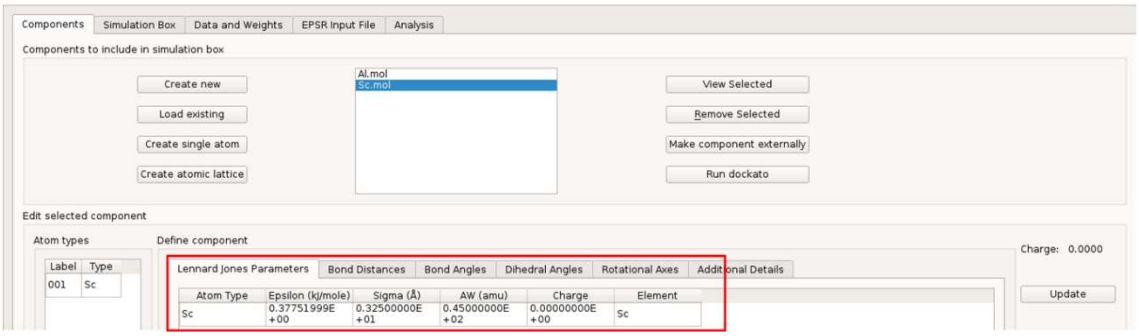

Fig. 3.16. The layout of the components tab

Table. 3.5. The Lennard-Jones potential parameters used in EPSR modelling

Atoms	Epsilon (kJ/mol)	Sigma (Å)	AW (Amu)	Charge
Al	0.32677	2.50	27	0
Sc	0.37725	3.25	45	0

(2) The simulation box tab

In the simulation box tab (see Fig. 3.17), the box was created. Firstly, the number of each component was added into the box, 16600 Al atoms and 40 Sc atoms were put in. Secondly, the atomic number density was given, that is 0.052656 atoms/Å^3 for Al-0.4Sc at 690 ºC. Thirdly, click the “Mixato” button to create a cubic simulation box with the given number of each component. The box size is determined by the number of each kind of atom. Here we got a simulation box with a side length of 68.11 Å. Enough components should be added to the box to make the box big enough so that half the length of the simulation box is larger than the largest $g(r)$ to be studied. Fourthly, it is necessary to click “Randomise” to distribute the components randomly.

In the box and then click Run fmole (e.g. 10000 interations). Considering that Al and Al-0.4%Sc are highly similar in the chemical components, hence the density of Al-0.4%Sc is approximately equal to that of pure Al at the same temperature. The atomic number density for Al and Al-0.4%Sc used in EPSR simulation at different temperatures are shown in Table. 3.6, and the density of Al refers to the literature [248].

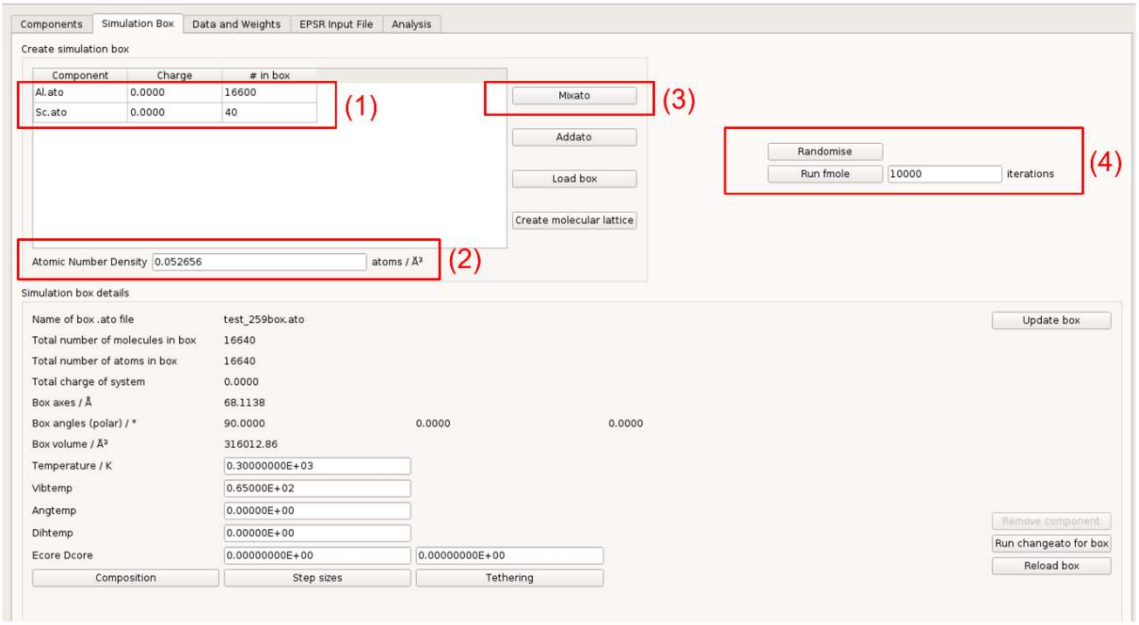

Fig. 3.17. The layout of the simulation box tab

Table. 3.6. The atomic density and number of Al and Sc atoms used in the EPSR modelling at the temperature where total scattering was collected [168]

Alloy	Temperature (°C)	Atomic density (atoms/Å^3)	Number of Al atoms	Number of Sc atoms
Al	690	0.05257	16600	0
	665	0.05282	16600	0
	660	0.05284	16600	0
Al-0.4Sc	690	0.05257	16600	40
	665	0.05282	16600	40
	657	0.05284	16923	50

(3) Data and weights tab

The data and weight tab in Fig. 3.18 is for EPSR to correctly calculate the structure factor ("theoretical") from the simulation box for a given experimental dataset, scattering weights files need to be created that specify that the data was collected using neutrons or X-rays, which atoms are isotopically substituted and whether any of the atoms can exchange. For the SXTS data, then X-ray dataset is opened by selecting the X-rays dataset and clicking 'browse' button. After clicking the 'Make .wt file' button, the .wts file is then shown in the data file table.

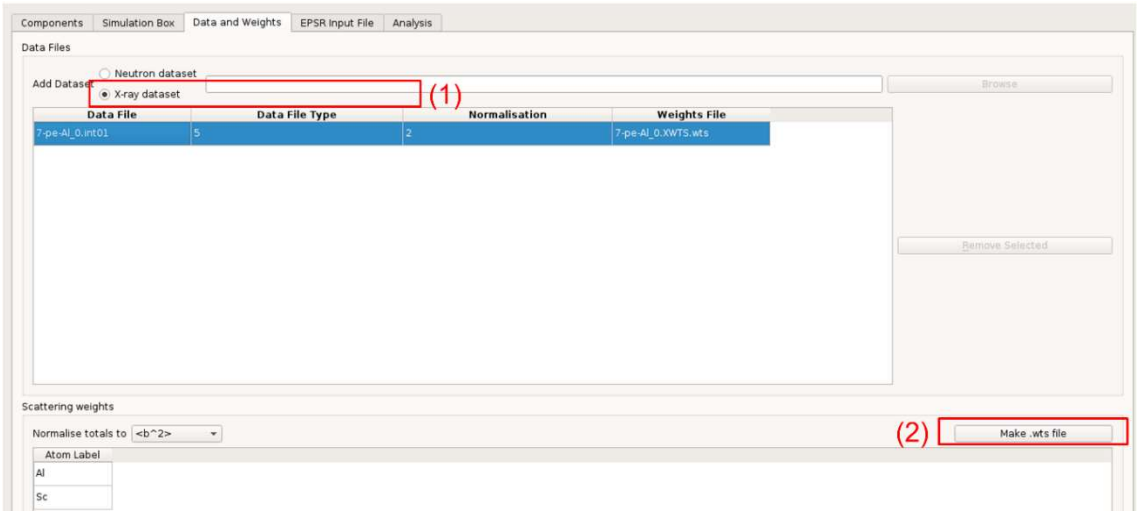

Fig. 3.18. The layout of the data and weights tab

(4) EPSR input file tab

The EPSR input file is presented in Fig. 3.19, which contains the parameters that define the simulation settings. By clicking on the "Setup EPSR input file" button, the EPSR settings can be refined. This action creates an input file with the default settings, which includes the components, simulation box, SXTS data, and the created weights files. However, to enhance the refinement of the empirical potential, it is necessary to modify the default settings. The key parameters that play a significant role in the refinement process are highlighted using a red rectangle, as they are often edited when running the simulation. One of the crucial parameters is "ereq" which represents the amount of energy given to the empirical potential to overcome the reference potential and refine the simulation further. Once the simulation has been improved to the maximum extent possible, each frame from the interaction can be accumulated to build a 3D atomic model of the simulation box. The value "-1" indicates that frames have not been accumulated yet. To obtain the frame of the latest interaction, the value "0" should be used to start the accumulation process. The number "40580" signifies that 40,580 frames have been accumulated thus far.

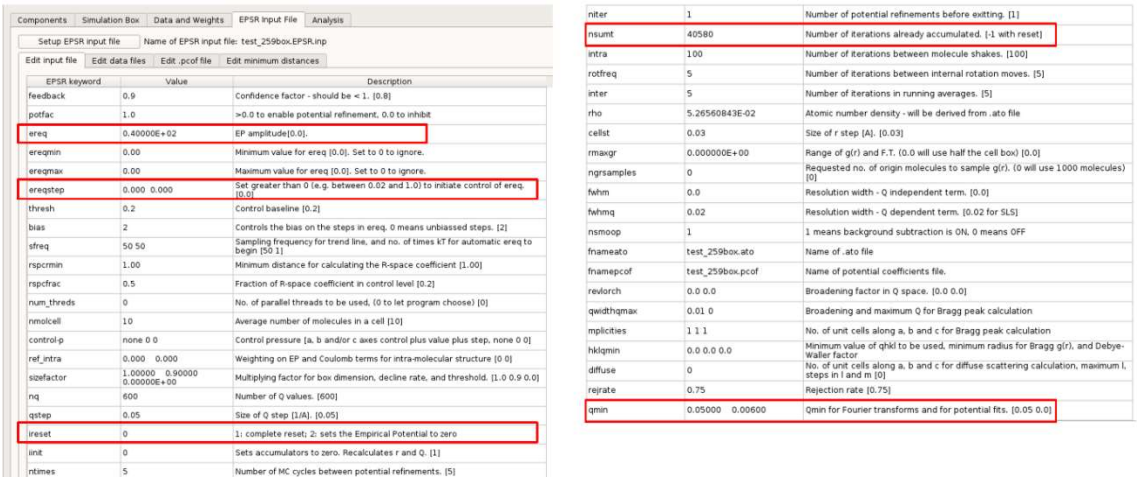

Fig. 3.19. The layout of the EPSR input file tab

(5) Analysis tab

Once the simulation has achieved a good fit with the data, the analysis of the simulation box can be initiated. To set up EPSR for running the analysis or plotting routines available within EPSRshell, navigate to the Analysis tab and select the desired routine from the dropdown menu. There are two options: (1) Enter a name for a new output routine, then click “Setup”. This allows us to create a new routine specifically for the analysis you wish to perform. (2) Select an existing output routine from the list, then click Setup. This enables us to use a previously defined routine for the analysis. Fig. 3.20 shows the routines of how to calculate the number of Al atoms coordinated the centred Sc atoms.

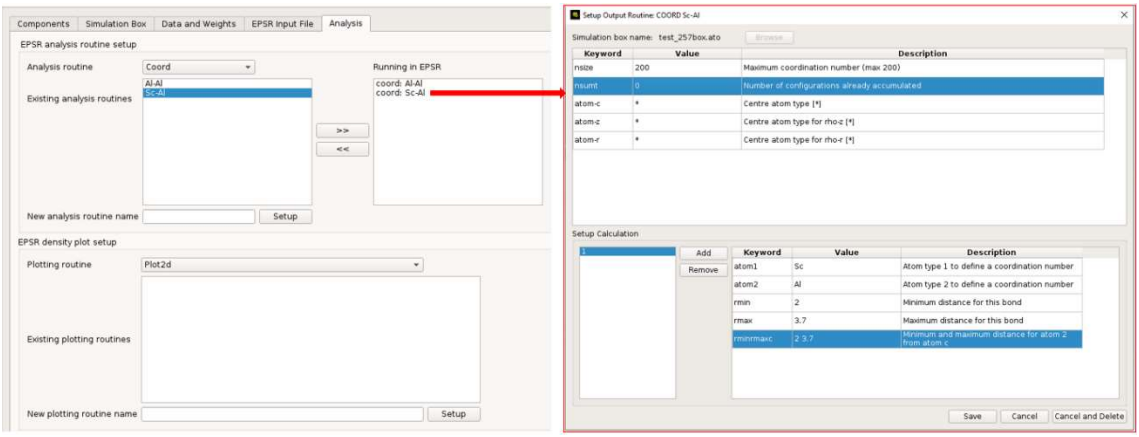

Fig. 3.20. The layout of the analysis tab.

3.4.6 Different types of connections among atom clusters

Voronoi tessellation analysis is the most common tool to clarify the nature of clustering behaviour [249]. However, in some special cases, lower solute concentration might result in no apparent symmetry in the inter-cluster distribution. Instead, more studies found the existence of a string-like pattern in the inter-cluster packing (as shown in Fig. 3.21a and b), researchers then turn to investigate the neighbouring nature between clusters [250]. The connection modes were originally developed in the structure studies of metallic glass. Mainstream research [16, 251, 252] indicates that there are four neighbouring and linking patterns in liquid or metallic glass, and they are vertex-sharing, edge-sharing, face-sharing and volume/tetrahedral-sharing.

In our case, the solute element concentration in Al alloy melts is even much lower than that of $A_{10}B_{90}$, we found that more of these solute element-centred clusters connect each other by atom bonds compared to the above four connection modes. Hence in our study, we define this kind of connection mode as bonds-sharing [168]. Including the bonds-sharing, the snapshots of five types of MRO connection modes are shown in Fig. 3.21c. More interestingly, clusters connected by bond-sharing (BS) do not share any atom, while in vertex sharing (VS) and edge sharing (ES), they share one and two atoms respectively. For Face sharing (FS), the clusters share three or more three atoms. Tetrahedra sharing (TS) is another special case where the two centred atoms of two individual clusters are linked directly, which means that one central atom is in the first shell of the other centred atom (within the cut-off distance of the first shell).

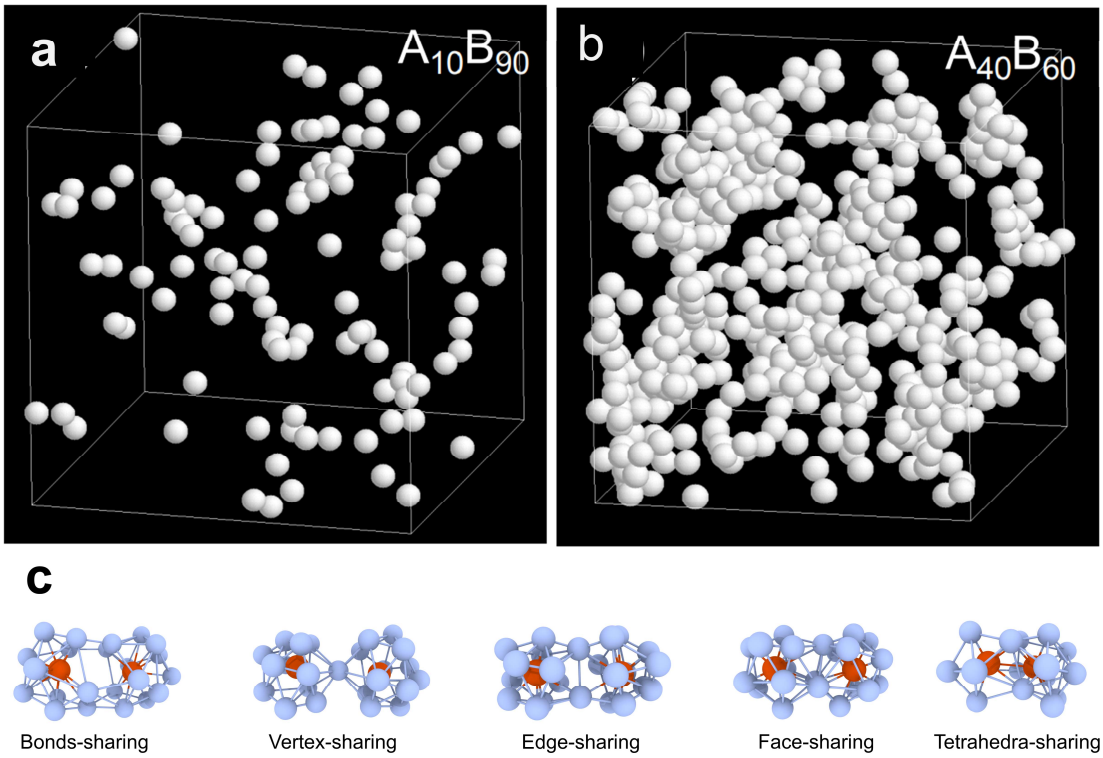

Fig. 3.21. Snapshot of the spatial distribution of the icosahedral clusters in (a) $A_{90}B_{10}$ glass and (b) $A_{40}B_{60}$ glass [250]. The white spheres donate the atom positioned at the centre of the icosahedral clusters. (c) Five representative connection modes in this work.

Based on the local structure characteristics of the five types of connection modes, we have developed an algorithm (see Fig. 3.22) to calculate the fraction of each connection mode in the liquid. Taking the Fe-centered clusters in the Al-Cu-Fe-Si melts as an example, a cut-off distance of 3.85 Å is set for the first shell of the Fe centre atom. Firstly, for any two individual Fe-centred SROs, we need to determine whether they are connected to form MROs. Secondly, if they are in connection, their mode of connection is grouped into five different types: (1) TS (the two Fe atoms are directly in touch); (2) BS (sharing no X atom); (3) VS (sharing one X atom); (4) ES (sharing two X atoms) and (5) FS (share more than two X atoms). Fig. 3.22 shows the detailed calculation algorithm. Additionally, the Matlab code implementing this algorithm is provided in Appendix 2.

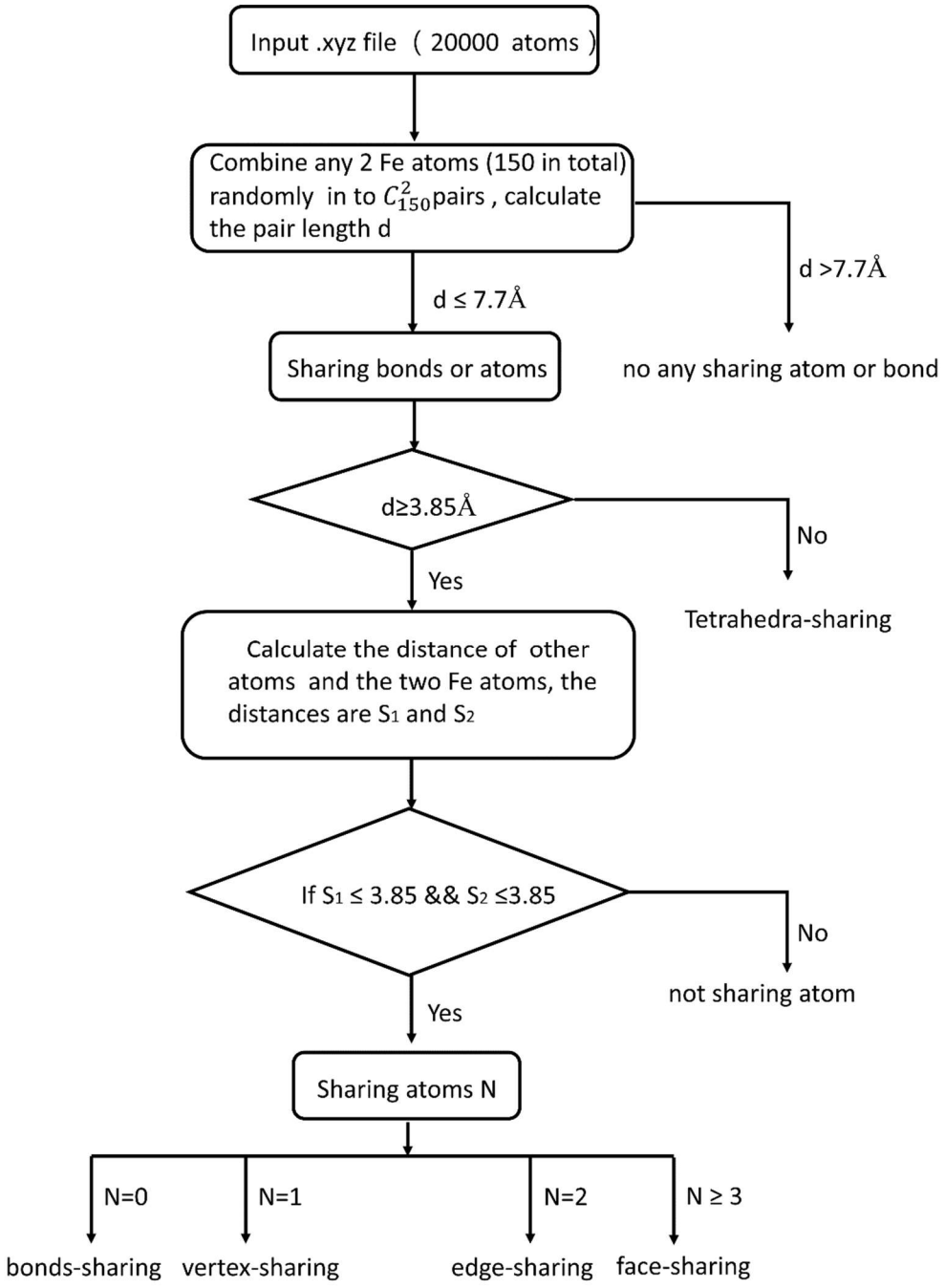

Fig. 3.22. The algorithm for classifying the connection modes of Fe-centred clusters.

3.4.7 BOO parameter analyses

In Chapter 2, the concept and capabilities of the geometrical structural descriptor BOO were given. However, the calculation methods for (BOO) parameters are currently limited. While common neighbour analysis and Voronoi tessellation analysis can be performed using software such as LAMMPS or OVITO, there are only a few available implementations for calculating BOO parameters within the research community. Two notable methods include the one proposed by Lechner [253] and another introduced by Wang et al [254]. For the data collected in I15, I utilized the C++ code developed by Lechner [253] to calculate the $\widehat{W}_6$ parameter. A more computationally efficient and user-friendly method called the bopcalc program was recently developed by Szymon [255]. It was used to analyse the BOO parameters for data collected in I12. This program is capable of calculating BOO parameters for atomic configurations obtained from various simulations. It provides accurate and fast analysis of local atomic arrangements and supports xyz files as well as trajectory files generated by LAMMPS (.lammps and .lammpstrjbin). With bopcalc, we can perform the following tasks: (1) Calculate local BOO parameters for individual atoms. (2) Calculate global BOO parameters for the entire sample. (3) Compute the distribution of BOO parameters (system and time-averaged). (4) Classify the local atomic structure and quantify the occurrence of different crystalline phases.

When using the bopcalc program, the input file is crucial for defining the parameters during the computations. Therefore, it is essential to provide appropriate values for the input parameters before calculating the BOO parameters. For instance, when working with a single frame of atomic configuration (.xyz file), the bopcalc program determines nearest neighbours, requiring the specification of a cut-off distance for the first shell. In our work, the bopcalc program calculates three local BOO parameters for each atom in the liquidus: two second-order invariants (Q_4 and Q_6) and one third-order invariant ($\widehat{W}_6$). Thanks to the help from the program developer Szymon on modifying the input file.

In this work, I also introduced the normalized BOO as a criterion to quantify the pre-ordered atoms in the liquid metal. The normalized BOO parameter

$\sqrt{Q_4^2+Q_6^2}/\sqrt{Q_{4fcc}^2+Q_{6fcc}^2}$ was first defined by Yang et al. [62], where Q_{4fcc} and Q_{6fc} are the Q_4 and Q_6 values for a perfect fcc lattice. The normalized BOO parameter is between 0 and 1, where 0 means that $Q_4 = Q_6 = 0$ and 1 represents a perfect fcc structure. To determine the cut-off values of the normalized BOO, we used pure Al [168] during the cooling process as the baseline reference. Fig. 3.23a and b show that when the normalized parameter of 0.793 (the red dash curves) was chosen as the boundary line to separate the pre-ordered structures from the normal liquid structures. This criterion can track the atomic evolution of pure Al cooled down from 690°C to 660°C. The atoms below this line were considered to have a normal liquid structure (lower symmetry than hcp, bcc and fcc), and those above were considered as pre-ordered atoms. This criterion also worked well for the liquid Al-5Cu-1.5Fe-1Si at 720°C and 660°C (see in Fig. 3.23c and d).

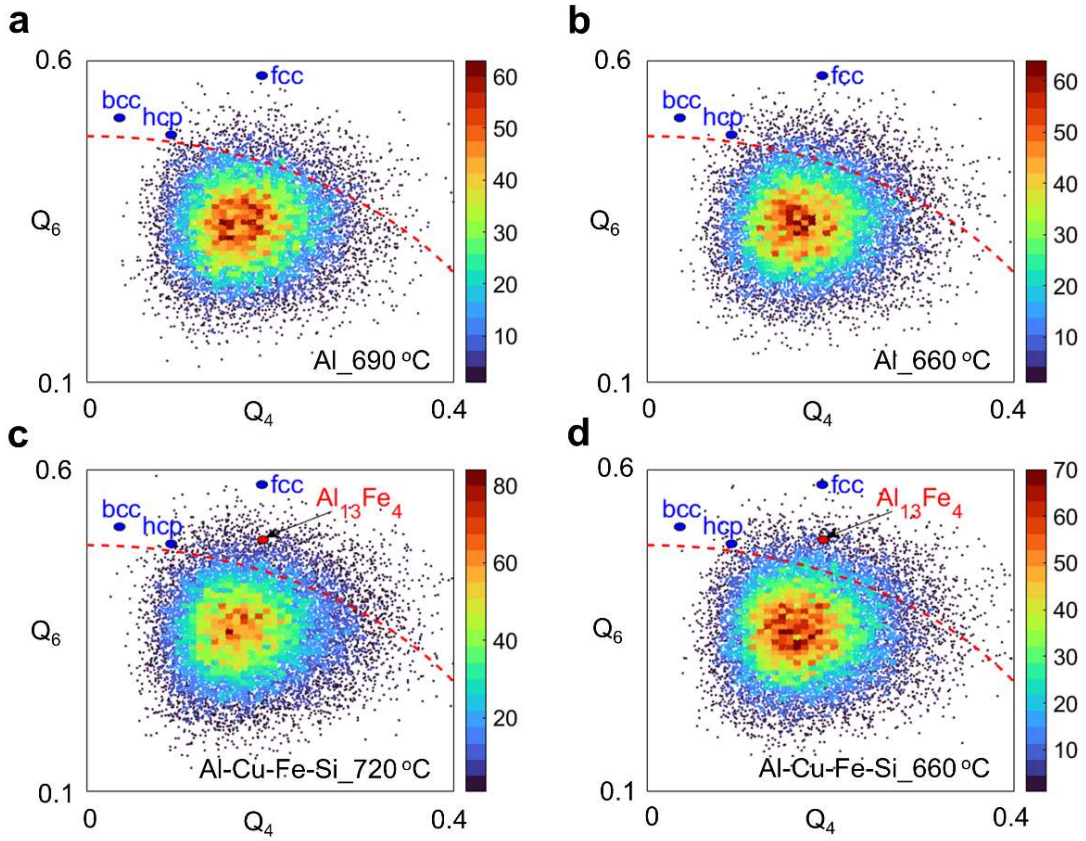

Fig. 3.23. (a, b) Q_4-Q_6 planes for all of the atoms in the supercooled liquid of pure Al [168] at 690°C and 660°C, from which a normalized parameter of 0.793 (red dash curve) was chosen as a division line to distinguish the atoms in the pre-ordered

or normal liquid zone. The fraction of pre-ordered Al atoms increases from 4.6% to 7.3% from 690°C to 660°C. (c, d) Q_4-Q_6 planes for all of the atoms in the supercooled liquid of Al-5Cu-1.5Fe-1Si, to which as the above-defined normalized parameter is applied, it suggests that the fraction of preordered atoms account for 4.86% at 720°C and 6.23% at 660°C.

3.4.8 Voronoi tessellation analyses

In this work, the Voronoi index, e.g., < n_3, n_4, n_5, n_6> was used to effectively characterize the arrangement of the nearest neighbours by counting the number of polyhedral facets that have 3, 4, 5 and 6 vertices/edges. The total number of polygons is equivalent to the coordination number (CN) of the central atom. Systematic Voronoi analyses of the geometrical arrangement of the atoms around their central atom in the studied alloys were done using an open-source visualization software (OVITO) [256].

3.5 Summary

Upgrade of counter-gravity casting apparatus and two special furnaces for operando SXTS experiment were done and used successfully at I15-1 and I12 beamlines for collecting systematically the total scattering data. Using accurate data reduction methods, I confidently conducted EPSR data analysis based on the processed data. The simulation results agreed well with the collected SXTS data which demonstrate atomic structure evolution in the cooling process of liquid metal. The detailed results are presented in chapters 4, 5, and 6

Chapter 4 Results and discussion of a dilute binary alloy: Al-0.4Sc alloy

This chapter presents the SXTS experiment results of the pure Al and Al-0.4Sc alloy obtained at the I15-1 beamline (Experiment EE20883-1). The research studied 3D atomic structure evolution versus temperature from the liquid state until the semisolid state with a special emphasis on revealing how the Sc-centred short-range ordered structures evolve and the link to nucleation of the Al_3Sc primary phase.

4.1. Experimentally acquired SXTS patterns, structure factors, PDFs and EPSR modelled PDFs

The measured temperature profiles and diffraction (scattering) patterns for pure Al and Al-0.4%Sc Fig. 4.1. The total scattering patterns acquired at the temperatures above the melting point exhibited the typical disordered characteristics of a liquid (i.e., a diffuse halo pattern). The scattering patterns acquired at temperatures below the melting point contained the Bragg spots from the solidified crystalline phases [168]. Pure Al, Al-0.4Sc, Al-5Cu-1.5Fe alloys and $Fe_{48}Cr_{15}Mo_{14}C_{15}B_6Gd_2$ metallic glass were used in this experiment, the detailed experiment parameters for these samples can be found in Table. 4.1, 4.2 and 4.3 respectively. In this chapter, only the pure and Al-Sc results are presented.

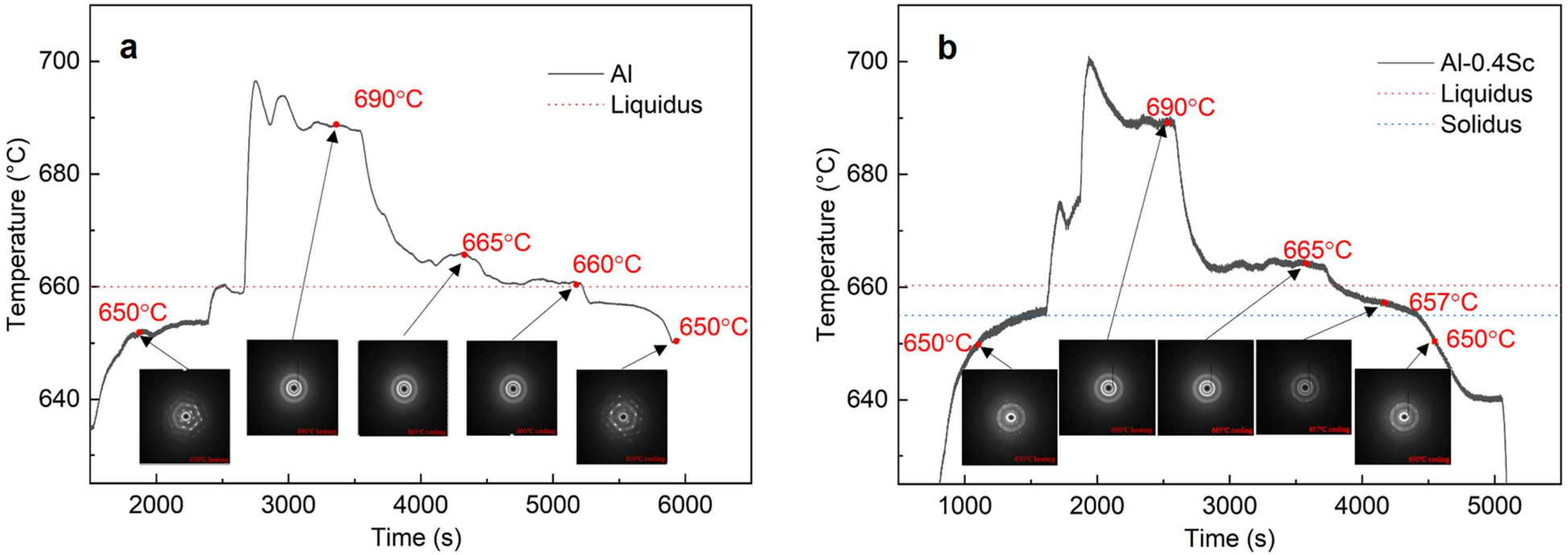

Fig. 4.1. The measured temperature profiles and the 2D scattering patterns acquired at the target temperatures during heating and cooling for (a) a pure Al sample, and (b) an Al-0.4Sc sample respectively.

Table. 4.1. Sample temperature, energy, exposure time used and file number of the SXTS of pure Al

Sample temperature (°C)	Theoretical energy (eV)	Exposure time (s)	File number of flat field	File number of dark field	File number of diffraction pattern	Process
25	50239	120	289252	289555	289556	
650	50239	240	289270	289559	289560	Heating
690	50239	240	289270	289561	289562	
665	50239	240	289270	289563	289564	
660	50239	240	289270	289565	289566	Cooling
650	50239	240	289270	289567	289568	

Table. 4.2. Sample temperature, energy, exposure time used and file number of the total scattering experiment of Al-0.4%Sc

Sample temperature (°C)	Theoretical energy (eV)	Exposure time (s)	File number of flat field	File number of dark field	File number of diffraction pattern	Process
25	50239	120	289252	289575	289576	
650	50239	240	289270	289577	289578	Heating
690	50239	240	289270	289579	289580	
665	50239	240	289270	289581	289582	
657	50239	240	289270	289583	289584	Cooling
650	50239	240	289270	289585	289586	
300	50239	240	289270	289587	289588	

Table. 4.3. Energy, exposure time used and file number of the total scattering experiment of Al-5%Cu-1.5%Fe and $Fe_{48}Cr_{15}Mo_{14}C_{15}B_6Gd_2$ in room temperature

Sample	Theoretical energy (eV)	Exposure time (s)	File number of flat field	File number of dark field	File number of diffraction pattern
Al-5%Cu-1.5%Fe	48239	10	289252	289185	289186
$Fe_{48}Cr_{15}Mo_{14}C_{15}B_6Gd_2$	48239	30	289252	289179	289180
	48239	60	289252	289181	289182
	52239	30	289252	289171	289172
	52239	60	289252	289173	289174

Fig. 4.2 shows the structure factor $S(Q)$, and PDF $g(r)$ obtained from the SXTS experiments and the corresponding EPSR modelling at different temperatures for pure Al and Al-0.4Sc melts. The simulated results with a satisfactory R-factor of $<10^{-3}$, matching the experimental data very well. A pre-peak appeared at ~1.8 $Å^{-1}$ in the $F(Q)$ of the Al-0.4Sc alloy at 657 °C (red dashed circle in Fig. 4.3a). Correspondingly, there is a minor shoulder (red dash rectangular in Fig. 4.3b) appeared at ~4.0 Å of the $g(r)$. Within the studied temperature range, there is no obvious difference between the structure factors and PDFs for both pure Al and Al-0.4Sc under different temperatures.

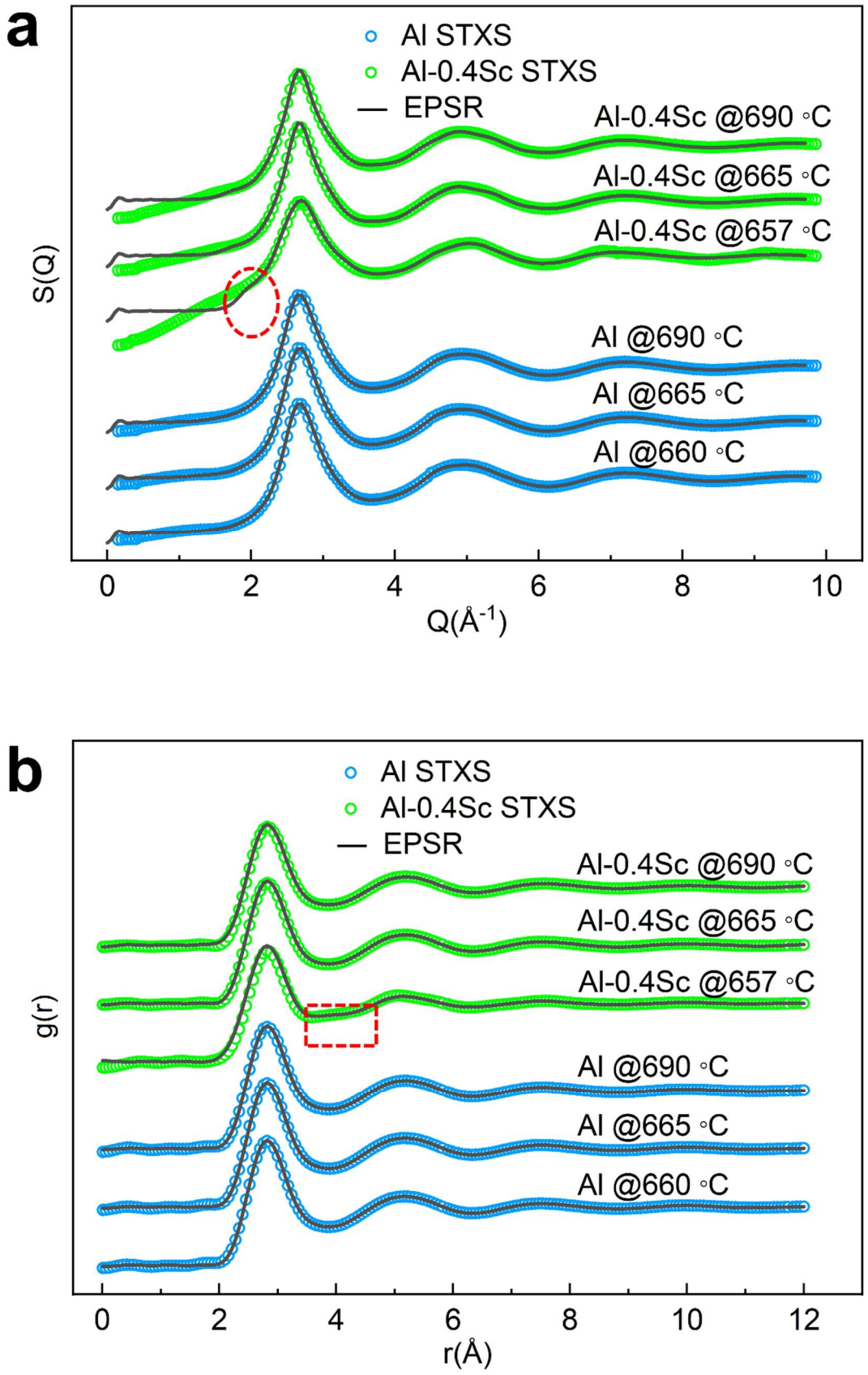

Fig. 4.2. The experimental and EPSR simulated (a) structure factors, $S(Q)$; and (b) total PDFs, $g(r)$ for the liquid Al and Al-0.4Sc melt at different temperatures.

Fig. 4.3 shows the partial PDFs obtained from the EPSR modelling for both alloys at different temperatures. In the liquid Al melt, the first peak position of the $g(r)_{Al-Al}$ remained almost at the same r value while the peak height increased slightly as the temperature decreased (Fig. 4.3a), indicating that the melt structure gradually became more ordered as the melt was cooled. There is an expanding trend of the Al-Al pair in pure Al upon cooling as the first peak position shifts to a high-value position. Fig. 4.3b and c show the partial PDFs of the Al-Al and Al-Sc pairs in the Al-0.4Sc melt, respectively. A similar 'expanding' behaviour can be found in the Al-Al pair in Al-0.4Sc melt, as the temperature decreased from 690 °C to 657 °C, the 1st peak position of $g(r)_{Al-}$ moved from ~2.79 Å to ~2.82 Å. Interestingly, the 1st peak position of $g(r)_{Al-Sc}$ moved from 2.61 Å to 2.58 Å (Fig. 4.3c). Simultaneously, a minor shoulder appeared at ~4.0 Å in the $g(r)_{Al-Al}$ at 657 °C (framed by a red dashed rectangle in Fig. 4.3b). Generally, when a material is heated, it is supposed to dilate, that is to say, when a material is cooled, it is proposed to shrink. The 'shrinking' behaviour in pure Al upon heating has been reported by Lou et al. [257], consistently, here we present the 'expanding' behaviour of the Al-Al pair in pure Al upon cooling, while the Al-Sc pair contracts. Hence it is necessary to conduct a systematic structural analysis of the 3d atomic structure generated by EPSR modelling. Also, the local coordination environment of Sc atoms should provide some clues that the evolution difference of Al-Al pairs and Al-Sc pair in dilute Al-0.4Sc.

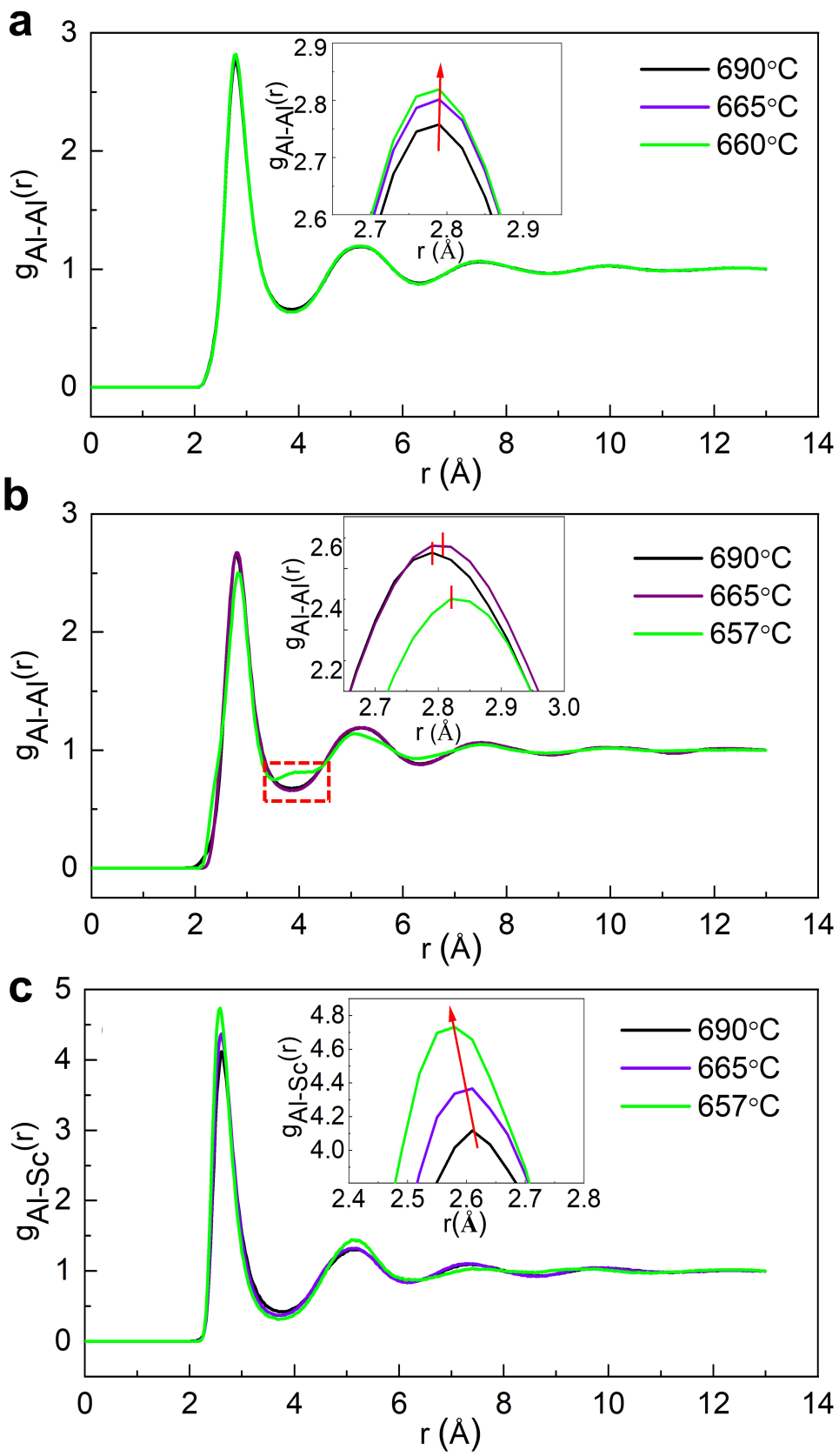

Fig. 4.3. (a) The PDFs of the Al-Al pair obtained from the EPSR modelling in pure liquid Al at different temperatures. (b) The partial PDFs of the Al-Al pair and (c) Al-Sc pair in the Al-0.4Sc melt at different temperatures

4.2 3D atom structures and their evolution versus temperature

Fig. 4.4 shows the snapshots of the reconstructed entire simulation box of Al-Sc melt at (a) 690°C (b) 665 °C and (c) 657°C respectively. For the Al-Sc work, all the atomic configurations were drawn by Jmol [258], which is an open-source Java viewer for chemical structures in 3D with features for chemicals, crystals, materials and biomolecules. EPSR modelling generates a XYZ file specifying the atomic geometries. Then Jmol [258] was used to read the XYZ file and output the configurations. To give a more clear view of the location of Sc atoms, all the Al atoms in the (a), (b) and (c) were set to be transparent, and the atom ratio here is not the real atom ratio. To study the Al atom configuration around an arbitrary reference Sc atom at different temperatures, the Al atoms in the first neighbouring shell were extracted from the EPSR models at the three different temperatures (see in Fig. 4.4d, e and f). The cut-off distances were defined by the partial PDFs of the Al-Sc pair at different temperatures respectively.

Fig.4.4 shows that in such a dilute system, a lower solute concentration of Sc might result in no apparent symmetry in the inter-cluster distribution. In a liquid state at 690 °C, the Sc-centred atom clusters (named Sc-centred polyhedrons) were more sparsely distributed. A zoom-in view of an individual cluster (see Fig. 4.5) indicated that it is a Frank-Kasper type polyhedral (full-icosahedra, <0, 0, 12, 0>). Some also exhibited the characteristics of fragmented icosahedra and icosahedra-like polyhedra with five-fold bonds. Hence, there are some ISROs in the Sc coordination environment in a liquid state. As the melt is cooled down, a more string-like pattern in the inter-cluster packing appears instead, we then turn to investigate the neighbouring nature between clusters. Contrary to the previous mainstream research holds that there are four neighbouring and linking patterns in liquid or metallic glass, and they are VS, ES, FS and TS. In our study, we found that the Sc-centred polyhedrons moved closer to each other after cooled from 665 °C to 657 °C, starting to link together via the Al-Al bonds (without any sharing Al atom), vertex, edge and/or face-sharing (without inter-penetration) [259], and forming four different configurations [251] as illustrated by the inserts in Fig. 4.6. The Al-Al bonds connected configuration was dominant at 665 °C with 71.4%. It decreased to 35.7% at 657 °C. Edge-sharing and face-

sharing connected configurations appeared at 657 °C, indicating more atoms were connected as cooling proceeded.

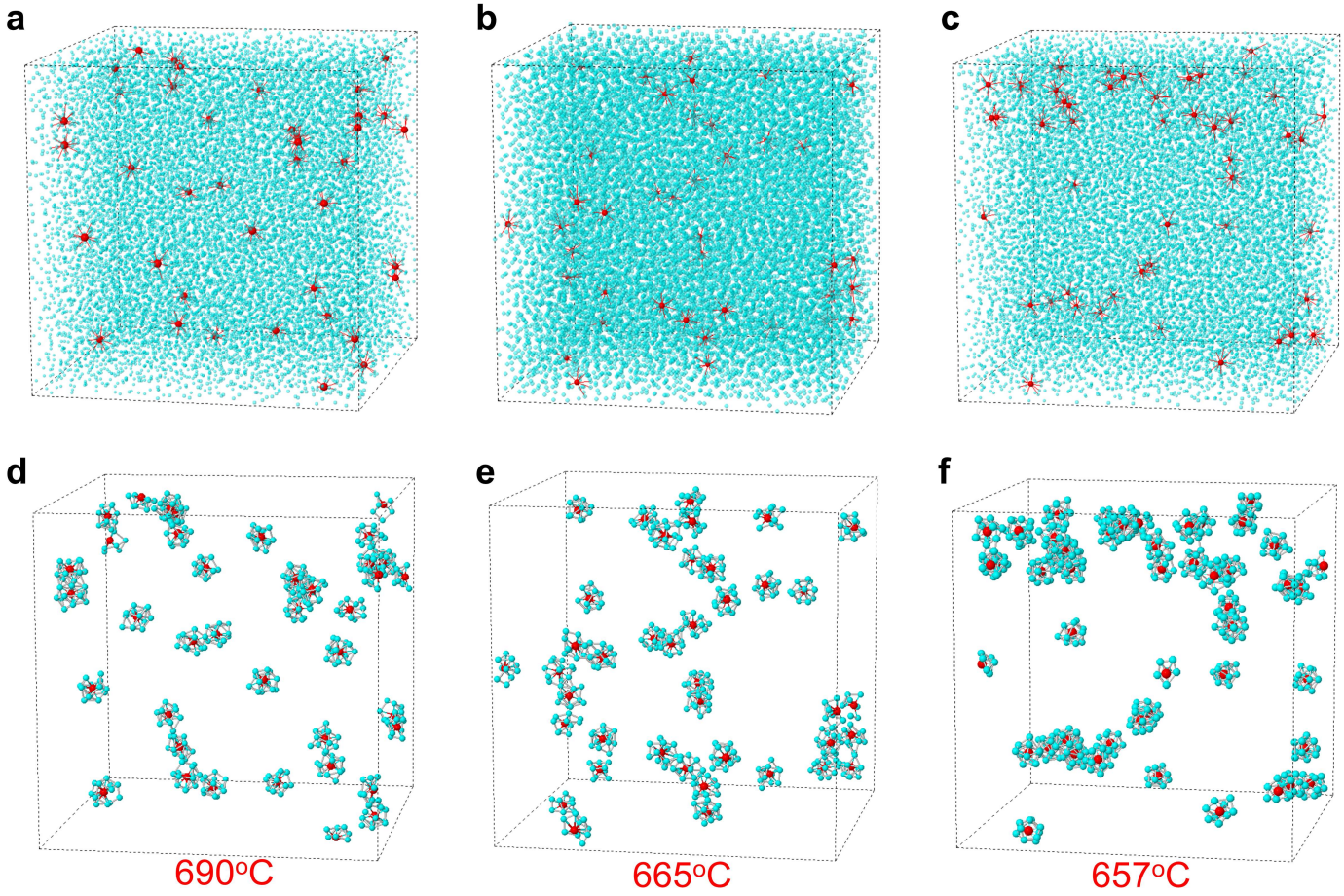

Fig. 4.4. The snapshots of the reconstructed simulation box of Al-Sc melt at (a) 690°C (b) 665 °C and (c) 657°C respectively; the Sc-centred Al atom clusters in the Al-0.4Sc melt at (d) 690 °C, (e) 665 °C and (f) 657 °C respectively extracted from the EPSR models.

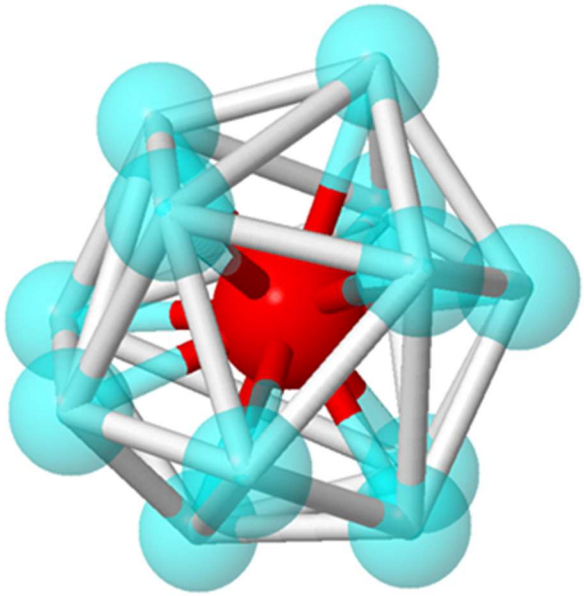

Fig. 4.5. An enlarged view of a Sc-centred Frank-Kasper polyhedra with CN of 12 for the Al-0.4Sc melt at 690 °C.

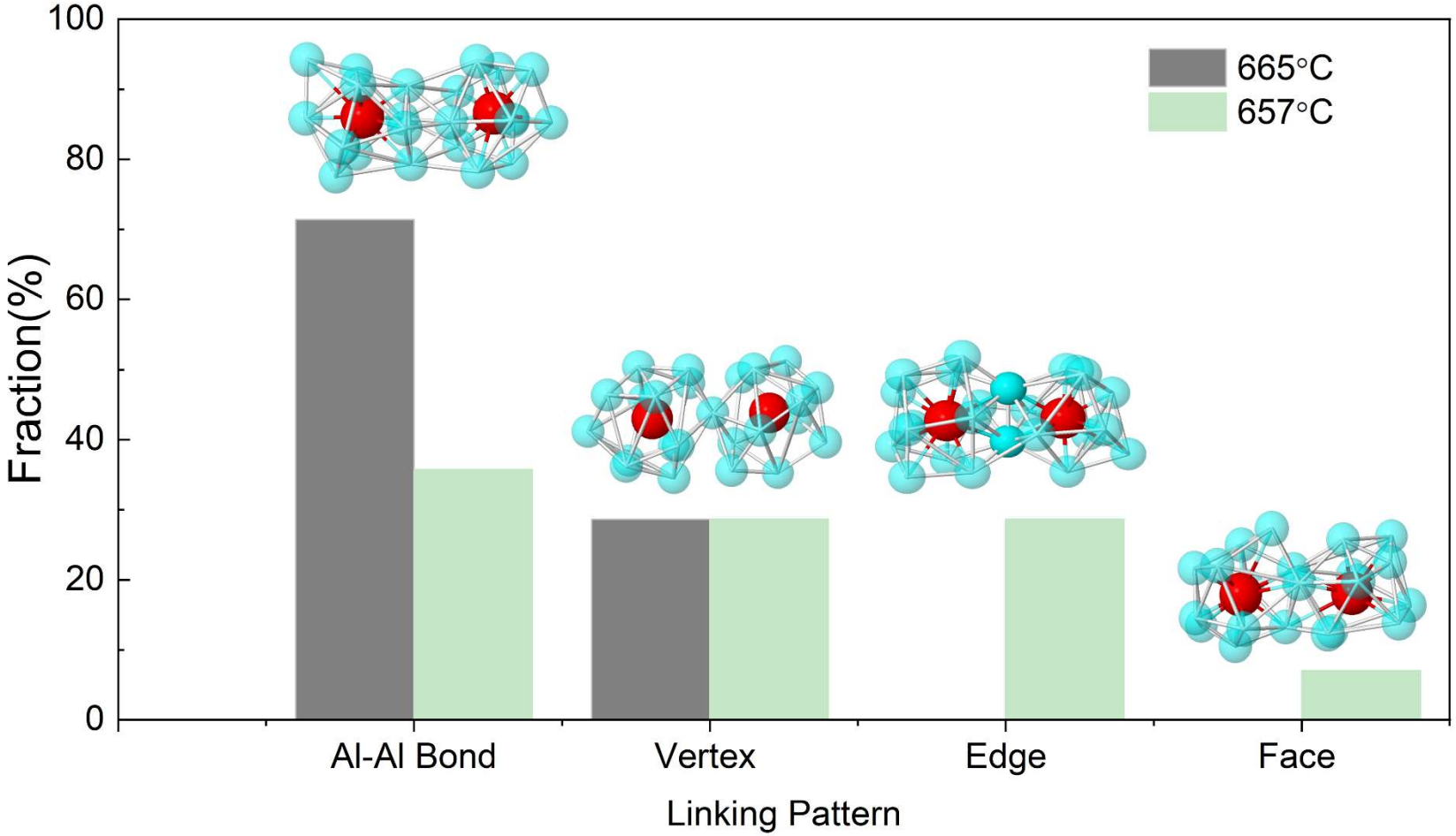

Fig. 4.6. The fraction of four different types of MROs formed by sharing the Al-Al bond, vertex, edge, and face between the neighbouring clusters

4.3 Sc-centred short-range ordered structures

Geometrical analyses using coordination number, bond length, bond orientational and Voronoi parameter were done to reveal the fine structural characteristics for the 3D atom coordination environment surrounding the Sc atom,

Fig. 4.7a shows the coordination number (CN) distribution of the Sc-centred polyhedrons at different temperatures. Clearly, at 690 °C and 665 °C, the peak value is at CN=11. While at 657 °C, the peak value is CN=12. Fig. 4.7b also shows that, as the temperature decreased, the average CN increased from 11.1 to 11.52; while the mean bond length of the Al-Sc atom pairs decreased from 2.85 Å to 2.79 Å, indicating these Sc-centred polyhedrons become more compact. In this paper, $\widehat{W}_6$ calculation was performed using the C++ code Lechne [253] developed. Fig. 4.8a shows the frequency density of the $\widehat{W}_6$ invariant calculated on 50 Sc-centred polyhedrons (50 Sc atoms and 575 Al atoms) in the simulation box of Al-Sc melt at 657 °C. For a 13-atom cluster, the values for the perfect icosahedron and FCC structures are -0.169754 and -0.013161 respectively [207]. The frequency density of $\widehat{W}_6$ shows that $\widehat{W}_6$ between the ideal icosahedron and FCC configuration are dominant, and the $\widehat{W}_6$ value is -0.08984, suggesting that most local atomic arrangements have an intermediate structure between the icosahedron and FCC configuration [61].

The Voronoi analysis of the atomic arrangement around Sc atoms was analysed systematically using an open visualization software (OVITO) [256]. Fig. 4.8b shows the fraction of 6 typical polyhedrons detected in the Sc atoms coordination environment. These prevailing clusters such as <0 1 10 2>, <0 2 8 1> and <0 2 8 0> were reported to contain both icosahedra-like and FCC-like structure features associated with geometric frustration, similar to the distorted <0 0 12 0> icosahedron [61].

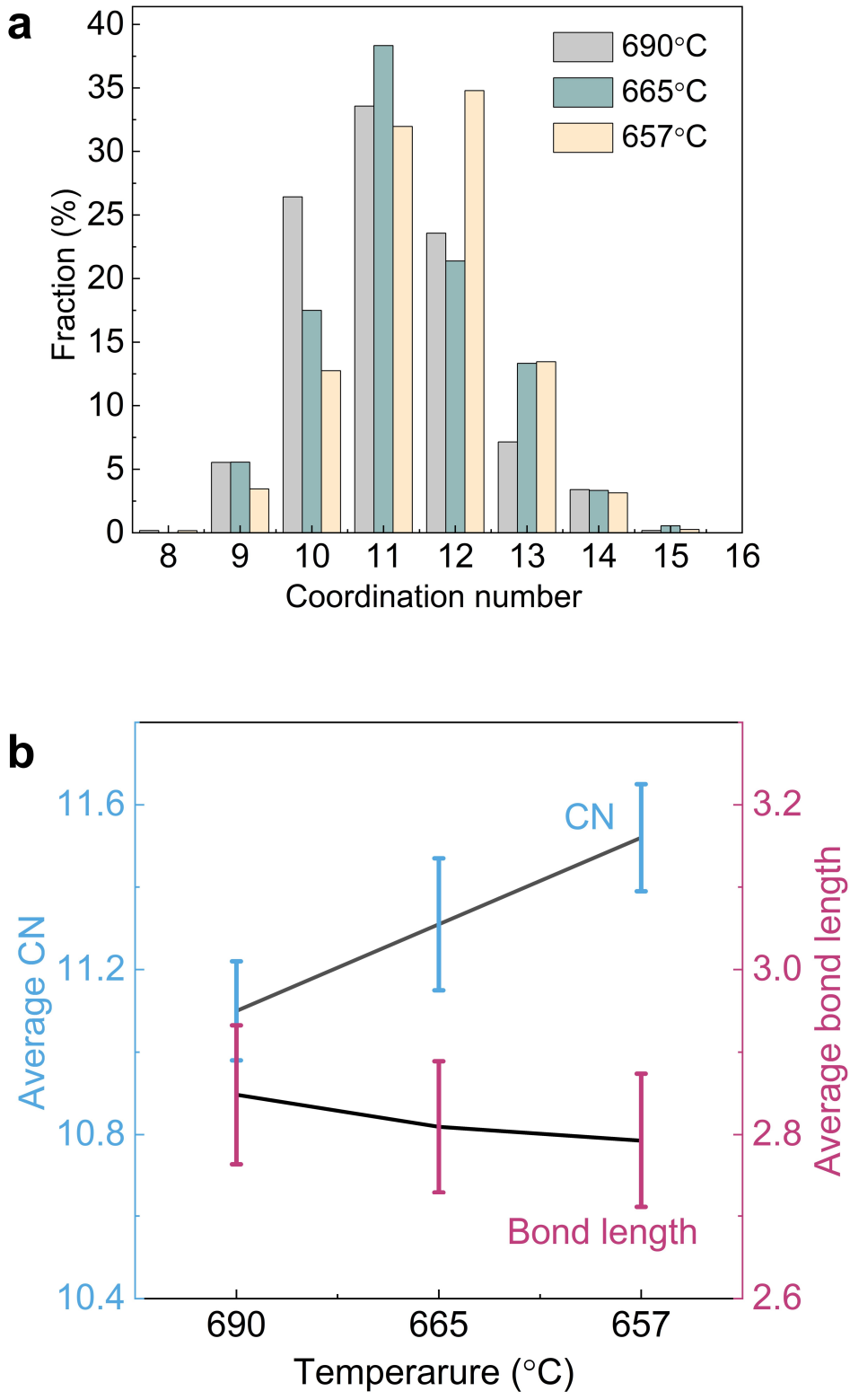

Fig. 4.7.(a) the coordination number distribution of the Sc atoms in the Al-0.4Sc melt at 690 °C, 665 °C and 657 °C respectively. (b) the average CN and average bond length of the Al-Sc atom pair as a function of temperature.

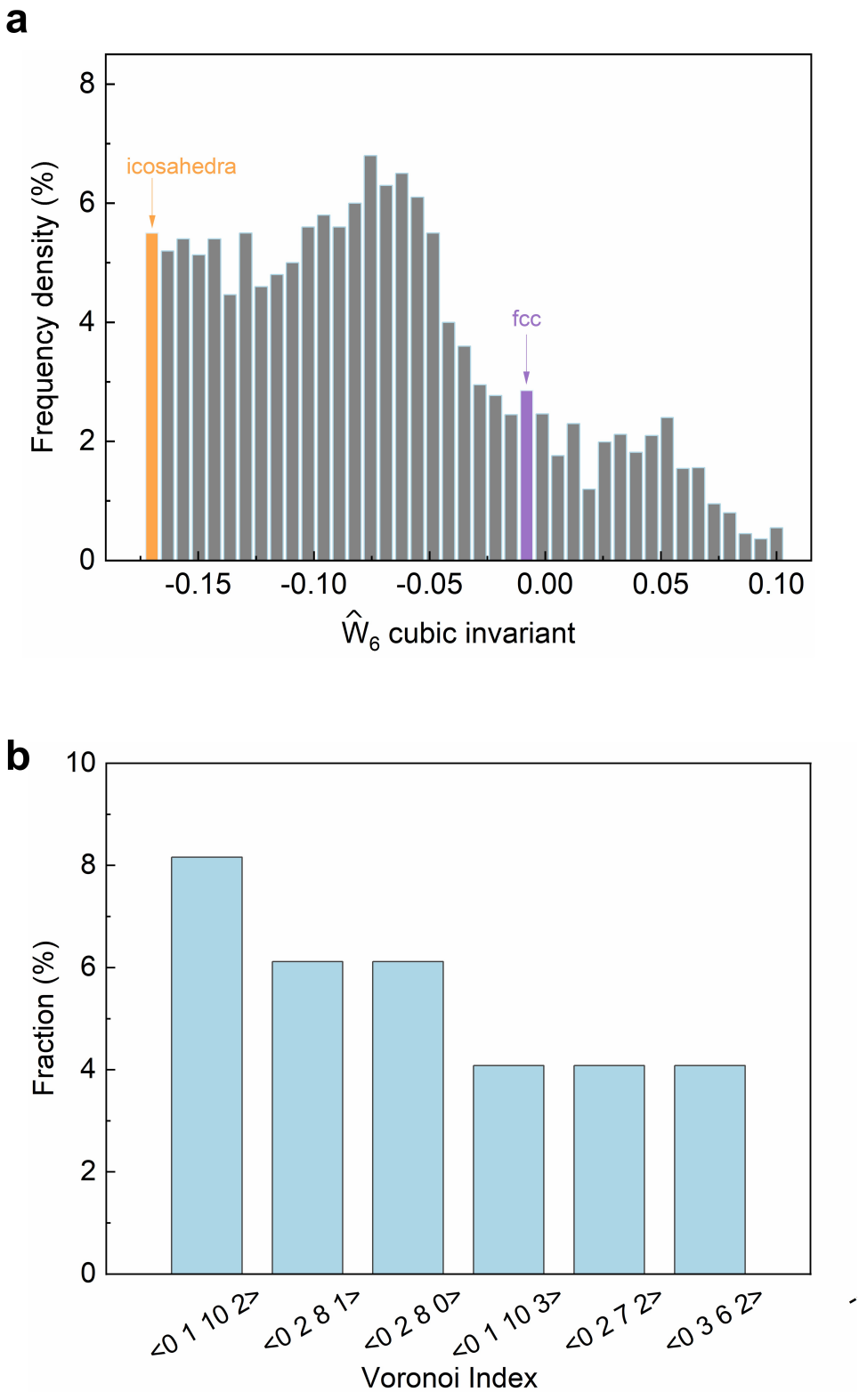

Fig. 4.8. (a) A histogram of the frequency density of the $\hat{W}_6$ invariant, showing the local geometry distribution around Sc atoms in the Al-Sc melt for the case at 657 °C. (b) Voronoi polyhedral analysis for the Sc-centred polyhedrons, and 6 typical polyhedrons.

4.4 Discussion

Previously, liquid melt structures of several Al transition metal alloys have been reported [260-262]. Our studies on Al-0.4Sc have shown that, above the melting temperature, the addition of 0.4wt% Sc did not result in changes to the structure factor nor to the PDF when compared to the liquid Al. In the semisolid region at 657 °C, a minor shoulder appeared at ~4 Å in the $g(r)$ and $g(r)_{Al-Al}$. Compared to the peak located at ~4.1 Å^{-1} for the $g(r)$ of a reference crystalline fcc phase [31] and pure Al at 400 K [111], the minor shoulder indicated the formation of MRO fcc coordinated clusters in the semisolid melt. Generally, the pre-peaks observed in the structure factors of liquid alloys at small Q-values are attributed to the medium-range order in liquid Al-TM alloys [263]. In this case, the pre-peak appeared at ~1.8 Å^{-1} in the $S(Q)$ of the Al-0.4Sc alloy at 657 °C (red dashed circle in Fig. 4.3b) which suggests the formation of the MROs. Meanwhile, since solid α-Al already formed in Al-0.4Sc at 657 °C, this appearance of MRO in the undercooled melt could be considered as a precursor of the fcc α-Al.

Since icosahedral structure is not structurally compatible with L_{12} fcc crystalline order, the presence of ISRO and connected icosahedrons (Fig. 4.6) is widely considered as an inhibitor for crystal nucleation and leads to metastable icosahedral-phase formation [264, 265]. The growing and enhanced icosahedral ISRO in the Al-Sc melt could result in a higher nucleation barrier. However, Redwill and Zangwill [266] proved that the icosahedral phase was not able to form in an Al-Sc binary alloy through casting by using the total-energy calculation and a self-consistent effective-medium theory. It should be noted that α-Al and Al_3Sc phases had already formed upon cooling down to 657 °C. As a result and considering the very low Sc concentration in the liquid, we can confirm that ISRO does not reach a level that can impact nucleation. Ideally, if each ISRO is isolated, it would naturally tend to minimize the local energy density by forming the densest and most symmetrical icosahedron. However, the constituent atoms shared by neighbouring clusters may not always sit at the minima of all pairwise interactions with all of their nearest neighbours, owing to chemical variation and kinetic fluctuation[267]. In our case, isolated Sc-centred polyhedral get connected with temperature decreases, a higher percentage of edge-sharing and face-sharing of

Sc-centred polyhedral indicates they are sharing more Al atoms at lower temperature. Common neighbour analysis [268] on the face-sharing clusters shows that they possess partial $L1_2$ symmetry, and the distorted icosahedra were proved to have higher total energy than perfect icosahedra and the fcc cluster, thus this order can be considered to be in an intermediate state between these two densely packed configurations. This kind of geometry frustration was often attributed to the competition between two low-energy states ($L1_2$ and icosahedron) with dense atomic packing, and this kind of competition has been widely discussed in metallic glass, undercooled pure Al and Sm-doped liquid Al [267, 269, 270]. Doping of Sm in liquid Al liquid was reported to be able to help ISRO to win over fcc order and hence can lead to glass formation under rapid cooling conditions [269], however, the formation of primary $L1_2$ ordered Al_3Sc phase indicates that $L1_2$ order wins over ISRO under casting condition. An ISRO compromise is generally required to minimize the total energy of 12 Al atoms surrounding a transition metal atom, while quantitative total energy calculation shows that ISRO compromise is not necessary for Al-Sc alloy, substitutional fcc structure also satisfies the low total energy requirement[271]. The fcc symmetry is the energetically and geometrically favourable arrangement of the distorted parts of the icosahedron because an fcc structure has dense atomic packing with 12 coordinated atoms (same as an icosahedron) and low energy. Importantly, the local translational symmetry of the fcc configuration makes the distorted icosahedra easy to geometrically match with neighbouring clusters for long-range dense packing. From this point, we proposed that Sc-centered CN=12 Kasper polyhedra could be $L1_2$ precursors that form small ordered $L1_2$ clusters. These $L1_2$ clusters keep on forming at the solid-liquid interface, and subsequently transform into Al_3Sc particles with a $L1_2$ structure, resting in a lower free-energy barrier of nucleation [272]. Due to the low concentration of Sc and rapid crystallization speed below the melting, Sc centred $L1_2$ ordered cluster has not been seized in the amorphous part of Al-0.4Sc below the melting point.

4.5 Summary

In this chapter, the evolutions of 3D local atomic structures of an Al and an Al-0.4Sc alloy melt from liquid to liquid-solid coexisting state were systemically studied in operando and in real time using synchrotron X-ray total scattering and EPSR modelling. The simulated structure factors and PDFs match the experimental data quite well. The reconstructed 3D atomic structures show that, in the liquid state, icosahedral short-range ordered Sc-centred Al polyhedrons form and most of them with Al coordination number of 10-12. As the melt is cooled to semisolid state, the polyhedrons become more connected atom clusters via vertex, edge and face-sharing. The medium-range ordered Sc-centred clusters with face-sharing are proved to be the “precursors” for the $L1_2$ Al_3Sc primary phase in the liquid-solid coexisting region.

Chapter 5 Results and discussion of the multiple-component Fe-containing Al recycled alloys

In this chapter, the experimental and EPSR modelling results of three Fe-containing Al alloys (Al-1.5Fe, Al-5Cu-1.5Fe and Al-5Cu-1.5Fe-1Si) are presented and discussed. First temperature-dependent liquid atomic structural evolutions in the short- and medium-atomic range were quantified systematically for the three alloys by PDF analyses. Then, the fine structures that are not able to be revealed by PDFs were further characterised and quantified by other methods like Warren-Cowley parameter, Voronoi tessellation and Bond orientational order. The SRO structure heterogeneities due to multiple atom interactions, Fe-centred MRO structure heterogeneities and their evolutions versus temperature as well as their roles on crystal nucleation of the primary $Al_{13}Fe_4$ are all discussed and elucidated.

5.1 Experimentally acquired SXTS patterns, structure factors, PDFs and EPSR modelled PDFs

Fig. 5.1a, c and e show the synchrotron X-ray total scattering spectra, which were converted from the acquired 2D patterns during the experiments. Fig. 5.1b, d, f show how the $Al_{13}Fe_4$ primary phase was indexed in each alloy. The spectra at 660 °C (for the Al-1.5Fe), 641 °C (for the Al-5Cu-1.5Fe) and 630 °C (for the Al-5Cu-1.5Fe-1Si) were used in the EPSR modelling as the cases just prior to the nucleation. Fig. 5.2 shows the structure factor,$S(Q)$ and PDF, $g(r)$ obtained from the SXTS experiments and the corresponding EPSR modelling at different temperatures for the three alloys. The simulated results matched the experimental data very well.

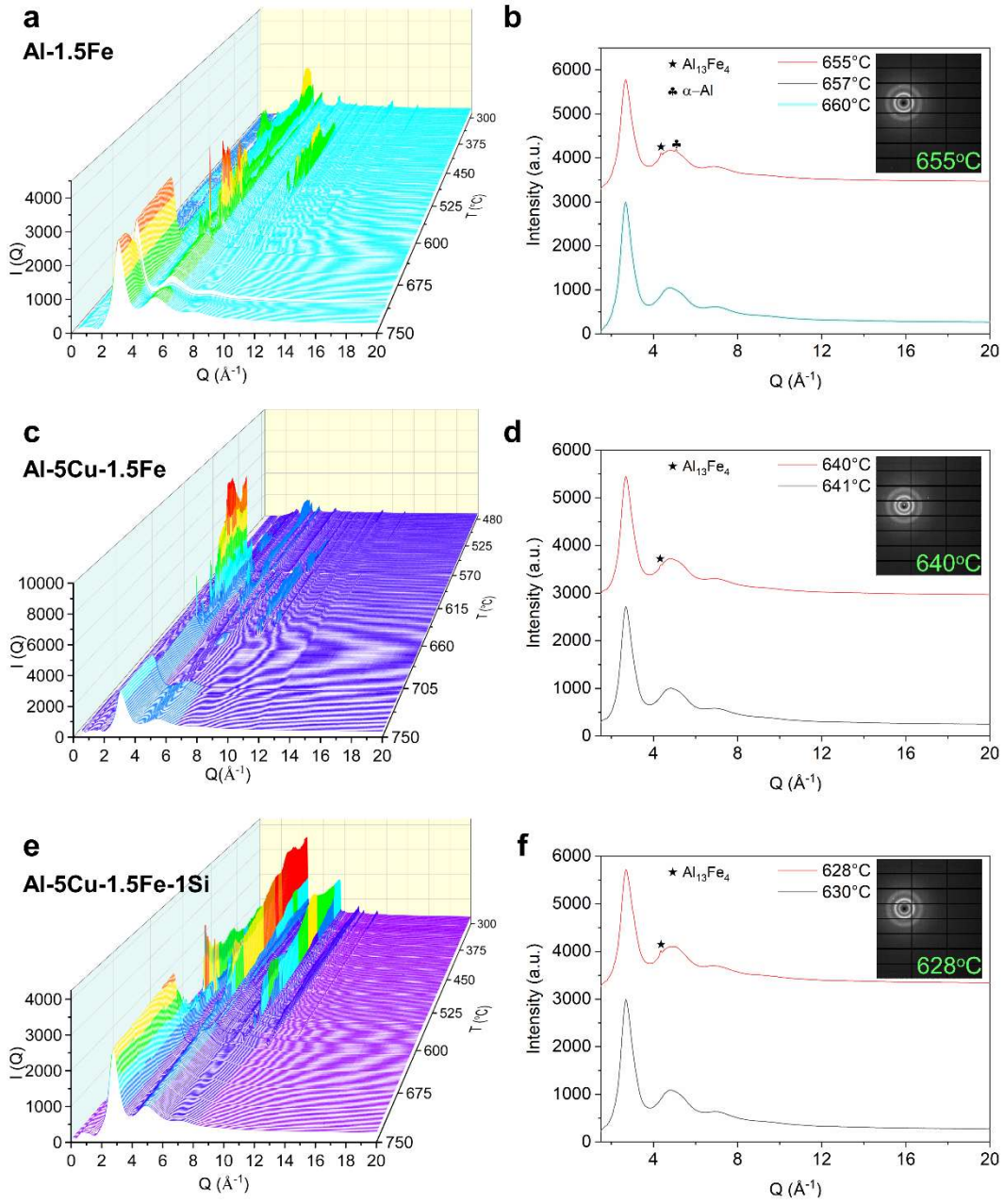

Fig. 5.1. Left: the continuously collected synchrotron X-ray total scattering spectra (integrated from the corresponding 2D patterns) during the cooling process. Right: the diffraction curves that show the nucleation of the $Al_{13}Fe_4$ (the first appearance of the $Al_{13}Fe_4$ crystalline spots) and those prior to the nucleation. (a) and (b) for the Al-1.5Fe, (c) and (d) for the Al-5Cu-1.5Fe, and (e) and (f) for the Al-5Cu-1.5Fe-1Si. The insets show their corresponding 2D scattering patterns and the temperatures when the $Al_{13}Fe_4$ primary phase initially nucleated in liquid. For the Al-1.5Fe sample, the scattering pattern at 660°C and 657°C is almost identical.

Hence, the spectrum at 660°C was used for the Al-1.5Fe alloy, rather than that at 657°C.

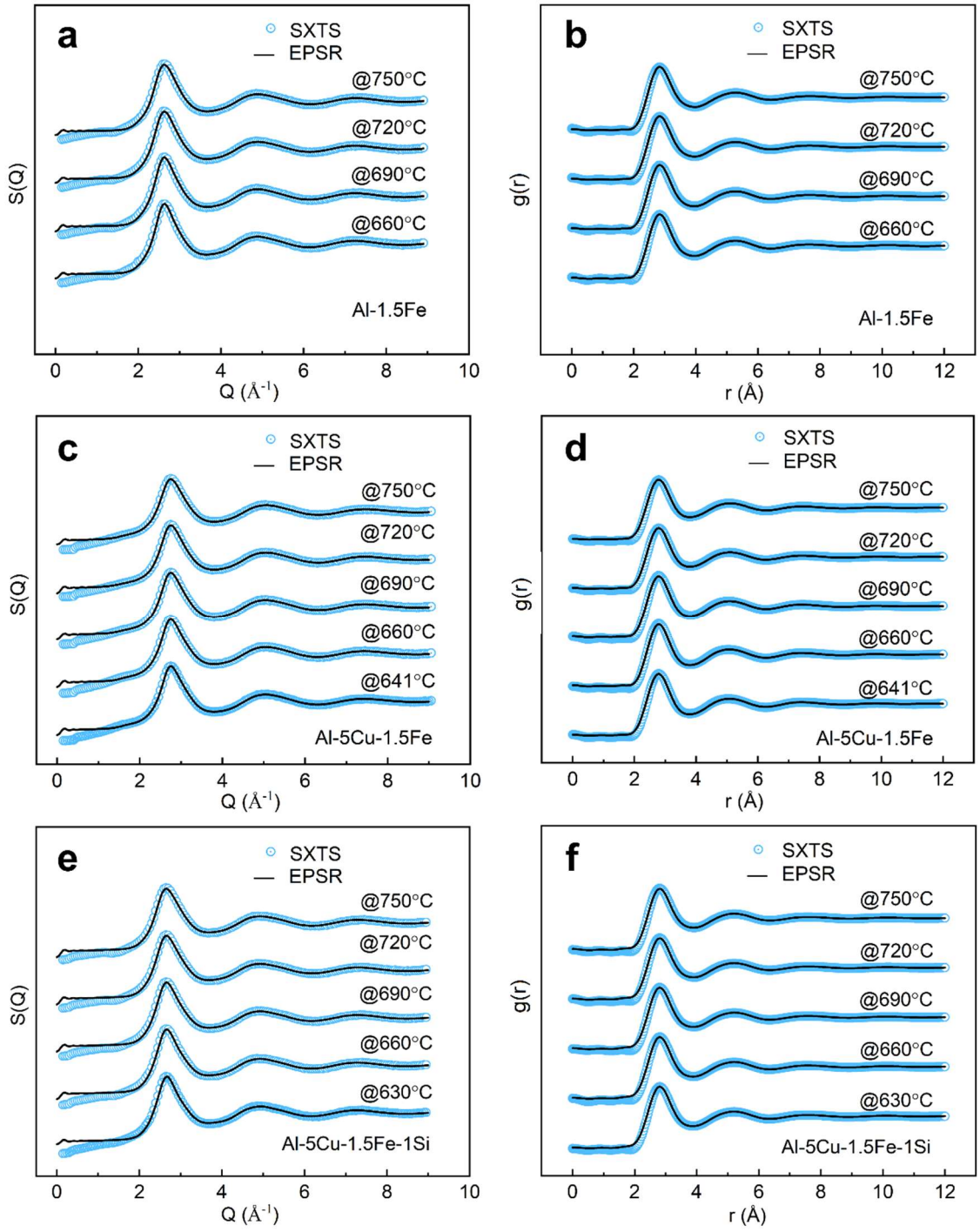

Fig. 5.2. The experimental and EPSR simulated structure factors, $S(Q)$ and total PDF, $g(r)$. (a) and (b) for the Al-1.5Fe, (c) and (d) for the Al-5Cu-1.5Fe, and (e) and (f) for the Al-5Cu-1.5Fe-1Si alloy melt respectively.

Fig. 5.3 shows the PDF, $g(r)$ for the pure Al, Al-1.5Fe, Al-5Cu-1.5Fe and Al-5Cu-1.5Fe-1Si melt obtained at 660°C from the experiments. Fig. 5.1 shows that

660°C is the reasonable temperature for the 3 alloys prior to crystal nucleation. Comparison of their $g(r)$ at 660°C gives us some insight of the effects of different solute elements on the resulting atomic structures as explained below.

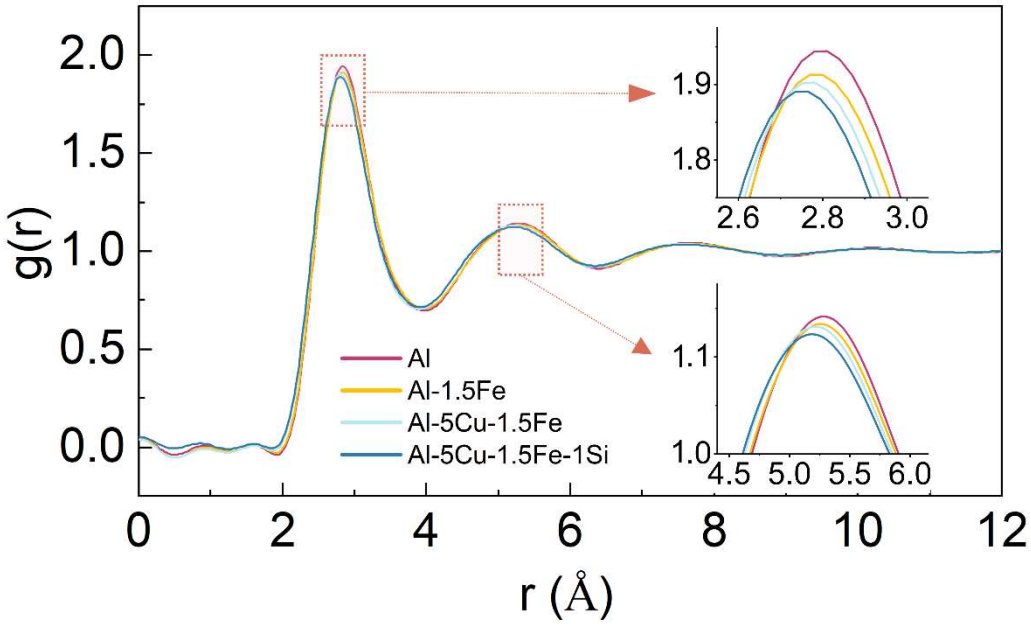

Fig. 5.3. The PDFs for the pure Al, Al-1.5Fe, Al-5Cu-1.5Fe and Al-5Cu-1.5Fe-1Si obtained by the SXTS experiments at 660°C.

Using the $g(r)$ of pure Al as the baseline, it is very clear that, in the $g(r)$ of all 3 alloys, the positions of the 1st, 2nd and 3rd peaks all shift towards smaller $\boldsymbol{r}$. However, the added Cu in the Al-5Cu-1.5Fe and the Cu and Si in the Al-5Cu-1.5Fe-Si alloy further shift the positions of these peaks of $g(r)$ toward even smaller $\boldsymbol{r}$. The atomic radius information is that Al = 143 pm, Fe = 126 pm, Cu = 128 pm and Si = 111 pm [273]. The results indicate that when larger radius atoms are replaced by smaller ones as the cases in the Al-5Cu-1.5Fe and Al-5Cu-1.5Fe-Si, the average interatomic distance decrease, resulting in the 1st $g(r)$ peak positions shift towards smaller $\boldsymbol{r}$ [274].

To quantify the variation of the bonding characteristics of the solute atoms in the nearest-neighbour coordination shell, the partial PDFs of the 3 alloys are extracted from the EPSR models as shown in Figs. 5.4, 5.5 and 5.6. Only the Al-Al and X-Al pairs (X = Cu, Fe and Si) are considered because the X-X pairs had much low-concentration. In all 3 melts, the 1st peak positions of the $g(r)_{Al-Al}$ are at ~2.78 Å, while the 1st peak positions of all $g(r)_{X-Al}$ are at smaller $\boldsymbol{r}$ than that of

$g(r)_{Al-A}$. As temperature decreases, the 1st peak position of $g(r)_{Al-Al}$ in all three alloys shift towards larger **r**, indicating that the Al-Al pairs expand during cooling. While for the 1st peak positions of $g(r)_{Fe-Al}$, $g(r)_{Cu-Al}$ and $g(r)_{Si-Al}$, all move to smaller $\boldsymbol{r}$, indicating that the X-centered atomic clusters become more and more compacted. In addition, for the 1st peak $g(r)_{ij}$ height, all increase slightly during cooling, i.e., the corresponding melt structures become more and more ordered during cooling. These results are consistent with our previous work on the Al-0.4%Sc alloy [168].

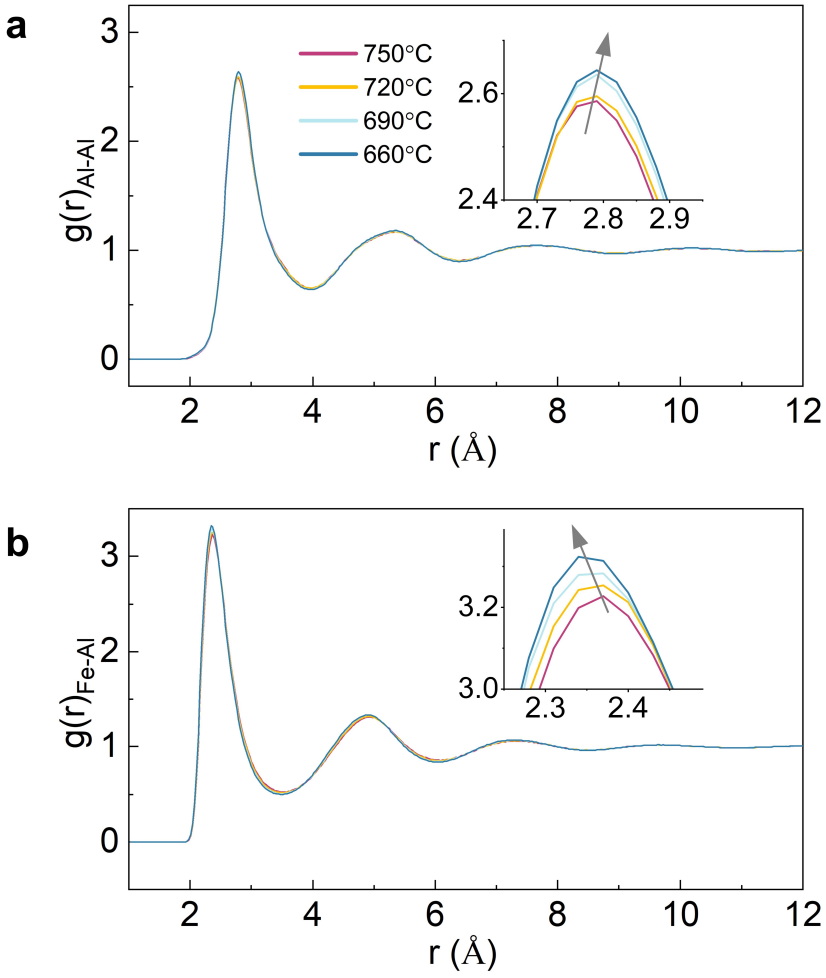

Fig. 5.4. The partial PDF of (a) Al-Al pair and (b) Fe-Al pair of Al-1.5Fe at various temperatures

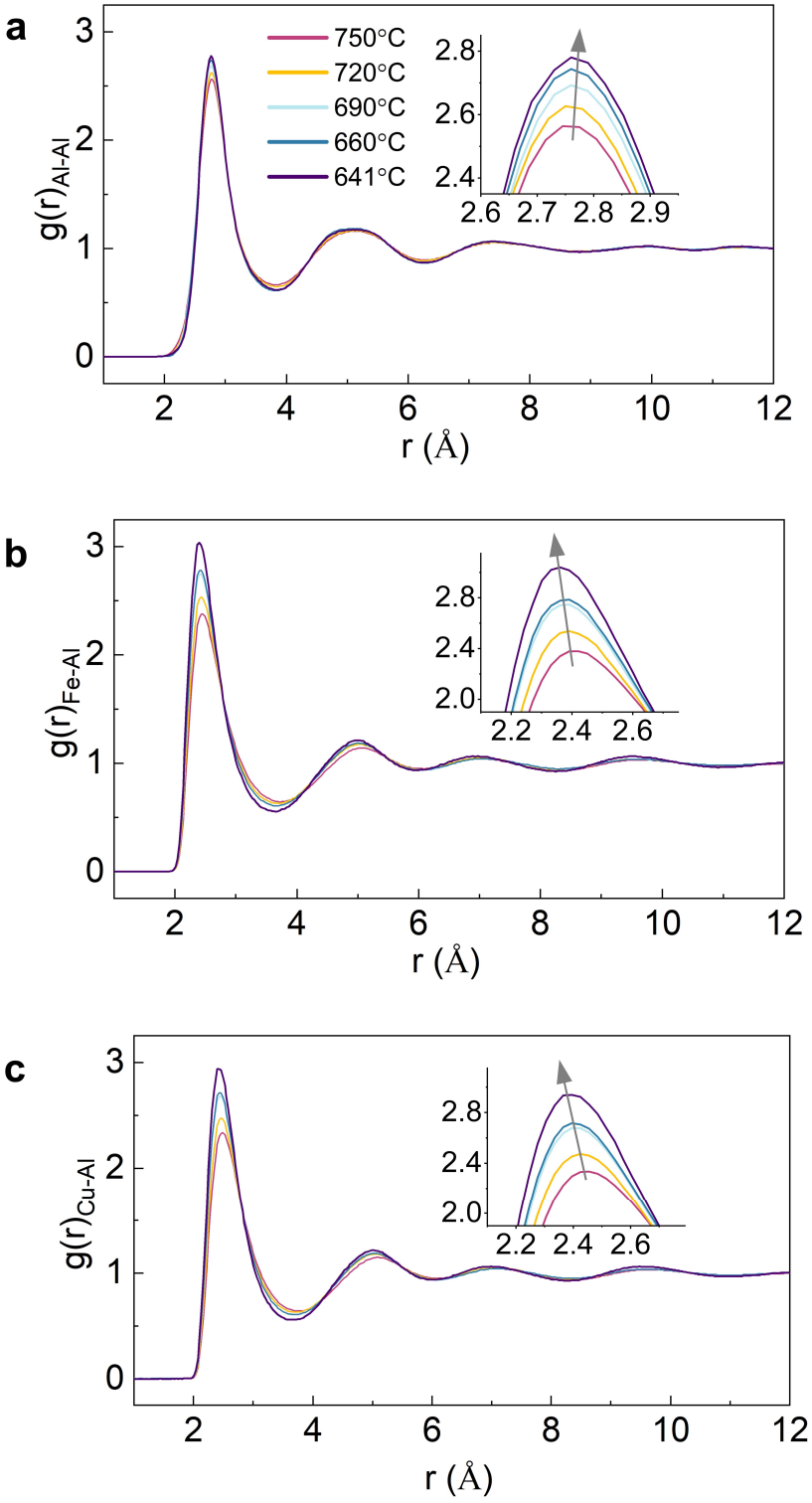

Fig. 5.5. The partial PDF of (a) Al-Al pair, (b) Fe-Al pair, (c) Cu-Al pair of Al-5Cu-1.5Fe at various temperatures

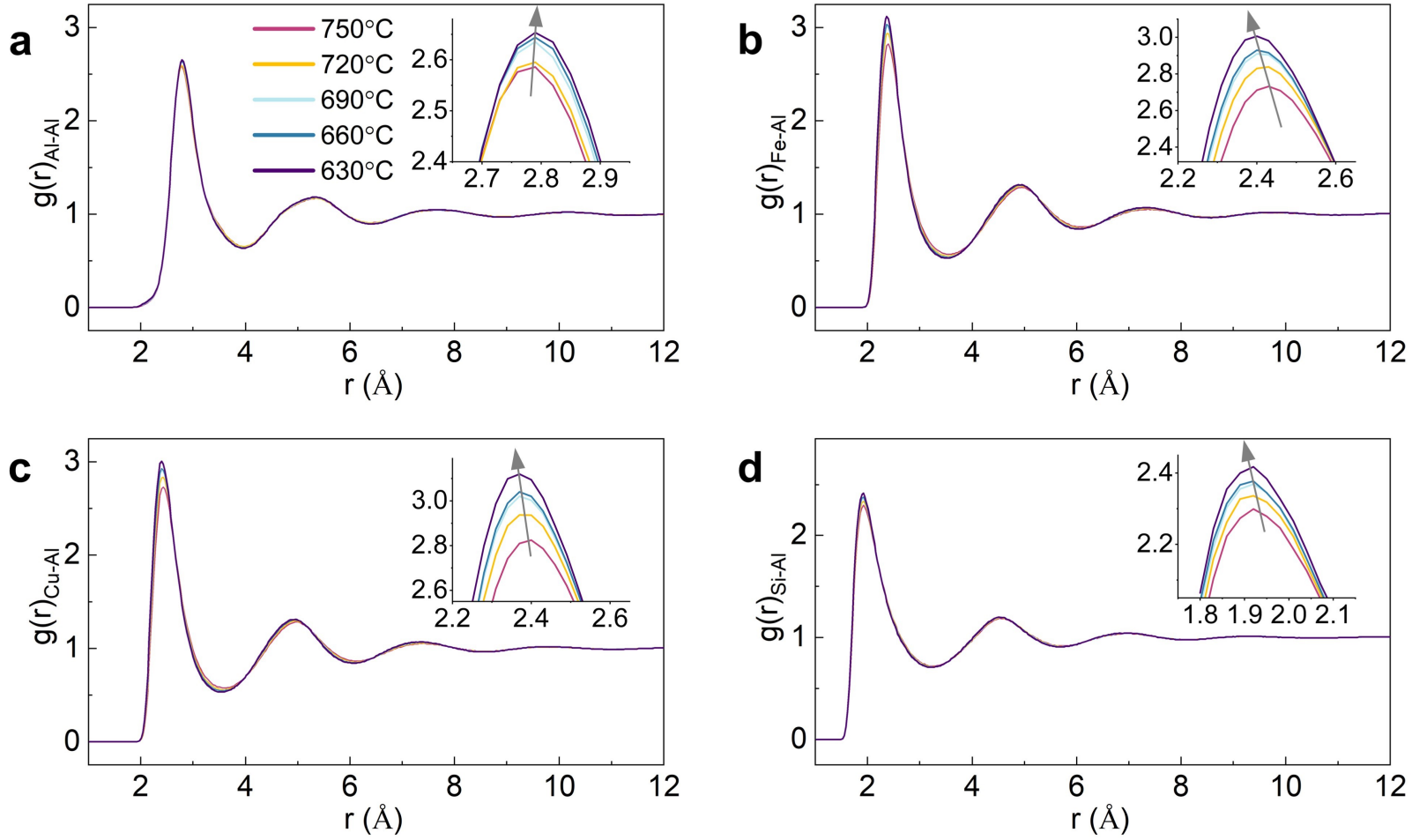

Fig. 5.6. The partial PDF of (a) Al-Al pair, (b) Fe-Al pair, (c) Cu-Al pair and of (d) Si-Al pair of Al-5Cu-1.5Fe-1Si at various temperatures.

5.2 SRO and MRO structures revealed by PDFs

To study the local atomic structure configuration around an arbitrary reference X atom at different temperatures, all atoms in the 1st shell of the X atoms in the EPSR models are extracted using a cut-off **r** value (the 1st valley position of **r** in the partial PDFs). Fig. 5.7 shows typical examples of the 3D atom configurations for the 3 alloys according to the selected SXTS diffraction patterns prior to the nucleation of $Al_{13}Fe_4$. Fig. 5.7a, c and f show all atoms in the simulation boxes. For each alloy, the X-centred polyhedra are also presented, Fig. 5.7b for the Fe-centred ones in the Al-1.5Fe; Fig. 5.7d, e for the Fe- and Cu- centred ones in the Al-5Cu-1.5Fe; Fig. 5g, h, i for the Fe-, Cu- and Si- centred ones in the Al-5Cu-1.5Fe-1Si alloy. Fe-centred atomic clusters for the three melts are also presented in accompanying video 1, 2 and 3. Clearly, all atom clusters are randomly distributed in the simulation boxes. Some clusters link together by different modes to form more complex MRO superclusters which is the basis of forming structural heterogeneities in these alloys in the liquid state. These connected superclusters tend to form string-like patterns.

To elucidate the structure heterogeneities in the liquid state prior to the nucleation of the primary $Al_{13}Fe_4$ phases, I focus on studying the Fe-centred MROs. Fig. 5.7j shows three typical Fe-centred superclusters extracted from the simulation box of the 3 alloy melts respectively. The Fe-centred superclusters in the Al-5Cu-1.5Fe and Al-5Cu-1.5Fe-1Si melt consist of 3 and 4 types of atoms accordingly. The size of these superclusters is typically beyond the 3rd coordination shell and extended to nanometer range. The superclusters are connected with the Fe-centered SROs via five different connection modes, which are by sharing the Al-Al bonds (BS), vertex (VS), edge (ES), face (FS) and tetrahedra (TS) between the neighbouring clusters (Fig. 5k insets) [168, 250, 251]. The section 3.6.5 describes how to extract such information from the EPSR modelled results. Fig. 5.7k also provides the calculated fractions of each connection mode for the Fe-centered MROs in the 3 alloys at 660°C, 641°C and 630°C, respectively. Clearly, the BS is the main connection mode in all 3 melts.

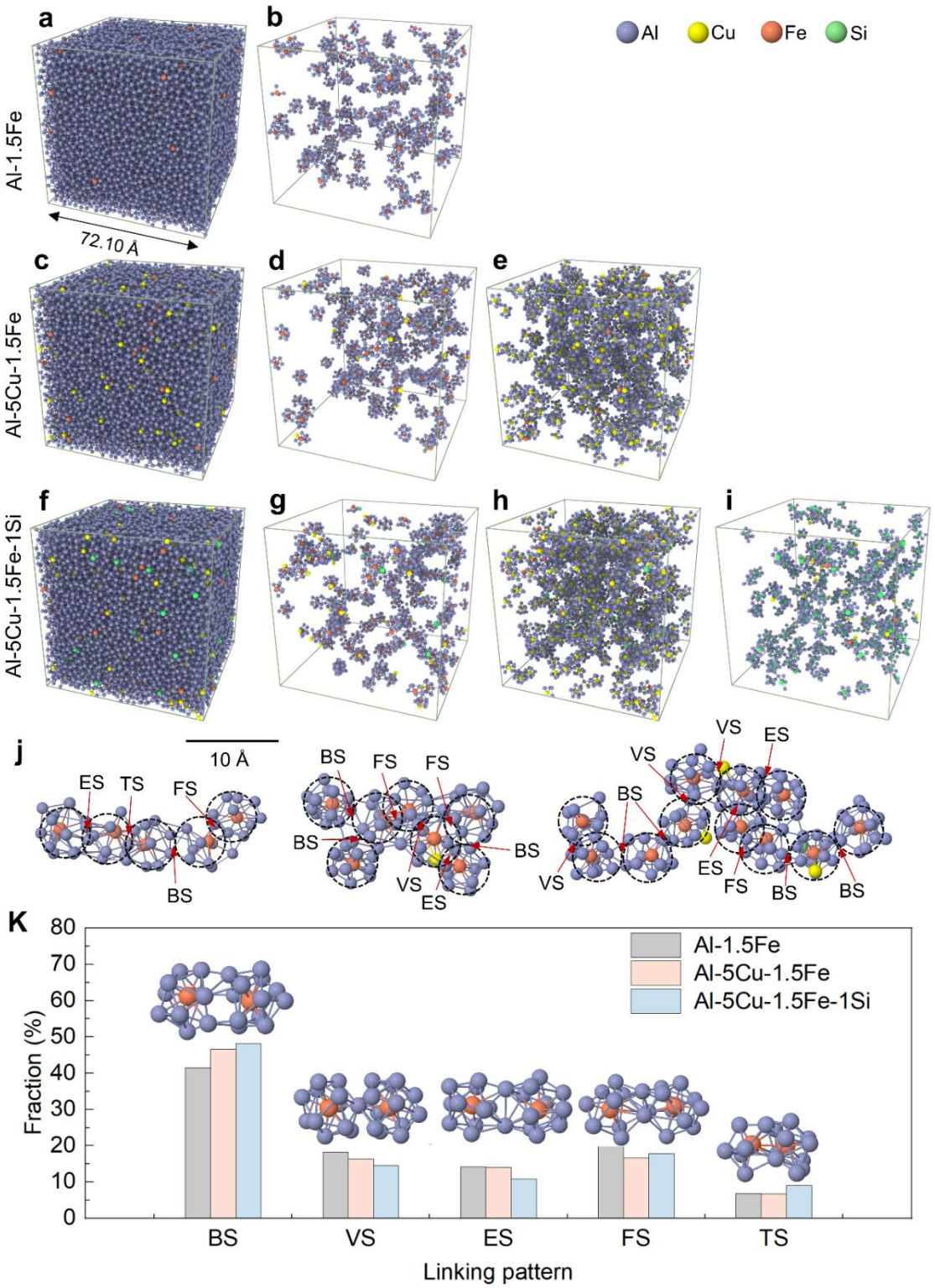

Fig. 5.7. A snapshot of all atoms and typical solute atom-centred clusters in the simulation box for (a-b) Al-1.5Fe at 660 ºC, (c-e) Al-5Cu-1.5Fe at 641 ºC and (f-i) Al-5Cu-1.5Fe-1Si at 630 ºC. (j) Typical Fe-centred superclusters extracted from b, d and g respectively. (k) The corresponding fraction of the five connection modes for the Fe-centred MROs in the 3 alloys at the onset prior to crystallization.

The insets show the 3D configuration of the Fe-centred MROs constructed by different connection modes.

To further quantify the atomic structure evolution during cooling, especially the heterogeneities of the Fe-containing atom clusters, changes of the connection modes and the total coordination number (CN) as a function of temperature are analysed. Fig. 5.8a, b and c clearly show that, in all 3 alloy melts, the BS fraction decreases monotonously during cooling, from 54.7% to 41.4% in the Al-1.5Fe; 54.5% to 46.3% in the Al-5Cu-1.5Fe, and 55.0% to 47.5% in the Al-5Cu-1.5Fe-1Si melt. The fraction of ES and FS instead gradually increases. While that of the TS remains almost unchanged. However, the fraction of VS varies differently, increases in the Al-1.5Fe but decreases in the other two cases. Such trends indicate that some of the BS-connected superclusters change into the ES- and FS- connected ones during cooling as the Fe-centered MROs become more compacted.

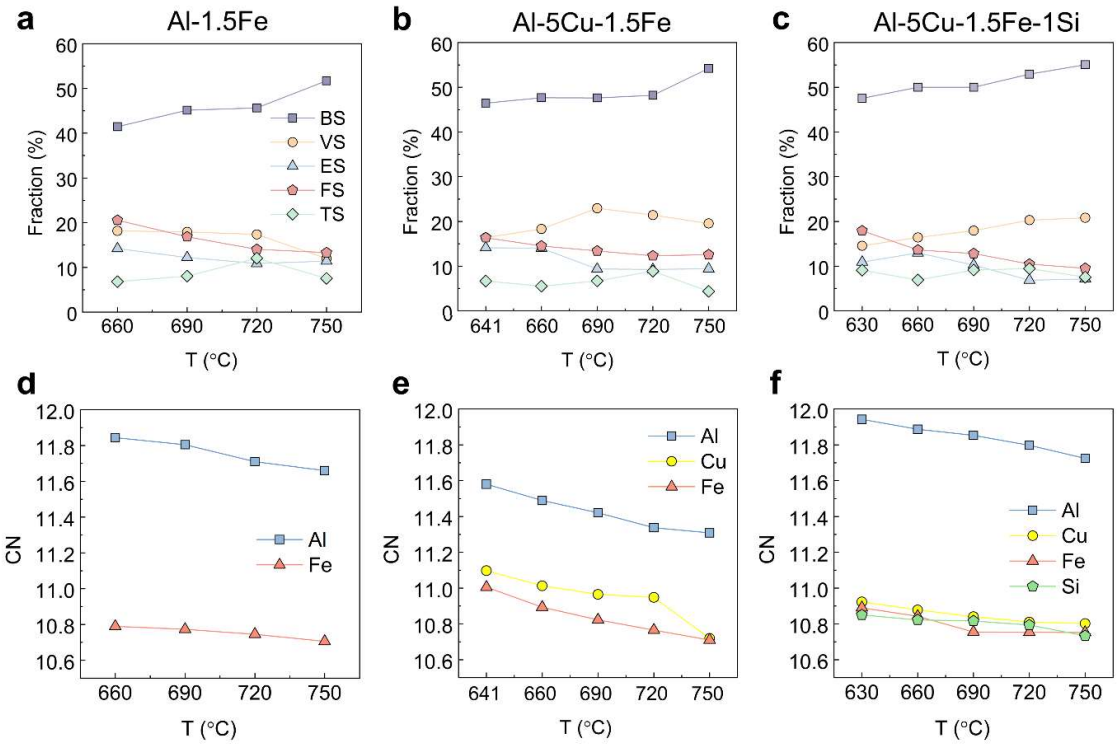

Fig. 5.8. Supercluster connection modes and the total coordination number (CN) as function of temperature during cooling for the 3 alloy melts. (a-c) for the connection modes. (d-f) for the total CN.

Fig. 5.8d-f shows the evolution of the total CN, calculated by averaging all atoms in the 1st shell of the central reference atom. For the Al-1.5Fe melt, the CN_{Al} increases from 11.61 to 11.82, while that of the CN_{Fe} from 11.0 to 11.17. The CN_{Al}, CN_{Cu} and CN_{Fe} in the Al-Cu-Fe melt also increase with the similar trend. The CN_{Al} reached ~11.6, while CN_{Cu} and CN_{Fe} to ~11.1 respectively. In the Al-Cu-Fe-Si melt, the CN_{Al}, CN_{Cu}, CN_{Fe} and CN_{Si} are up to 11.92, 10.87, 10.84 and 10.82 respectively. The trends of the CNs are in a good agreement with the trends shown by the changes of the connection mode. i.e., the Fe-centred local ordering for the 3 melts become more close-packed as temperature decreases.

5.3 Fine atomic structures beyond PDFs

5.3.1 Structure characteristics quantified by Warren-Cowley parameter

To understand more quantitatively the interactions of multiple atoms in the 3 alloy melts, the chemical short-range order (CSRO) for each element was calculated and the Warren-Cowley parameters $\boldsymbol{\alpha_{ij}}$ for all atom pairs in the 3 melts during cooling (see Table 3). $\boldsymbol{\alpha_{ij}}$ is calculated by:

$$\boldsymbol{\alpha_{ij} = 1 - Z_{ij}/(c_j Z_i)} \quad (6)$$

where $\boldsymbol{c_j}$ is the mole fraction of atom j, $\boldsymbol{Z_{ij}}$ and $\boldsymbol{Z_i}$ are the partial and total CN [196, 198, 199]. $\boldsymbol{\alpha_{ij}} = 0$ means a completely random distribution of atoms *i* and *j*; $\boldsymbol{\alpha_{ij}} < 0$ indicates that the number of j atoms in the 1st shell of i atoms exceeds the average concentration of j atoms. $\boldsymbol{\alpha_{ij}} > 0$ means there is a chemical preference not in favour of the $i - j$ nearest-neighbour pair. Table 5.1 shows clearly that all Al-Al and X-Al pairs have negative values, but they are very close to zero. Such phenomena suggest that when the pure Al liquid is doped with solute atoms, the liquid is in an almost completely random state, but there exists some degree of chemical preference between different atom pairs, although not strong. There are more coordinated Al atoms in the 1st shell of a centre reference atom (Al and X) than its average concentration in the liquid for all 3 alloys. This means the Al atoms and X atoms somehow compete to attract Al atoms in their 1st nearest neighbour shell as temperature decreases. Thus, the competition to form either

Al-centred or X-centred SROs drives the structural dynamic evolution in the 3 liquids [275]. The X atoms in the 1st shell of Al atom are less than its average concentration in the 3 melts at different temperatures.

Table 5.1. Warren-Cowley parameter α_{ij} for the alloys at different temperatures

Composition	Pair	Temperature (ºC)				
		750	720	690	660	
Al-1.5Fe	Al-Al	-0.0008	-0.0006	-0.0006	-0.0006	
	Al-Fe	0.1107	0.0782	0.0859	0.0869	
	Fe-Al	-0.0002	-0.0008	-0.0016	-0.0037	
	Fe-Fe	0.0319	0.1162	0.0217	0.0501	
		750	720	690	660	641
Al-5Cu-1.5Fe	Al-Al	-0.0045	-0.0065	-0.0069	-0.0078	-0.0087
	Al-Fe	0.0452	0.0866	0.0925	0.0955	0.0657
	Al-Cu	0.0627	0.0632	0.0851	0.0856	0.0755
	Fe-Al	-0.0065	-0.0055	-0.0066	-0.0079	-0.0046
	Fe-Fe	0.1245	0.1124	0.0989	0.1576	0.2357
	Fe-Cu	-0.0155	-0.0214	-0.0357	-0.0216	-0.1587
	Cu-Al	-0.0057	-0.0642	-0.0038	-0.0078	-0.0052
	Cu-Fe	0.1232	0.0950	0.0327	0.1267	0.0656
		750	720	690	660	630
Al-5Cu-1.5Fe-1Si	Al-Al	-0.0034	-0.0034	-0.0034	-0.0024	-0.0034
	Al-Fe	0.0880	0.0800	0.0869	0.0969	0.0891
	Al-Cu	0.0798	0.0790	0.0802	0.0804	0.0804
	Al-Si	0.0879	0.0893	0.0862	0.0039	0.0905
	Fe-Al	-0.0020	-0.0016	-0.0064	-0.0023	-0.0027
	Fe-Fe	0.2328	0.1874	0.4191	0.2860	0.0988
	Fe-Cu	0.0107	-0.1083	-0.0121	-0.0124	-0.0200
	Fe-Si	-0.0294	0.2050	0.3495	-0.0244	0.2833
	Cu-Al	-0.0012	-0.0010	-0.0058	-0.0050	-0.0058
	Cu-Fe	0.0153	-0.1024	0.1159	-0.0091	-0.0112
	Cu-Cu	-0.0724	0.0120	0.2235	0.2026	0.2313
	Cu-Si	0.0362	-0.0481	-0.0206	0.0330	0.0551
	Si-Al	-0.0160	-0.0014	-0.0019	-0.0029	-0.0071
	Si-Fe	-0.0294	0.2050	0.3495	0.0687	0.2833
	Si-Cu	0.0426	-0.0556	-0.0228	0.1164	0.0417
	Si-Si	-0.1647	0.0650	-0.0691	-0.0676	0.3327

5.3.2 Structure characteristics quantified by Voronoi tessellation

To further quantify the local atomic configuration and the SRO structural evolution during cooling, we apply the Voronoi tessellation method. Fig. 5.9a, c, show shows the fraction of the main VPs (for all atoms) in the 3 melts, while those of the Fe-centred VPs in the 3 melts are given in Fig. 5.9b, d and f (the Voronoi indexes for the typical Fe-centred superclusters are shown in Fig. 5.10). These VPs are classified into 3 different types according to Cheng et al. [16] :(a) Icosahedra-like (ICO-like) SROs, including < 0 0 12 0>, <0 1 10 x> and < 0 2 8 x>, where x=1, 2 …4. A polyhedron with Voronoi index <0 0 12 0> represents a perfect icosahedral structure with a five-fold symmetry, while <0 1 10 x> and < 0 2 8 x> can be considered as distorted icosahedral clusters. (b) crystal-like SROs, including <0 3 6 x > (x=2, 3, 4 and 5) and <0 4 4 x> (x=4, 5, 6 and 7), and (c) those not possessing the symmetries as the above two cases [16]. Within the studied temperature range, the ICO-like and crystal-like VPs for all atoms are prevalent in the 3 melts (see Fig. 7a, c and e), where the fraction of crystal-like VPs is always higher than that of ICO-like. As temperature decreases, the fraction of both ICO-like and crystal-like VPs increases. The gradually increased VP numbers in the 3 melts indicated that the atomic structures of the 3 melts become more heterogeneous as the temperature is cooled down. The continuous increase of the crystal-like VP number increase also reflected in the fact that the 1st peak of PDFs become sharper and sharper as the temperature is decreased [21]. It can be found from Fig. 5.9b, d and f that the fraction of both ICO-like and crystal-like Fe-centred VPs increases more obviously, reaching a higher value at the temperature prior to onset of nucleation for three melts. Such a phenomenon indicates that the local environment of Fe atoms becomes more ordered than the liquid containing all atoms. For Al-Fe melt, the fraction of ICO-like VPs is always higher, while that of crystal-like in Al-Cu-Fe-Si is always higher. The fraction of crystal-like Fe-centred VPs exceeded that of ICO-like at 641 ºC in Al-Cu-Fe melt. We propose that adding other solute atoms might result in local structure changes of Fe atoms.

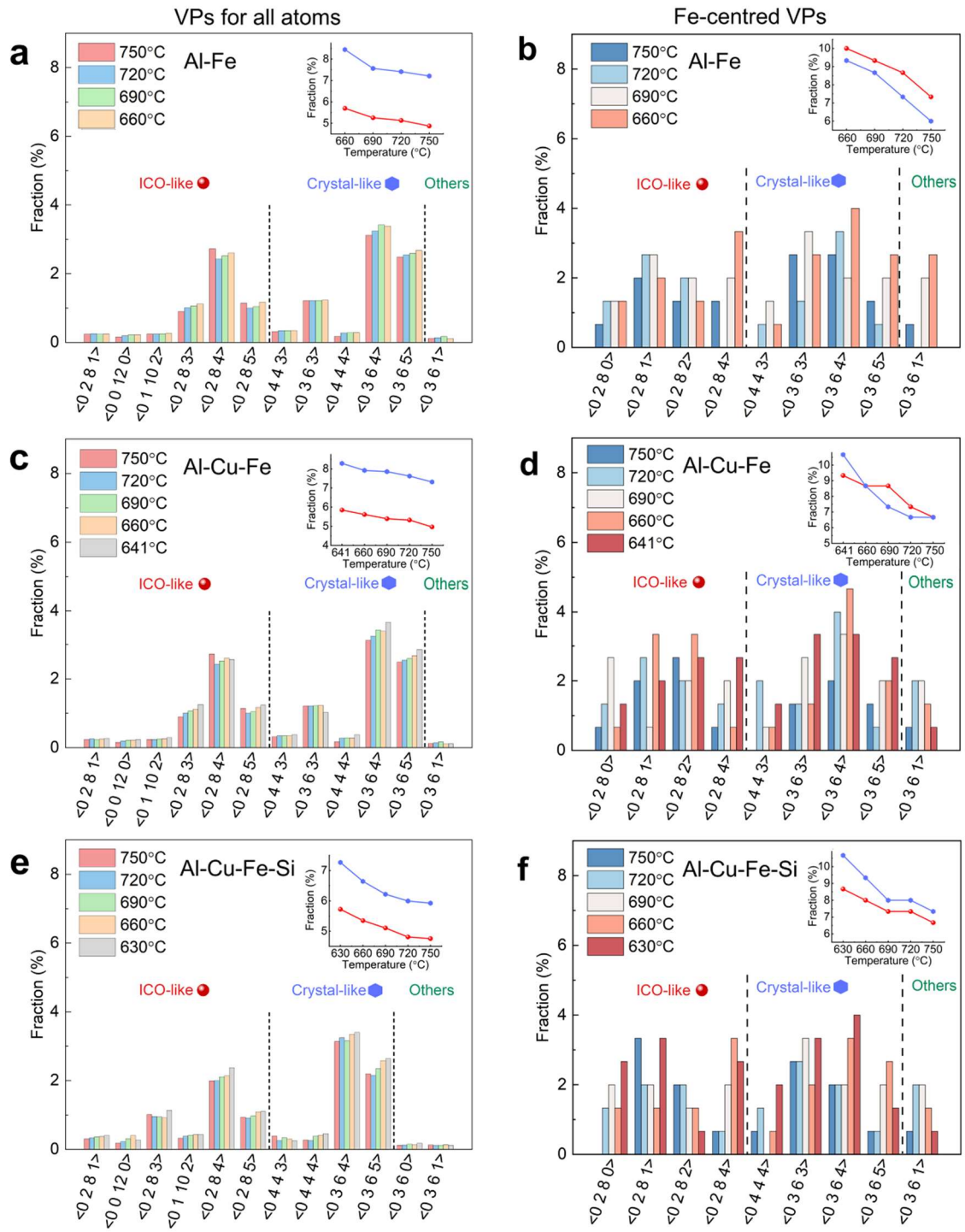

Fig. 5.9. Left: the number distribution of the main VPs for all atoms at different temperatures. Right: those for the Fe-centred VPs only. (a) and (b) for the Al-1.5Fe, (c) and (d) for the Al-5Cu-1.5Fe, and (e) and (f) for the Al-5Cu-1.5Fe-1Si melt respectively. The insets show the temperature-dependent fraction of the ICO-like and crystal-like VPs during cooling.

Fig. 5.10 shows 3 typical Fe-centred superclusters (containing different type solute atoms) extracted from the simulation box of the Al-5Cu-1.5Fe-1Si at 630°C. The superclusters were formed by connecting the Fe-centered VPs via different connection modes.

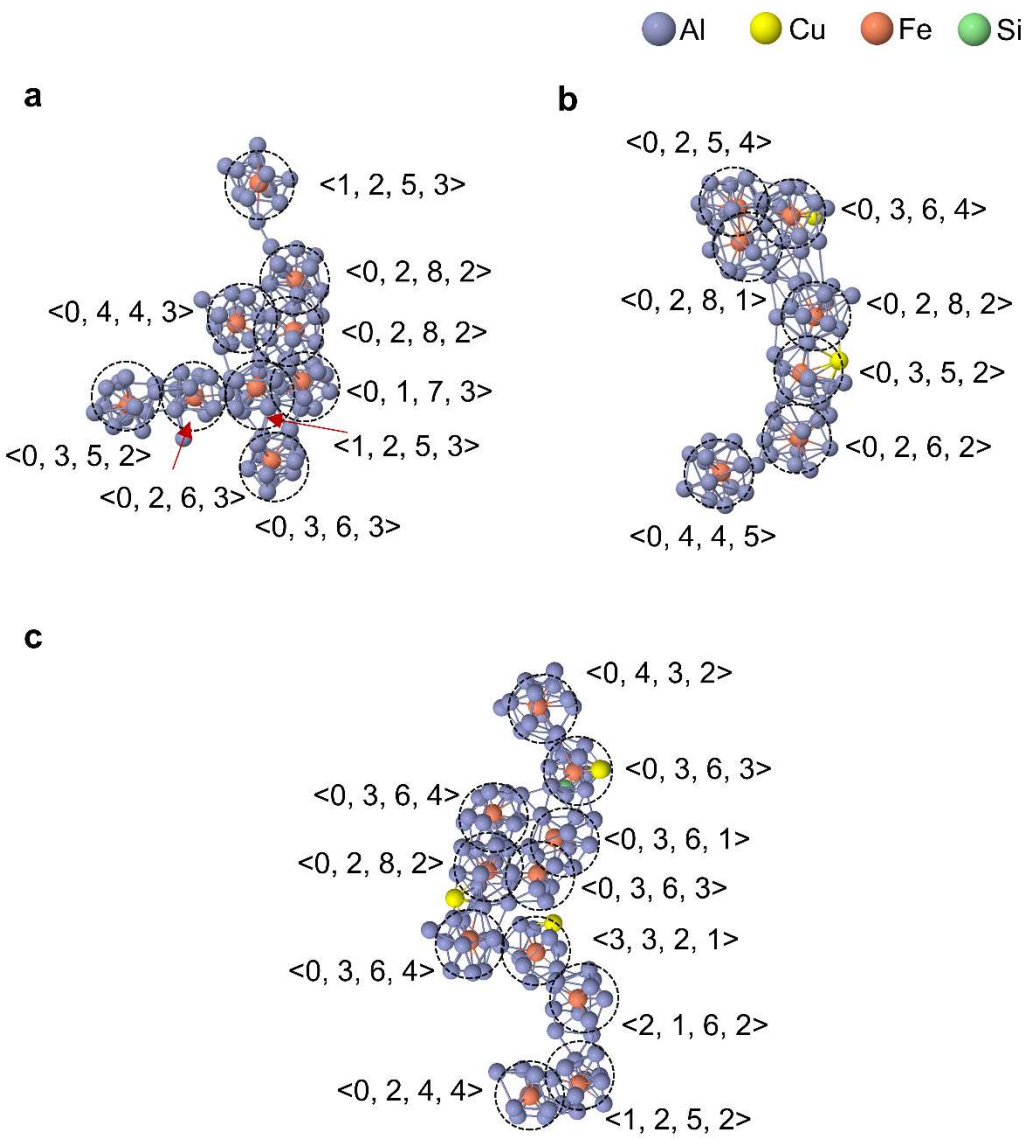

Fig. 5.10. The Voronoi indexes of 3 typical Fe-centred superclusters in the Al-Cu-Fe-Si melt, consisting of (a) Al and Fe atoms, (b) Al, Cu and Fe atoms, (c) Al, Cu, Fe and Si atoms.

5.3.3 Structure characteristics quantified by Bond orientational order

I also use the BOO parameters to characterize the temperature-dependent local structure evolution around individual elements. The spherical harmonics-based BOO analysis can provide a quantitative description of local rotational symmetry around an arbitrary central reference atom. Among these parameters, the $\widehat{W}_6$ cubic invariant is the most sensitive indicator for icosahedral symmetry [61]. Q_6 is useful in measuring the degree of crystallinity (i.e., how far a precursor is away from its crystal nucleus [2]). Q_4 is useful in quantifying the difference in symmetries (i.e., lattice match) [23].

Fig. 5.11a shows the $\widehat{W}_6$ as function of temperature for the Al- and Fe-centred atomic clusters in the Al-1.5Fe melt. During cooling, $\widehat{W}_6$ of the Al- decreases gradually, while that of the Fe- decreases with slightly higher rate. In the Al-5Cu-1.5Fe melt (Fig. 5.11b), $\widehat{W}_6$ of the Al- and that of the Cu- are quite similar, while $\widehat{W}_6$ of the Fe- exhibits the similar trend as that in the Al-1.5Fe case but with approximately 10% lower in their absolute value. In the Al-Cu-Fe-Si case (Fig. 5.11c), $\widehat{W}_6$ of the Fe- decreases sharply from 750 to 690 ºC, and then slowly to 630 ºC. While those for the Al-, Si- and Cu- remain relatively stable. In summary, the decrease of $\widehat{W}_6$ for all atom clusters in the 3 melts indicates that there are more and more atom clusters with the five-fold symmetry (due to icosahedral structure) in the melts as the temperature decreases.

Fig. 5.11d, e and f show the Q_6 as function of temperature for the individual elements in the 3 melts. Compared to all Q_6 in the 3 figures, it is very clear that Q_6 of all atoms (except the Si case in the Al-Cu-Fe-Si melt) increases as the temperature decreases. Among all Q_6, that of the Fe has the highest value (except in the Al-Cu-Fe-Si case at 720 and 750 ºC), followed by the Cu, Al and Si. In the Al-Cu-Fe-Si melt, Q_6 of the Fe increases sharply from 0.361 to 0.396 from 750 to 630 ºC. While Q_6 of the Al, Cu and Si remain relatively flat. Such results indicate that the Fe coordination environment contains a higher proportion of the crystal-like order compared to that of the other elements.

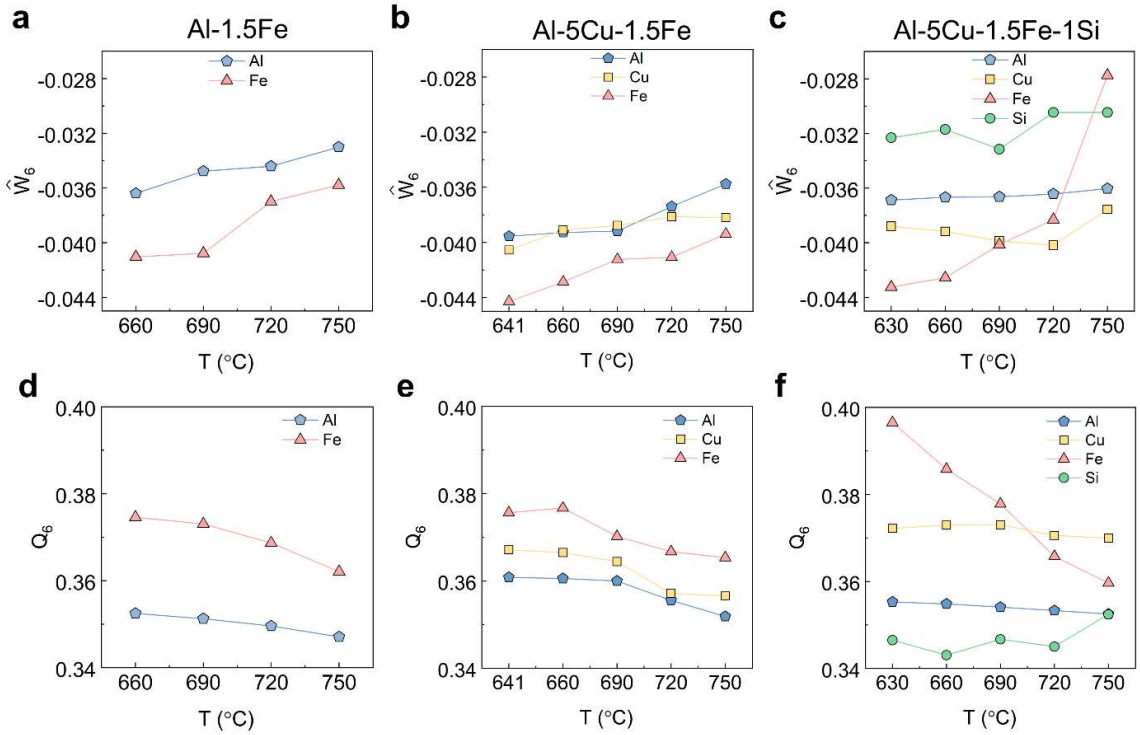

Fig. 5.11. The temperature-dependent $\widehat{W}_6$ (a-c) and Q_6 (d-f) of different atoms in the 3 alloy melts.

To further elucidate the temperature-dependent structural heterogeneity evolution, the Q_4-Q_6 value for each atom is calculated. Fig. 5.12 shows the Q_4-Q_6 distribution map for each atom in the 3 melts. Clearly, the majority of the atoms deviate markedly from the fcc (Q_4 = 0.191, Q_6 = 0.574), hcp (Q_4 = 0.097, Q_6 = 0.485), bcc (Q_4 = 0.036, Q_6 = 0.511) [276] and the monoclinic $Al_{13}Fe_4$ (Q_4 = 0.192, Q_6= 0.491) structure. To illustrate the temperature-dependent evolution more clearly in the Q_4-Q_6 map, the normalized BOO parameter defined by Yang et al. [32] is used here. It is calculated by $\sqrt{Q_4^2+Q_6^2}/\sqrt{Q_{4fcc}^2+Q_{6fcc}^2}$, where Q_{4fcc} and Q_{6fcc} are the Q_4 and Q_6 for a perfect fcc lattice. The normalized BOO parameter is between 0 and 1, where 0 means that $Q_4 = Q_6 = 0$, 1 represents a perfect fcc structure. Using this method, all atoms in the 3 melts are classified into two different types: the atoms with normal liquid structure, and the others with pre-ordered liquid structure, i.e., with higher bond-orientational order. Here, I use the two points on the Q_4-Q_6 map, i.e., point ($Q_4 = 0, Q_6 = 0.48$) on the Q_6 axis, and the point ($Q_4 = 0.48, Q_6 = 0$) on the Q_4 axis to define the boundary line. It is

calculated as $0.793 = \sqrt{Q_4^2+Q_6^2}/\sqrt{Q_{4fc}^2 + Q_{6fcc}^2}$ (see all red-dash lines on Fig. 5.12a-n), above which the atoms have pre-ordered structure, below which the atoms have normal liquid structure. The 0.793 is determined by the result of pure Al at 690 ºC and 660 ºC during the cooling process [168] . Clearly, Fig. 5.12a-n show that the majority of the atoms in the 3 melts are below the red curves, i.e., having liquid structures. A big portion of the atoms above the red curve are near the $Al_{13}Fe_4$ or fcc region. As temperature decreases, the percentage of the atoms with pre-ordered structure increases steadily as illustrated in Fig. 5.12o. As the temperature approaches the nucleation stage (i.e., below 690 ºC for the Al-Fe case, and below 660 ºC for the Al-Cu-Fe and Al-Cu-Fe-Si case), the percentage of the atoms with pre-ordered structure increases more quickly, reaching 8% to 9% at the temperature just prior to nucleation. Such relatively ordered structures serve as the precursors of crystal nuclei, and they are the atomic structures at the intermediate steps prior to crystal nucleation [17]. In our case, these pre-ordered atoms with high BOO parameters are the precursors of the $Al_{13}Fe_4$ primary phase in the crystallization process as discussed in detail below.

Fig. 5.12p plots average Q_6 versus Q_4 for Fe atoms only in the liquid state and that of $Al_{13}Fe_4$ in the solid state. Clearly, Q_6 and Q_4 of the Fe-centred polyhedra gradually approach those of the $Al_{13}Fe_4$ crystalline phase (0.186, 0.494), indicating that the atoms undergo gradual structural changes, i.e., the crystallization process does not occur abruptly, instead, it occurs progressively.

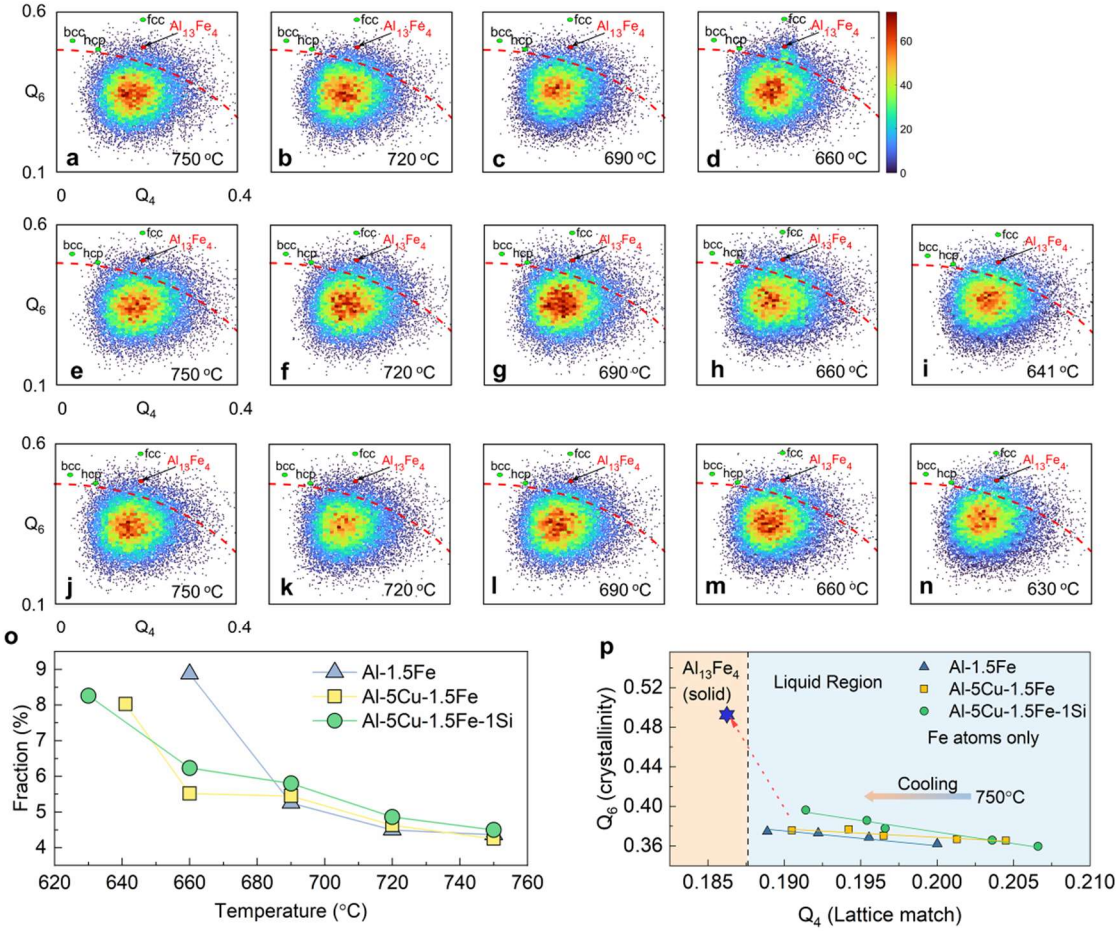

Fig. 5.12. Temperature-dependent Q_4-Q_6 distribution map for all atoms in (a-d) Al-1.5Fe, (e-i) Al-5Cu-1.5Fe and (j-n) Al-5Cu-1.5Fe-1Si melts. The red dash curves are the boundaries with the normalized BOO parameter of 0.793. The perfect bcc, hcp and fcc structures are marked by the green dots, while the monoclinic structure ($Al_{13}Fe_4$) is marked by the red dot. (o) Fractions of the pre-ordered atoms as a function of temperature in the 3 melts. (p) The average (Q_4,Q_6) evolution pathway of the Fe atoms in the liquid region for 3 melts during cooling.

5.4 Discussion

5.4.1 Variations in SROs due to multiple atom interactions

The interactions of multiple atoms in the liquid state for the 3 melts during cooling are clearly revealed by the Warren-Cowley SRO parameter and changes of the CN. As the temperature decreases, in the short atom range, the central reference Al or X atoms compete against each other, attracting other Al atoms to their 1st shell, forming either Al-centred or X-centred SROs. For the Al-centred clusters, more Al atoms appear in the 1st shell and the Al-Al bond length is larger, hence the 1st peak position of the $g(r)_{Al-Al}$ in all 3 alloys shifts towards larger $\boldsymbol{r}$ (see Fig. 5.4, 5.5 and 5.6). For the X-centred clusters, more Al atoms also appear in their 1st shell, but the X-Al bond length is smaller, hence the 1st peak position of the $g(r)_{X-Al}$ in all 3 alloys shifts towards smaller $\boldsymbol{r}$ (see Fig. 5.4, 5.5 and 5.6). In addition, the $\boldsymbol{\alpha_{ij}}$ of the Al-X pairs (see Table 5.1) in the 3 melts are all positive, indicating there is chemical preference against the Al-X pairs during cooling.

Fig. 5.13a shows that the 1st peak positions of $g(r)_{Fe-Al}$ in the Al-Fe melt are lower than those in the Al-Cu-Fe and Al-Cu-Fe-Si melts. While that of the $g(r)_{Cu-Al}$ in the Al-Cu-Fe melt is lower than that in the Al-Cu-Fe-Si melt. Such phenomena indicate the competition for attracting Al atoms between different types of X atoms. As shown in Table 3, the Warren-Cowley parameters of X-Al pairs are negative. For the Fe-Al pair, when Cu atoms are added, the Cu and Fe atoms are competing to attract Al atoms to their 1st shell as temperature decreases [275]. Adding Cu atoms weaken the attractive interaction between Fe atoms and the Al atoms in their 1st shell as the 1st peak position of $g(r)_{Fe-Al}$ become larger at the same temperature (see Fig. 5.13a). Adding Si atoms further weaken the attractive interaction between the Fe-Al and Cu-Al pairs (see Fig. 5.13b).

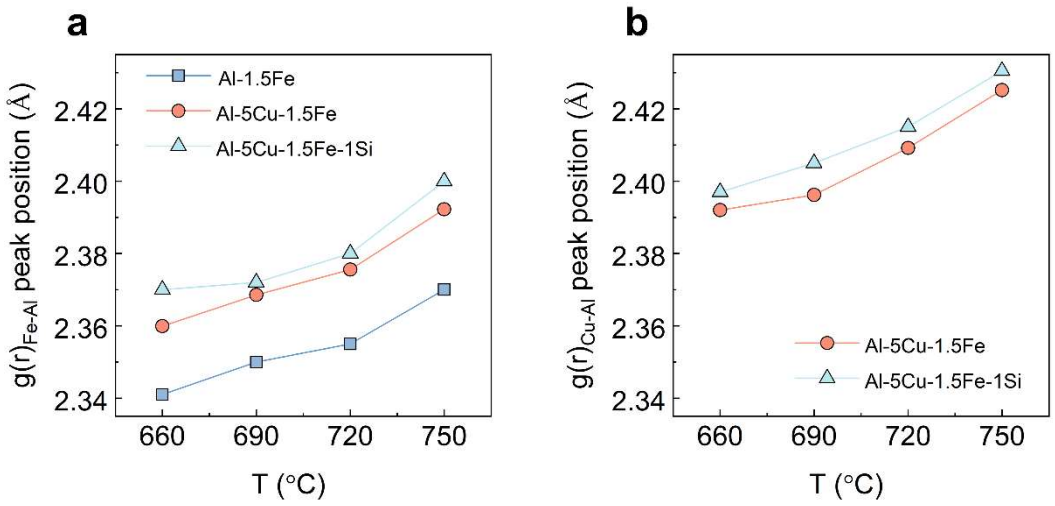

Fig. 5.13. Effect of temperature on the 1st peak position of (a) $g(r)_{Fe-}$ and (b) $g(r)_{Cu-Al}$ in the 3 alloy melts.

5.4.2 SRO structure heterogeneities quantified by the rotational symmetry

Fig. 5.9a, c and e show the atomic structure heterogeneities (different type SROs) for all atoms in the 3 melts. Fig. 5.9b, d and f show those for the Fe atoms only. Among them, the ICO-like and crystal-like structures are of sufficient percentage. As temperature decreases, the fractions of the two structures steadily increase but also continue to compete against each other (see all insets in Fig. 5.9). Such competition can be explained well by the two-order-parameter model [277, 278]. The BOO analyses also indicate that there are higher degree of crystallinity and higher fractions of five-fold symmetry in the low-temperature region for the 1st shell coordination environment. The development of structural heterogeneities during cooling at SRO scale is mainly due to the growing portion and competition between the ICO-like and crystal-like structures.

By using the normalized BOO parameter (i.e., the 0.793 line in Fig. 5.12) in the Q_4-Q_6 map, we can separate and quantify the pre-ordered clusters away from the clusters of normal liquid structure. The monoclinic structure (the $Al_{13}Fe_4$ phase) is located between the fcc structure and the normal liquid (with the icosahedral symmetry) in the Q_4-Q_6 map. This is because the monoclinic structure can be viewed as a distorted fcc lattice, and it also has partially icosahedral symmetry

[279, 280]. As the temperature decreases, the atoms that are positioned around the monoclinic $Al_{13}Fe_4$ site (the red dots in Fig. 5.12a-n) should have a similar structural arrangement as compared to the monoclinic $Al_{13}Fe_4$ phase. To be more specific, the structural similarity can also be confirmed by looking at the Fe-centred VPs in liquid (see Fig. 5.9b, d and f), where the dominant <0 2 8 1>, < 0 2 8 2 >, < 0 2 8 3 > VPs contain partially five-fold symmetry [61] as does in the $Al_{13}Fe_4$. Fig. 5.12a-n clearly show that the number of atoms surrounding the $Al_{13}Fe_4$ (the red dots) is much higher compared to those surrounding the fcc, bcc and hcp cases. Hence, it can be concluded that pre-ordered atoms in the region surrounding the red dots are the intermediate structures between the liquid and the $Al_{13}Fe_4$ phase, i.e., the nucleation precursor for the primary $Al_{13}Fe_4$ phase. Previous numerical and experimental studies suggest that the solid-liquid interfacial energy of monoclinic $Al_{13}Fe_4$ is smaller than that of the bcc and hcp/fcc phase [281-283]. Hence the $Al_{13}Fe_4$ phase first appears in the 3 melts. Our results also show that, at the pre-nucleation stage, the fraction of precursor in the liquid increases as temperature decreases together with the increase of structure heterogeneity (see Fig. 5.9b, d, and f). At the same time, the rotational symmetry of the Fe atom (see in Fig. 5.12p) in the liquid region evolves progressively towards that for the solid $Al_{13}Fe_4$. SRO structure heterogeneities quantified by rotational symmetry indicated that the disorder-to-order transition is a progressive behaviour, containing numerous steps. To address the role of the local structure of Fe atoms on the nucleation, I further discuss the evolution behaviour of Fe-centred MROs during cooling in section 5.6.3.

5.4.3 Fe-centred MRO structure heterogeneities and their evolutions

Warren-Cowley parameter analysis show that $\alpha_{\mathrm{FeFe}} > 0$ in the cooling process, hence the Fe-centred clusters tend to be "against" the Fe atoms in their 1st shell. This explains why the fraction of tetrahedral-sharing Fe-centred MROs (see the TS in Fig. 5.8a, b, and c) is the lowest among all connection modes. As the temperature decreases, the fraction of Fe-centred MROs connected by BS (Fig. 5.7 and 5.8) in the 3 melts decreases. While both ES and FS increase gradually in 3 melts during cooling. The fraction of VS in the Al-1.5Fe increases, while that in Al-5Cu-1.5Fe and Al-5Cu-1.5Fe-1Si melts decreases slightly. The above phenomena indicate that during the cooling process, the Fe-centred MROs become more compact, resulting in gradual changes in the connection modes. The increased fraction of ES and FS shows that the Fe-centred clusters connect each other by sharing more atoms. Clearly, one possible pathway is that the BS connected MROs evolve into those connected by VS and ES, and then into the MROs connected by FS (see Fig. 5.14a). As shown in Fig. 5.14b, among the FS clusters, they share 3 or 4 atoms, and the 3-atom sharing is the dominant mode for all 3 melts. Fig. 5.14c shows a unit cell of the monoclinic $Al_{13}Fe_4$ phase [280]. It clearly shows that multiple Fe-centred clusters are linked by the FS connection with their nearest Fe atoms. In the cell, 63.64% of Fe atoms connect the neighbouring Fe atoms via FS with 3-atom sharing. These 3-atom face-sharing motifs in the liquid match very well to the structures of the crystalline $Al_{13}Fe_4$ phase. Monoclinic crystal with partial five-fold symmetry is an energetically and geometrically favourable arrangement of the Fe-centred SROs containing five-fold symmetry [279]. Hence crystal nucleation starts with the formation of MRO clusters with the similar structures to the subsequently nucleated crystal [7, 284]. In the cooling process, Fe-centred clusters form more MROs via FS, the same type of connection mode exists in the monoclinic long-range packing $Al_{13}Fe_4$ primary phase. Hence, we conclude that the Fe-centred clusters connected by FS are the nucleation precursors in the medium-atomic range scale in the 3 alloy melts.

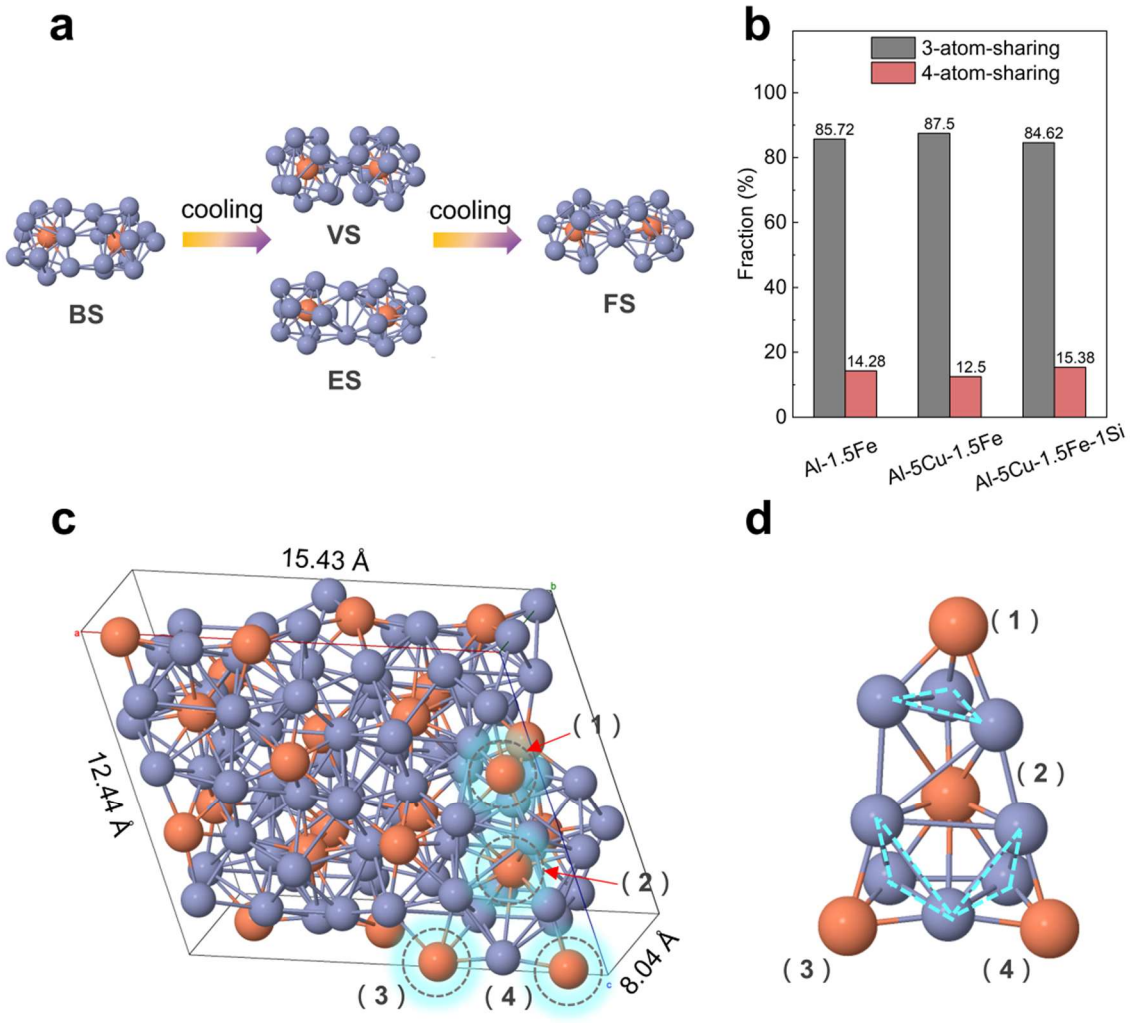

Fig. 5.14. (a) A schematic of Fe-centred MROs evolution pathway during cooling. (b) The fraction of 3-atom sharing and 4-atom sharing in the face-sharing modes for the 3 alloy melts prior to nucleation. (c) A unit cell of the monoclinic $Al_{13}Fe_4$ phase (C2/m space group), containing 78 Al atoms (blue) and 24 Fe atoms (orange) [280]. Four representative Fe atoms (marked by the black dash circles) are selected to illustrate one of the typical connection modes of the Fe-centred MROs. (d) An enlarged illustration of the selected Fe-centred cluster linked by the FS connection with the nearest Fe atoms. In the unit cell in (c), 63.64% of the Fe atoms connect their neighbour Fe atoms via FS.

5.5 Summary

In this chapter, the 3D atomic structures of 3 Fe-containing Al alloys in the liquid state have studied systematically in operando conditions, as well as their structural heterogeneities and evolutions versus temperature. The main new scientific findings are:

1. The EPSR method is a computationally efficient modelling tool for searching and reconstructing the 3D atomic structures of multiple-component alloy systems in the liquid state according to the X-ray total scattering data.
2. Atomic structural heterogeneities do exist in the 1st atomic shell and beyond, which are driven by the multiple atom interactions in the systems during the cooling process. The degree of structural heterogeneities are determined by the difference in atom radius, atomic bond length and the chemical preference between different atoms in the multiple-component systems.
3. At the short-range atom scale, the development of structural heterogeneities is mainly due to the existence and growth of the ICO-like and crystal-like structures. During cooling, the Fe atoms show a higher degree of crystallinity than the other atoms in the liquids. At the onset of crystal nucleation, the fraction of the Fe-centred ICO-like and crystal-like VPs reach 8-10%, while the others are in the range of 5.8-8.5%.
4. Using a pre-defined normalized bond orientational order parameter of 0.793, the pre-ordered atoms in the 3 alloy melts are quantified. They grow almost linearly with temperature from 750 to 690 ºC and then accelerate at the late stage of cooling, reaching 8%-9% at the onset of nucleation, indicating clearly the progressive nature prior to crystal nucleation.
5. The Fe-centred SROs tend to connect together via five different modes to form larger Fe-centred MROs by consuming mainly the bond-sharing Fe-clusters. Their percentages increase almost linearly with temperature, reaching approximately 18-20% in the 3 melts at the onset of nucleation. The Fe-centred MROs gradually approach to the structures of the $Al_{13}Fe_4$

primary phase (monoclinic structure) and are indeed the nucleation precursors for the $Al_{13}Fe_4$ phases.

Chapter 6 Progressive nucleation mechanism in solidification of multiple-component alloy

Results of the three Fe-containing Al alloys presented in chapter 5 indicated that the ICO-like and crystal-like structures co-exist and grow simultaneously as the melt is cooled. However, some researchers argued that higher degree of ICO-like structure would suppress crystal nucleation [56, 208, 216]. To deepen understanding of the role of the ICO-like and crystal-like structures on crystal nucleation, in this chapter, attention was paid to some of the key results from the Al-5Cu-1.5Fe-1Si case.

Fig. 6.1 shows emergence of small peaks at 628.4°C in the 1D pattern, corresponding to the Bragg spots in Fig. 5.1. The peaks were indexed as the $Al_{13}Fe_4$ phase, in good agreement with the results of computational phase calculation using the Scheil model [285]. As the temperature decreased to 614.1 °C, the peaks of α-Al and Al_8Fe_2Si (α-Fe) appeared. Such phase transformation sequence was reported [286], the primary $Al_{13}Fe_4$ phase in liquid is metastable in liquid, with further cooling, the diffused Si and Fe atoms can be incorporated in $Al_{13}Fe_4$, forming other Fe-rich intermetallic phases. The primary monoclinic $Al_{13}Fe_4$ thus can be viewed as a metastable phase.

Compared to stable phases like fcc/bcc with small unit cell, Fig. 6.2 show that the $Al_{13}Fe_4$ cell is much more complicated. The monoclinic unit cell consists of 102 atoms and has a quasicrystal-like structure with faulted periodicity, comprising columns with five-fold symmetry along the (0 1 0) direction (pentagonal columns) [279, 280]. Given that it in liquid is metastable, as cooling continued, more Si and Fe atoms diffused into the $Al_{13}Fe_4$, forming other Fe-rich intermetallic phases [286]. In most previous studies [48], crystallization was mainly interpreted as the conversion of five-fold symmetry into crystalline symmetry. However, for the crystalline phases that exhibit partial five-fold symmetry (e.g., crystal approximants, C14 Laves phase, icosahedral quasicrystal, monoclinic $Al_{13}Fe_4$), and their nucleation pathway are still not fully understood [58]. To reveal the nucleation pathway, more systematic Voronoi tessellation analysis for each element in the liquid was made.

In addition, the BOO analysis (both $\widehat{W}_6$ and (Q_4,Q_6)) for the Fe atoms in liquid and solid state are compared.

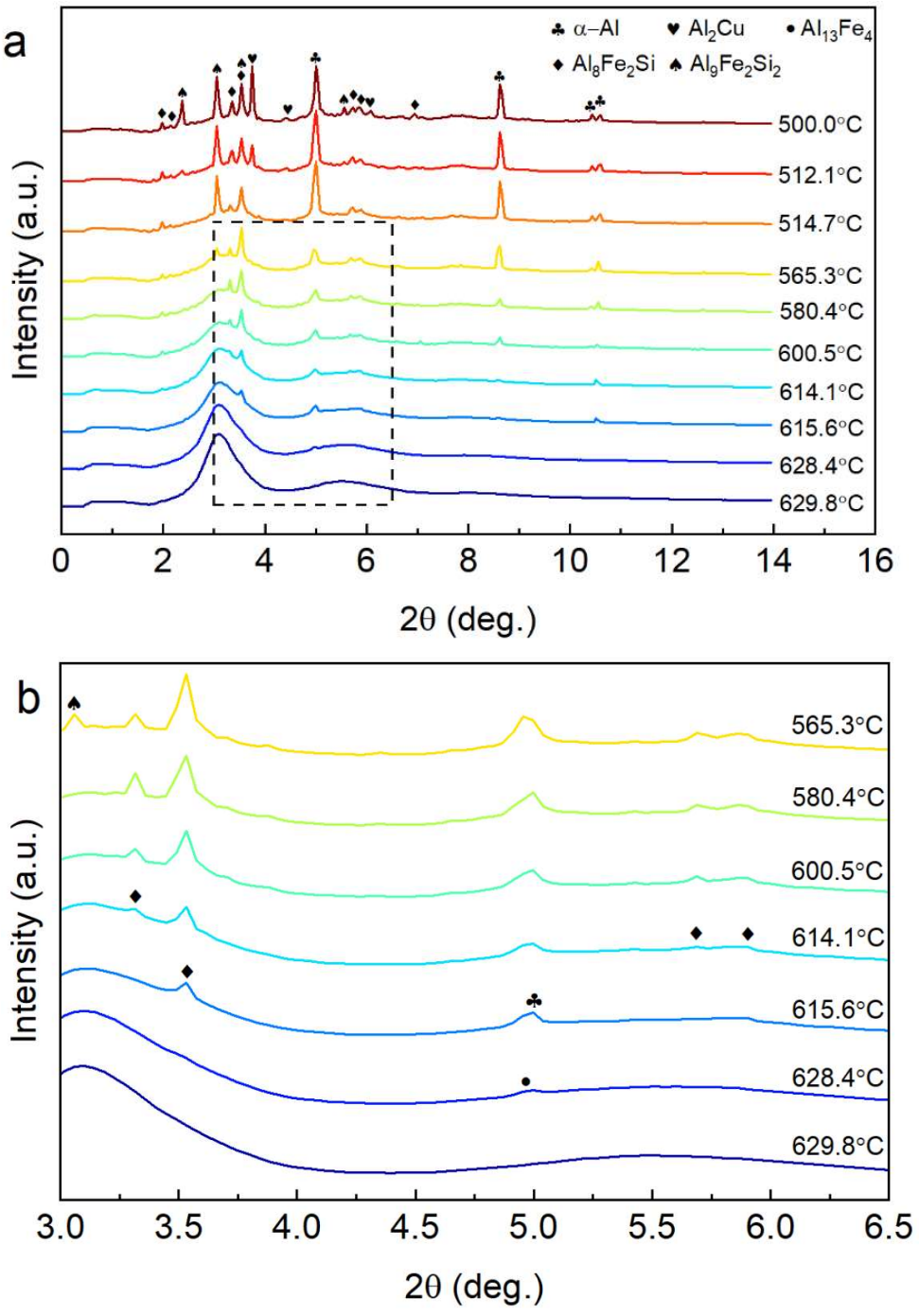

Fig. 6.1. (a) The 1D X-ray scattering intensity (converted from the 2D patterns) at the selected temperatures, (b) the enlarged profile of the boxed region in (a).

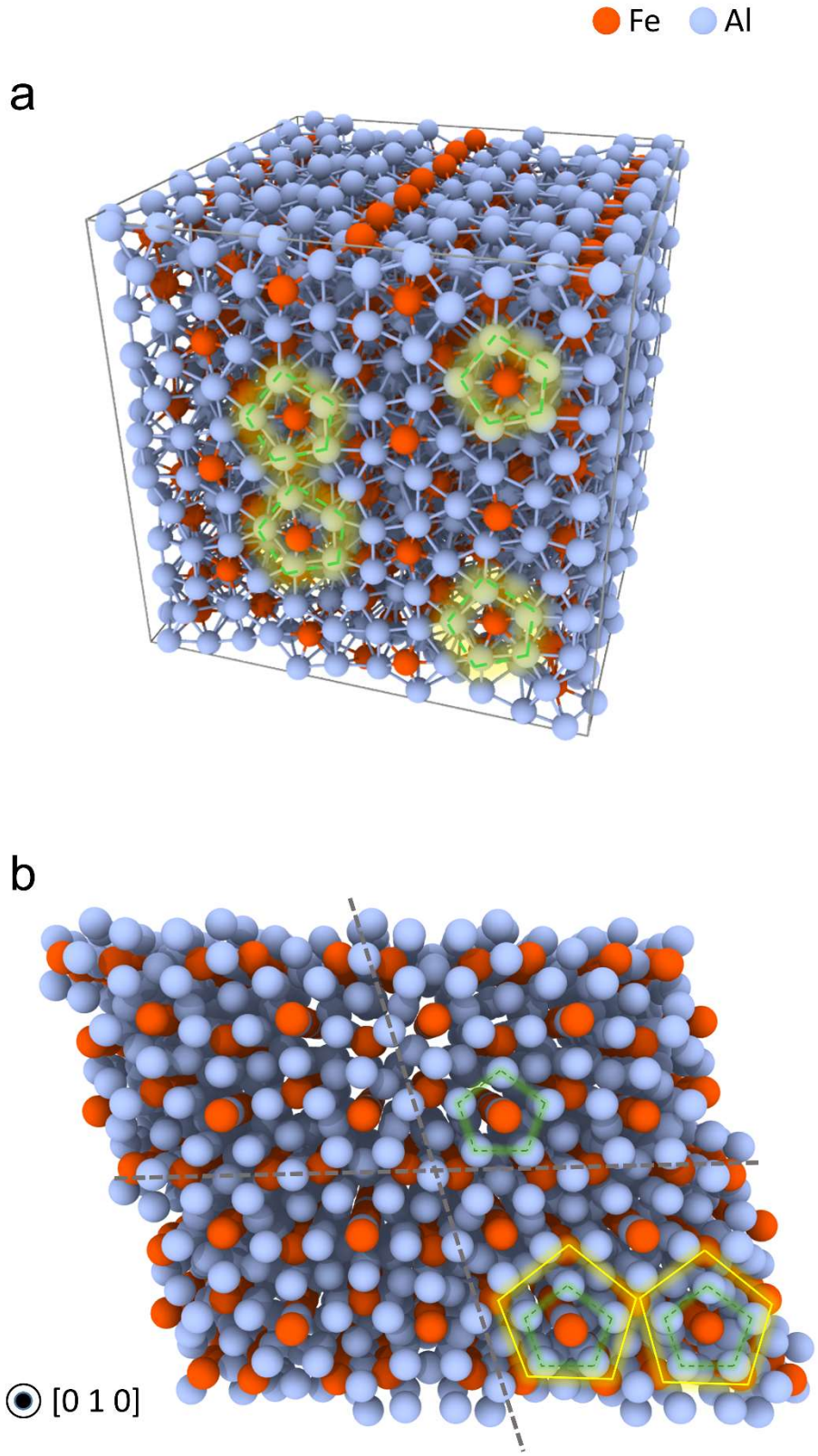

Fig. 6.2. (a) An $Al_{13}Fe_4$ crystal structure containing 2499 atoms in total, and (b) a big crystal cell made of 4 unit cells of monoclinic $Al_{13}Fe_4$ phase [287], and the structure is composed of atom clusters forming Fe-centred five-fold symmetry in SRO and MRO scale when it is viewed along the [0 1 0] direction.

Fig. 6.3 illustrates the fraction distributions of the ten major Voronoi polyhedron (VPs, the counting threshold is > 0.2). As shown in all insets in Fig. 6.3, the fraction of the ICO-like SROs (i.e., the red curve) and that of the crystal-like SROs (the blue curve) increase gradually as the temperature decreases from 750 ºC to 630 ºC. Such trends indicate that when the melt was cooled further, the degree of structure heterogeneities in the liquid increased, coinciding with the changes in the first peaks of the partial PDFs, i.e., becoming sharper and higher (Fig. 5.6).

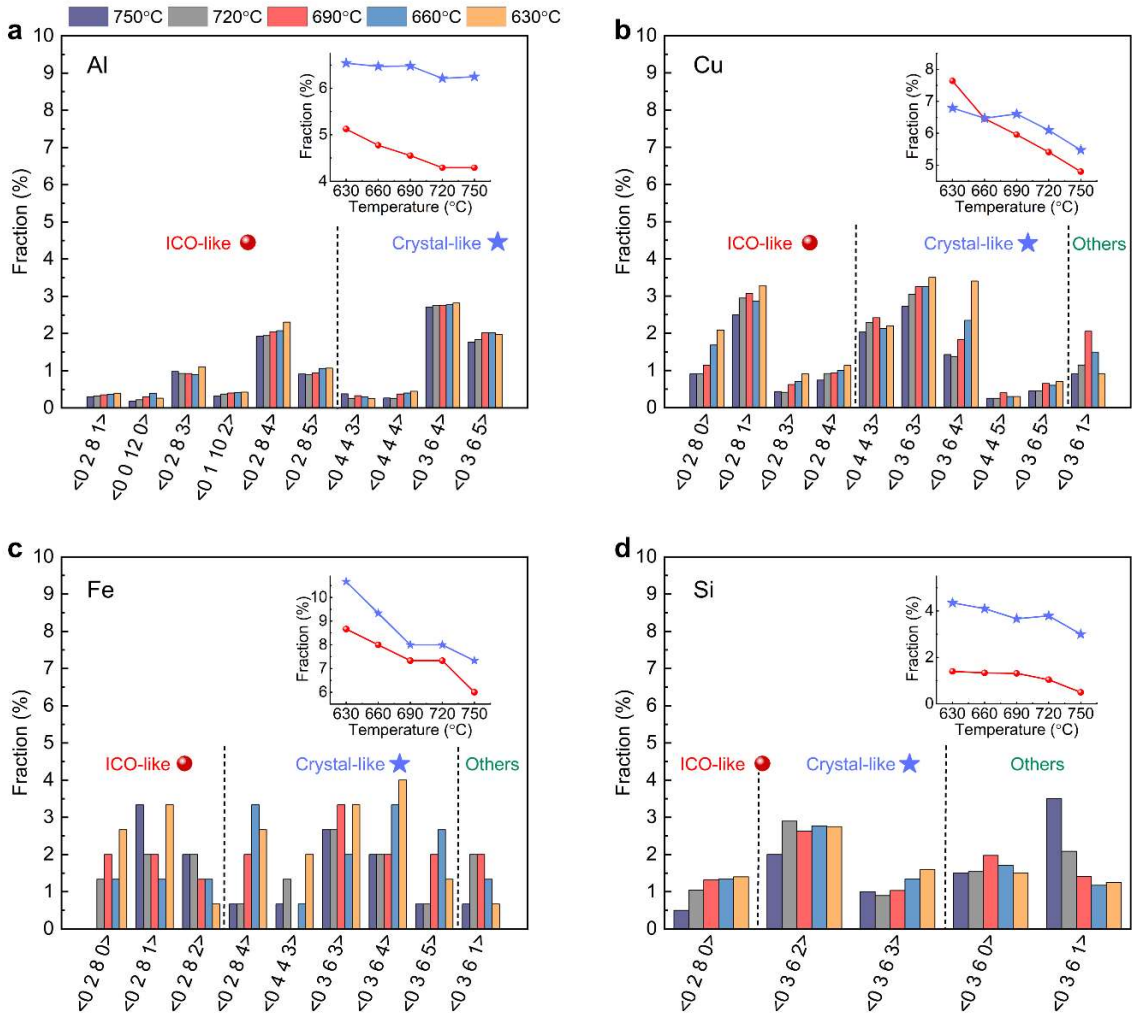

Fig. 6.3. Distribution of the leading population of Voronoi polyhedron in the liquid Al-5Cu-1.5Fe-Si alloy: (a) Al-, (b) Cu-, (c) Fe- and (d) Si-centred polydera. For the Al, Cu and Fe cases, the top ten VPs are presented. However, for the Si case, only five VPs are above 0.2%. Interestingly, for the Al case, the top ten VPs consist of only ICO-like and crystal-like structures.

For Fe-centred VPs, the red curve and the blue curve show very similar trends of increasing versus temperature (i.e., similar slope for both lines) and reached the highest fractions for both curves at 630 ºC compared to the other three cases. Such a phenomenon demonstrates that the Fe-centred atomic clusters exhibited the highest degree of structural heterogeneities. In addition, the fraction of the crystal-like structure is always higher than the ICO-like SROs in the melt. This evidence pointed out that the structural heterogeneities were developed via the co-growth of ICO- and crystal-like SROs as explained in the two-order-parameter model [213].

The BOO evolution of Fe atoms in liquid Al-5Cu-1.5Fe-1Si during cooling is also presented here. The invariant $\widehat{W}_6$ of the dominant Fe-centred atomic clusters (see in Fig. 6.4a) in the melt at 630 ºC seems to have values in between those of icosahedron and fcc configurations, suggesting that most of the Fe-centred local atomic arrangements have an intermediated structure between icosahedron and fcc. The icosahedron degree for Fe atoms in solid $Al_{13}Fe_4$ is higher than that in liquid. During the cooling process, the icosahedron degree is enhanced, approaching that of solid $Al_{13}Fe_4$. In addition, the average (Q_4,Q_6) value of all Fe atoms in the liquid state is plotted in Fig. 6.4b. The (Q_4,Q_6) value of the Fe atoms approaches towards that of the $Al_{13}Fe_4$ crystalline phase. The monoclinic $Al_{13}Fe_4$ possess Fe-centred five-fold symmetry in SRO and MRO scale when it is viewed along the (0 1 0) direction (see in Fig. 6.3).

SROs with five-fold symmetry in liquid was often considered to act as nucleation barrier, but an exception for quasicrystal according to previous studies [58], it can also act as a template for icosahedron quasicrystals due to the smaller solid-liquid interfacial energy. The drastic growth of icosahedron symmetry will increase nucleation barrier for crystals with translational periodicity, while the co-growth of icosahedron symmetry and crystalline symmetry in our case result in a smaller difference in local structural ordering between crystal and liquid (configurations entropy difference), decreasing $Al_{13}Fe_4$-liquid interfacial energy. Unlike common nucleation pathway where five-sold symmetry clusters convert into crystalline clusters, our study here presents a special scenario where Al-Cu-Fe-Si melt firstly transfer into a quasicrystal-like, metastable monoclinic $Al_{13}Fe_4$ phase, which

owns higher five-fold and crystalline symmetry degree than the liquid. Upon cooling, the Fe-centred five-fold and crystalline symmetry both get enhanced in liquid, leading to smaller the $Al_{13}Fe_4$-liquid configuration entropy difference and interfacial free energy. Contrary to the common beliefs, it can be found that the drastic development of Fe-centred five-fold symmetry in liquid upon cooling might not suppress but facilitates the nucleation of primary phase. Our findings provide the unambiguous evidence that crystal nucleation in multicomponent alloys is a dynamic evolution process, shedding light on fundamental understanding of nucleation mechanism of a metastable crystalline phase containing five-fold symmetry in multi-component liquids.

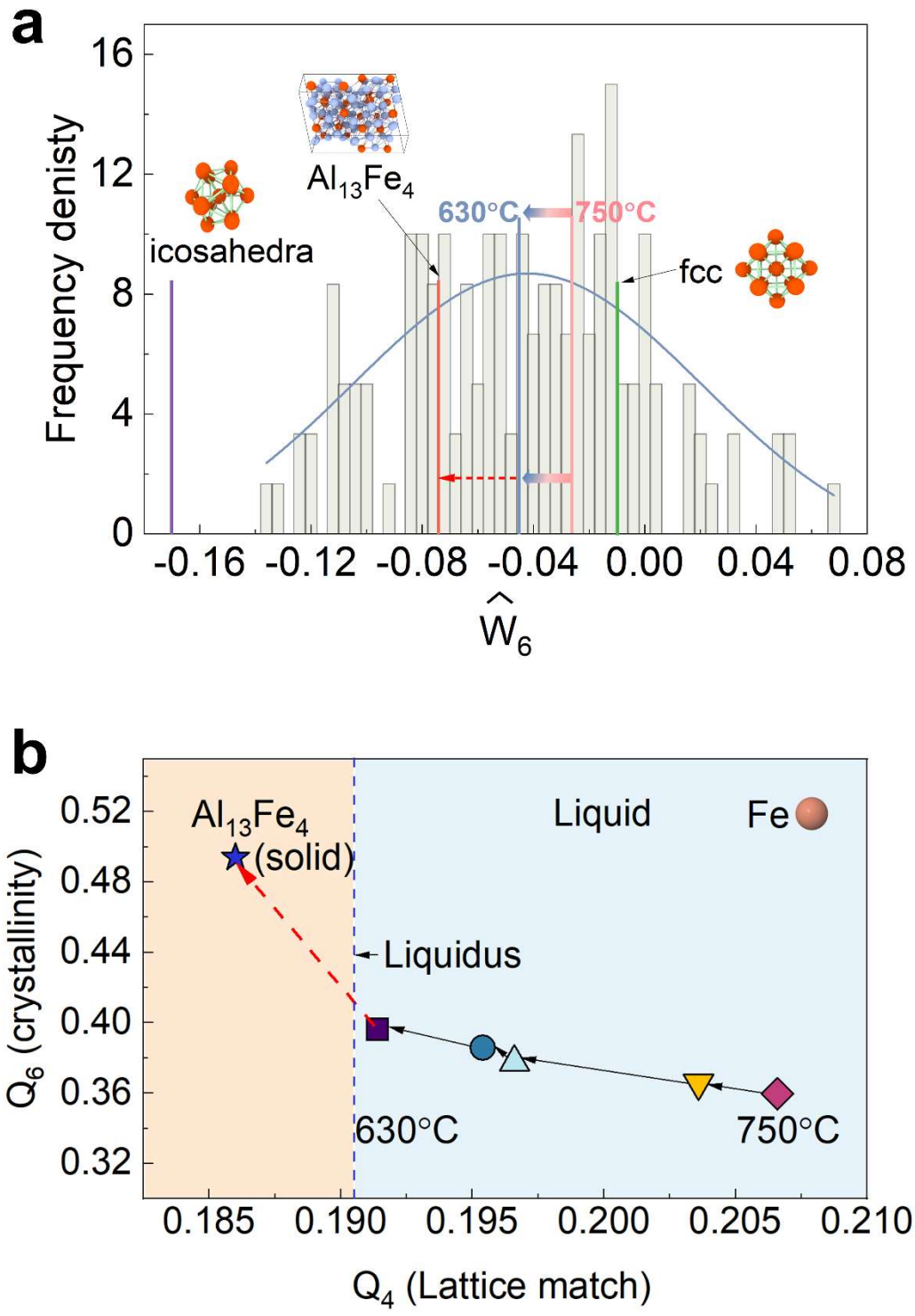

Fig. 6.4. (a) Histogram of the frequency density of the cubic invariant $\hat{W}_6$ monitoring the local geometry around each Fe atom in the melt at 630, together with the characteristic values for an ideal icosahedron (-0.169754), fcc cluster (-0.013161), Fe atoms in solid $Al_{13}Fe_4$, melt at 750 (-0.027746) and 630 ºC (-0.043246). (b) The averaged Q_4 and Q_6 value for all Fe atoms at different temperatures, indicating the trajectory towards the monoclinic $Al_{13}Fe_4$ phase.

Chapter 7 Conclusions and future works

7.1 Conclusions

Systematic experimental and modelling studies have been carried out to study the atomic structures of 4 Al alloys in the liquid state and their dynamic evolution with temperatures. The key conclusions of this thesis are:

(1) Upgrade of the counter-gravity casting apparatus was completed. Safer and semi-automatic operations have been achieved.

(2) Upgrade of the special furnaces for synchrotron X-ray total scattering and tomography studies was completed which were successfully used in a series of operando experiments in the university lab and the Diamond Light Source.

(3) Throughout this research, the EPSR is demonstrated to be one of the most computationally efficient methods for searching and reconstructing the 3D atomic structures of multiple-component alloys in the liquid state.

(4) For the Al-0.4Sc, in the liquid-solid coexisting region (657 °C), the Sc-centred polyhedrons form medium-range order via face-sharing, the same type of connection exists in the FCC long-range packing Al_3Sc primary phase. These polyhedrons exhibit partially icosahedral and partially face-centred-cubic symmetry. The medium-range ordered Sc-centred clusters with face-sharing are proved to be the “precursors” for the $L1_2$ fcc Al_3Sc primary phase in the liquid-solid coexisting region.

(5) For the three Fe-containing Al alloys, the atomic structural heterogeneities, consisting of the icosahedra-like and crystal-like structures, do exist in the short- and medium-range scale. As the temperature cools down, the factions of both structures increase approximately linearly. In the Fe-centred atom clusters, more and more large medium-range ordered clusters form due to the increasing number of face-sharing connections in the 3 alloy melts. Such face-sharing Fe-centred clusters are the nucleation precursors for the $Al_{13}Fe_4$ phase, indicating that crystal nucleation is a progressive process rather than a sudden and abrupt event.

(6) The monoclinic $Al_{13}Fe_4$ has higher degree of icosahedron and crystallinity than liquid. The enhancement of five-fold symmetry increases the local structure similarity between liquid and solid primary phase, as well as the development of crystal-like structure. The development of icosahedron degree result in smaller interfacial free energy between the $Al_{13}Fe_4$ and liquid. This finding should deepen the fundamental understanding of the nucleation mechanism of complex crystals with high five-fold symmetry in multi-component systems.

7.2 Future works

In this research, all total scattering experiments were conducted at DLS. Due to the limited X-ray fluxes, it typically takes 20 to 30s to complete the collection of one scattering pattern. As a result, part of the nucleation pathway (as shown in Fig. 6.4b) was missing. Therefore, higher photon flux that can acquire diffraction patterns 10 or 100 times faster is needed for obtaining the missing data at the critical temperature points. Moreover, 3DXRD (3-Dimensional X-ray Diffraction) the best technique for studying phase nucleation and evolution in true 3D space which can track the centre of mass of each crystal (see Fig. 7.1k) [288, 289]. The method is based on the use of high-energy X-rays from synchrotron sources and a 'tomographic' approach to diffraction, compared to the traditional total scattering techniques, such method requires sample rotation when collecting diffraction pattern. With 3DXRD the structure of the embedded grains within polycrystals or powders can be characterised non-destructively within millimetre to centimetre size specimens. The dynamics of the individual grains can be studied in the bulk sample. The patterns give direct information on both the liquid (Fig. 7.1a and e) and solid phases during the solidification process (Fig. 7.1d). We will use the PDF method to process the diffraction data for the sample in liquid region and 3DXRD method for the following crystallization process. More importantly, the 3D XRD can collect the pair distribution function (PDF) information for the remaining liquid after the primary intermetallic phase appear (Fig. 7.1b, c, f and g), which is essential to validate the simulation results of partially crystalline liquid metal.

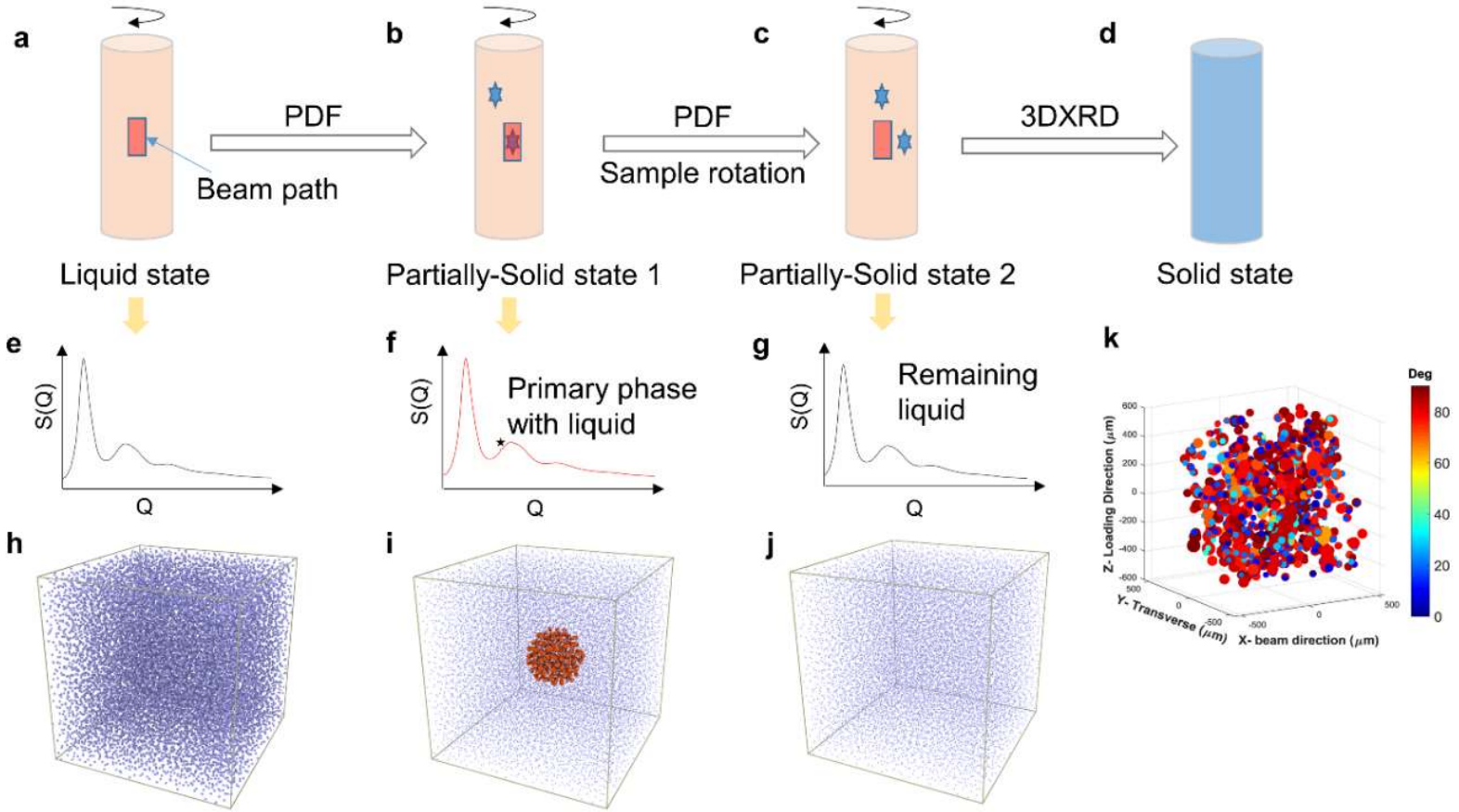

Fig. 7.1 (a-d) Sample in different states during the cooling process and the corresponding data analysis methods. (e-j) The scattering spectra of samples at different states and the expected simulation box. (k) A typical 3D view of measured grain map acquired 3DXRD technique [291].

For modelling multiple-components or dilute alloys, it is necessary to use a larger simulation box that can handle and process hundreds of thousands of atoms or millions of atoms. The latest EPSR package (26) can do simulation with 100,000 atoms. While the EPSR 25 used in this research can only handle 50,000 atoms. Recently, ISIS team has just made the Dissolve (a new code based on the EPSR) available to users. Dissolve employs a full classical force field and can accommodate multi-configuration simulations with millions of atoms. Dissolve [290] is designed to be flexible and extensible, allowing for the study of simple molecular liquids as well as complex and heterogeneous systems. It offers the potential to investigate partially crystalline liquid metals, as depicted in Fig. 7.1f and i.

In the liquid-to-solid phase transformation of metallic alloys, nucleation typically occurs in the atomic length scale and in ps to ns time scale. Although atomistic modelling can be used routinely to simulate phase nucleation events, to capture in real-time the nucleation dynamics by experiments are extremely difficult. In this aspect, the exceptionally high brightness of the X-ray free electron Laser is the ideal source for time-resolved experiments with time resolution of tens of fs. Using XFEL, it is possible image phase nucleation from fs onwards.

References

1. Kelton, K. F.; Greer, A. L., Nucleation in condensed matter: applications in materials and biology. Elsevier: 2010.
2. Kawasaki, T.; Tanaka, H., Formation of a crystal nucleus from liquid. Proceedings of the National Academy of Sciences **2010,** 107 (32), 14036-14041.
3. Myerson, A. S.; Trout, B. L., Nucleation from solution. Science **2013,** 341 (6148), 855-856.
4. Debenedetti, P., Concepts and principles. Princeton University Press, Princeton: 1996.
5. Onuki, A., Phase transition dynamics. Cambridge University Press: 2002.
6. Binder, K., Theory of first-order phase transitions. Reports on progress in physics **1987,** 50 (7), 783.
7. Leocmach, M.; Tanaka, H., Roles of icosahedral and crystal-like order in the hard spheres glass transition. Nature communications **2012,** 3 (1), 1-8.
8. Weeks, E. R.; Weitz, D., Properties of cage rearrangements observed near the colloidal glass transition. Physical review letters **2002,** 89 (9), 095704.
9. Conrad, J.; Starr, F. W.; Weitz, D., Weak correlations between local density and dynamics near the glass transition. The Journal of Physical Chemistry B **2005,** 109 (45), 21235-21240.
10. Patrick Royall, C.; Williams, S. R.; Ohtsuka, T.; Tanaka, H., Direct observation of a local structural mechanism for dynamic arrest. Nature materials **2008,** 7 (7), 556-561.
11. Kawasaki, T.; Tanaka, H., Structural origin of dynamic heterogeneity in three-dimensional colloidal glass formers and its link to crystal nucleation. Journal of Physics: Condensed Matter **2010,** 22 (23), 232102.
12. Widmer-Cooper, A.; Harrowell, P., Predicting the long-time dynamic heterogeneity in a supercooled liquid on the basis of short-time heterogeneities. Physical review letters **2006,** 96 (18), 185701.
13. Brito, C.; Wyart, M., Geometric interpretation of previtrification in hard sphere liquids. The Journal of chemical physics **2009,** 131 (2), 149.
14. Speck, T.; Malins, A.; Royall, C. P., First-order phase transition in a model glass former: Coupling of local structure and dynamics. Physical review letters **2012,** 109 (19), 195703.
15. Taffs, J.; Patrick Royall, C., The role of fivefold symmetry in suppressing crystallization. Nature communications **2016,** 7 (1), 1-7.
16. Cheng, Y.; Ma, E., Atomic-level structure and structure–property relationship in metallic glasses. Progress in materials science **2011,** 56 (4), 379-473.
17. Tan, P.; Xu, N.; Xu, L., Visualizing kinetic pathways of homogeneous nucleation in colloidal crystallization. Nature Physics **2014,** 10 (1), 73-79.
18. Wolde, P. R. t.; Frenkel, D., Enhancement of protein crystal nucleation by critical density fluctuations. Science **1997,** 277 (5334), 1975-1978.
19. Lechner, W.; Dellago, C.; Bolhuis, P. G., Role of the prestructured surface cloud in crystal nucleation. Physical review letters **2011,** 106 (8), 085701.
20. Savage, J.; Dinsmore, A., Experimental evidence for two-step nucleation in colloidal crystallization. Physical review letters **2009,** 102 (19), 198302.

21. Zhang, Q.; Wang, J.; Tang, S.; Wang, Y.; Li, J.; Zhou, W.; Wang, Z., Molecular dynamics investigation of the local structure in iron melts and its role in crystal nucleation during rapid solidification. Physical Chemistry Chemical Physics **2019,** 21 (8), 4122-4135.
22. Díaz Leines, G.; Drautz, R.; Rogal, J., Atomistic insight into the non-classical nucleation mechanism during solidification in Ni. The Journal of chemical physics **2017,** 146 (15), 154702.
23. Leines, G. D.; Rogal, J., Template-Induced Precursor Formation in Heterogeneous Nucleation: Controlling Polymorph Selection and Nucleation Efficiency. Physical Review Letters **2022,** 128 (16), 166001.
24. Leines, G. D.; Michaelides, A.; Rogal, J., Interplay of structural and dynamical heterogeneity in the nucleation mechanism in nickel. Faraday Discussions **2022**.
25. Hu, Y.-C.; Tanaka, H., Physical origin of glass formation from multicomponent systems. Science advances **2020,** 6 (50), eabd2928.
26. Hu, Y.-C.; Tanaka, H., Revealing the role of liquid preordering in crystallisation of supercooled liquids. Nature communications **2022,** 13 (1), 1-12.
27. Simonet, V.; Hippert, F.; Klein, H.; Audier, M.; Bellissent, R.; Fischer, H.; Murani, A.; Boursier, D., Local order and magnetism in liquid Al-Pd-Mn alloys. Physical Review B **1998,** 58 (10), 6273.
28. Simonet, V.; Hippert, F.; Audier, M.; Bellissent, R., Local order in liquids forming quasicrystals and approximant phases. Physical Review B **2001,** 65 (2), 024203.
29. Holland-Moritz, D.; Schenk, T.; Simonet, V.; Bellissent, R.; Convert, P.; Hansen, T.; Herlach, D., Short-range order in undercooled metallic liquids. Materials Science and Engineering: A **2004,** 375, 98-103.
30. Fang, X.; Wang, C.; Yao, Y.; Ding, Z.; Ho, K., Competition between fcc and icosahedral short-range orders in pure and samarium-doped liquid aluminum from first principles. Physical Review B **2011,** 83 (22), 224203.
31. Choudhuri, D.; Majumdar, B. S., Structural changes during crystallization and vitrification of dilute FCC-based binary alloys. Materialia **2020,** 12, 100816.
32. Yang, Y.; Zhou, J.; Zhu, F.; Yuan, Y.; Chang, D. J.; Kim, D. S.; Pham, M.; Rana, A.; Tian, X.; Yao, Y., Determining the three-dimensional atomic structure of an amorphous solid. Nature **2021,** 592 (7852), 60-64.
33. Jingyu, Q.; Xiufang, B.; Sliusarenko, S.; Weimin, W., Pre-peak in the structure factor of liquid Al-Fe alloy. Journal of Physics: Condensed Matter **1998,** 10 (6), 1211.
34. Das, S.; Horbach, J.; Koza, M.; Mavila Chatoth, S.; Meyer, A., Influence of chemical short-range order on atomic diffusion in Al–Ni melts. Applied Physics Letters **2005,** 86 (1), 011918.
35. Roik, O.; Samsonnikov, O.; Kazimirov, V.; Sokolskii, V.; Galushko, S., Medium-range order in Al-based liquid binary alloys. Journal of Molecular Liquids **2010,** 151 (1), 42-49.
36. Wang, P.; Bu, Y.; Liu, J.; Li, Q.; Wang, H.; Yang, W., Atomic deformation mechanism and interface toughening in metastable high entropy alloy. Materials Today **2020,** 37, 64-73.
37. Guan, R.-G.; Tie, D., A review on grain refinement of aluminum alloys: progresses, challenges and prospects. Acta Metallurgica Sinica (English Letters) **2017,** 30, 409-432.

38. Norman, A.; Prangnell, P.; McEwen, R., The solidification behaviour of dilute aluminium–scandium alloys. Acta materialia **1998,** 46 (16), 5715-5732.
39. Hyde, K.; Norman, A.; Prangnell, P., The effect of cooling rate on the morphology of primary Al3Sc intermetallic particles in Al–Sc alloys. Acta Materialia **2001,** 49 (8), 1327-1337.
40. Costa, S.; Puga, H.; Barbosa, J.; Pinto, A., The effect of Sc additions on the microstructure and age hardening behaviour of as cast Al–Sc alloys. Materials & Design **2012,** 42, 347-352.
41. Zakharov, V., Effect of scandium on the structure and properties of aluminum alloys. Metal science and heat treatment **2003,** 45 (7-8), 246-253.
42. Zhao, Y.; Zhang, W.; Koe, B.; Du, W.; Wang, M.; Wang, W.; Boller, E.; Rack, A.; Sun, Z.; Shu, D., Multiscale characterization of the nucleation and 3D structure of Al3Sc phases using electron microscopy and synchrotron X-ray tomography. Materials Characterization **2020,** 164, 110353.
43. Zhao, Y.; Song, D.; Wang, H.; Li, X.; Chen, L.; Sun, Z.; Wang, Z.; Zhai, T.; Fu, Y.; Wang, Y., Revealing the nucleation and growth mechanisms of Fe-rich phases in Al–Cu–Fe (-Si) alloys under the influence of Al–Ti–B. Intermetallics **2022,** 146, 107584.
44. Li, Z.; Qin, L.; Guo, B.; Yuan, J.; Zhang, Z.; Li, W.; Mi, J., Characterization of the Convoluted 3D Intermetallic Phases in a Recycled Al Alloy by Synchrotron X-ray Tomography and Machine Learning. Acta Metallurgica Sinica (English Letters) **2022,** 35 (1), 115-123.
45. Shabestari, S., The effect of iron and manganese on the formation of intermetallic compounds in aluminum–silicon alloys. Materials Science and Engineering: A **2004,** 383 (2), 289-298.
46. Malakhov, D. V.; Panahi, D.; Gallerneault, M., On the formation of intermetallics in rapidly solidifying Al–Fe–Si alloys. Calphad **2010,** 34 (2), 159-166.
47. Il'Inskii, A.; Slyusarenko, S.; Slukhovskii, O.; Kaban, I.; Hoyer, W., Structure of liquid Fe–Al alloys. Materials Science and Engineering: A **2002,** 325 (1-2), 98-102.
48. Golde, S.; Palberg, T.; Schöpe, H. J., Correlation between dynamical and structural heterogeneities in colloidal hard-sphere suspensions. Nature Physics **2016,** 12 (7), 712-717.
49. Debenedetti, P. G.; Stillinger, F. H., Supercooled liquids and the glass transition. Nature **2001,** 410 (6825), 259-267.
50. Arav, A.; Natan, Y., The near future of vitrification of oocytes and embryos: looking into past experience and planning into the future. Transfusion Medicine and Hemotherapy **2019,** 46 (3), 182-187.
51. Luyet, B. J.; Gehenio, M. P., Life and death at low temperatures. **1940**.
52. Mousson, A., Einige Thatsachen betreffend das Schmelzen und Gefrieren des Wassers. Annalen der Physik **1858,** 181 (10), 161-174.
53. Luyet, B. J.; Hodapp, E. L., Revival of frog's spermatozoa vitrified in liquid air. Proceedings of the Society for Experimental Biology and Medicine **1938,** 39 (3), 433-434.
54. Russo, J.; Romano, F.; Tanaka, H., Glass forming ability in systems with competing orderings. Physical Review X **2018,** 8 (2), 021040.
55. Turnbull, D., Formation of crystal nuclei in liquid metals. Journal of Applied Physics **1950,** 21 (10), 1022-1028.

56. Frank, F. C., Supercooling of liquids. Proceedings of the Royal Society of London. Series A. Mathematical Physical Sciences **1952,** 215 (1120), 43-46.
57. Rappaz, M.; Jarry, P.; Kurtuldu, G.; Zollinger, J., Solidification of metallic alloys: Does the structure of the liquid matter? Metallurgical and Materials Transactions A **2020,** 51, 2651-2664.
58. Kelton, K.; Lee, G.; Gangopadhyay, A. K.; Hyers, R.; Rathz, T.; Rogers, J.; Robinson, M.; Robinson, D., First x-ray scattering studies on electrostatically levitated metallic liquids: Demonstrated influence of local icosahedral order on the nucleation barrier. Physical Review Letters **2003,** 90 (19), 195504.
59. Reichert, H.; Klein, O.; Dosch, H.; Denk, M.; Honkimäki, V.; Lippmann, T.; Reiter, G., Observation of five-fold local symmetry in liquid lead. Nature **2000,** 408 (6814), 839-841.
60. Schenk, T.; Holland-Moritz, D.; Simonet, V.; Bellissent, R.; Herlach, D., Icosahedral short-range order in deeply undercooled metallic melts. Physical review letters **2002,** 89 (7), 075507.
61. Hirata, A.; Kang, L.; Fujita, T.; Klumov, B.; Matsue, K.; Kotani, M.; Yavari, A.; Chen, M., Geometric frustration of icosahedron in metallic glasses. Science **2013,** 341 (6144), 376-379.
62. Yang, Y.; Zhou, J.; Zhu, F.; Yuan, Y.; Chang, D.; Kim, D. S.; Pham, M.; Rana, A.; Tian, X.; Yao, Y., Determining the three-dimensional atomic structure of a metallic glass. arXiv preprint arXiv:2004.02266 **2020**.
63. Giles Jr, N. H., Comparative studies of the cytogenetical effects of neutrons and X-rays. Genetics **1943,** 28 (5), 398.
64. Guo, W.; Dmowski, W.; Noh, J.-Y.; Rack, P.; Liaw, P. K.; Egami, T., Local atomic structure of a high-entropy alloy: an X-ray and neutron scattering study. Metallurgical and Materials Transactions A **2013,** 44, 1994-1997.
65. Cockayne, D. J., The study of nanovolumes of amorphous materials using electron scattering. Annu. Rev. Mater. Res. **2007,** 37, 159-187.
66. Junior, J. B. S.; Schleder, G. R.; Bettini, J.; Nogueira, I. C.; Fazzio, A.; Leite, E. R., Pair distribution function obtained from electron diffraction: an advanced real-space structural characterization tool. Matter **2021,** 4 (2), 441-460.
67. Massiot, D.; Messinger, R. J.; Cadars, S.; Deschamps, M.; Montouillout, V.; Pellerin, N.; Veron, E.; Allix, M.; Florian, P.; Fayon, F., Topological, geometric, and chemical order in materials: insights from solid-state NMR. Accounts of Chemical Research **2013,** 46 (9), 1975-1984.
68. Vaccari, M.; Aquilanti, G.; Pascarelli, S.; Mathon, O., A new EXAFS investigation of local structural changes in amorphous and crystalline GeO2 at high pressure. Journal of Physics: Condensed Matter **2009,** 21 (14), 145403.
69. Holst, J. R.; Gillan, E. G., From triazines to heptazines: deciphering the local structure of amorphous nitrogen-rich carbon nitride materials. Journal of the American Chemical Society **2008,** 130 (23), 7373-7379.
70. Watanabe, I.; Noguchi, S.; Shimizu, T., Study on local structure in amorphous Sb S films by Raman scattering. Journal of Non-Crystalline Solids **1983,** 58 (1), 35-40.
71. Brodsky, M.; Cardona, M., Local order as determined by electronic and vibrational spectroscopy: amorphous semiconductors. Journal of non-crystalline solids **1978,** 31 (1-2), 81-108.
72. Müller-Warmuth, W.; Eckert, H., Nuclear magnetic resonance and Mössbauer spectroscopy of glasses. Physics Reports **1982,** 88 (2), 91-149.

73. Cliffe, M. J.; Dove, M. T.; Drabold, D.; Goodwin, A. L., Structure determination of disordered materials from diffraction data. Physical review letters **2010,** 104 (12), 125501.
74. McGreevy, R.; Pusztai, L., Reverse Monte Carlo simulation: a new technique for the determination of disordered structures. Molecular simulation **1988,** 1 (6), 359-367.
75. Soper, A., Empirical potential Monte Carlo simulation of fluid structure. Chemical Physics **1996,** 202 (2-3), 295-306.
76. Shi, C.; Alderman, O. L.; Berman, D.; Du, J.; Neuefeind, J.; Tamalonis, A.; Weber, J. R.; You, J.; Benmore, C. J., The structure of amorphous and deeply supercooled liquid alumina. Frontiers in Materials **2019,** 6, 38.
77. Skinner, L. B.; Barnes, A. C.; Salmon, P. S.; Hennet, L.; Fischer, H. E.; Benmore, C. J.; Kohara, S.; Weber, J. R.; Bytchkov, A.; Wilding, M. C., Joint diffraction and modeling approach to the structure of liquid alumina. Physical Review B **2013,** 87 (2), 024201.
78. Proffen, T.; Neder, R., DISCUS, a program for diffuse scattering and defect structure simulations–update. Journal of Applied Crystallography **1999,** 32 (4), 838-839.
79. Juhás, P.; Granlund, L.; Duxbury, P.; Punch, W.; Billinge, S., The Liga algorithm for ab initio determination of nanostructure. Acta Crystallographica Section A: Foundations of Crystallography **2008,** 64 (6), 631-640.
80. Juhás, P.; Cherba, D.; Duxbury, P.; Punch, W.; Billinge, S., Ab initio determination of solid-state nanostructure. Nature **2006,** 440 (7084), 655-658.
81. Michel, F. M.; Ehm, L.; Antao, S. M.; Lee, P. L.; Chupas, P. J.; Liu, G.; Strongin, D. R.; Schoonen, M. A.; Phillips, B. L.; Parise, J. B., The structure of ferrihydrite, a nanocrystalline material. Science **2007,** 316 (5832), 1726-1729.
82. Dinnebier, R. E.; Billinge, S. J., Powder diffraction: theory and practice. Royal society of chemistry: 2008.
83. Masadeh, A. S., Total scattering atomic pair distribution function: new methodology for nanostructure determination. Journal of Experimental Nanoscience **2016,** 11 (12), 951-974.
84. Suslick, K. S., Encyclopedia of physical science and technology. Sonoluminescence and sonochemistry, 3rd edn. Elsevier Science Ltd, Massachusetts **2001**, 1-20.
85. Egami, T.; Billinge, S. J., Underneath the Bragg peaks: structural analysis of complex materials. Elsevier: 2003.
86. Soper, A. K.; Barney, E. R., Extracting the pair distribution function from white-beam X-ray total scattering data. Journal of Applied Crystallography **2011,** 44 (4), 714-726.
87. Billinge, S. J. In Pair distribution function technique: principles and methods, Uniting Electron Crystallography and Powder Diffraction, Springer: 2012; pp 183-193.
88. Liao, Y., Practical electron microscopy and database. An Online Book **2006**.
89. Egami, T.; Billinge, S. J., Underneath the Bragg peaks: structural analysis of complex materials. Newnes: 2012.
90. Billinge, S. J., The rise of the X-ray atomic pair distribution function method: a series of fortunate events. Philosophical Transactions of the Royal Society A **2019,** 377 (2147), 20180413.

91. Keen, D. A., A comparison of various commonly used correlation functions for describing total scattering. Journal of Applied Crystallography **2001,** 34 (2), 172-177.
92. Keen, D. A., Total scattering and the pair distribution function in crystallography. Crystallography Reviews **2020,** 26 (3), 143-201.
93. Sears, V. F., Neutron scattering lengths and cross sections. Neutron news **1992,** 3 (3), 26-37.
94. Cuello, G. J., Structure factor determination of amorphous materials by neutron diffraction. Journal of Physics: Condensed Matter **2008,** 20 (24), 244109.
95. Cristiglio, V.; Cuello, G. J.; Piarristeguy, A. A.; Pradel, A., The coordination number calculation from total structure factor measurements. Journal of non-crystalline solids **2009,** 355 (37-42), 1811-1814.
96. Finney, J. L., Bernal's road to random packing and the structure of liquids. Philosophical Magazine **2013,** 93 (31-33), 3940-3969.
97. Meyers, H.; Myers, H., Introductory solid state physics. CRC press: 1997.
98. Ingham, B., X-ray scattering characterisation of nanoparticles. Crystallography Reviews **2015,** 21 (4), 229-303.
99. Billinge, S. J.; Kanatzidis, M. G., Beyond crystallography: the study of disorder, nanocrystallinity and crystallographically challenged materials with pair distribution functions. Chemical communications **2004,** (7), 749-760.
100. Peterson, P. F.; Božin, E. S.; Proffen, T.; Billinge, S. J., Improved measures of quality for the atomic pair distribution function. Journal of applied crystallography **2003,** 36 (1), 53-64.
101. Proffen, T.; Kim, H., Advances in total scattering analysis. Journal of Materials Chemistry **2009,** 19 (29), 5078-5088.
102. Kaszkur, Z., Convolutional approach to the normalization of intensity scattered by polycrystalline substances. Journal of applied crystallography **1990,** 23 (3), 180-185.
103. Haverkamp, R. G.; Wallwork, K. S., X-ray pair distribution function analysis of nanostructured materials using a Mythen detector. Journal of synchrotron radiation **2009,** 16 (6), 849-856.
104. Kofalt, D.; Nanao, S.; Egami, T.; Wong, K.; Poon, S., Differential anomalous-X-ray-scattering study of icosahedral and amorphous Pd 58.8 U 20.6 Si 20.6. Physical review letters **1986,** 57 (1), 114.
105. Kofalt, D.; Morrison, I.; Egami, T.; Preische, S.; Poon, S.; Steinhardt, P., Quasicrystallinity of icosahedral Pd 58.8 U 20.6 Si 20.6. Physical Review B **1987,** 35 (9), 4489.
106. Nanao, S.; Dmowski, W.; Egami, T.; Richardson Jr, J.; Jorgensen, J., Structure of Al-Mn-Cr-Si quasicrystals studied by pulsed neutron scattering. Physical Review B **1987,** 35 (2), 435.
107. McGreevy, R. L., Reverse monte carlo modelling. Journal of Physics: Condensed Matter **2001,** 13 (46), R877.
108. Proffen, T.; Billinge, S., PDFFIT, a program for full profile structural refinement of the atomic pair distribution function. Journal of Applied Crystallography **1999,** 32 (3), 572-575.
109. Sokolov, A.; Kisliuk, A.; Soltwisch, M.; Quitmann, D., Medium-range order in glasses: Comparison of Raman and diffraction measurements. Physical Review Letters **1992,** 69 (10), 1540.

110. Pan, S.; Qin, J.; Wang, W.; Gu, T., Origin of splitting of the second peak in the pair-distribution function for metallic glasses. Physical Review B **2011,** 84 (9), 092201.
111. Lou, H.; Wang, X.; Cao, Q.; Zhang, D.; Zhang, J.; Hu, T.; Mao, H.-k.; Jiang, J.-Z. J. P. o. t. N. A. o. S., Negative expansions of interatomic distances in metallic melts. **2013,** 110 (25), 10068-10072.
112. Tanaka, H.; Tong, H.; Shi, R.; Russo, J., Revealing key structural features hidden in liquids and glasses. Nature Reviews Physics **2019,** 1 (5), 333-348.
113. Farrow, C.; Juhas, P.; Liu, J.; Bryndin, D.; Božin, E.; Bloch, J.; Proffen, T.; Billinge, S., PDFfit2 and PDFgui: computer programs for studying nanostructure in crystals. Journal of Physics: Condensed Matter **2007,** 19 (33), 335219.
114. Yang, X.; Juhas, P.; Farrow, C. L.; Billinge, S. J., xPDFsuite: an end-to-end software solution for high throughput pair distribution function transformation, visualization and analysis. arXiv preprint arXiv:1402.3163 **2014**.
115. Rantanen, J.; Majda, D.; Riikonen, J.; Lehto, V.-P., The atomic local ordering of SBA-15 studied with pair distribution function analysis, and its relationship to porous structure and thermal stability. Acta Materialia **2019,** 175, 341-347.
116. Owen, L.; Stone, H.; Playford, H., The assessment of local lattice strains in alloys using total scattering. Acta Materialia **2019,** 170, 38-49.
117. Canu, G.; Confalonieri, G.; Deluca, M.; Curecheriu, L.; Buscaglia, M. T.; Asandulesa, M.; Horchidan, N.; Dapiaggi, M.; Mitoseriu, L.; Buscaglia, V., Structure-property correlations and origin of relaxor behaviour in BaCexTi1-xO3. Acta Materialia **2018,** 152, 258-268.
118. Metropolis, N.; Rosenbluth, A. W.; Rosenbluth, M. N.; Teller, A. H.; Teller, E., Equation of state calculations by fast computing machines. The journal of chemical physics **1953,** 21 (6), 1087-1092.
119. Tucker, M. G.; Keen, D. A.; Dove, M. T.; Goodwin, A. L.; Hui, Q., RMCProfile: reverse Monte Carlo for polycrystalline materials. Journal of Physics: Condensed Matter **2007,** 19 (33), 335218.
120. Soper, A., Tests of the empirical potential structure refinement method and a new method of application to neutron diffraction data on water. Molecular Physics **2001,** 99 (17), 1503-1516.
121. Gereben, O.; Jóvári, P.; Temleitner, L.; Pusztai, L., A new version of the RMC++ Reverse Monte Carlo programme, aimed at investigating the structure of covalent glasses. Journal of Optoelectronics and Advanced Materials **2007,** 9 (10), 3021.
122. Gereben, O.; Pusztai, L., RMC_POT: a computer code for reverse Monte Carlo modeling the structure of disordered systems containing molecules of arbitrary complexity. Journal of computational chemistry **2012,** 33 (29), 2285-2291.
123. Sillrén, P.; Swenson, J.; Mattsson, J.; Bowron, D.; Matic, A., The temperature dependent structure of liquid 1-propanol as studied by neutron diffraction and EPSR simulations. The Journal of chemical physics **2013,** 138 (21), 214501.
124. Bowron, D. T.; Finney, J. L.; Soper, A. K., The structure of liquid tetrahydrofuran. Journal of the American Chemical Society **2006,** 128 (15), 5119-5126.

125. Hardacre, C.; McMath, S. J.; Nieuwenhuyzen, M.; Bowron, D. T.; Soper, A. K., Liquid structure of 1, 3-dimethylimidazolium salts. Journal of Physics: Condensed Matter **2002,** 15 (1), S159.
126. Weigel, C.; Cormier, L.; Calas, G.; Galoisy, L.; Bowron, D. T., Nature and distribution of iron sites in a sodium silicate glass investigated by neutron diffraction and EPSR simulation. Journal of Non-Crystalline Solids **2008,** 354 (52-54), 5378-5385.
127. Soper, A. K.; McLain, S.; Klotz, S.; Straessle, T.; Imberti, S.; Hargreaves, R.; Youngs, T.; Callear, S.; Salzmann, C., Empirical Potential Structure Refinement. 2012.
128. Soper, A. K., Empirical Potential Structure Refinement: EPSRshell: a User's Guide: Version 18: May 2011. STFC: 2011.
129. Berg, B. A.; Neuhaus, T., Multicanonical algorithms for first order phase transitions. Physics Letters B **1991,** 267 (2), 249-253.
130. Soper, A. K., The radial distribution functions of water as derived from radiation total scattering experiments: Is there anything we can say for sure? International Scholarly Research Notices **2013,** 2013.
131. Read, J.; Lauritsen, C. C., An Investigation of the Klein-Nishina Formula for X-ray Scattering, in the Wave-length Region 50 to 20 X-units. Physical Review **1934,** 45 (7), 433.
132. Seibert, J. A.; Boone, J. M., X-ray imaging physics for nuclear medicine technologists. Part 2: X-ray interactions and image formation. Journal of nuclear medicine technology **2005,** 33 (1), 3-18.
133. Sarkar, T. K.; Abdallah, M. N.; Salazar-Palma, M.; Dyab, W. M., Surface Plasmons-Polaritons, Surface Waves, and Zenneck Waves: Clarification of the terms and a description of the concepts and their evolution. IEEE Antennas and Propagation Magazine **2017,** 59 (3), 77-93.
134. Carroll, J.; Karamian, S.; Rivlin, L. A.; Zadernovsky, A., X-ray-driven gamma emission. Hyperfine Interactions **2001,** 135, 3-50.
135. Cooper, M.; Mijnarends, P.; Shiotani, N.; Sakai, N.; Bansil, A., X-ray Compton scattering. OUP Oxford: 2004; Vol. 5.
136. Russ, J. C., Fundamentals of energy dispersive X-ray analysis: Butterworths monographs in materials. Butterworth-Heinemann: 2013.
137. Bushberg, J. T., The AAPM/RSNA physics tutorial for residents. X-ray interactions. Radiographics **1998,** 18 (2), 457-468.
138. Merzbacher, E.; Lewis, H., X-ray production by heavy charged particles. Corpuscles and Radiation in Matter II/Korpuskeln und Strahlung in Materie II **1958**, 166-192.
139. Lee, N.; Choi, S. H.; Hyeon, T., Nano-sized CT contrast agents. Advanced Materials **2013,** 25 (19), 2641-2660.
140. Grodstein, G. W., X-ray attenuation coefficients from 10 keV to 100 MeV. US Department of Commerce, National Bureau of Standards: 1957.
141. Bencivelli, W.; Bertolucci, E.; Bottigli, U.; Del Guerra, A.; Messineo, A.; Nelson, W.; Randaccio, P.; Rosso, V.; Russo, P.; Stefanini, A., Evaluation of elemental and compound semiconductors for X-ray digital radiography. Nuclear Instruments and Methods in Physics Research Section A: Accelerators, Spectrometers, Detectors and Associated Equipment **1991,** 310 (1-2), 210-214.
142. Hubbell, J. H., Electron–positron pair production by photons: A historical overview. Radiation Physics and Chemistry **2006,** 75 (6), 614-623.

143. Wille, K., Synchrotron radiation sources. Reports on Progress in Physics **1991,** 54 (8), 1005.
144. Mould, R. F., A century of X-rays and radioactivity in medicine: with emphasis on photographic records of the early years. CRC Press: 1993.
145. Lynch, D. W., Tantalus, a 240MeV Dedicated Source of Synchrotron Radiation, 1968–1986. Journal of Synchrotron Radiation **1997,** 4 (6), 334-343.
146. Robinson, A. L., History of synchrotron radiation. Synchrotron Radiation News **2015,** 28 (4), 4-9.
147. Daukantas, P., Synchrotron light sources for the 21st century. Optics and Photonics News **2021,** 32 (9), 32-39.
148. Barletta, W.; Bisognano, J.; Corlett, J.; Emma, P.; Huang, Z.; Kim, K.-J.; Lindberg, R.; Murphy, J.; Neil, G.; Nguyen, D., Free electron lasers: Present status and future challenges. Nuclear Instruments and Methods in Physics Research Section A: Accelerators, Spectrometers, Detectors and Associated Equipment **2010,** 618 (1-3), 69-96.
149. Cerantola, V.; Rosa, A. D.; Konôpková, Z.; Torchio, R.; Brambrink, E.; Rack, A.; Zastrau, U.; Pascarelli, S., New frontiers in extreme conditions science at synchrotrons and free electron lasers. Journal of Physics: Condensed Matter **2021,** 33 (27), 274003.
150. Serkez, S.; Geloni, G.; Tomin, S.; Feng, G.; Gryzlova, E.; Grum-Grzhimailo, A.; Meyer, M., Overview of options for generating high-brightness attosecond x-ray pulses at free-electron lasers and applications at the European XFEL. Journal of Optics **2018,** 20 (2), 024005.
151. Martin-Garcia, J. M.; Conrad, C. E.; Coe, J.; Roy-Chowdhury, S.; Fromme, P., Serial femtosecond crystallography: A revolution in structural biology. Archives of biochemistry and biophysics **2016,** 602, 32-47.
152. Tosha, T.; Nomura, T.; Nishida, T.; Saeki, N.; Okubayashi, K.; Yamagiwa, R.; Sugahara, M.; Nakane, T.; Yamashita, K.; Hirata, K., Capturing an initial intermediate during the P450nor enzymatic reaction using time-resolved XFEL crystallography and caged-substrate. Nature communications **2017,** 8 (1), 1585.
153. Boutet, S.; Yabashi, M., X-ray free electron lasers and their applications. X-ray Free Electron Lasers: A Revolution in Structural Biology **2018**, 1-21.
154. Stankus, B.; Yong, H.; Zotev, N.; Ruddock, J. M.; Bellshaw, D.; Lane, T. J.; Liang, M.; Boutet, S.; Carbajo, S.; Robinson, J. S., Ultrafast X-ray scattering reveals vibrational coherence following Rydberg excitation. Nature chemistry **2019,** 11 (8), 716-721.
155. Soper, A. K., GudrunN and GudrunX: programs for correcting raw neutron and X-ray diffraction data to differential scattering cross section. Science & Technology Facilities Council Swindon, UK: 2011.
156. Drakopoulos, M.; Connolley, T.; Reinhard, C.; Atwood, R.; Magdysyuk, O.; Vo, N.; Hart, M.; Connor, L.; Humphreys, B.; Howell, G., I12: the joint engineering, environment and processing (JEEP) beamline at diamond light source. Journal of synchrotron radiation **2015,** 22 (3), 828-838.
157. Hou, D.; Zhao, C.; Paterson, A. R.; Li, S.; Jones, J. L., Local structures of perovskite dielectrics and ferroelectrics via pair distribution function analyses. Journal of the European Ceramic Society **2018,** 38 (4), 971-987.
158. Sutter, J. P.; Chater, P. A.; Hillman, M. R.; Keeble, D. S.; Tucker, M. G.; Wilhelm, H. In Three-energy focusing Laue monochromator for the diamond light

source x-ray pair distribution function beamline I15-1, AIP Conference Proceedings, AIP Publishing LLC: 2016; p 040005.
159. Sutter, J. P.; Chater, P. A.; Signorato, R.; Keeble, D. S.; Hillman, M. R.; Tucker, M. G.; Alcock, S. G.; Nistea, I.-T.; Wilhelm, H., 1 m long multilayer-coated deformable piezoelectric bimorph mirror for adjustable focusing of high-energy X-rays. Optics express **2019,** 27 (11), 16121-16142.
160. Connolley, T.; Beavers, C. M.; Chater, P., High-Energy Adventures at Diamond Light Source. Synchrotron radiation newS **2020,** 33 (6), 31-36.
161. Gimenez, E.; Chater, P.; Crevatin, G.; Dennis, G.; Fairley, A.; Horswell, I.; Omar, D.; Spiers, J.; Tartoni, N. In Arc-detector: design of a CdTe photon-counting detector for the X-ray pair distribution function beamline at Diamond Light Source, 2019 IEEE Nuclear Science Symposium and Medical Imaging Conference (NSS/MIC), IEEE: 2019; pp 1-3.
162. Zhou, C.; Stepniewska, M.; Longley, L.; Ashling, C. W.; Chater, P. A.; Keen, D. A.; Bennett, T. D.; Yue, Y., Thermodynamic features and enthalpy relaxation in a metal–organic framework glass. Physical Chemistry Chemical Physics **2018,** 20 (27), 18291-18296.
163. Frentzel-Beyme, L.; Kloß, M.; Pallach, R.; Salamon, S.; Moldenhauer, H.; Landers, J.; Wende, H.; Debus, J.; Henke, S., Porous purple glass–a cobalt imidazolate glass with accessible porosity from a meltable cobalt imidazolate framework. Journal of Materials Chemistry A **2019,** 7 (3), 985-990.
164. Gaillac, R.; Pullumbi, P.; Beyer, K. A.; Chapman, K. W.; Keen, D. A.; Bennett, T. D.; Coudert, F.-X., Liquid metal–organic frameworks. Nature materials **2017,** 16 (11), 1149-1154.
165. Zhou, C.; Longley, L.; Krajnc, A.; Smales, G. J.; Qiao, A.; Erucar, I.; Doherty, C. M.; Thornton, A. W.; Hill, A. J.; Ashling, C. W., Metal-organic framework glasses with permanent accessible porosity. Nature communications **2018,** 9 (1), 1-9.
166. An, Z.; Yokota, H.; Zhang, N.; Paściak, M.; Fábry, J.; Kopecký, M.; Kub, J.; Zhang, G.; Glazer, A.; Welberry, T., Multiple structural components and their competition in the intermediate state of antiferroelectric Pb (Zr, Ti) O 3. Physical Review B **2021,** 103 (5), 054113.
167. Shaw, B. K.; Hughes, A. R.; Ducamp, M.; Moss, S.; Debnath, A.; Sapnik, A. F.; Thorne, M. F.; McHugh, L. N.; Pugliese, A.; Keeble, D. S., Melting of hybrid organic–inorganic perovskites. Nature chemistry **2021,** 13 (8), 778-785.
168. Huang, S.; Luo, S.; Qin, L.; Shu, D.; Sun, B.; Lunt, A. J.; Korsunsky, A. M.; Mi, J., 3D local atomic structure evolution in a solidifying Al-0.4 Sc dilute alloy melt revealed in operando by synchrotron X-ray total scattering and modelling. Scripta Materialia **2022**, 114484.
169. Chen, T.; Ellis, I.; Hooper, T. J.; Liberti, E.; Ye, L.; Lo, B. T.; O'Leary, C.; Sheader, A. A.; Martinez, G. T.; Jones, L., Interstitial boron atoms in the palladium lattice of an industrial type of nanocatalyst: properties and structural modifications. Journal of the American Chemical Society **2019,** 141 (50), 19616-19624.
170. Entwistle, J. E.; Booth, S. G.; Keeble, D. S.; Ayub, F.; Yan, M.; Corr, S. A.; Cumming, D. J.; Patwardhan, S. V., Insights into the Electrochemical Reduction Products and Processes in Silica Anodes for Next-Generation Lithium-Ion Batteries. Advanced Energy Materials **2020,** 10 (43), 2001826.

171. Jacrot, B.; Zaccai, G., Determination of molecular weight by neutron scattering. Biopolymers: Original Research on Biomolecules **1981,** 20 (11), 2413-2426.
172. Santodonato, L. J.; Liaw, P. K.; Unocic, R. R.; Bei, H.; Morris, J. R., Predictive multiphase evolution in Al-containing high-entropy alloys. Nature Communications **2018,** 9 (1), 4520.
173. Deng, B.; Shi, Y.; Zhou, Q.; Bauchy, M., Revealing the structural role of MgO in aluminosilicate glasses. Acta Materialia **2022,** 222, 117417.
174. Wu, Y.; Ma, D.; Li, Q.; Stoica, A. D.; Song, W.; Wang, H.; Liu, X.; Stoica, G. M.; Wang, G.; An, K., Transformation-induced plasticity in bulk metallic glass composites evidenced by in-situ neutron diffraction. Acta Materialia **2017,** 124, 478-488.
175. Sakai, V. G.; Arbe, A., Quasielastic neutron scattering in soft matter. Current Opinion in Colloid & Interface Science **2009,** 14 (6), 381-390.
176. Shibayama, M., Small-angle neutron scattering on polymer gels: phase behavior, inhomogeneities and deformation mechanisms. Polymer journal **2011,** 43 (1), 18-34.
177. Kotlarchyk, M.; Chen, S. H., Analysis of small angle neutron scattering spectra from polydisperse interacting colloids. The Journal of chemical physics **1983,** 79 (5), 2461-2469.
178. Chen, S.-H., Small angle neutron scattering studies of the structure and interaction in micellar and microemulsion systems. Annual Review of Physical Chemistry **1986,** 37 (1), 351-399.
179. Ohshita, H.; Uno, S.; Otomo, T.; Koike, T.; Murakami, T.; Satoh, S.; Sekimoto, M.; Uchida, T., Development of a neutron detector with a GEM. Nuclear Instruments and Methods in Physics Research Section A: Accelerators, Spectrometers, Detectors and Associated Equipment **2010,** 623 (1), 126-128.
180. Stolte, C.; Tang, D.; Hanrahan, P., Polaris: A system for query, analysis, and visualization of multidimensional relational databases. IEEE Transactions on Visualization and Computer Graphics **2002,** 8 (1), 52-65.
181. Smith, R.; Hull, S.; Tucker, M.; Playford, H.; McPhail, D.; Waller, S.; Norberg, S., The upgraded Polaris powder diffractometer at the ISIS neutron source. Review of scientific instruments **2019,** 90 (11), 115101.
182. http://worldsciencereport.blogspot.com/.
183. Mathon, O.; Beteva, A.; Borrel, J.; Bugnazet, D.; Gatla, S.; Hino, R.; Kantor, I.; Mairs, T.; Munoz, M.; Pasternak, S., The time-resolved and extreme conditions XAS (TEXAS) facility at the European Synchrotron Radiation Facility: the general-purpose EXAFS bending-magnet beamline BM23. Journal of synchrotron radiation **2015,** 22 (6), 1548-1554.
184. Timoshenko, J.; Roldan Cuenya, B., In situ/operando electrocatalyst characterization by X-ray absorption spectroscopy. Chemical reviews **2020,** 121 (2), 882-961.
185. Yano, J.; Yachandra, V. K., X-ray absorption spectroscopy. Photosynthesis research **2009,** 102, 241-254.
186. .
187. Miao, J.; Ercius, P.; Billinge, S. J., Atomic electron tomography: 3D structures without crystals. Science **2016,** 353 (6306), aaf2157.
188. Yuan, Y.; Kim, D. S.; Zhou, J.; Chang, D. J.; Zhu, F.; Nagaoka, Y.; Yang, Y.; Pham, M.; Osher, S. J.; Chen, O., Three-dimensional atomic packing

in amorphous solids with liquid-like structure. Nature materials **2022,** 21 (1), 95-102.
189. Pryor Jr, A.; Yang, Y.; Rana, A.; Gallagher-Jones, M.; Zhou, J.; Lo, Y. H.; Melinte, G.; Chiu, W.; Rodriguez, J. A.; Miao, J., GENFIRE: A generalized Fourier iterative reconstruction algorithm for high-resolution 3D imaging. Scientific reports **2017,** 7 (1), 10409.
190. Pusztai, L.; Tóth, G., On the uniqueness of the Reverse Monte Carlo simulation. I. Simple liquids, partial radial distribution functions. The Journal of chemical physics **1991,** 94 (4), 3042-3049.
191. Haymet, A., Orientational environments in liquids and solids. Chemical physics letters **1984,** 107 (1), 77-82.
192. McGreevy, R.; Pusztai, L., The structure of molten salts. Proceedings of the Royal Society of London. Series A: Mathematical and Physical Sciences **1990,** 430 (1878), 241-261.
193. Balucani, U.; Vallauri, R., Evolution of bond-angle distribution from liquid to glassy states. Chemical physics letters **1990,** 166 (1), 77-81.
194. Geesink, H. J.; Jerman, I.; Meijer, D. K., Water, the cradle of life via its coherent quantum frequencies. Water **2020,** 11, 78-108.
195. Qiao, C.; Bai, K.; Xu, M.; Wang, S.; Wang, C.-Z.; Ho, K.-M.; Miao, X.; Xu, M., Ultrafast crystallization mechanism of amorphous Ge15Sb85 unraveled by pressure-driven simulations. Acta Materialia **2021,** 216, 117123.
196. Cowley, J., An approximate theory of order in alloys. Physical Review **1950,** 77 (5), 669.
197. Cargill III, G.; Spaepen, F., Description of chemical ordering in amorphous alloys. Journal of Non-Crystalline Solids **1981,** 43 (1), 91-97.
198. Han, J.; Wang, W.; Liu, X.; Wang, C.; Hui, X.; Liu, Z., Effect of solute atoms on glass-forming ability for Fe–Y–B alloy: an ab initio molecular dynamics study. Acta materialia **2014,** 77, 96-110.
199. Alam, A.; Chouhan, R. K.; Mookerjee, A., Phonon modes and vibrational entropy of disordered alloys with short-range order: A first-principles calculation. Physical Review B **2011,** 83 (5), 054201.
200. Honeycutt, J. D.; Andersen, H. C., Molecular dynamics study of melting and freezing of small Lennard-Jones clusters. Journal of Physical Chemistry **1987,** 91 (19), 4950-4963.
201. Wen, D.; Peng, P.; Jiang, Y.; Tian, Z.; Li, W.; Liu, R., Correlation of the heredity of icosahedral clusters with the glass forming ability of rapidly solidified CuxZr100− x alloys. Journal of Non-Crystalline Solids **2015,** 427, 199-207.
202. Finney, J., Modelling the structures of amorphous metals and alloys. Nature **1977,** 266 (5600), 309-314.
203. Finney, J., Random packings and the structure of simple liquids. I. The geometry of random close packing. Proceedings of the Royal Society of London. A. Mathematical and Physical Sciences **1970,** 319 (1539), 479-493.
204. Zou, P.; Bader, R., A topological definition of a Wigner–Seitz cell and the atomic scattering factor. Acta Crystallographica Section A: Foundations of Crystallography **1994,** 50 (6), 714-725.
205. Yu, D.-Q.; Chen, M.; Han, X.-J., Structure analysis methods for crystalline solids and supercooled liquids. Physical Review E **2005,** 72 (5), 051202.
206. Cape, J. N.; Finney, J. L.; Woodcock, L. V., An analysis of crystallization by homogeneous nucleation in a 4000-atom soft-sphere model. The Journal of Chemical Physics **1981,** 75 (5), 2366-2373.

207. Steinhardt, P. J.; Nelson, D. R.; Ronchetti, M., Bond-orientational order in liquids and glasses. Phys. Rev. B **1983,** 28 (2), 784.
208. Tanaka, H., Bond orientational ordering in a metastable supercooled liquid: a shadow of crystallization and liquid–liquid transition. Journal of Statistical Mechanics: Theory and Experiment **2010,** 2010 (12), P12001.
209. Tanaka, H., Simple physical explanation of the unusual thermodynamic behavior of liquid water. Physical review letters **1998,** 80 (26), 5750.
210. Tanaka, H., Thermodynamic anomaly and polyamorphism of water. EPL (Europhysics Letters) **2000,** 50 (3), 340.
211. Tanaka, H., Simple physical model of liquid water. The Journal of Chemical Physics **2000,** 112 (2), 799-809.
212. Tanaka, H., Simple view of waterlike anomalies of atomic liquids with directional bonding. Physical Review B **2002,** 66 (6), 064202.
213. Tanaka, H., Two-order-parameter description of liquids: Critical phenomena and phase separation of supercooled liquids. Journal of Physics: Condensed Matter **1999,** 11 (15), L159.
214. Tanaka, H., General view of a liquid-liquid phase transition. Physical Review E **2000,** 62 (5), 6968.
215. Debenedetti, P. G., Metastable liquids: concepts and principles. **1996**.
216. Lee, G.; Gangopadhyay, A.; Croat, T.; Rathz, T.; Hyers, R.; Rogers, J.; Kelton, K., Link between liquid structure and the nucleation barrier for icosahedral quasicrystal, polytetrahedral, and simple crystalline phases in Ti− Zr− Ni alloys: Verification of Frank's hypothesis. Physical Review B **2005,** 72 (17), 174107.
217. Holland-Moritz, D.; Herlach, D.; Urban, K., Observation of the undercoolability of quasicrystal-forming alloys by electromagnetic levitation. Physical review letters **1993,** 71 (8), 1196.
218. Ostwald, W., Studies on the formation and change of solid matter. Z. Phys. Chem. **1897,** 22, 289-302.
219. Alexander, S.; McTague, J., Should all crystals be bcc? Landau theory of solidification and crystal nucleation. Physical Review Letters **1978,** 41 (10), 702.
220. Jeon, S.; Heo, T.; Hwang, S.-Y.; Ciston, J.; Bustillo, K. C.; Reed, B. W.; Ham, J.; Kang, S.; Kim, S.; Lim, J., Reversible disorder-order transitions in atomic crystal nucleation. Science **2021,** 371 (6528), 498-503.
221. Baumgartner, J.; Dey, A.; Bomans, P. H.; Le Coadou, C.; Fratzl, P.; Sommerdijk, N. A.; Faivre, D., Nucleation and growth of magnetite from solution. Nature materials **2013,** 12 (4), 310-314.
222. Vekilov, P. G., Dense liquid precursor for the nucleation of ordered solid phases from solution. Crystal Growth Design **2004,** 4 (4), 671-685.
223. Shibuta, Y.; Sakane, S.; Miyoshi, E.; Okita, S.; Takaki, T.; Ohno, M., Heterogeneity in homogeneous nucleation from billion-atom molecular dynamics simulation of solidification of pure metal. Nature communications **2017,** 8 (1), 1-9.
224. Xu, W.; Sandor, M. T.; Yu, Y.; Ke, H.-B.; Zhang, H.-P.; Li, M.-Z.; Wang, W.-H.; Liu, L.; Wu, Y., Evidence of liquid–liquid transition in glass-forming La50Al35Ni15 melt above liquidus temperature. Nature communications **2015,** 6 (1), 7696.
225. Manuwong, T.; Zhang, W.; Kazinczi, P. L.; Bodey, A. J.; Rau, C.; Mi, J., Solidification of Al alloys under electromagnetic pulses and characterization of the 3D microstructures using synchrotron X-ray tomography. Metallurgical and Materials Transactions A **2015,** 46, 2908-2915.

226. Tan, D. In situ ultrafast synchrotron X-ray imaging studies of the dynamics of ultrasonic bubbles in liquids. University of Hull, 2015.
227. Zhang, W. Study of the multi-length scale structure of metallic glasses using synchrotron X-rays and phase-field crystal modelling. University of Hull, 2016.
228. Lee, T. L.; Khong, J. C.; Fezzaa, K.; Mi, J. W. In Ultrafast X-ray imaging and modelling of ultrasonic cavitations in liquid metal, Materials Science Forum, Trans Tech Publ: 2013; pp 190-194.
229. Huang, Y.; Khong, J.; Connolley, T.; Mi, J., Understanding the deformation mechanism of individual phases of a ZrTi-based bulk metallic glass matrix composite using in situ diffraction and imaging methods. Appl. Phys. Lett. **2014,** 104 (3), 031912.
230. Hammersley, A., FIT2D: a multi-purpose data reduction, analysis and visualization program. Journal of Applied Crystallography **2016,** 49 (2), 646-652.
231. Filik, J.; Ashton, A.; Chang, P.; Chater, P.; Day, S.; Drakopoulos, M.; Gerring, M.; Hart, M.; Magdysyuk, O.; Michalik, S., Processing two-dimensional X-ray diffraction and small-angle scattering data in DAWN 2. Journal of applied crystallography **2017,** 50 (3), 959-966.
232. Krogh-Moe, J., A method for converting experimental X-ray intensities to an absolute scale. Acta Crystallographica **1956,** 9 (11), 951-953.
233. Norman, N., The Fourier transform method for normalizing intensities. Acta Crystallographica **1957,** 10 (5), 370-373.
234. Faber, T.; Ziman, J., A theory of the electrical properties of liquid metals: III. The resistivity of binary alloys. Philosophical Magazine **1965,** 11 (109), 153-173.
235. Hille, E., Analytic function theory. American Mathematical Soc.: 2002; Vol. 2.
236. Smith, V.; Thakkar, A.; Chapman, D. J. A. C. S. A. C. P., Diffraction, Theoretical; Crystallography, G., A new analytic approximation to atomic incoherent X-ray scattering intensities. **1975,** 31 (3), 391-392.
237. Kaplow, R.; Strong, S.; Averbach, B., Radial density functions for liquid mercury and lead. Physical Review **1965,** 138 (5A), A1336.
238. Eggert, J. H.; Weck, G.; Loubeyre, P.; Mezouar, M., Quantitative structure factor and density measurements of high-pressure fluids in diamond anvil cells by x-ray diffraction: Argon and water. Physical Review B **2002,** 65 (17), 174105.
239. Luo, S.; Khong, J. C.; Daisenberger, D.; Huang, S.; McMillan, P. F.; Mi, J., Synchrotron x-ray total scattering and modeling study of high-pressure-induced inhomogeneous atom reconfiguration in an equiatomic Zr 50 Cu 50 metallic glassy alloy. Physical Review B **2022,** 105 (6), 064203.
240. Decremps, F.; Morard, G.; Garbarino, G.; Casula, M., Polyamorphism of a Ce-based bulk metallic glass by high-pressure and high-temperature density measurements. Physical Review B **2016,** 93 (5), 054209.
241. Assael, M. J.; Kakosimos, K.; Banish, R. M.; Brillo, J.; Egry, I.; Brooks, R.; Quested, P. N.; Mills, K. C.; Nagashima, A.; Sato, Y., Reference data for the density and viscosity of liquid aluminum and liquid iron. Journal of physical and chemical reference data **2006,** 35 (1), 285-300.
242. Soper, A. K., Computer simulation as a tool for the interpretation of total scattering data from glasses and liquids. Molecular Simulation **2012,** 38 (14-15), 1171-1185.

243. Soper, A., Partial structure factors from disordered materials diffraction data: An approach using empirical potential structure refinement. Phys. Rev. B **2005,** 72 (10), 104204.
244. Magomedov, M. N., The calculation of the parameters of the Mie-Lennard-Jones potential. High Temp **2006,** 44 (4), 513-529.
245. Soper, A., Partial structure factors from disordered materials diffraction data: An approach using empirical potential structure refinement. Physical Review B **2005,** 72 (10), 104204.
246. Soper, A. K., Empirical potential Monte Carlo simulation of fluid structure. Chem Phys **1996,** 202 (2-3), 295-306.
247. Soper, A., Empirical Potential Structure Refinement-A User's Guide. ISIS, Rutherford Appleton Labortory, Didcot, UK **2006**.
248. Sarou-Kanian, V.; Millot, F.; Rifflet, J.-C., Surface tension and density of oxygen-free liquid aluminum at high temperature. International journal of Thermophysics **2003,** 24 (1), 277-286.
249. Martinez, V. J.; Jones, B. J.; Dominguez-Tenreiro, R.; Weygaert, R., Clustering paradigms and multifractal measures. Astrophysical Journal **1990,** 357, 50-61.
250. Shimono, M.; Onodera, H. In Icosahedral order in supercooled liquids and glassy alloys, Materials science forum, Trans Tech Publ: 2007; pp 2031-2035.
251. Lee, M.; Lee, C.-M.; Lee, K.-R.; Ma, E.; Lee, J.-C., Networked interpenetrating connections of icosahedra: Effects on shear transformations in metallic glass. Acta Materialia **2011,** 59 (1), 159-170.
252. Wang, W. H., Dynamic relaxations and relaxation-property relationships in metallic glasses. Progress in Materials Science **2019,** 106, 100561.
253. Lechner, W. Bond order analysis. https://github.com/WolfgangLechner/StructureAnalysis.
254. Wang, Z.; Stroud, D., Bond-orientational order in liquid Si. The Journal of chemical physics **1991,** 94 (5), 3896-3900.
255. Winczewski, S.; Dziedzic, J.; Rybicki, J., A highly-efficient technique for evaluating bond-orientational order parameters. Computer Physics Communications **2016,** 198, 128-138.
256. Stukowski, A., Visualization and analysis of atomistic simulation data with OVITO–the Open Visualization Tool. Model Simul Mat Sci Eng **2009,** 18 (1), 015012.
257. Lou, H.; Wang, X.; Cao, Q.; Zhang, D.; Zhang, J.; Hu, T.; Mao, H.-k.; Jiang, J.-Z., Negative expansions of interatomic distances in metallic melts. Proceedings of the National Academy of Sciences **2013,** 110 (25), 10068-10072.
258. Hanson, R. M., Jmol–a paradigm shift in crystallographic visualization. Journal of Applied Crystallography **2010,** 43 (5), 1250-1260.
259. Ding, J.; Cheng, Y.-Q.; Ma, E., Full icosahedra dominate local order in Cu64Zr34 metallic glass and supercooled liquid. Acta materialia **2014,** 69, 343-354.
260. Roik, O.; Anikeenko, A.; Medvedev, N., Investigation of the particular features of the structure factor of liquid Al-based alloys. Journal of Molecular Liquids **2011,** 161 (2), 78-84.
261. Egry, I.; Hennet, L.; Kehr, M.; Mathiak, G.; De Panfilis, S.; Pozdnyakova, I.; Zanghi, D., Chemical short-range order in liquid Al–Ni alloys. The Journal of chemical physics **2008,** 129 (6), 064508.

262. Holland-Moritz, D.; Jacobs, G.; Egry, I., Investigations of the short-range order in melts of quasicrystal-forming Al–Cu–Co alloys by EXAFS. Materials Science and Engineering: A **2000,** 294, 369-372.
263. Roik, O.; Samsonnikov, O.; Kazimirov, V.; Sokolskii, V.; Galushko, S. J. J. o. M. L., Medium-range order in Al-based liquid binary alloys. **2010,** 151 (1), 42-49.
264. Desgranges, C.; Delhommelle, J., Can Ordered Precursors Promote the Nucleation of Solid Solutions? Physical review letters **2019,** 123 (19), 195701.
265. Desgranges, C.; Delhommelle, J., Unusual crystallization behavior close to the glass transition. Physical review letters **2018,** 120 (11), 115701.
266. Redfield, A. C.; Zangwill, A., Energetics of icosahedral phase stability in metallic alloys. Physical review letters **1987,** 58 (22), 2322.
267. Hirata, A.; Kang, L.; Fujita, T.; Klumov, B.; Matsue, K.; Kotani, M.; Yavari, A.; Chen, M. J. S., Geometric frustration of icosahedron in metallic glasses. **2013,** 341 (6144), 376-379.
268. Faken, D.; Jónsson, H. J. C. M. S., Systematic analysis of local atomic structure combined with 3D computer graphics. **1994,** 2 (2), 279-286.
269. Fang, X.; Wang, C.; Yao, Y.; Ding, Z.; Ho, K. J. P. R. B., Competition between fcc and icosahedral short-range orders in pure and samarium-doped liquid aluminum from first principles. **2011,** 83 (22), 224203.
270. Choudhuri, D.; Majumdar, B. S. J. M., Structural changes during crystallization and vitrification of dilute FCC-based binary alloys. **2020,** 12, 100816.
271. Redfield, A. C.; Zangwill, A. J. P. r. l., Energetics of icosahedral phase stability in metallic alloys. **1987,** 58 (22), 2322.
272. Desgranges, C.; Delhommelle, J. J. P. R. L., Can ordered precursors promote the nucleation of solid solutions? **2019,** 123 (19), 195701.
273. Speight, J., Lange's handbook of chemistry. McGraw-Hill Education: 2005.
274. Jiang, H.-R.; Hu, J.-Y.; Neuber, N.; Bochtler, B.; Adam, B.; Riegler, S. S.; Frey, M.; Ruschel, L.; Lu, W.-F.; Feng, A.-H., Effect of sulfur on the glass-forming ability, phase transformation, and thermal stability of Cu-Zr-Al bulk metallic glass. Acta Materialia **2021,** 212, 116923.
275. Wang, W.; Han, J.; Fang, H.; Wang, J.; Liang, Y.; Shang, S.; Wang, Y.; Liu, X.; Kecskes, L.; Mathaudhu, S., Anomalous structural dynamics in liquid Al80Cu20: An ab initio molecular dynamics study. Acta Materialia **2015,** 97, 75-85.
276. Aste, T.; Saadatfar, M.; Senden, T., Geometrical structure of disordered sphere packings. Physical Review E **2005,** 71 (6), 061302.
277. Tanaka, H., Bond orientational order in liquids: Towards a unified description of water-like anomalies, liquid-liquid transition, glass transition, and crystallization. The European Physical Journal E **2012,** 35 (10), 1-84.
278. Tanaka, H., A simple physical model of liquid-glass transition: Intrinsic fluctuating interactions and random fields hidden in glass-forming liquids. Journal of Physics: Condensed Matter **1998,** 10 (14), L207.
279. Barbier, J.-N.; Tamura, N.; Verger-Gaugry, J.-L., Monoclinic Al13Fe4 approximant phase: a link between icosahedral and decagonal phases. Journal of non-crystalline solids **1993,** 153, 126-131.
280. Matilainen, A.; Pussi, K.; Diehl, R.; Hahne, M.; Gille, P.; Gaudry, É.; Loli, L. S.; McGuirk, G.; De Weerd, M.-C.; Fournée, V., Structure of the

monoclinic A l 13 F e 4 (010) complex metallic alloy surface determined by low-energy electron diffraction. Physical Review B **2015,** 92 (1), 014109.
281. Holland-Moritz, D.; Schroers, J.; Herlach, D.; Grushko, B.; Urban, K., Undercooling and solidification behaviour of melts of the quasicrystal-forming alloysAl–Cu–Fe and Al–Cu–Co. Acta materialia **1998,** 46 (5), 1601-1615.
282. Holland-Moritz, D., Nucleation Behavior and Solid-Liquid Interfacial Energy of Polytetrahedral Phases. MRS Online Proceedings Library (OPL) **1999,** 580.
283. Holland-Moritz, D., On the energy of the interface between a melt and quasicrystalline and polytetrahedral phases. Journal of non-crystalline solids **1999,** 250, 839-843.
284. Tang, S.; Wang, J.; Svendsen, B.; Raabe, D., Competitive bcc and fcc crystal nucleation from non-equilibrium liquids studied by phase-field crystal simulation. Acta Materialia **2017,** 139, 196-204.
285. Du, W. In-situ synchrotron X-ray imaging and tomography studies of the evolution of solidification microstructures under pulse electromagnetic fields. University of Hull, 2018.
286. Que, Z.; Mendis, C. L., Formation of θ-Al13Fe4 and the multi-step phase transformations to α-Al8Fe2Si, β-Al5FeSi and δ-Al4FeSi2 in Al–20Si-0.7 Fe alloy. Intermetallics **2020,** 127, 106960.
287. Sugiyama, K.; Obata, T.; Hiraga, K., The Crystalline Structure of O-AlFePd. Materials Transactions **2012**, M2012130.
288. Henningsson, N. A.; Hall, S. A.; Wright, J. P.; Hektor, J., Reconstructing intragranular strain fields in polycrystalline materials from scanning 3DXRD data. Journal of applied crystallography **2020,** 53 (2), 314-325.
289. Ball, J. A.; Kareer, A.; Magdysyuk, O. V.; Michalik, S.; Vrettou, A.; Parkes, N.; Connolley, T.; Collins, D. M., Implementing and evaluating far-field 3D X-ray diffraction at the I12 JEEP beamline, Diamond Light Source. Journal of Synchrotron Radiation **2022,** 29 (4).
290. Youngs, T., Dissolve: next generation software for the interrogation of total scattering data by empirical potential generation. Molecular Physics **2019,** 117 (22), 3464-3477.
291. Louca, K.; Abdolvand, H.; Mareau, C.; Majkut, M.; Wright, J., Formation and annihilation of stressed deformation twins in magnesium. Communications Materials **2021,** 2 (1), 9.

Appendices

Appendix 1: Design of the furnace

Base plate (P2)

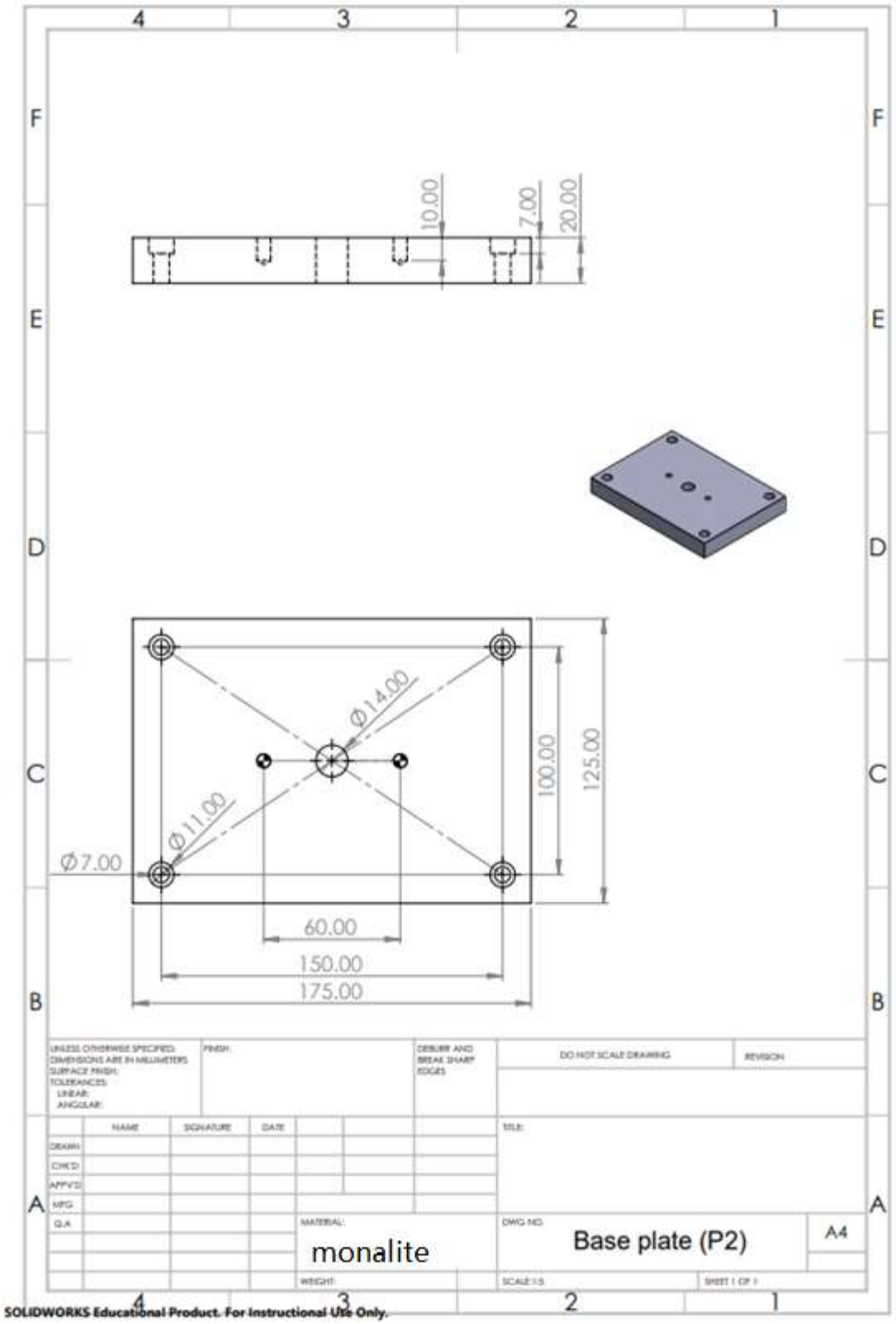

Position plate (P3)

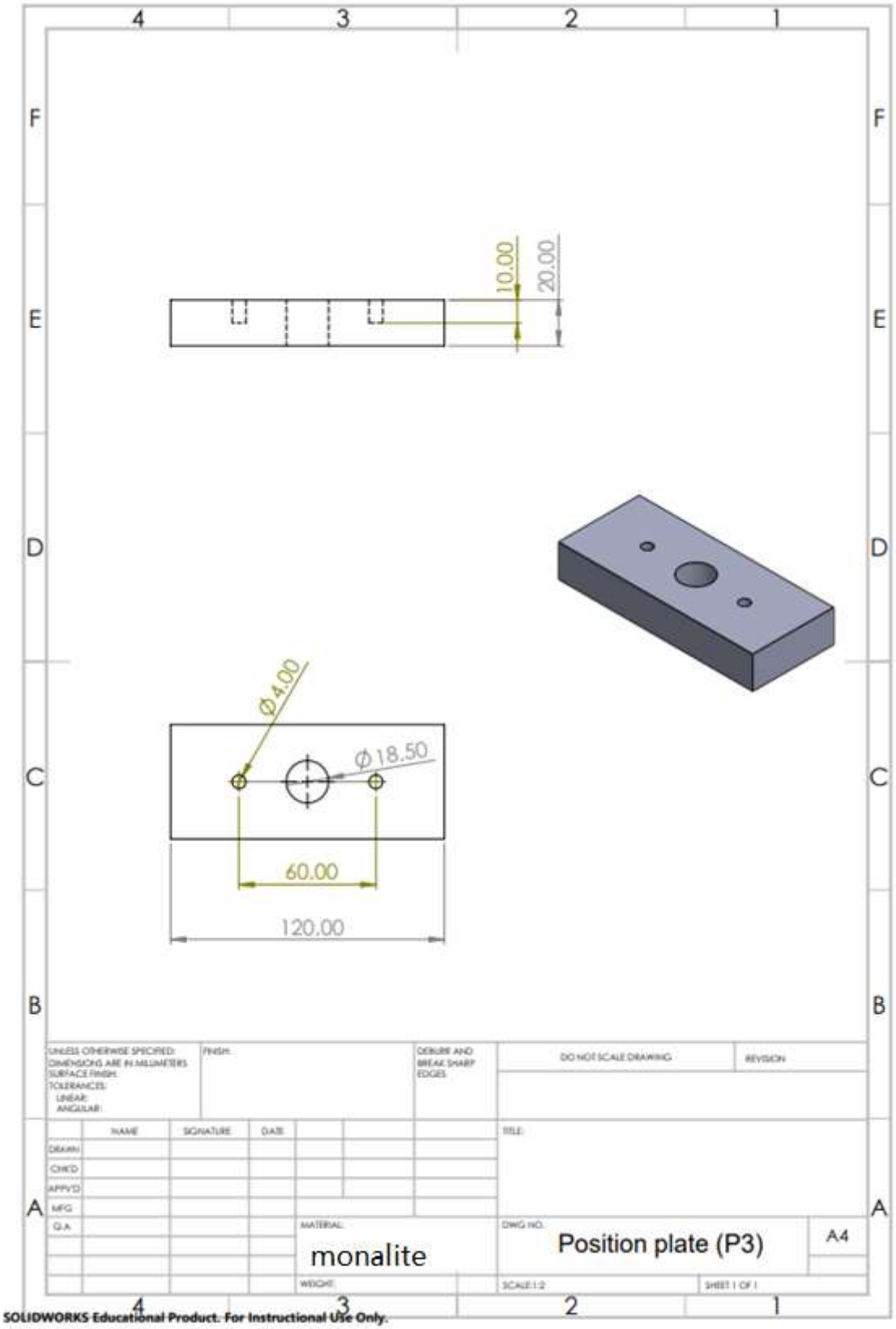

Position plate (P4)

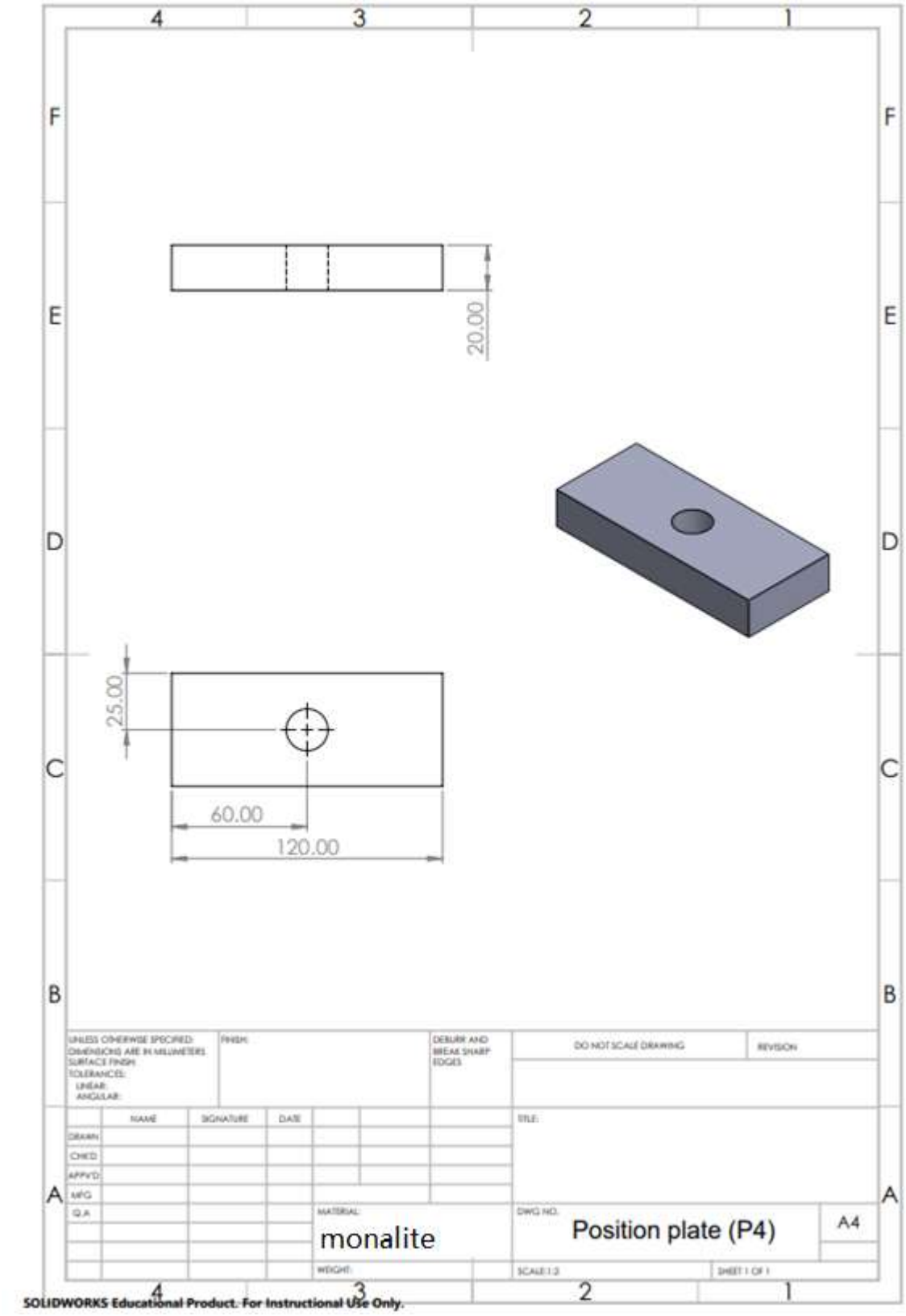

Side plate (P5)

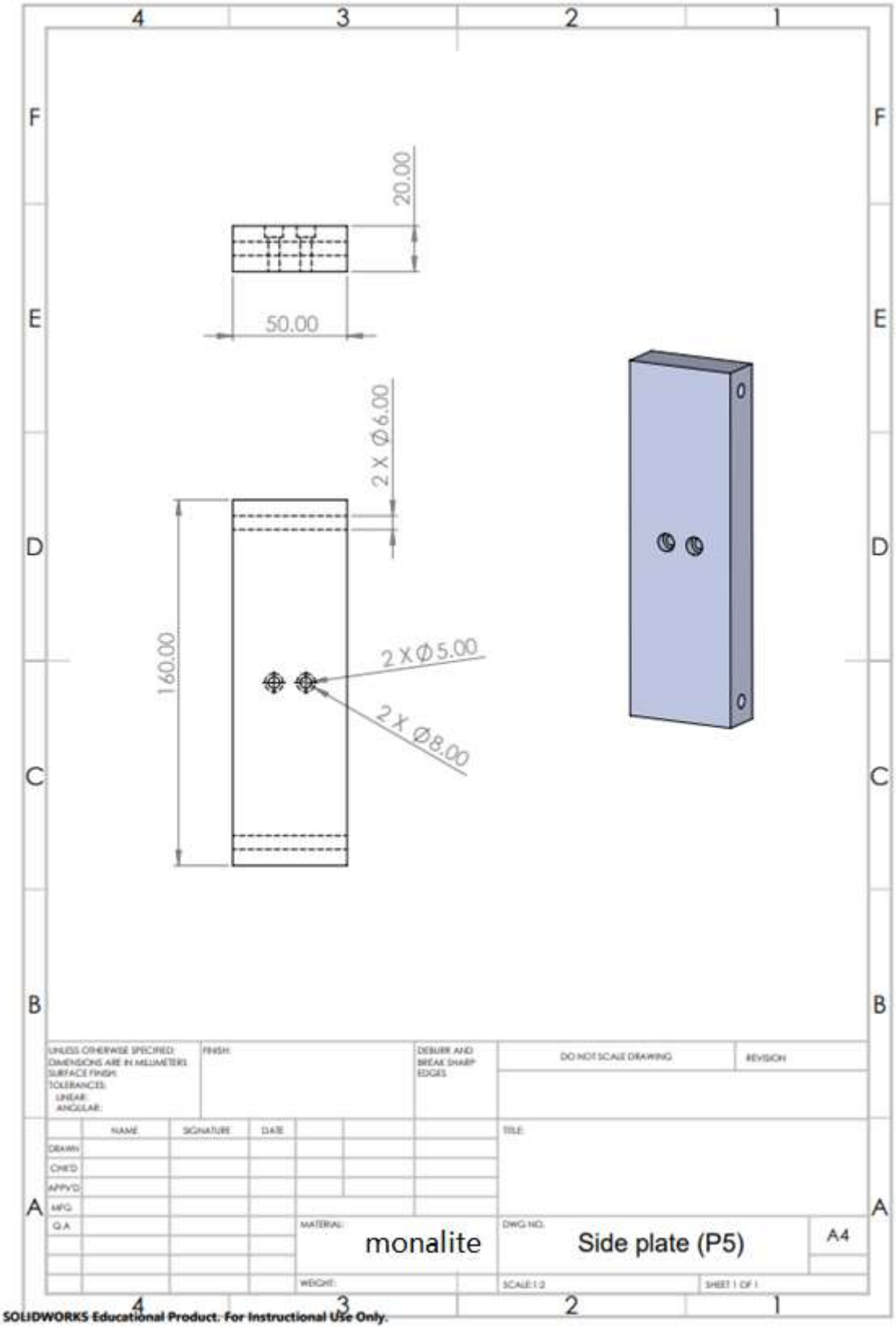
20.00
50.00
2 X Ø6.00
160.00
2 X Ø5.00
2 X Ø8.00
UNLESS OTHERWISE SPECIFIED:
DIMENSIONS ARE IN MILLIMETERS
SURFACE FINISH:
TOLERANCES:
LINEAR:
ANGULAR:
FINISH:
DEBURR AND BREAK SHARP EDGES
DO NOT SCALE DRAWING
REVISION
NAME
SIGNATURE
DATE
DRAWN
CHK'D
APPV'D
MFG
Q.A
TITLE:
MATERIAL:
monalite
DWG NO.
Side plate (P5)
A4
WEIGHT:
SCALE:1:2
SHEET 1 OF 1
SOLIDWORKS Educational Product. For Instructional Use Only.

Side plate (P6)

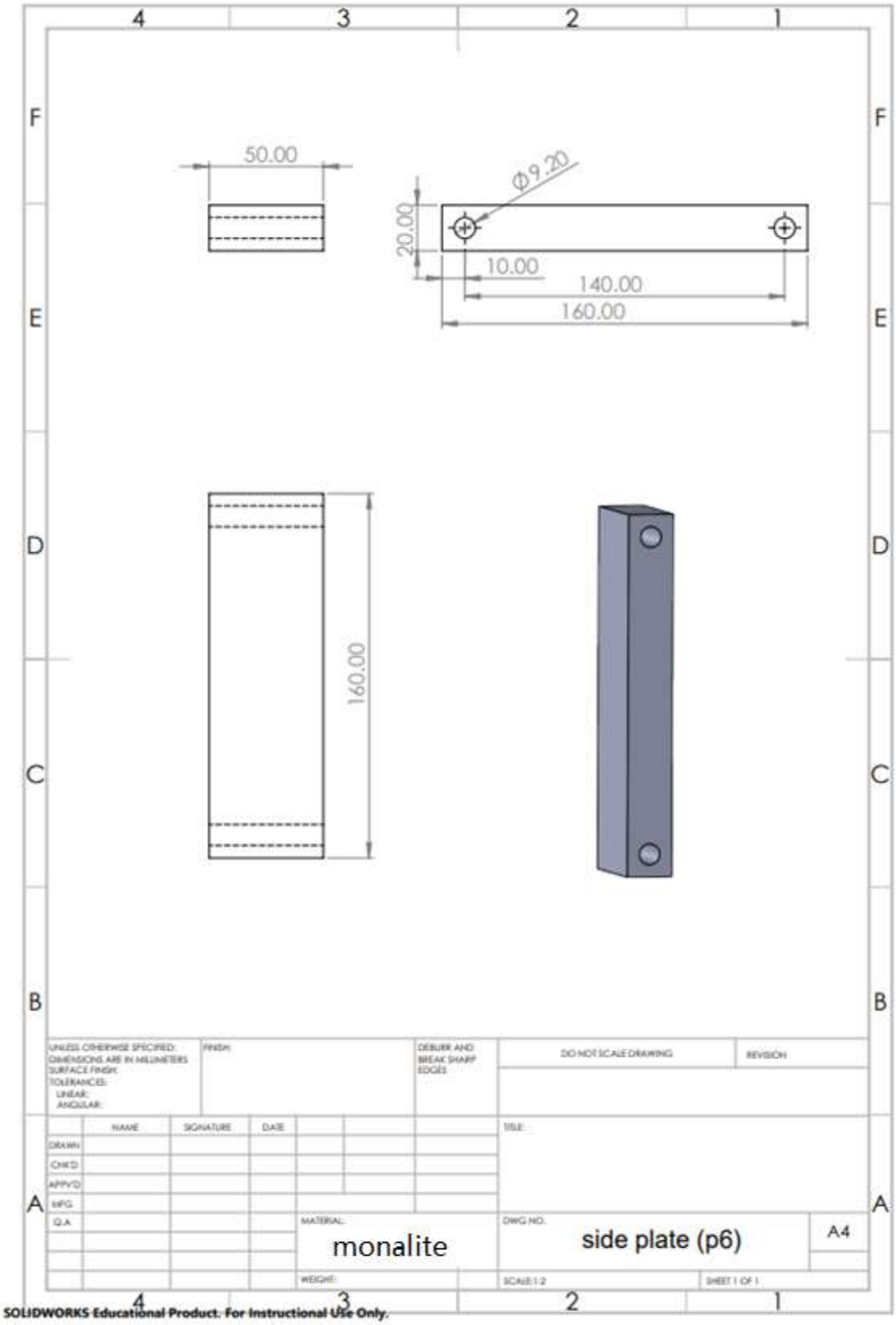

Resistance heater (P7)

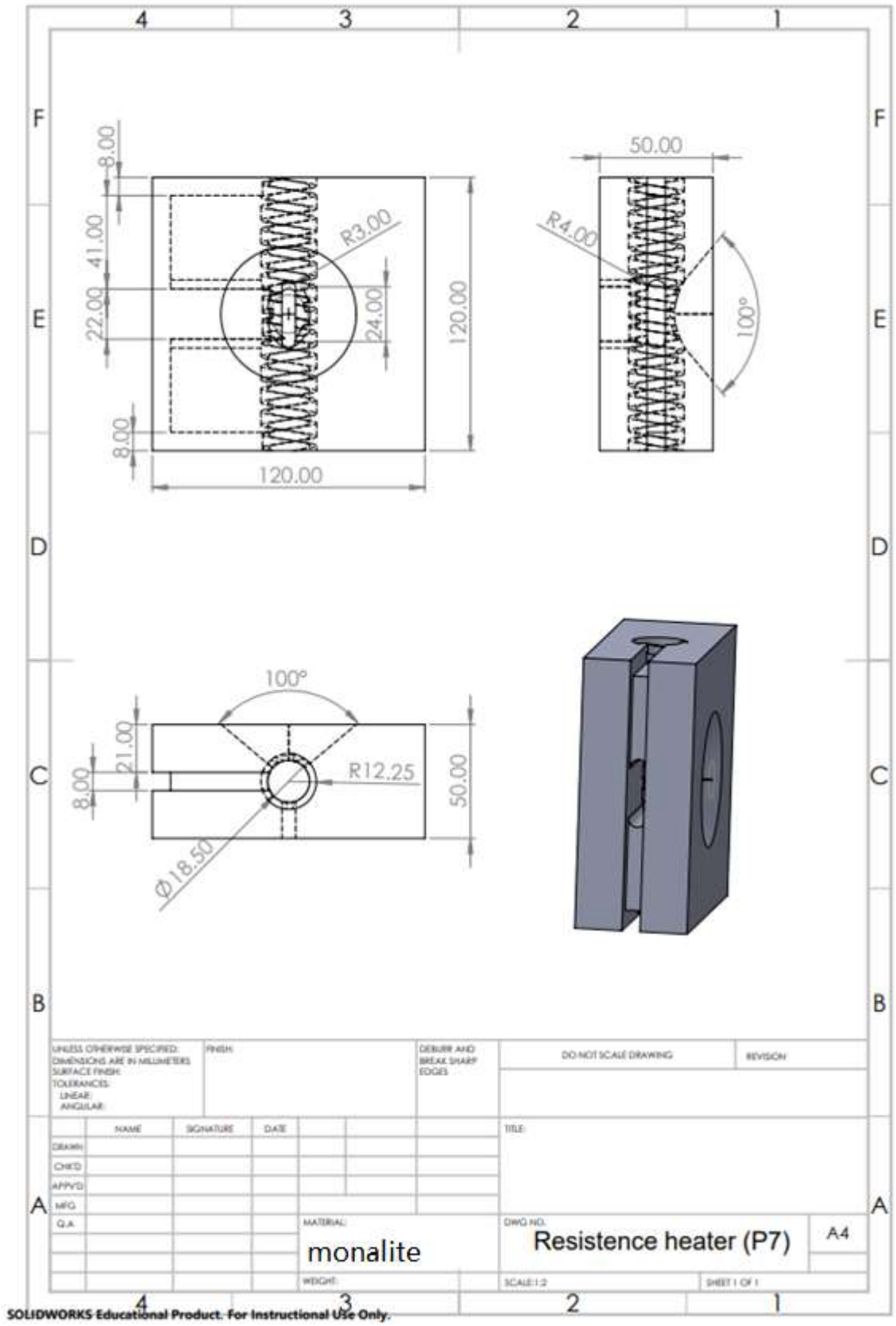

Front plate (P9)

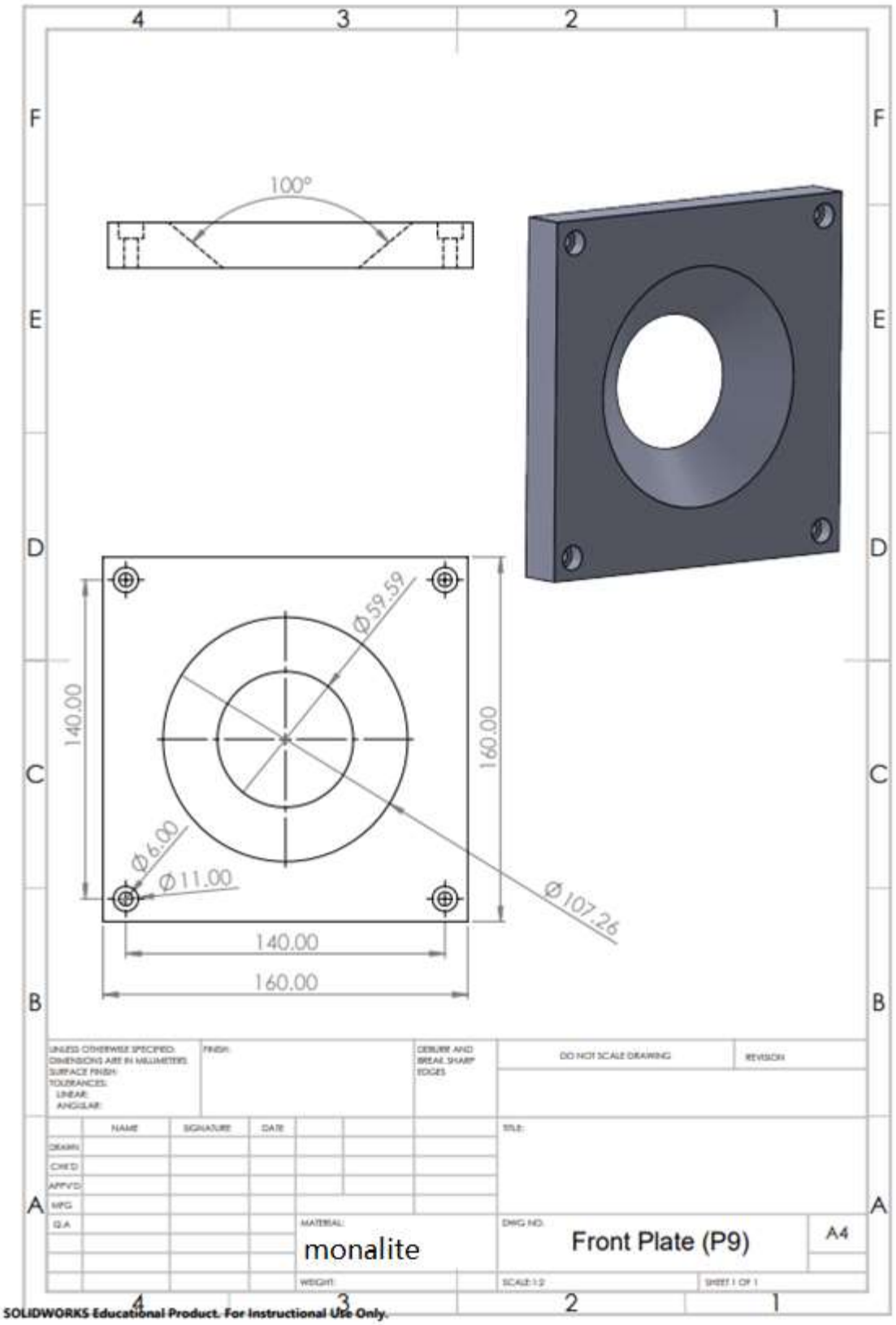

Back plate (P10)

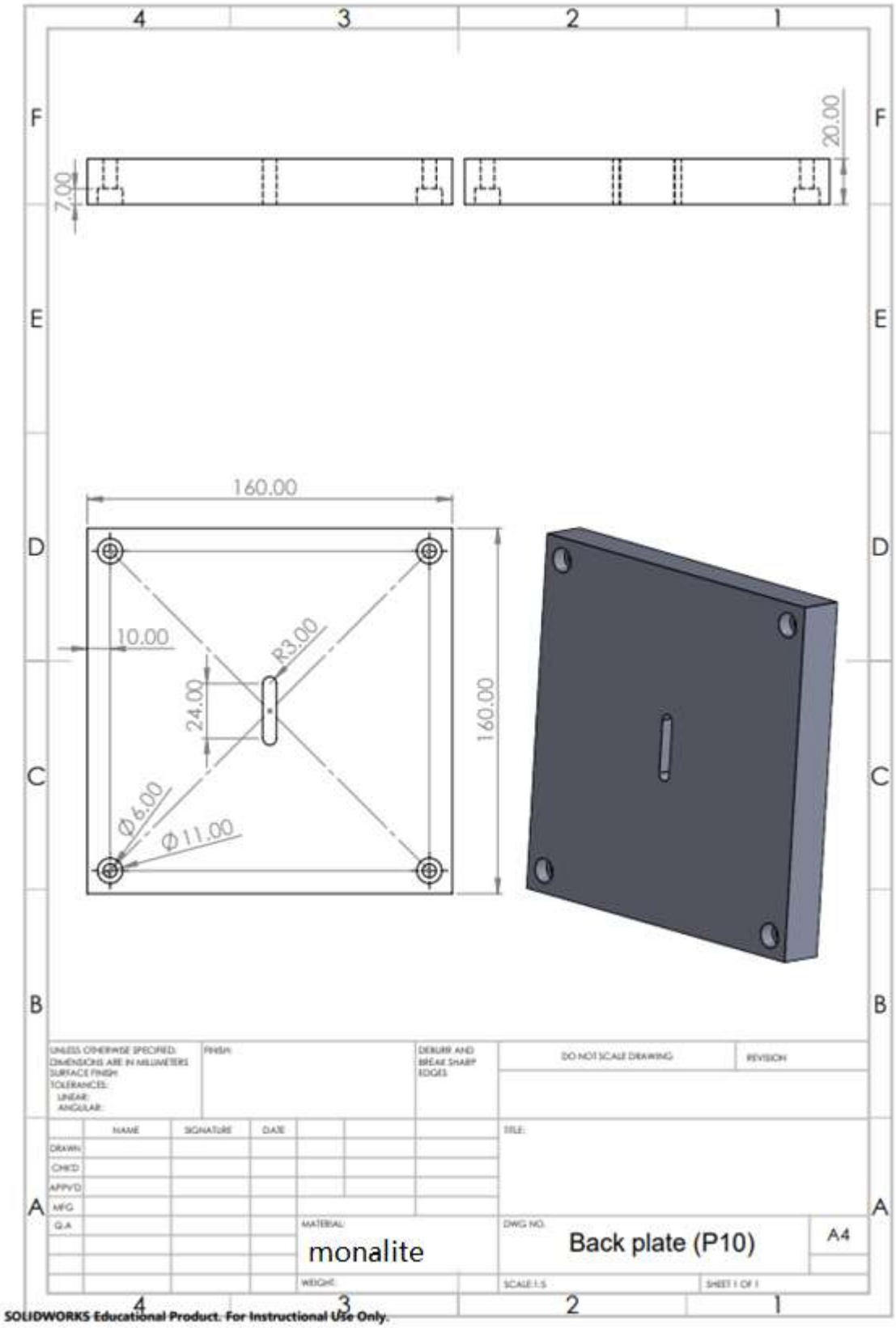

Top cover (P11)

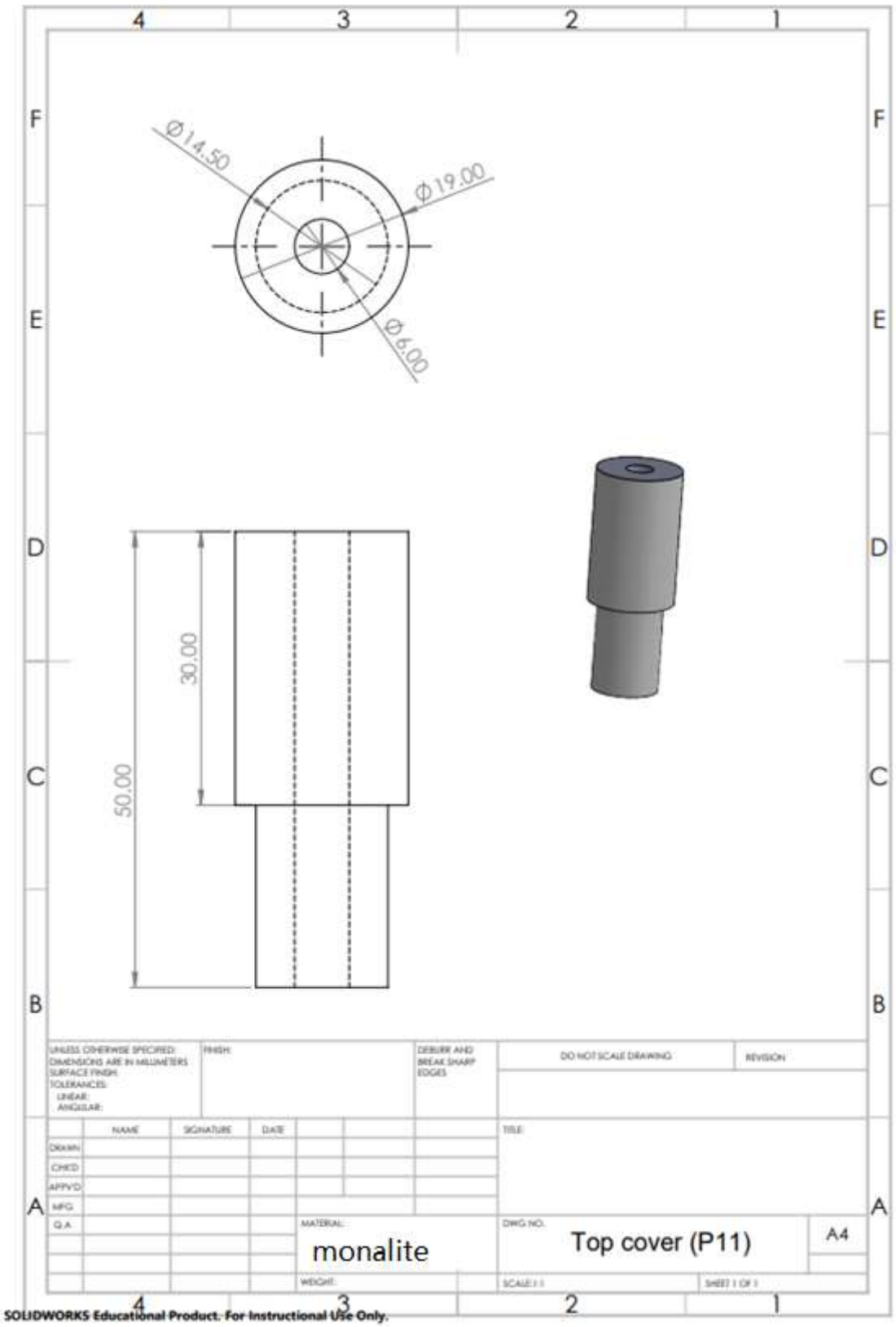

Sample adaptor (P14)

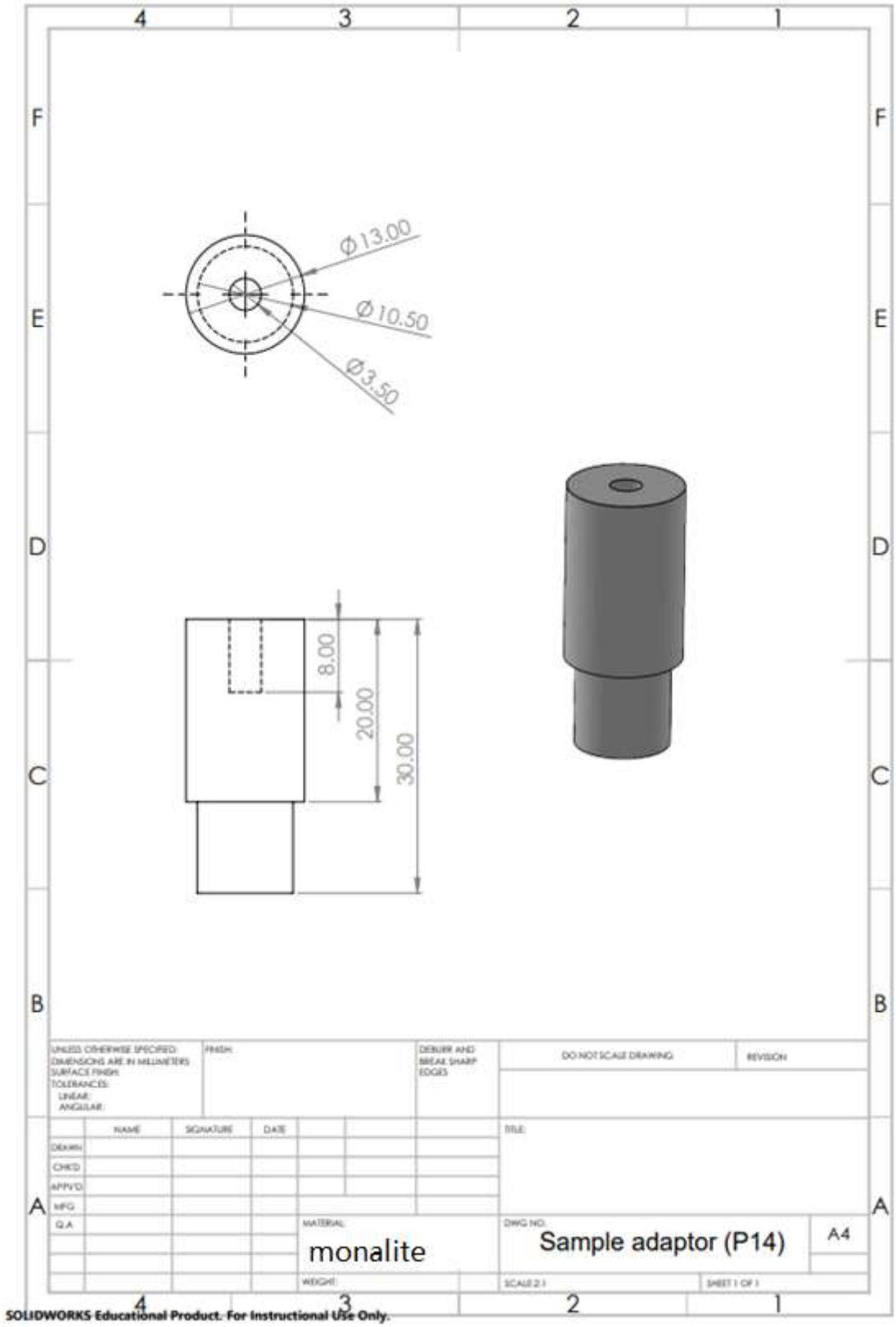

Adaptor (P16)

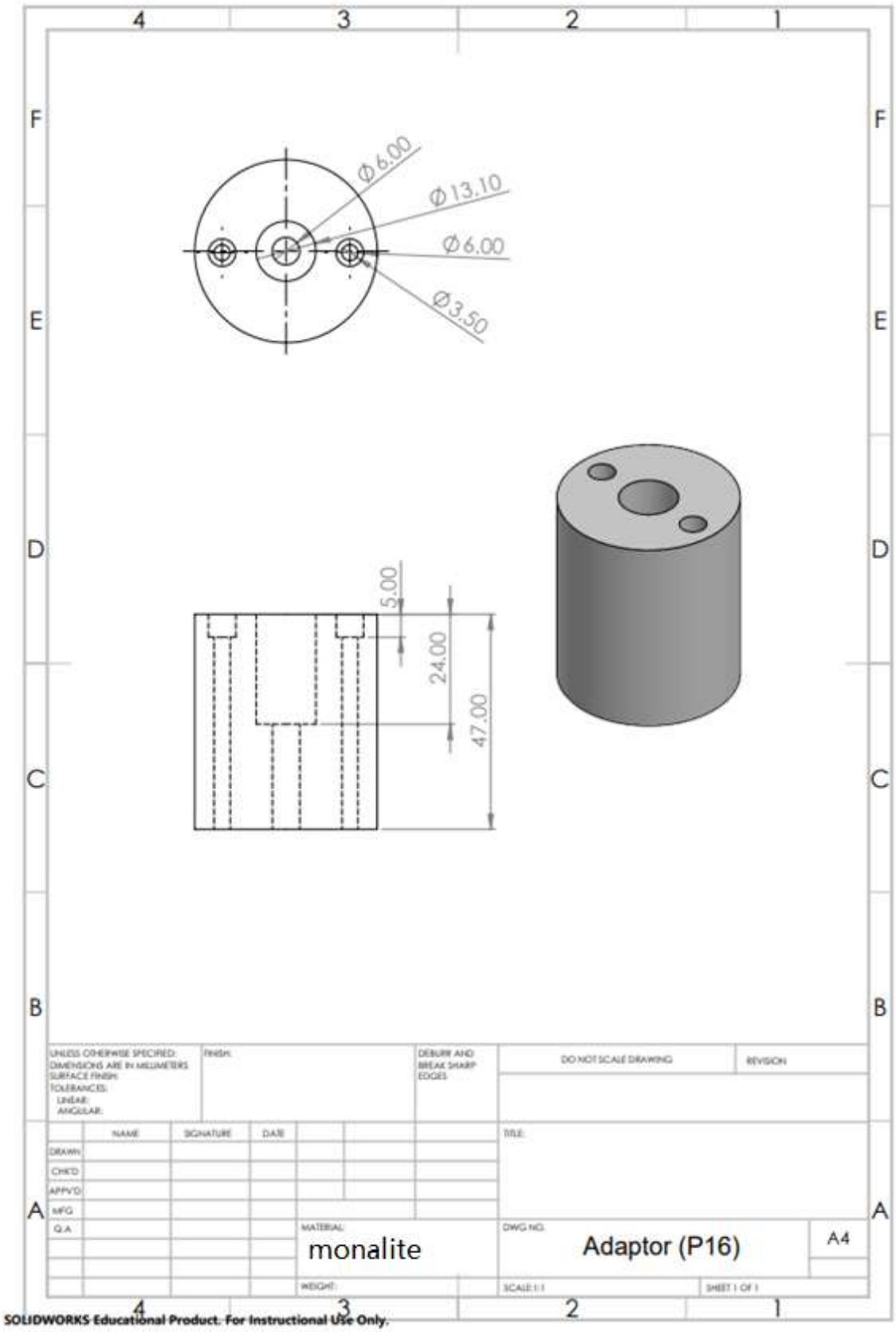
Ø6.00
Ø13.10
Ø6.00
Ø3.50
5.00
24.00
47.00
monalite
Adaptor (P16)
A4
SOLIDWORKS Educational Product. For Instructional Use Only.

Steel plate (P17)

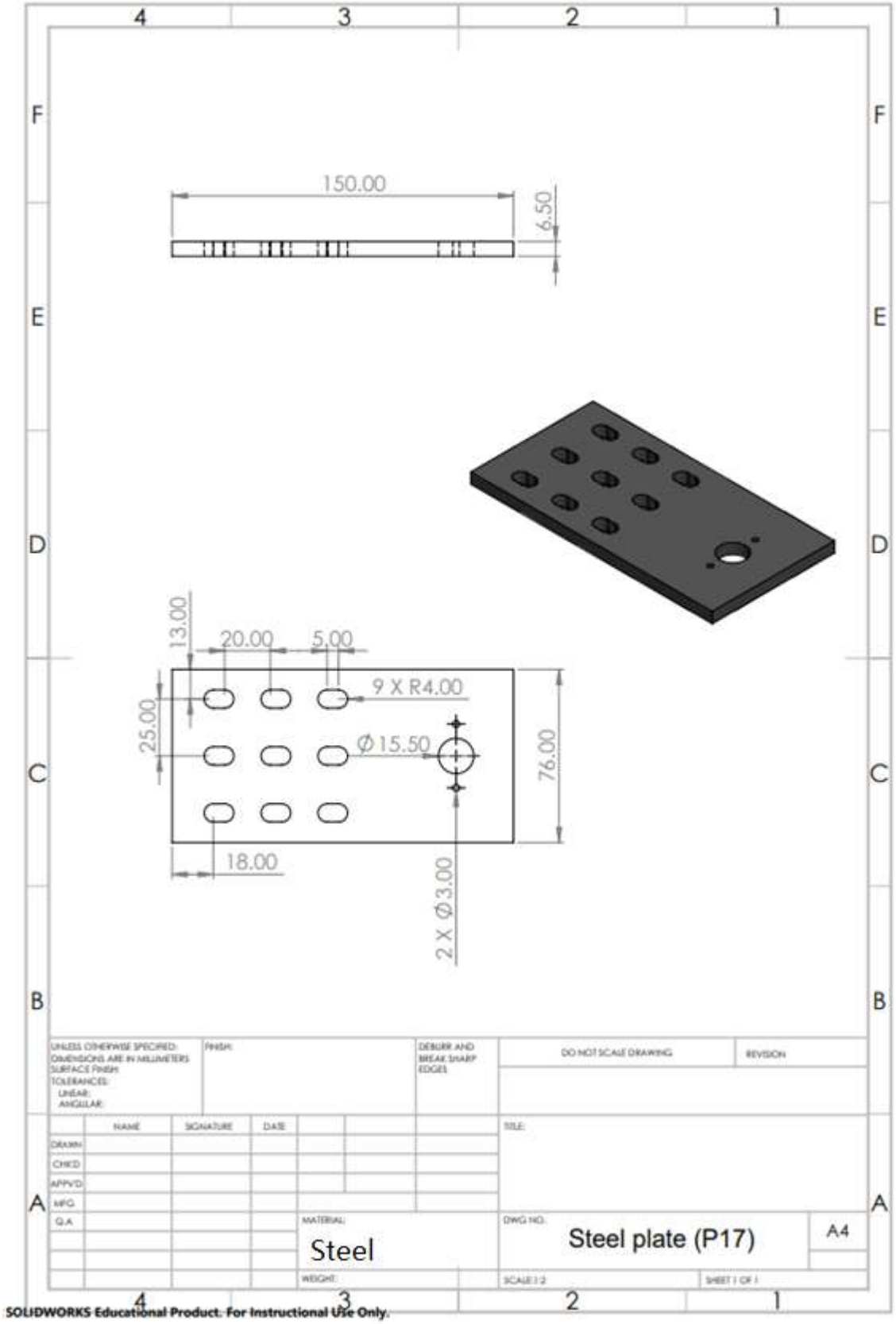

Appendix 2: MATLAB code used for sharing modes calculation

```
clear all;
%%
Type1_pair = []; %empty matrix of Type1 (tedrahedra-sharing)
Type2_pair = []; %empty matrix of Type2 (Bonds, vertex, edge and face-
sharing(3 4 5 6...)
%%
All_data = importdata('5477-750-1box_1.txt');
Fe_index = find(strcmp(All_data.textdata, 'Fe'));
Fe_number = size(Fe_index, 1); %Number of Fe
%%
for i=1:Fe_number
    for j=i+1:Fe_number
        dis = Eu_dis(All_data, Fe_index(i), Fe_index(j));
        if(dis<=4)
            Type1_pair = [Type1_pair; Fe_index(i), Fe_index(j)];
        elseif (dis>=4 && dis<=8)
            Type2_pair = [Type2_pair; Fe_index(i), Fe_index(j)];
        end
    end
end

%% define different sharing mode
Q = length(Type2_pair); %Count the number of Type2, which is Q
Type2_pair_shaired = cell(Q, 1);
for i=1:Q
    shaired_atoms = []; %
    rest_index = (1:size(All_data.data, 1))';
    rest_index([Type2_pair(i, 1), Type2_pair(i, 2)], :)=[];
    M = size(rest_index, 1); %Get 19998 remaining digits M
    for j=1:M
        dis1 = Eu_dis(All_data, Type2_pair(i, 1),
rest_index(j)); %calculate d1
        dis2 = Eu_dis(All_data, Type2_pair(i, 2),
rest_index(j)); %calculate d2
        if(dis1<=4 && dis2<=4)
            shaired_atoms=[shaired_atoms, rest_index(j)]; %Get the
shared atom index for each Fe-Fe of Type2
            Type2_pair_shaired{292} = shaired_atoms; %Save to cell array
        end
    end
end
%% Calculate the sum number of type1 and type 2, the fraction of each
types of sharing mode
num_type=[]; % s
for i=1:Q
    number = length(Type2_pair_shaired{i});
    if(number==0)
        num_type = num_type; %Unchanged if the pair has no shared
atoms
    else
        num_type = [num_type, number]; %Otherwise increase the number
of shared atoms for each pair of atoms
    end
end
%%
statistic = []; %A matrix used to count the number of different atomic
types
```

```
statistic(1,:) = unique(num_type); %The first line of statistic is the
number of different shared atoms
statistic(2,:) = hist(num_type,unique(num_type)); %The second line of
statistic is the number of different shared atomic numbers
for i=1:size(statistic, 2)
    statistic(3,i) = statistic(2,i)/(sum(statistic(2,:))+1); %The
third line of statistic is the percentage of different atomic number
types
end
percent_type1 = 1/(sum(statistic(2,:))+1);
%%
non_exist = []; %Fe atom index not present in Type1 and Type2
for i=1:Fe_number
    if(ismember(Fe_index(i), Type2_pair) || ismember(Fe_index(i),
Type1_pair)) %Appears in both Type1 and Type2, then non_exist remains
unchanged
        non_exist = non_exist;
    else
        non_exist = [non_exist, Fe_index(i)]; %Otherwise, the index
does not appear in Type1 and Type2
    end
end
non_exist_percent = length(non_exist)/Fe_number; %Non-occurring Fe as
a percentage of all Fe atoms
```